UNIVERSITY OF SOUTHAMPTON

FACULTY OF PHYSICAL SCIENCES AND ENGINEERING

Electronic & Computer Sciences

Microfluidic Devices for the Temporal Resolution of T Lymphocyte Competition

Volume I of I

by

Faith Bateman

Thesis for the degree of Doctor of Philosophy

April 2016

UNIVERSITY OF SOUTHAMPTON

ABSTRACT

FACULTY OF PHYSICAL SCIENCES AND ENGINEERING

Electronic and Computer Sciences

Doctor of Philosophy

MICROFLUIDIC DEVICES FOR THE TEMPORAL RESOLUTION OF T LYMPHOCYTE COMPETITION

by Faith Bateman

Every cell in the human body is unique. In the immune system this is essential so that a wide range of invading pathogens can be recognised. To achieve the heterogeneity in lymphocytes, immature T lymphocytes and B lymphocytes undergo 'priming' in the thymus and bone marrow to diversify the cell surface receptors. As such, bulk analysis of immune cells and overlooking outliers, such as cells exhibiting unusual characteristics or responses, could lead to interesting cell characteristics being disregarded.

By tracking the activation profile of a T lymphocyte against an antigen presenting cell in a high-throughput manner at the single cell level, the variation in activation levels of individual T lymphocytes will be identified. This will lead to an improved understanding of why certain T lymphocytes are more efficient at eradicating diseases.

This thesis describes the design and development of a bespoke microfluidic device able to trap thousands of individual cells in nanolitre wells, for the analysis of cell-cell interactions. The device is optically transparent, enabling T lymphocyte activation to be observed in real time using fluorescent microscopy and calcium staining; thousands of cells may be observed within a single microscope field of view. Cell-cell contact is controllable by the device, allowing the activation of T lymphocytes against antigen presenting cells to be viewed in real time, in a high-throughput manner.

The device has been used to investigate T lymphocyte activation against soluble stimulants, as well as antigen presenting cells. Specifically, the temporal calcium response of single cells has been studied and experimental results are presented. The findings reveal differences in activation profiles of individual cells within a clone population, which are not evident using state-of-the art bulk cell analysis techniques such as flow cytometry. This work highlights the importance of assessing single cell responses in an immune interaction.

Table of Contents

List of Tables

List of Figures

DECLARATION OF AUTHORSHIP

I, FAITH BATEMAN, declare that this thesis and the work presented in it are my own and has been generated by me as the result of my own original research.

Microfluidic Devices for the Temporal Resolution of T Lymphocyte Competition.

I confirm that:

1. This work was done wholly or mainly while in candidature for a research degree at this University;
2. Where any part of this thesis has previously been submitted for a degree or any other qualification at this University or any other institution, this has been clearly stated;
3. Where I have consulted the published work of others, this is always clearly attributed;
4. Where I have quoted from the work of others, the source is always given. With the exception of such quotations, this thesis is entirely my own work;
5. I have acknowledged all main sources of help;
6. Where the thesis is based on work done by myself jointly with others, I have made clear exactly what was done by others and what I have contributed myself;
7. None of this work has been published before submission.

Signed:.....

Date: .....

Acknowledgements

I would like to thank my supervisors Professor Hywel Morgan and Professor Tim Elliott for offering me the chance to undertake my PhD in this interdisciplinary area, and for their invaluable support and encouragement. I also want to thank Dr. Edd James for being my mentor and for always giving me great advice.

I wish to thank my friends for their support, in particular Michael Waite, for being the person who has stood by me through the ups and downs of my research.

Finally, I would like to dedicate this work in memory of my Mum, who I think of everyday and who taught me the importance of finding a job that inspires you.

Definitions and Abbreviations

ADP	Adenosine Diphosphate
AM	Acetoxymethyl
APC	Antigen Presenting Cell
Ca^{2+}	Calcium
cADPR	Cyclic Adenosine Diphosphate Ribose
CO_2	Carbon Dioxide
COC	Cyclic Olefin Copolymer
COP	Cyclic Olefin Polymer
DEP	Dielectrophoresis
DI	De-ionised
DMSO	Dimethyl Sulfoxide
DV	DeltaVision
EDTA	Ethylenediaminetetraacetic Acid
ER	Endoplasmic Reticulum
FACS	Fluorescence Activated Cell Sorting
FITC	Fluorescein Isothiocyanate
FSC	Forward Scatter

HCP	Hexagonal Close Packed
$I_{CRAC}C$	Calcium Release Activated Calcium Current Channel
IP_3	Inositol Triphosphate
IP_3R	Inositol Triphosphate Receptor
IPA	Isopropanol
ITAM	Immunoreceptor Tyrosine-based Activation Motif
K^+C	Potassium Channel
MFI	Mean Fluorescent Intensity
MHC	Major Histocompatibility Complex
MNP	Magnetic Nanoparticle
NAADPR	Nicotinic Acid Adenine Dinucleotide Phosphate Receptor
NK	Natural Killer
PBS	Phosphate Buffered Saline
PDMS	Polydimethylsiloxane
PEB	Post Expose Bake
PEG	Polyethylene Glycol
PIP_2	Phosphoinositol Biophosphate
PLCγ	Phospholipase Cγ

PLL-g-PEG	Poly-L-Lysine-grafted-Polyethylene Glycol
pMHC	Peptide-MHC
PMMA	Polymethyl Methacrylate
RBC	Red Blood Cell
RER	Rough Endoplasmic Reticulum
ROI	Region of Interest
RyR	Ryanodine Receptor
SD	Standard Deviation
SDS-PAGE	Sodium Dodecyl Sulfate Polyacrylamide Gel Electrophoresis
SEM	Standard Error of the Mean
SiOH	Silanol
SOC	Store Operated Calcium channel
SSC	Side Scatter
TAE	Tris-Acetate-EDTA
TAP	Transporter Associated with Antigen Processing
TCR	T Cell Receptor
TCR:pMHC	T Cell Receptor-peptide Major Histocompatibility Complex
UV	Ultraviolet

Chapter 1: Introduction and Motivations

1.1 Background

The purpose of the immune system is to protect the body from infection. It exists in two parts:

1. The innate immune system, which acts as the first line of defence against infection in a non-specific manner.
2. The adaptive immune system, which is a specific response against invading pathogens that is slower, but more accurate.

The adaptive immune system is comprised of cells that have specific receptors, designed to recognise distinct pathogens and mount an immune response. The white blood cells 'T lymphocytes' are members of the adaptive immune system that account for approximately 0.024% of blood cells. T lymphocytes are divided into two populations:

1. $CD4^+$ T lymphocytes, which are generally helper cells that secrete cytokines and activate B cells.
2. $CD8^+$ T lymphocytes that are cytotoxic cells.

$CD8^+$ T lymphocytes recognise and eliminate pathogen-infected cells by releasing granules that contain cytotoxins into the cell [1]. There is approximately one $CD8^+$ T lymphocyte per ten thousand blood cells [2], which equates to around 5.3×10^5 cells per mL of blood.

1.1.1 Immune system activation

When a pathogen invades the human body, an Antigen Presenting Cell (APC) processes it through the cytosolic pathway, before presenting it on the cell surface in conjunction with the Major Histocompatibility Complex (MHC). A cytotoxic T lymphocyte with the correct receptor will then recognise the infected cell [1].

Inside the APC, after being infected by the pathogen, proteasomes within the cytosol randomly degrade the proteins into short peptide sequences. The resultant peptide sequences are known as antigenic epitopes. The Transporter Associated with Antigen Processing (TAP) protein then transports these epitopes into the Rough Endoplasmic Reticulum (RER). Inside the RER the epitopes associate with MHC 1 molecules and are

then transported to the APC cell surface via the Golgi apparatus; as depicted in Figure 1-1.

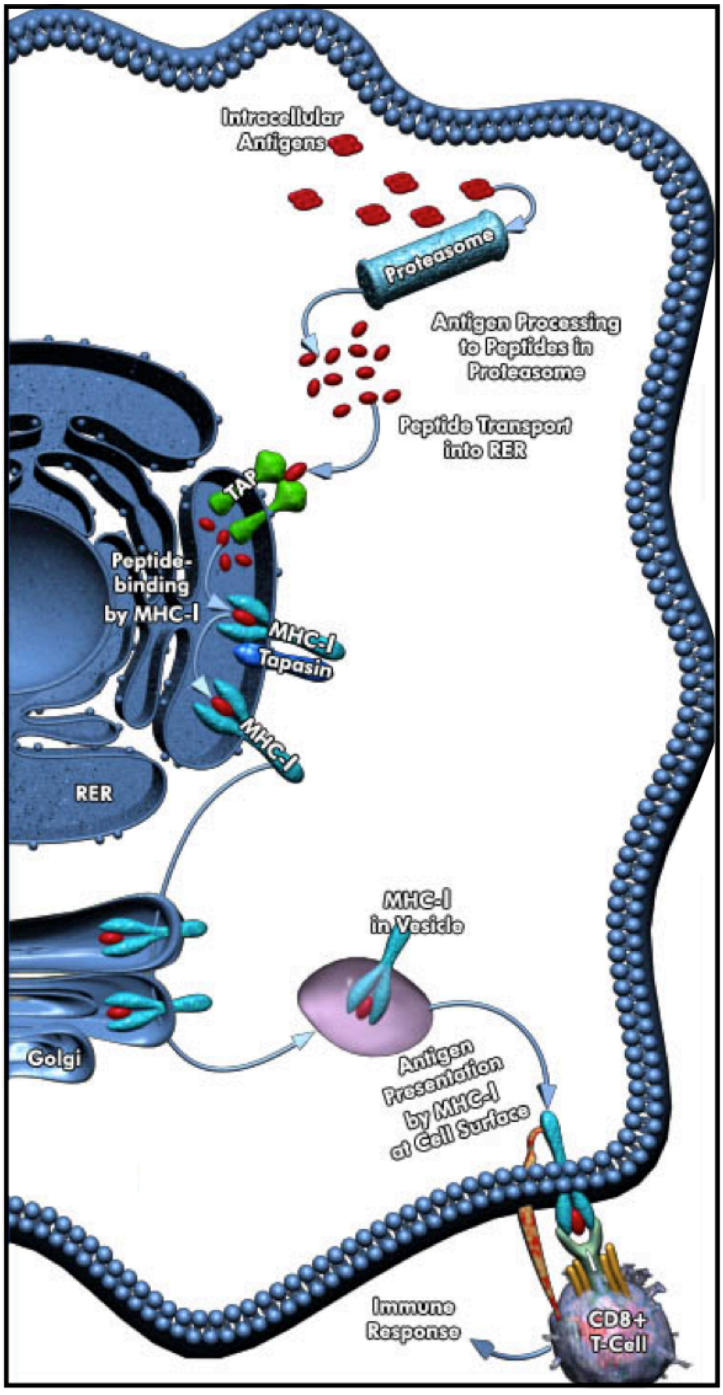

Figure 1-1: Diagrammatic representation of antigen processing and MHC 1 presentation, adapted from [3].

Once the antigen is displayed on the APC surface in conjunction with MHC 1, a $CD8^+$ T lymphocyte can recognise and bind to the APC via the T Cell Receptor (TCR); Figure 1-2. This event initiates an immune response, resulting in the eradication of the infected cell.

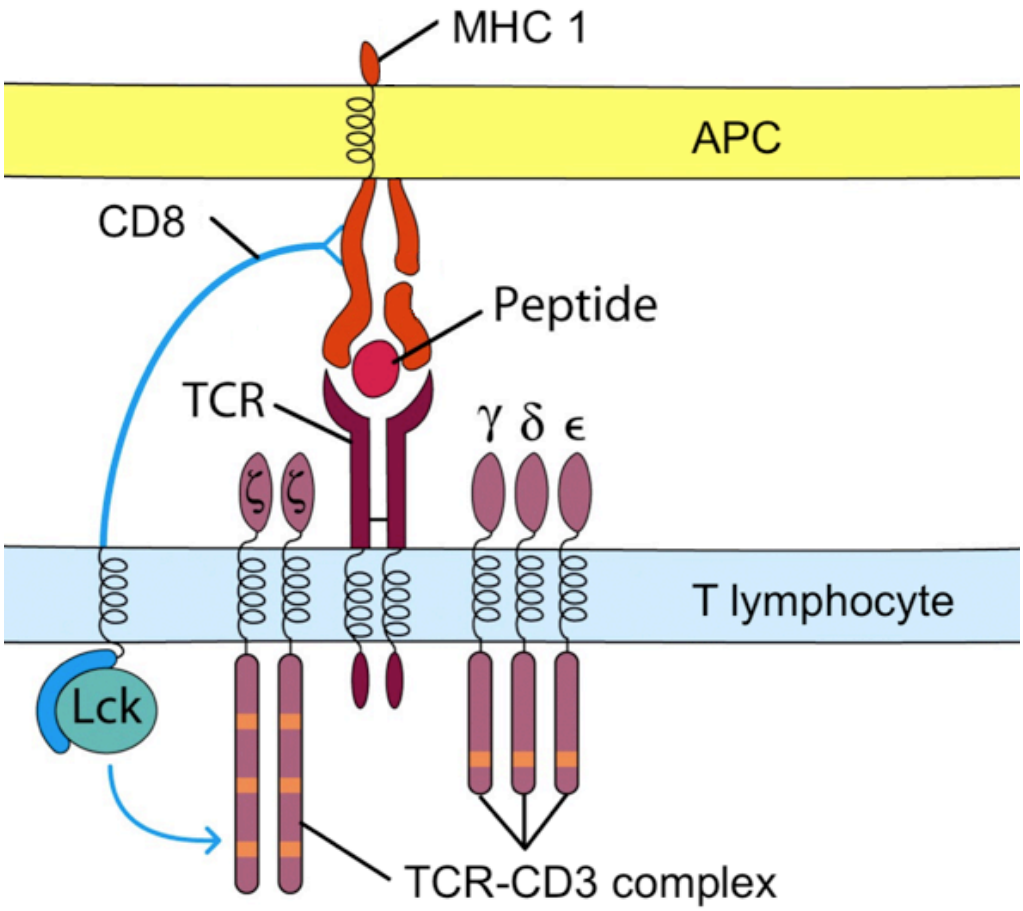

Figure 1-2: Recognition of an APC by a T lymphocyte, through the binding of the TCR to an antigen in conjunction with MHC 1. Adapted from [1].

T lymphocyte activation

When a T lymphocyte is activated via antigen receptor ligation (TCR:pMHC), a cascade phosphorylation reaction is induced within the cell, marking the beginning of an immune response. An early indicator of T lymphocyte activation is an increase in intracellular Calcium (Ca^{2+}), viewable by calcium-dependant fluorophores such as Fluo-8AM [4] (detailed in 'Fluo-8AM'). It is believed that Ca^{2+} signals aid in the stabilisation of

TCR:pMHC engagement by reorganisation of the cytoskeleton around the contact region, as well as augmenting subsequent gene activation [5].

The exact mechanisms of Ca^{2+} flux inside cells are still not entirely understood [6], but the general response is illustrated in Figure 1-3. Ca^{2+} flux has two phases during T lymphocyte activation:

1. TCR-APC ligation causes Ca^{2+} to be released from internal stores, in turn causing a fast increase in internal Ca^{2+} levels.
2. Depletion of Ca^{2+} levels in the internal stores results in Ca^{2+} channels in the cell membrane opening, allowing Ca^{2+} from the surrounding media to migrate into the cell.

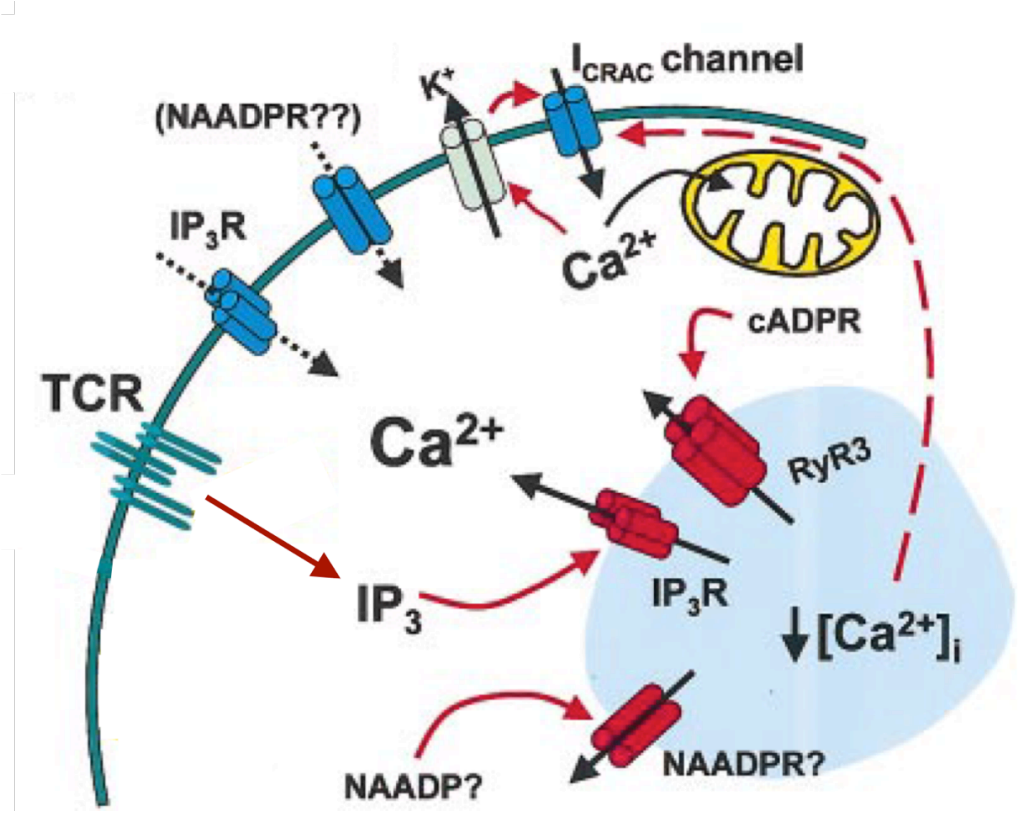

Figure 1-3: Diagram detailing the basic mechanisms of calcium flux in a T lymphocyte after TCR engagement. Adapted from [6].

After TCR:pMHC ligation, lipid rafts associate with the TCR complex and cause the tyrosine kinase $p56^{LcK}$ (Figure 1-2) to bind to the cytoplasmic tails of the TCR-CD3 complex [1]. This phosphorylates the Immunoreceptor Tyrosine-based Activation Motifs

(ITAMs) of the CD3 molecule; detailed in Chapter 4.1.2. The result of the phosphorylation cascade is the production of Inositol Triphosphate (IP_3).

IP_3 binds to Inositol Triphosphate Receptors (IP_3R) in the Endoplasmic Reticulum (ER) and Rough Endoplasmic Reticulum (RER), causing the IP_3R channel to open and allow Ca^{2+} to move into the cytoplasm; Figure 1-3. The RER also has Ryanodine Receptors (RyRs) in its membrane that help mediate Ca^{2+} release; the RyR is sensitised by Ca^{2+} in conjunction with Cyclic Adenosine Diphosphate Ribose (cADPR), so that additional Ca^{2+} causes the release of even more Ca^{2+} in a feed-forward mechanism. Additionally Nicotinic Acid Adenine Dinucleotide Phosphate Receptors (NAADPRs) play a role in the release of Ca^{2+} from intracellular stores; however the mechanisms of this are poorly understood to-date.

The resultant drop in Ca^{2+} levels in the intracellular stores prompts Store Operated Calcium channels (SOCs) that span the cell membrane to open, resulting in extracellular Ca^{2+} entering the cell. Again, the exact operation of these channels is not yet fully understood, but one SOC is thought to be an important route for Ca^{2+} entering the cell – the Calcium Release Activated Calcium Current Channel ($I_{CRAC}C$). Ca^{2+} moving through the $I_{CRAC}C$ is thought of as a current, and can be increased by Ca^{2+} binding to extracellular sites on the channel, or decreased by an excess of Ca^{2+} inside the cell close to the channel entrance. To prevent $I_{CRAC}C$ closure, mitochondria that are located close by work to sequester the excess Ca^{2+} so that the channel remains open. The exact number of $I_{CRAC}Cs$ in a T lymphocyte is unknown; although it is thought that an activated T lymphocyte has around 140.

As the influx of Ca^{2+} is dependant on the membrane potential (a more negative potential stimulates more Ca^{2+} influx), when a T lymphocyte is activated, voltage-gated Potassium Channels (K^+Cs) also activate, hyperpolarising the membrane making it more negatively charged.

In summary, Ca^{2+} flux inside a stimulated cell consists of an initial rise in intracellular Ca^{2+} from internal stores, followed by a longer, sustained level of Ca^{2+} owing to extracellular Ca^{2+} being brought into the cell. The increase in cytosolic Ca^{2+} can be used to assess T lymphocyte activation after TCR:pMHC engagement.

1.1.2 The importance of single cell studies

Cells, even clone cells that should be genetically identical, are all unique. This heterogeneity has been overlooked in cell biology for decades. Many standard analysis techniques utilise bulk analysis methods such as western blots or flow cytometry. These often give an output that is averaged across a population, masking phenotypic variation. The reason for using bulk analysis methods is that they are often well-established techniques, which are simpler than single cell analytical techniques [7]. The issue with bulk analysis on whole cell populations is that individual cell characteristics are overlooked and, more importantly, an average result can be completely incorrect.

Overlooking outliers, such as cells exhibiting unusual characteristics or responses, could lead to interesting cell characteristics being disregarded. This is of paramount importance in immune studies as immature T lymphocytes and B lymphocytes undergo 'priming' in the thymus and bone marrow. Priming ensures that the lymphocytes do not react against 'self' cells, and provokes the lymphocytes to gain specificity towards particular peptide epitopes. Hence, immune cells are inherently heterogeneous. As such, bulk analysis masks cell diversity and could yield misleading results [8], [9], [10].

Microfluidic devices present a practical solution for single cell capture and analysis [11]. Microfluidic dimensions are comparable to cell size (microns), require smaller sample and reagent volumes than traditional bulk analysis techniques due to their reduced size, and are generally both portable and disposable. Microfluidics are intrinsically well suited for immune studies. As mentioned previously, immune cells such as T lymphocytes are rare, and the progression of an immune response is very dynamic and relies on cell-cell interactions. As such, a device that requires small sample volumes and allows cell-cell interactions to be temporally studied will make detailed analyses possible. In the future, this could lead to advances in personalised medicine [11], as individual patient samples could be tested against specific biomarkers.

Immunophenotyping through the use of microfluidic devices could also hold the key to not only a better understanding of the immune system, but aid in the development of immunotherapies for the treatment of cancer and infectious diseases [11][12].

If tumour-specific T Lymphocytes could be isolated, a patient's own immune system could be used to fight tumours, averting the need for more aggressive treatments such as chemotherapy.

1.1.3 An application of single T Lymphocyte studies: Immunodominance

All T lymphocytes have different receptors, so not all T lymphocytes can recognise and activate against every antigen displayed on an APC. APCs display up to 10^5 different antigens on their cell surface and so could activate multiple different T lymphocytes; however, this does not generally occur. One T lymphocyte response will dominate and cause the other T lymphocyte responses to shut down. The reason for this is Immunodominance: the reproducible, hierarchical response of a T lymphocyte to different antigenic epitopes [13].

Immunodominance between T lymphocytes of different specificity is explained in Figure 1-4. T Cell 1 has the correct TCR to activate against an antigen epitope on the APC, as does T Cell 2. However, when T Cell 1 and T Cell 2 simultaneously recognise their antigen epitopes, two separate immune responses are not initiated; the response is unknown.

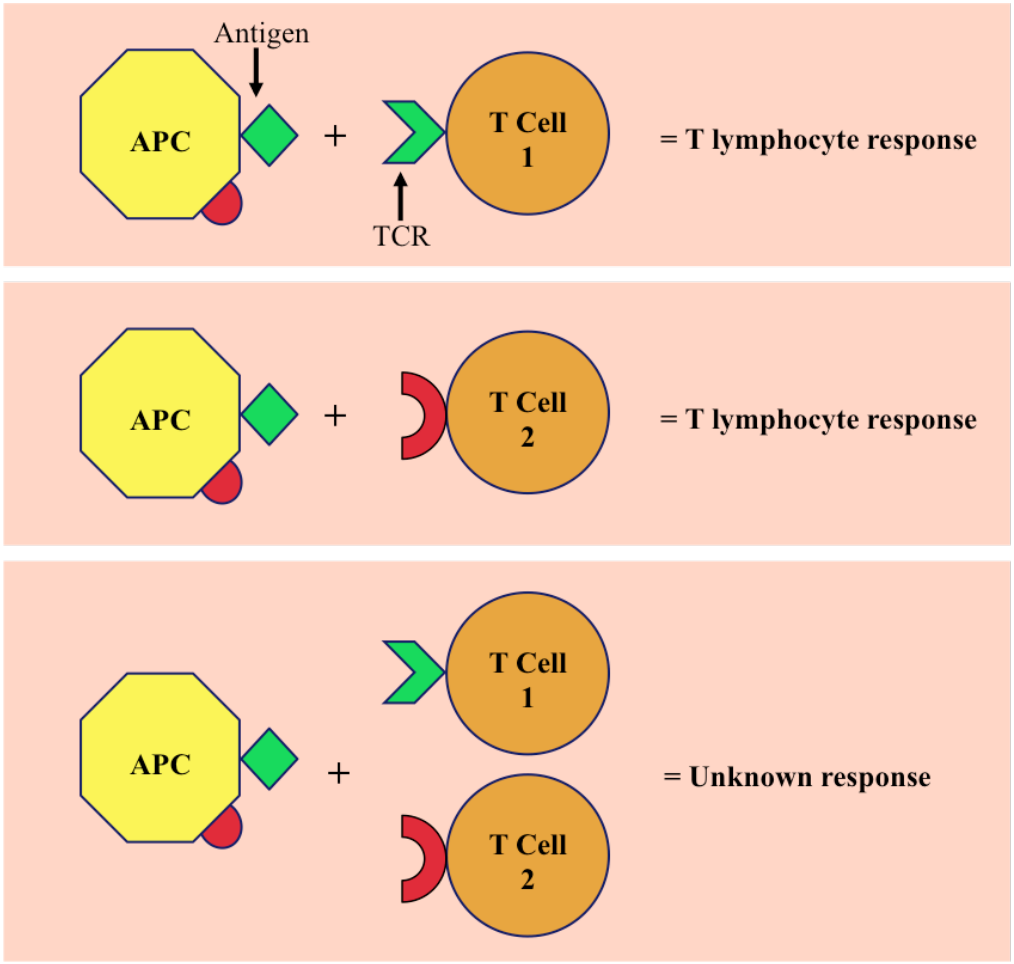

Figure 1-4: T lymphocyte activation via TCR:pMHC ligation; the immunodominance effect.

Immunodominance is the phenomenon behind why multiple vaccinations cannot be administered at the same time, and why some T lymphocytes are more likely to be activated against an APC than others. The immunogenicity of a peptide is determined by factors such as the processing rate of the peptide epitope by the APC, the binding efficiency of the peptide to the MHC complex and pMHC cell surface abundance and stability [14]; these factors influence cross-competition immunodominance [15][16]. However, the underlying reason behind immunodominance is not solely due to epitope immunogenicity. It is unknown why peptides that would elicit a response in a T lymphocyte when presented alone, do not provoke an immune response when presented in conjunction with other peptides [14][17].

Two possible theories are:

1. Immunodominance is the result of T lymphocyte competition for a limited resource, such as APC cell surface [13].
2. Immunodominant T lymphocytes have the functionality to supress the activation of other T lymphocytes [13][16].

Investigations of immunodominance to-date [15][18-20] have used bulk cell populations. It is hypothesised that the reason for immunodominance is the signalling that occurs between cells when they first interact (within a minute) [21]; hence, to study immunodominance it is necessary to investigate single cell-cell communications from the moment of TCR:pMHC ligation. Such a device would also be of great biological significance in other cell biology applications [22].

1.2 Aim

To develop a microfluidic device that allows observable, parallel activation of multiple T lymphocytes through single cell handling.

1.3 Project objectives

To create a microfluidic device capable of studying T lymphocyte activation at the single cell level, to gain a greater understanding of why certain T lymphocytes are activated more efficiently against an APC than other T lymphocytes. This project is an interdisciplinary endeavour between Engineering and Immunology, to develop the engineering solution which will further our understanding of the immune system through the creation of a microfluidic device that allows single cell-cell interactions to be studied.

To achieve this, a microfluidic device shall be developed that fulfils the following criteria:

- Ability to capture single cells.
- Enable high-throughput data acquisition.
- Functionality to bring two cells into contact for a defined period of time, after which it is possible to dissociate them, allowing sequential contact.
- Allow recovery of specific cells.

- Be optically transparent to permit observation of cell-cell interaction with microscopy.

1.4 Project motivation

Not all cells within a homogeneous population are identical; there is phenotypic variation that is difficult to assess using current bulk analysis methods. If a device could be created that allows single cell-cell interactions to be studied in a time dependent manner, interesting cells could be identified for further analysis.

Ultimately, if it became possible to identify and isolate immunodominant T lymphocytes, the reason behind immunodominance could be investigated. This could lead to a better understanding of how we could use the immune system to fight infections, and eventually cancer.

The end goal is for a patient with cancer to be treated using immunotherapy; evoking the patient's own immune system to combat the disease, rather than using more aggressive treatments such as chemotherapy or radiotherapy. These therapies also kill healthy cells within the body, and have a negative impact on a patient's quality of life.

1.5 Thesis structure

A breakdown of this thesis is given below:

Chapter 1: Introduction and Motivations
This chapter introduces the project background and the motivation behind the research question posed.

Chapter 2: Literature Review
A detailed literature review of work to-date on single cell capture is presented, with a focus on how these methods could be used to address the project objectives.

Chapter 3: Design and Fabrication of Single-Cell Arrays for the Time-Resolved Measurement of T Lymphocyte Activation
In this chapter, the work undertaken to create a cell capture device using the 'SlipChip' architecture is described. It contains information on the principles of SlipChip, fabrication, experimental results and operational issues. Finally it explains the shortcomings of this technology and why investigations using this device were ceased.

Chapter 4: Microwell Array Cell Traps for Single Cell Activation

This chapter details the investigation and fabrication of microwell arrays for single cell capture, and activation analysis. It includes results of T lymphocyte activation against the soluble stimulants, anti-CD3 and ionomycin.

Chapter 5: Measurement of Physiologically Relevant T Lymphocyte Activation Following Cell-Cell Contact in Microwell Array Cell Traps

In this chapter cell-cell contact is achieved through the use of two microwell array plates and a bespoke alignment rig. It describes the development of the microwell array cell-cell contact architecture, and results of B3Z T lymphocyte activation against the APC line K89.

Chapter 6: Conclusions and Future Recommendations

The final chapter of this thesis summarises the work undertaken in this project, and the experimental findings. It also details recommendations for future work, to augment the microwell array cell-cell architecture developed.

Chapter 2: Literature Review

2.1 Background

There are a number of well-established techniques for analysing single cells such as automated microscopy (taking multiple successive images of adherent cells over a period of time before performing image analysis), laser scanning cytometry (fluorescent analysis of fixed or adherent cells using a laser) and flow cytometry (fluorescent analysis of cells in liquid suspension). However, none of these techniques allow high-throughput single cell interactions to be studied. Flow cytometry is most commonly used and can assess qualities such as cell size, internal complexity and, when labelled with a fluorophore, fluorescence of a cell. Flow cytometry is also used to sort cell populations depending on their characteristics; however it cannot study more than one cell at a time and is unable to study cell-cell interaction. Additionally, flow cytometry only provides a 'snapshot' analysis of a cell and gives no temporal development information [23].

Microfluidic devices for cell manipulation are emerging as valuable tools within the life sciences to separate and study single cells, especially rare cells and cell populations that have non-Gaussian distributions; allowing a heterogeneous population to be fully described [24-26]. Due to the ability to handle small (nanolitre and microlitre) volumes, and having dimensions comparable to the size of single cells, microfluidic devices are well suited to work with single cells and allow reliable cell handling. The advantage of using microfluidics over standard laboratory protocols to analyse cells are that the volumes of samples and reagents required are much smaller, leading to reduced cost, waste and sample size. Additionally, it is possible to obtain integrated microfluidic chips that can multiplex protocol steps, reducing time and manpower.

The purpose of this review is to highlight the microfluidic technologies available for single cell analysis. The features will be discussed in respect to a particular application: trapping a single T lymphocyte and bringing it into contact with a single APC, in a timed event.

The technology should allow assessment of cell-cell interaction between a T lymphocyte and an APC, and the available functionality for the same APC to then be interacted with a subsequent, different, T lymphocyte. There should then be functionality to extract cells of interest for further analysis.

The review will be structured so that each available microfluidic technology is discussed and conclusions will be drawn at the end.

2.1.1 Requirements

The purpose of this project is to trap a single T lymphocyte and bring it into contact with a single APC, to assess the temporal activation profile of the T lymphocyte, once cell contact has been achieved. The investigation necessitates the inclusion of a fluorescent calcium marker (Fluo-8AM), so activation can be viewed in relation to time (Chapter 4: Fluo-8AM).

The technology must fulfil the following requirements:

- The cell trap must maintain the correct conditions for the cells to survive and sustain full function (i.e. correct temperature, media composition etc.);
- There must be a way to bring the cells into contact, and separate them;
- It must be possible for the interaction to be observed (i.e. using microscopy and a fluorescent calcium dye);
- The device needs to be easy to reproduce, portable and simple to use, so biologists could use it without an engineer present;
- It would be beneficial for there to be a way to extract the cells after the interaction, and control cell interaction time.

A suitable technology will embody all these capabilities.

2.2 Flow cytometry

Flow cytometry is the current state-of-the-art bulk analysis method. A basic overview of how a flow cytometer operates is displayed in Figure 2-1. The sample cells move through a fluidic stream that hydro-dynamically focuses the cells, ensuring single cells (or conjugates) move past the laser source. When a cell passes the laser source, it will scatter the light. This scattered light is filtered into different wavelengths of interest and then analysed, displaying cell properties such as cell size (forward scatter), granularity

(side scatter) and fluorescence (if the cell has been labelled with a fluorescent marker).

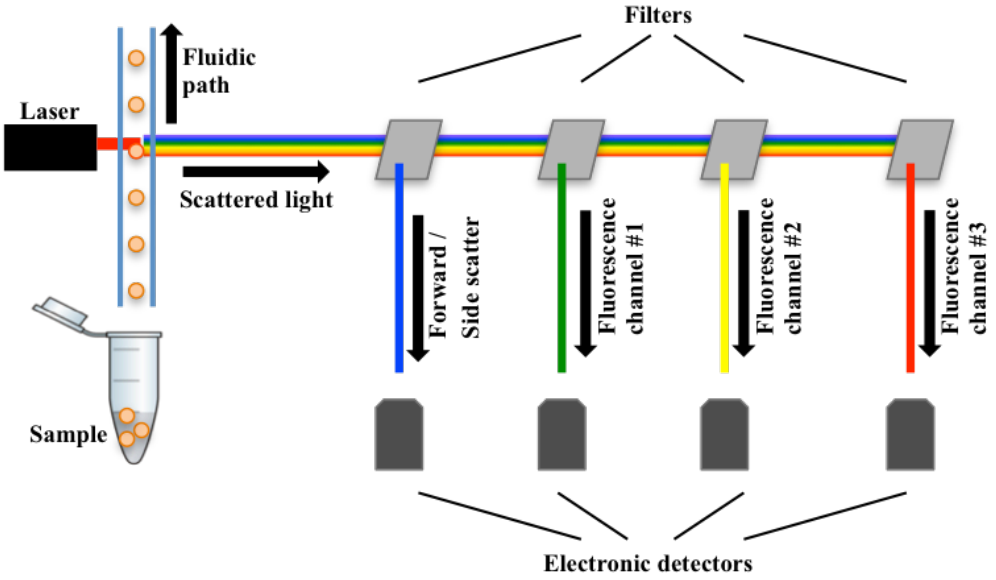

Figure 2-1: Schematic showing the basic concept of a flow cytometer.

The sample cells in liquid suspension move in single file past a laser. When a cell passes the laser it will interrupt the light beam and the scattered light is collected through various filters and sent to electronic detectors that analyse the results.

Flow cytometry is an important tool for looking at a whole population of cell responses and collecting average data. However, it is difficult to identify individual cells and there is no temporal control over cells, hence it is not an adequate solution for this project.

2.3 Microfluidic systems for monitoring single cell-cell interaction in a high-throughput manner, with heterotypic cell cultures

2.3.1 Cells in droplets

A way of separating individual cells is to encapsulate them in droplets. In 2001 Thorsen *et al* [27] developed a microfluidic device capable of creating variable sized droplets using a T-shaped junction between two fluid flows of oil and water; illustrated in Figure 2-2. As oil and water are immiscible fluids, at the junction the force of the water on the oil flow causes droplets to form.

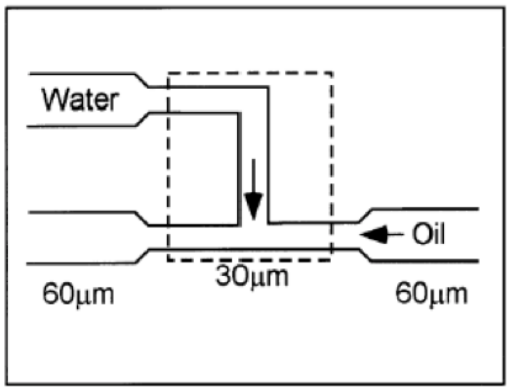

Figure 2-2: T-junction used to create droplets at the point of liquid intersection; adapted from [27].

Edd *et al* [28] encapsulated cells in droplets with high reliability using cross-flowing streams; Figure 2-3.

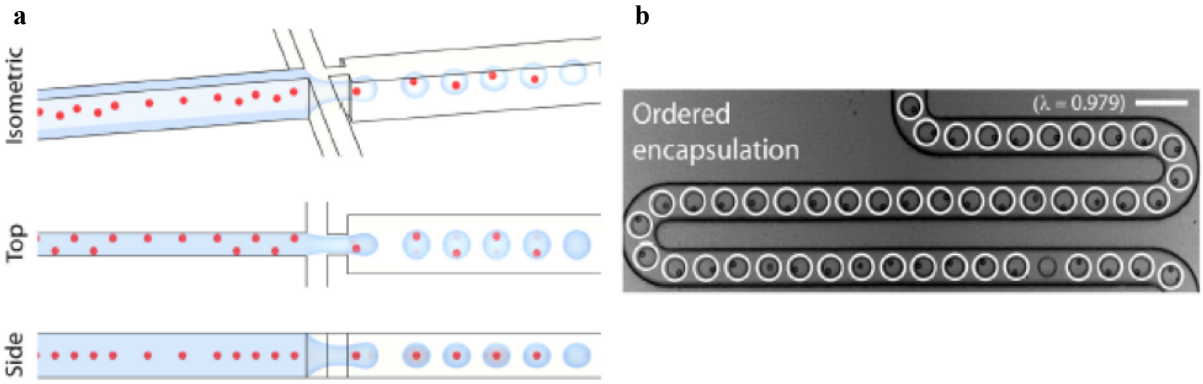

Figure 2-3: Diagram depicting device operation, taken from [28].

Organised cells within the liquid flow are forced through the cross at 13 µL /min and interact with fluorocarbon oil flowing at 85 µL/min, creating 14.6 pL droplets at 14.9 kHz. a) Diagram depicting cell flow and encapsulation, b) Microscope image of encapsulated beads, on average there are 0.979 (=λ) beads per droplet. Scale bar = 100 µm.

Edd *et al* report 0.966 cells per droplet with their device, resulting from the ordered encapsulation method they employ. Cells have equal spacing between them when they enter the cross flow stream due to a high density of cells being forced at high speed through a high aspect ratio microchannel. Aspect ratio = 1: 2: 2222 (W: H: L). The

authors achieved much higher single cell loading than earlier methods that use random encapsulation [29], which result in droplets containing a Poisson distribution of cells:

$$\boldsymbol{P(\lambda; k) = \lambda^k \exp(-\lambda) / k!} \qquad (2\text{-}1)$$

Where λ = average number of cells per droplet, k = number of cells in a droplet.

As a result of the Poisson distribution of cells in droplets, to obtain single cell occupancy in the majority of droplets, fewer cells are seeded into the stream. This results in the majority of droplets containing no cells, causing a very low-throughput experiment.

The use of droplets to encapsulate cells is a useful technique to separate individual cells; however for the purpose of this project, once encapsulated, two 'cells-in-droplets' would need to be merged for a defined amount of time for cell activation to take place. The droplets would then need to be separated so that individual cells could be extracted for further analysis.

Although there are a number of methods to merge droplets [30-32], all could cause high shear force on the cells, or result in droplet surfactant interacting with the cells and potentially causing cell lysis. To analyse the activation of the combined cells, the inclusion of a fluorescent dye would be necessary. This could be pre-included in one droplet-containing-cell [31], but calcium imaging of a moving droplet would be very difficult as the signal intensity is weak for a single cell. To release the cells, the surfactant layer would need to be disrupted by heating, chemical disruption, or subjecting them to an electric field (other methods are available); however, these processes would result in the loss of the extra-cellular fluid, which may contain ions or molecules of interest [10], and possibly harm the cells. Additionally, adherent cells (the majority of mammalian cells) may undergo apoptosis inside droplets if they have insufficient cell-matrix interactions [33].

This disorganised cell release would also make it difficult to select one cell in particular after the experiment. Finally, another issue with combined droplets is that there is no way to control the interaction time between the cells, an important factor for determining activation characteristics. For the reasons stated above, droplet encapsulation does not present a good method for causing cell-cell contact in a controlled manner.

2.3.2 Hydrodynamic traps

In 2005, Lee and Hung [34] showed that two fibroblast cell lines could be trapped side-by-side in a microfluidic device, allowing cell-cell communication to occur.

The device shown in Figure 2-4 works by flowing cells in using a syringe via a connecting port from 'West' to 'East', initially with the 'North' and 'South' channels closed. Once the cells are inside the device, the East port is closed and the South port is opened, causing the cells to be drawn towards the South port and then trapped in a version of patch clamping, originally developed by Neher and Sakmann in the late 1970s [35]. The remaining un-bound cells are washed from the device and the same protocol is then used to trap another cell population in the North ports. As the cells used in this experiment were around 12 µm in diameter, and the width of the channel is only 20 µm, the cell membranes of the two cell populations are touching. The West to East channel height is 50 µm, allowing un-bound cells to flow past full traps. See Figure 2-4.

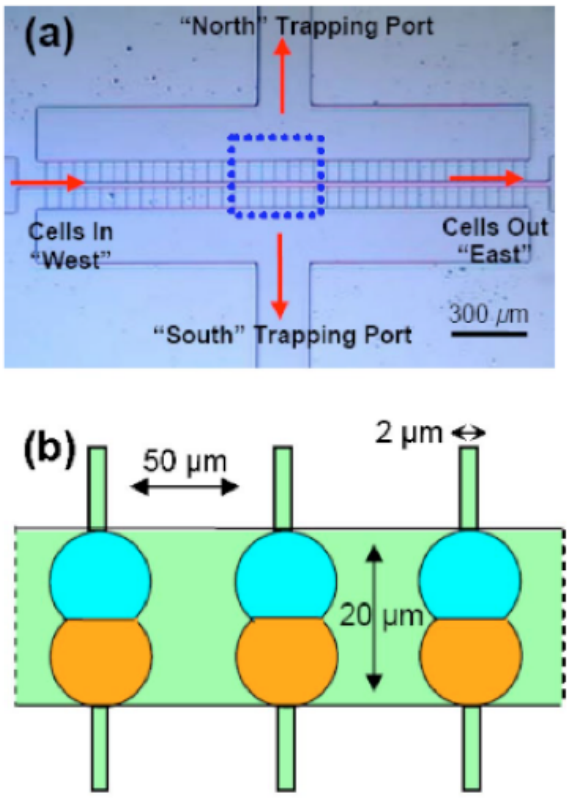

Figure 2-4: a) Microscope image of hydrodynamic cell trapping device, b) Illustration showing device dimensions. Adapted from [34].

This method of cell trapping is simple and would allow the cell-cell interaction between two different cell types to be studied. The extraction of specific cells of interest could be achieved by forcing air through the North or South port, but this device does not provide any time control over cell interaction.

Another method of hydrodynamically trapping single cells was shown by Di Carlo, Wu and Lee in 2006 [36, 37]. The authors created arrays of rounded traps in Polydimethylsiloxane (PDMS), using soft lithography from SU-8 masters. They then oxygen plasma bonded these to glass slides. Cells in suspension medium (Phosphate Buffered Saline (PBS)) flowed in through a branched channel as seen in Figure 2-5.

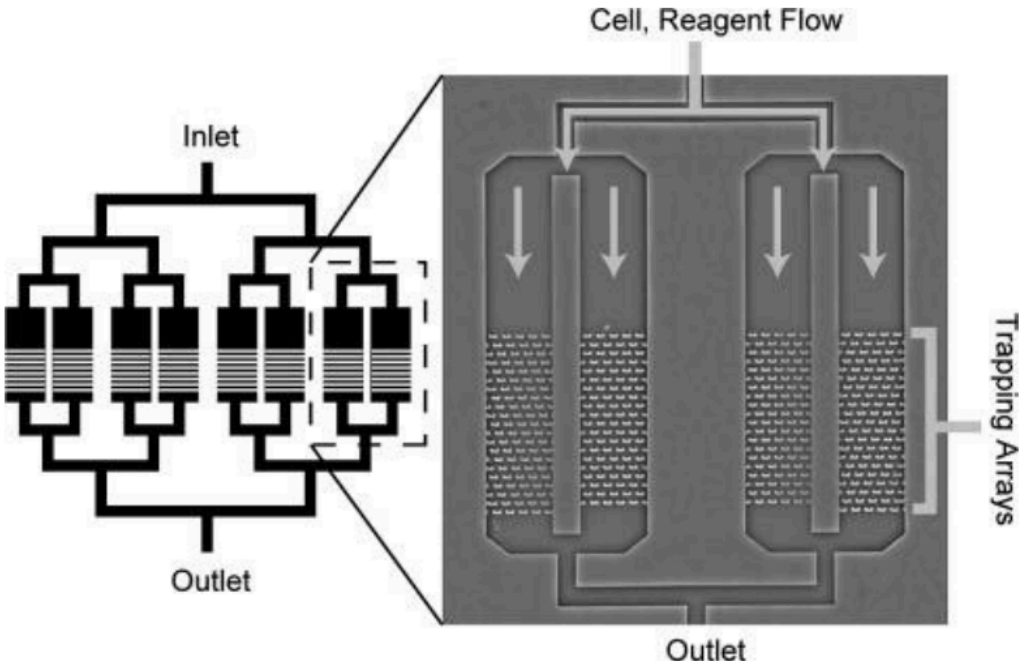

Figure 2-5: Diagram showing the device structure and trapping arrays, adapted from [36].

The traps are constructed to have a height of 40 μm with a 2 μm gap between the top of the PDMS trap and the glass slide. This allows a single cell to be caught and reside in a trap. Once at this location, the presence of the cell will divert the fluid flow so that no following cells will be trapped, thus increasing the likelihood of subsequent traps being occupied. This is diagrammatically explained in Figure 2-6.

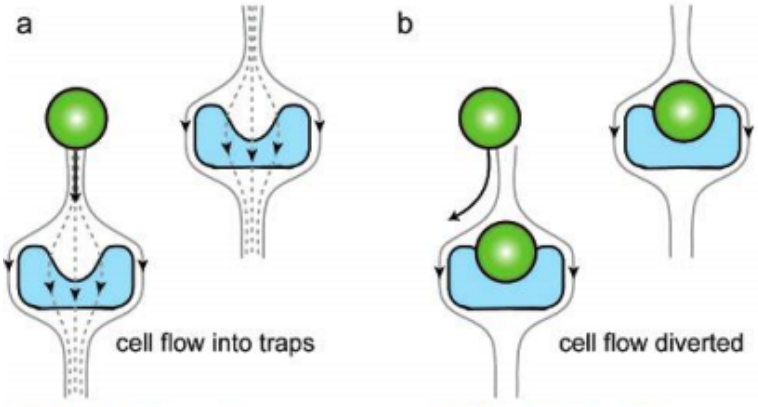

Figure 2-6: Diagram illustrating the diversion of fluid flow after a trap is occupied. Image copied from [36].

a) Cell is drawn into the trap due to the fluid flow through the 2 μm gap.

b) The cell blocks the fluid flow through the trap, causing subsequent cells to flow around the trap.

This method of cell trapping is very effective; a microscope image of trapped cells is shown in Figure 2-7.

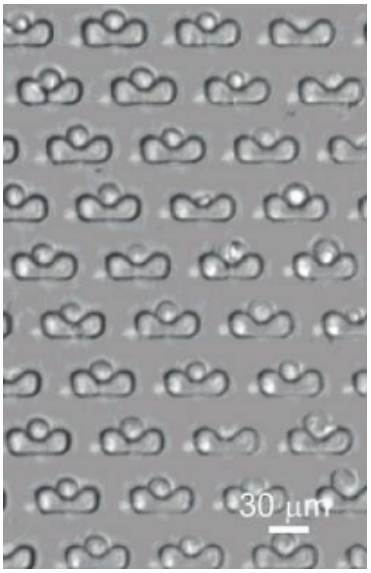

Figure 2-7: Phase contrast image of trapped cells, from [36]. Scale bar = 30 μm.

While this method proves efficient for capturing single cells, for the application in question it is necessary to trap two different cell types together. In 2009, Skelley *et al* [38] showed cell pairing and fusion using a similar model to Di Carlo, Wu and Lee. They

designed ‘trap cups’ with two cell trapping areas (wells), one at the ‘bottom’ and one at the ‘top’ of the cup; Figure 2-8.

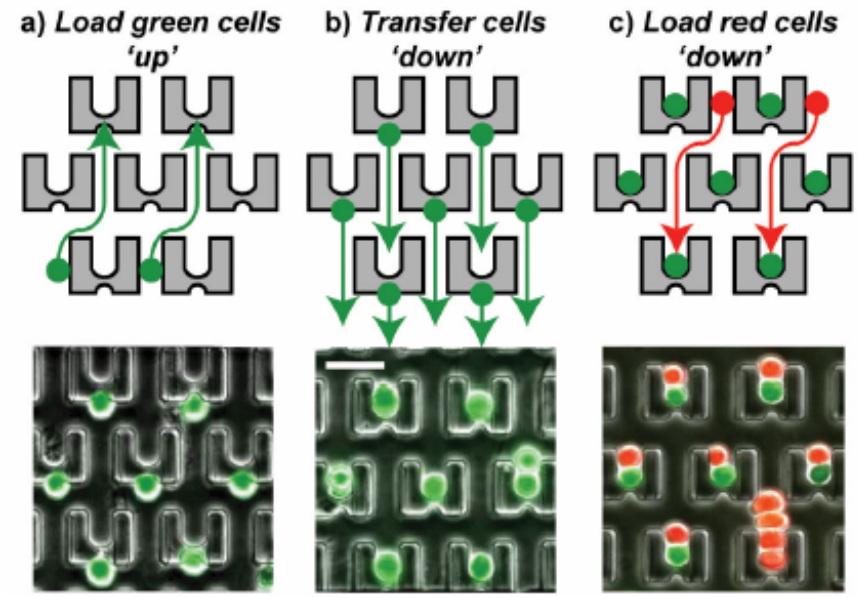

Figure 2-8: Diagram of capture cups and the three-step protocol to load cells. Scale bar = 50 µm. Adapted from [38].

a) Green cells are loaded and trapped in the smaller ‘bottom’ wells;

b) Green cells are pulled down into the larger ‘top’ capture wells by reversing flow direction;

c) Red cells are loaded into the same wells as the green cells.

In a similar way to Di Carlo, Wu and Lee [36], Skelley *et al* designed the device so that the traps have small gaps of 6-8 µm between the PDMS and the glass cover slides, maintained by ‘support pillars’, which create a fluid flow into the trap cups. Loading is accomplished as follows:

1) Cells are pulled through the device with a syringe pump at 15-50 µm/s and trapped in the smaller ‘bottom’ well of the capture cups.

2) These cells are then pulled directly down into the larger ‘top’ well traps by reversing the flow direction.

3) Finally, the second cell line is introduced and pulled into the larger ‘top’ well traps, which can hold up to two cells.

More recently, in 2014 the Voldman group (Dura, Liu and Voldman) used a similar device to force cell fusion [39]. The cup traps are modified to have a constriction region at the entrance; so once a cell has been forced into the trap (by high fluid flow) it is trapped inside, preventing cell loss. See Figure 2-9 for images of the trapping cups. Figure 2-10 diagrammatically explains the cell loading.

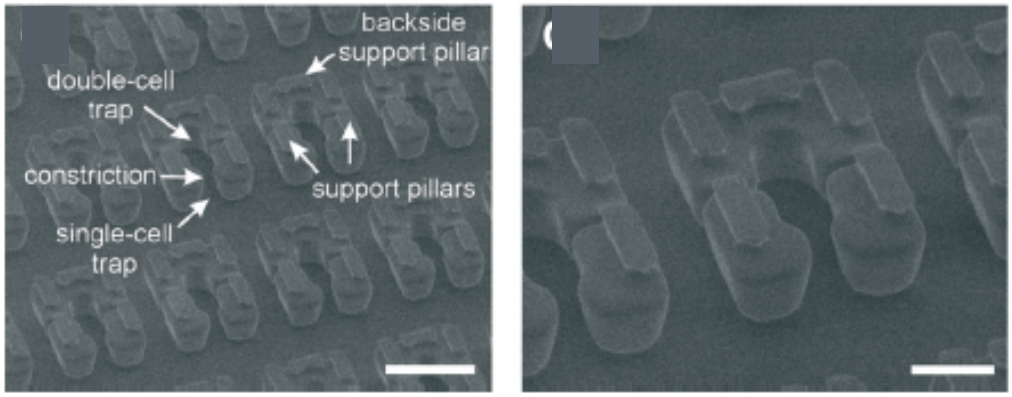

Figure 2-9: Scanning electron micrograph images of trapping cups with constriction regions. Scale bars = (left) 50 μm & (right) 20 μm. Image adapted from [39].

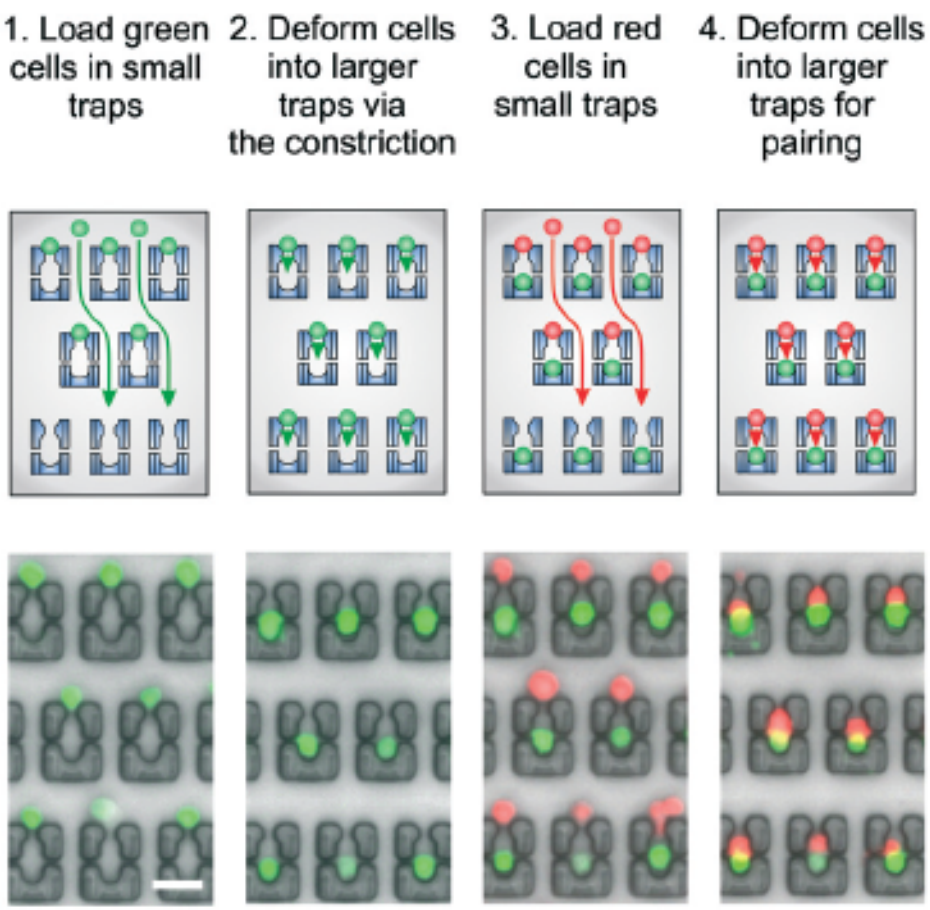

Figure 2-10: Diagram explaining cell loading inside constriction trap cups. Scale bar = 50 μm. Image adapted from [39].

The device is operated as follows:

1) Cells flow through the device from top to bottom. Due to the fluid flow through the trapping cups, cells are trapped at the opening of the cup. Once a cell has been trapped it diverts the fluid path around the cup, so subsequent cells are not captured.

2) Fluid flow is increased to squeeze cells through the constriction region.

3) Steps 1 & 2 are repeated for the secondary cell line.

Dura, Liu and Voldman report 50% - 80% capture of cells entering the device when the capture site dimensions are tailored to the cells chosen. Capture site loading efficiency is very high; see Figure 2-11. Additionally, due to the constricted trap entrance, the device can be moved after loading with minimal cell loss.

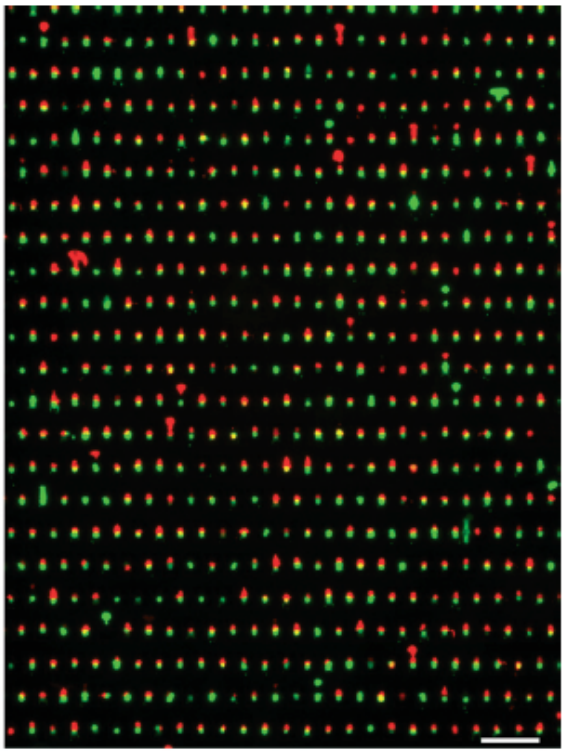

Figure 2-11: Fluorescent image showing capture efficiency of two cell types.
Scale bar = 200 μm. Figure adapted from [39].

This cell cup trapping method allows cell-cell interaction, but again has no control over interaction time, or a way to release the cells in a controlled manner so that individual cells of interest could be extracted. It would be possible to release the trapped cells by flowing in liquid so that it forces the cells out of the traps, but the conjugated cells would remain fused, and recovery of specific cells would not be possible. Consequently, it is not a useful technology for this project.

Alternatively, using a particle trap design by Tan and Takeuchi [40], in 2011 Frimat *et al* [41] demonstrated sequential cell trapping and cell-cell interaction using a serpentine path, as shown in Figure 2-12.

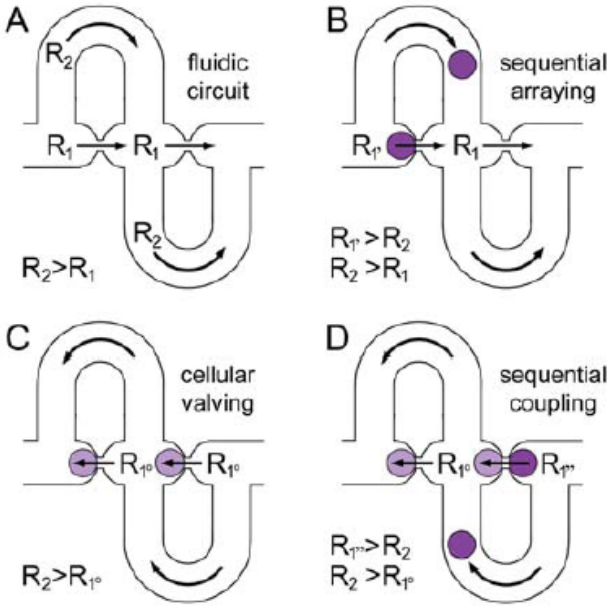

Figure 2-12: Concept of the serpentine channel and sequential cell trapping. Taken from [41].

The serpentine design operates as follows:

(A) Adherent cells in solution are flowed into the channel from left to right. As the path of least resistance 'R1' is straight ahead, a cell will flow into the trap and become caught. This blocks the R1 fluid flow, increasing the resistance so that so the remainder of the cells will flow around the longer route of the serpentine bend, which is lower resistance 'R2'. This continues until all the traps are subsequently filled, (B).

(C) After some time, the trapped adherent cells will adhere and flatten over the trap, becoming more permeable. This allows the fluid channel to open again, reducing the resistance '$R1^{0}$' of this fluid path.

(D) Finally, a secondary cell line is introduced into the device from right to left and undergoes steps 'A' and 'B' in reverse, until all the traps are full.

The mirrored trap arrangement seen in Figure 2-12 allows two cells to be trapped side-by-side with a gap between the mirrored traps of 5 μm. This is small enough for the cells to interact. Cell coupling is shown in the microscope image Figure 2-13.

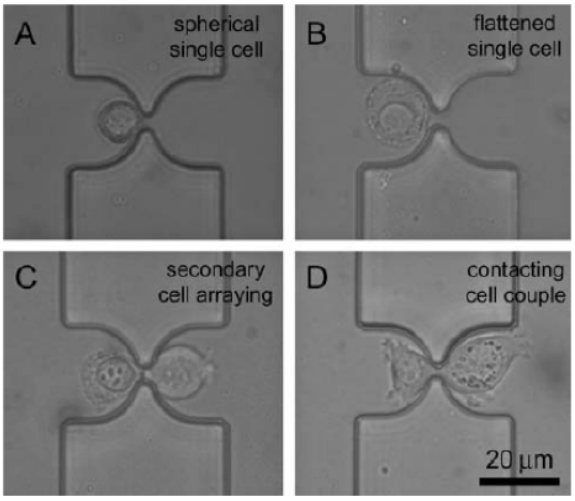

Figure 2-13: Seeding and interaction of cells in mirrored traps, taken from [41]. Scale bar = 20 µm.

However, as with the previous methods discussed, there is no time control over the interaction between the cells in this method, as well as no way to release or recover cells of interest.

In 2011, Chung, Kim and Yoon presented a method of single cell capture using hydrodynamic guiding structures [42]. They developed these to allow cell-cell interaction [43]. The 'paired single cell co-culture microenvironment' was published in Lab on a Chip in 2014 and allows isolation of two single cells, whilst maintaining correct nutrient conditions, through use of a media exchange membrane. The authors report culturing cells in the device for up to 7 days with a 75% survival rate.

Figure 2-14 is a side-view diagram of the device, showing cell capture inside cell culture chambers. The semi-permeable membrane allows media exchange whilst retaining cytokines that have been released from the cells inside the chambers. The membrane is porous for molecules up to 2 kDa; large enough for media exchange, but too small to allow cytokines (10s of kDa) to pass through.

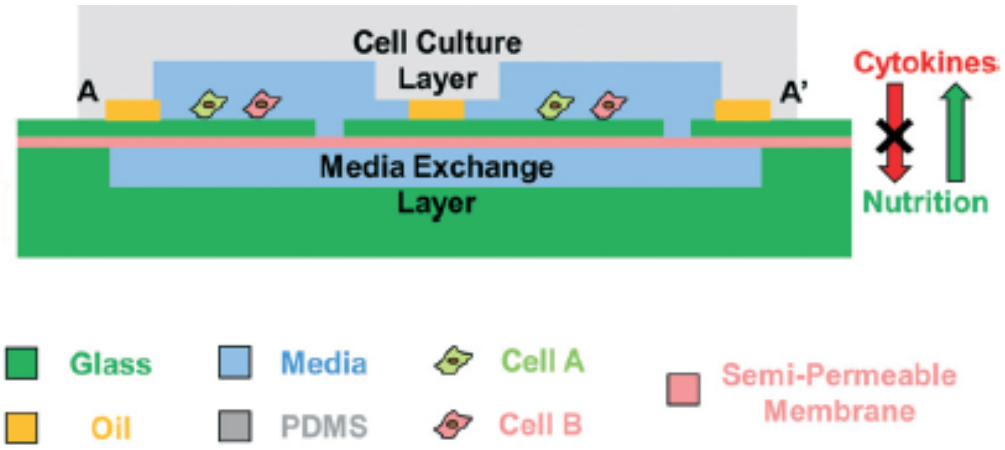

Figure 2-14: Side-view diagram of device operation. Cells are trapped inside PDMS microchambers and receive a supply of nutrients through the semi-porous membrane. Adapted from [43].

Cell-cell interaction is possible due to the 10 µm wide 'interaction bridge' fabricated between the cell traps, Figure 2-15.

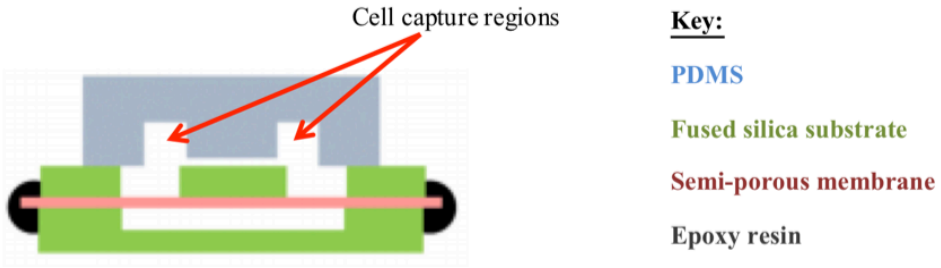

Figure 2-15: Side-view of cell capture region, showing cell interaction bridge. Adapted from supplementary information [43].

The cells are captured using hydrodynamic guiding structures [42]. A COMSOL model of the flow paths inside the guiding structures is shown in Figure 2-16. An image of cells captured in the device is shown in Figure 2-17.

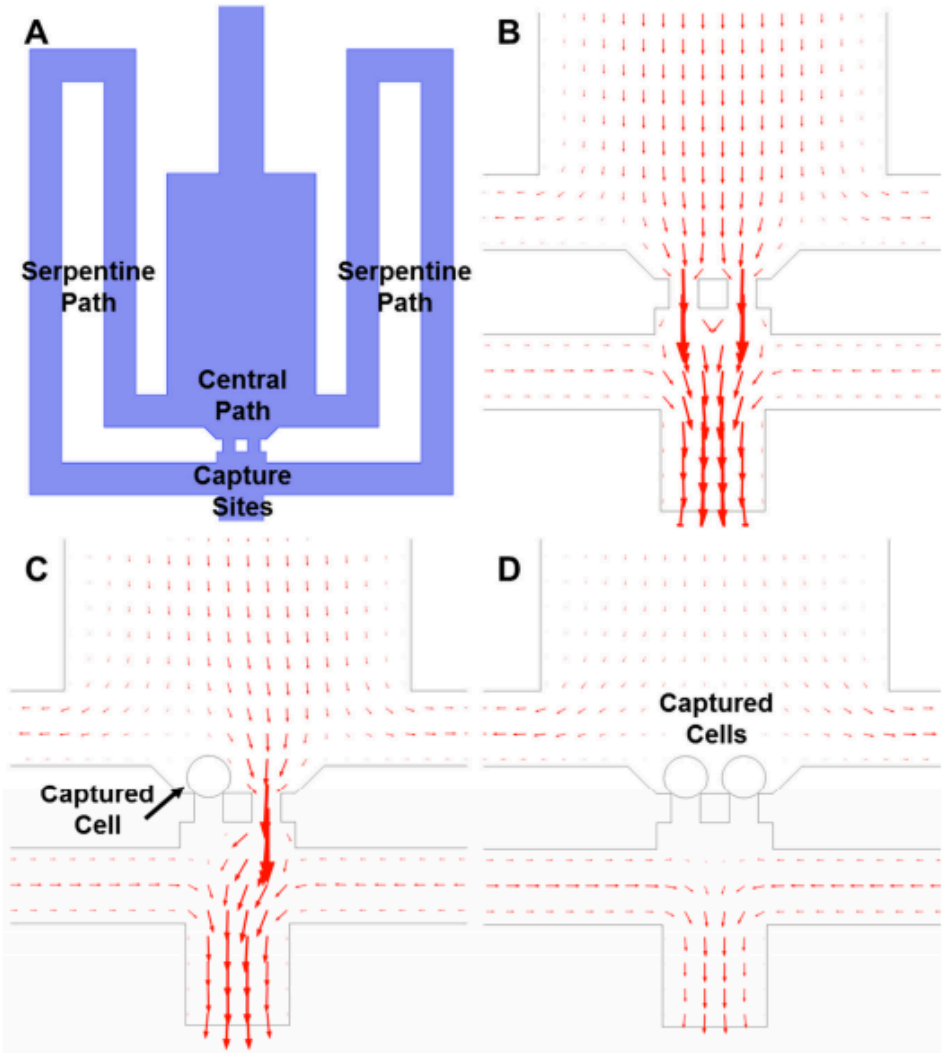

Figure 2-16: COMSOL simulation of fluidic paths through hydrodynamic flow structures. Figure copied from supplementary information [43].

A) Schematic of the device. B) Fluid is flowed into the device through the central path, some fluid travels through the serpentines. The main flow is directed towards the capture sites. C) Once a cell has been captured the flow path is changed, with the main flow directing the following cell towards the remaining trap. D) When both traps are full, the fluid flows fully through the serpentine paths, preventing multiple cell capture.

Figure 2-17: Brightfield image of two cells captured inside hydrodynamic flow device. Scale bar = 100 µm. Figure from [43].

The device allows cell-cell interactions to occur, provided the captured cells can bridge the 10 µm distance between capture sites. It is a good system for monitoring interactions over a prolonged period of time (days); however, there is no way to retrieve cells after the experiment has ended. Also, whilst it is advantageous to have a way to provide nutrients to the cells during the experiment (so that the cells maintain full functionality for extended periods of time) this should not be necessary for this project as T lymphocyte activation occurs within a few minutes [21].

2.3.3 Dielectrophoretic traps

Dielectrophoresis (DEP) is the movement of a polarisable object in the presence of a non-uniform electric field; illustrated in Figure 2-18.

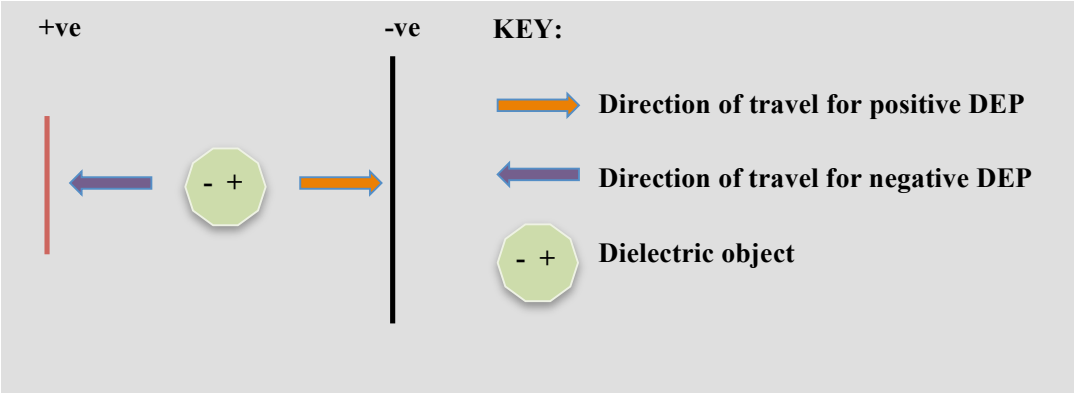

Figure 2-18: Diagram explaining DEP.

DEP can be used for cell arrangement and trapping. As an example, in 1993 Wang *et al* [44] used DEP to sort suspended yeast cells by separating the viable (live) from the non-viable (heat treated, dead cells) by the difference in the dielectric properties of alive and dead cells. This is useful for cell sorting, but did not show single cell confinement. Gray *et al* [45] created a microelectrode array capable of trapping thousands of cells using DEP; Figure 2-19.

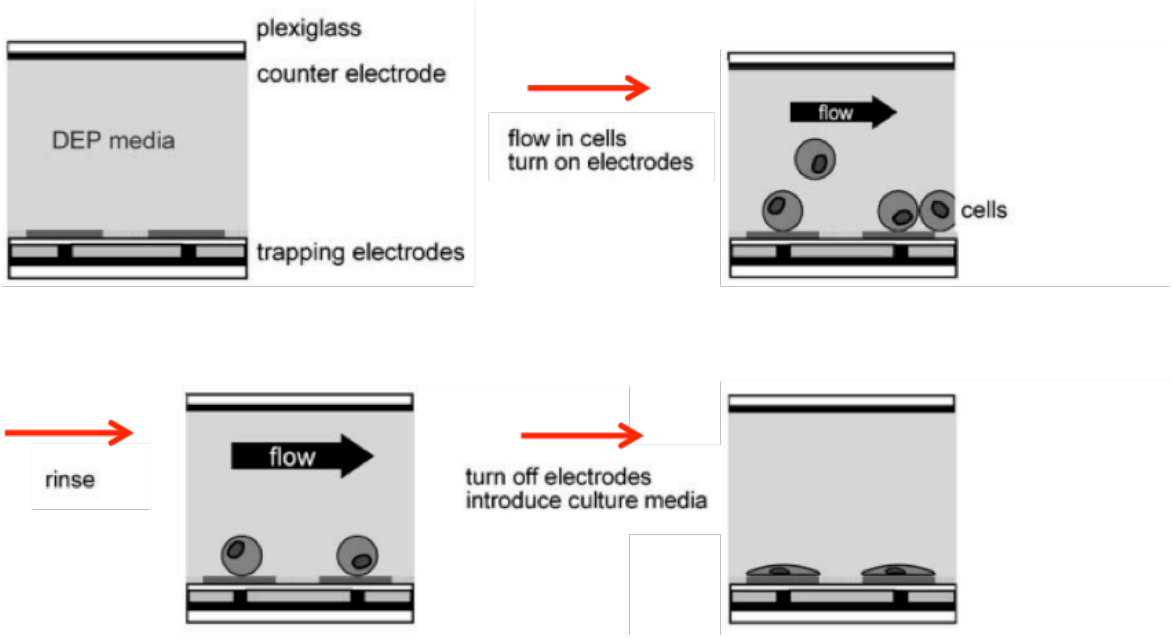

Figure 2-19: Microelectrode array protocol for trapping individual cells, adapted from [45].

The experiment worked by flowing cells in suspension into the device and then turning on the electric potential to pull the cells towards the electrodes. The electrodes were then turned off and the cells adhered to the fibronectin surface patterned above the electrodes.

Using this method, another cell culture could be flushed into the device to interact with the adhered cells leading to cell-cell interactions. However, it would be very difficult to interact another cell with the adhered cells in a timed manner. It may be possible to eject specific cells using the electrodes to force the cells back into the fluid flow, but this could be difficult once the cells have adhered to the surface. Additionally, the authors mention cell damage at voltages above 5V (due to heating of the media, disruption of cell membranes etc.), which could be a drawback of this technique if it is not possible to trap the cells with lower voltages.

In 2008 Kirschbaum *et al* used a 'dielectrophoresis-based microfluidic device' to activate individual T lymphocyte cells using microbeads coated in antibodies [46].
T lymphocytes, antibody-labelled 10 µm polystyrene beads and cell culture medium were injected into the device, before an array of electrodes was switched on/off to select individual T lymphocytes and microbeads. The device is shown in Figure 2-20.

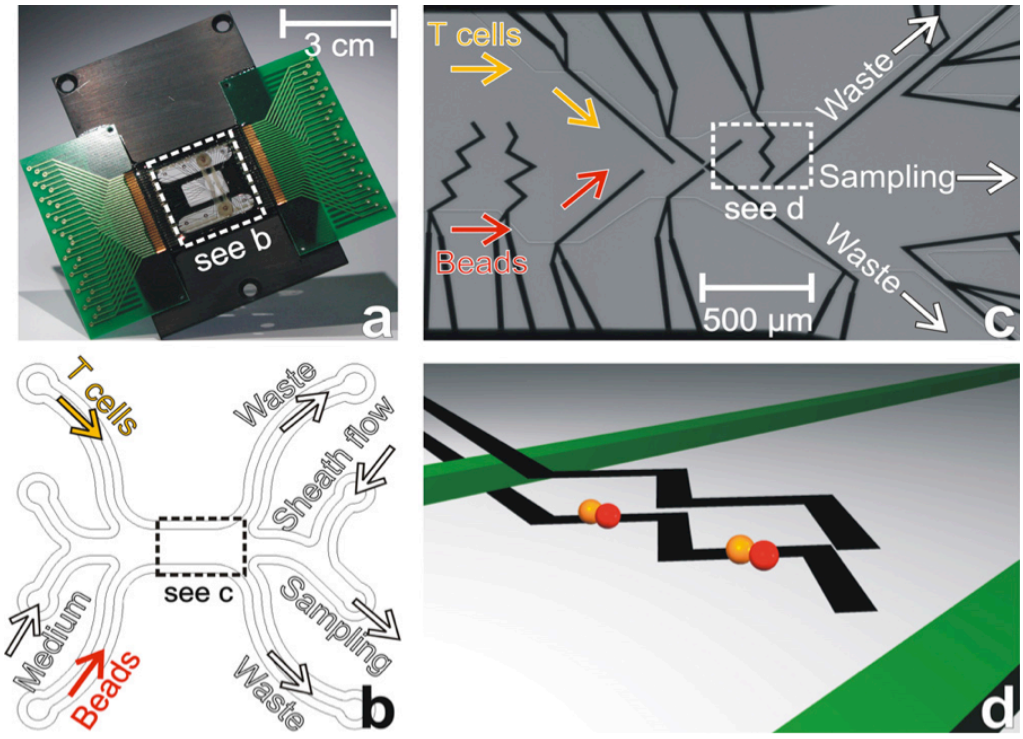

Figure 2-20: Dielectrophoresis-based microfluidic device, adapted from [46].

a) The full device, b) Diagram showing the inlet/outlet channels, c) Image of the electrodes, d) Schematic of where cell-bead pairs are formed and transported in microdroplets out of the device.

Once a T lymphocyte has bound to a microbead, the pair is transported out of the device in a microdroplet, using sheath flow, and collected in a microplate for further analysis.

This device is capable of single cell-cell interactions and extraction of specific cells of interest, but it would be difficult to split two cells apart. This could possibly be achieved using optical trapping, but a drawback to using optical trapping is that it can impact upon normal cell behaviour and therefore bias the results. Also there is no way to time the interaction.

2.3.4 Optical cell traps

In 1987 Ashkin, Dziedzic and Yamane showed that single cells could be manipulated using infrared laser beams in a process named 'optical trapping' [47]. The principle of optical trapping is that the Gaussian electric field profile of a laser beam will cause nearby dielectric particles to be drawn into its centre, thereby providing a way to direct particles [48].

Optical trapping has been used by multiple groups to immobilise single cells. Huser *et al* [49] used optical tweezers to force cell interactions between HIV-1 infected T cells and primary uninfected T cells, and Oddos *et al* used a combination of optical tweezers and confocal microscopy to view immune synapse formation between live cells [50].

Werner *et al* [51], in 2011 showed trapping of an array of yeast cells within a microfluidic chip; Figure 2-21.

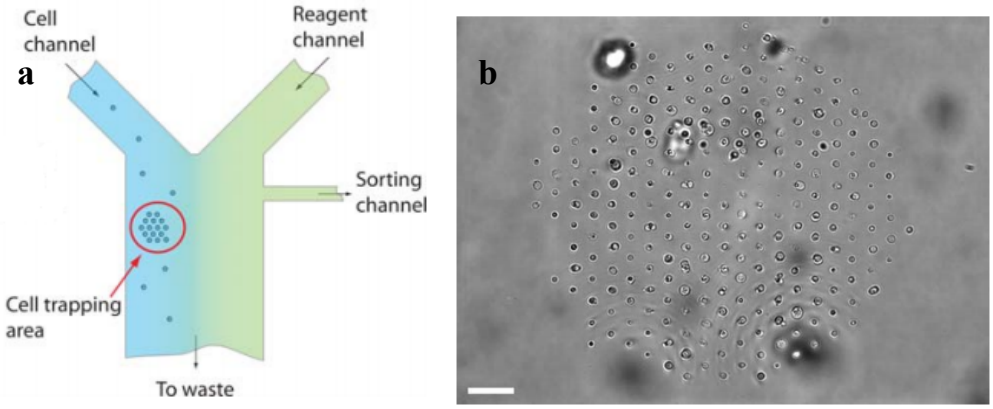

Figure 2-21: Schematic showing device operation and image of yeast cell array. Scale bar = 30 μm. Taken from [51].

a) Microfluidic device design, b) Microscope image showing the result of optical trapping of yeast cells spaced approximately 10 μm apart from each other.

The main issue with optical trapping is that the energy of the incident laser light can cause cell death. This is due to cells absorbing the laser energy and overheating. The authors calculated that the power required to trap cells in the array was between 15mW - 30mW, reporting that the yeast cells used were only viable for up to 15 minutes during optical trapping. However, an advantage of optical trapping is that it would be possible, with the correct computer programming, to release specific cells in a controlled manner.

Other issues with using optical trapping include the need for expensive lasers and a dedicated microscope for analysis, as well as complex computer software to run the lasers and implement trapping designs. This would prevent the device from being portable and also be very costly. Positioning of cells using optical tweezers could also affect the cell characteristics. Cells will absorb some light energy, the effect of which could bias the results. Hence, although it would be possible use optical trapping for cell interaction, it is uncertain how the laser energy would affect cell-cell communication and therefore disturb the experiment.

2.3.5 Magnetic cell traps

Magnetic trapping of cells normally requires coating of cells in small magnetic beads. Magnetic beads are attached to specific markers on the cell surface, before the cells are subjected to a magnetic field to manipulate them. This technique will not be discussed, as it is not ideal to coat the cell surface with magnetic particles; it would directly affect cell-cell interaction if there were magnetic particles between the cells.

However, Kolosnjaj-Tabi *et al* [52] showed magnetic translation of cells that have phagocytised super-paramagnetic iron oxide nanoparticles, leaving the cell surface particle-free. Mesenchymal stem cells were incubated with the magnetic nanoparticles (MNPs), resulting in particle uptake by the cells; the MNPs were contained within the endosomes and lysosomes of the cells. The stem cells could then be translated using a permanent magnet. Using this method it might be possible to cause single cell-cell interactions, however to do so in a high-throughput fashion would require additional cell containment to maintain single cell-cell contact and prevent cell clusters from forming.

2.3.6 Acoustic cell traps

Standing ultrasonic waves that create changes in pressure (nodes and antinodes) can be used to separate microparticles; as shown by Hertz in 1995 [53]. The method involves creating a standing wave (Figure 2-22) using two ultrasonic transducers and positioning this in a microparticle liquid suspension. Under the influence of the standing wave the particles congregate in the antinodes, resulting in the type of pattern displayed in Figure 2-23.

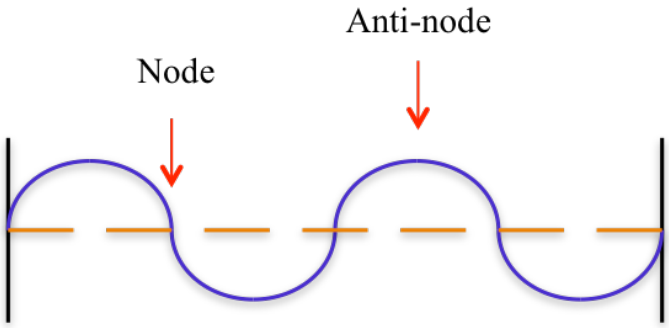

Figure 2-22: Standing wave between two points showing nodes and anti-nodes.

Figure 2-23: 2.1 µm diameter microparticles separated by a standing wave of frequency 11MHz, from [53].

Acoustic trapping could be used with cells, but at the frequencies necessary (10-100MHz) single cell separation is not possible; unless only one cell was included in the device, making it very low-throughput and also very time-consuming. Additionally, there is an issue with bringing another cell into contact for a defined period of time and there would

not be a way to extract specific cells. Hence, acoustic separation is not a practical solution for this project.

2.3.7 Cell trapping with surface modification

Cells can be immobilised on surfaces in designated areas by using adhesion promoters such as fibronectin, as shown by Azioune *et al* [54].

The concept is as follows: coat a substrate (such as glass) with poly-L-lysine-grafted-polyethylene glycol (PLL-g-PEG). This will adhere to the substrate, with the Polyethylene Glycol (PEG) component preventing proteins from sticking to the substrate. The substrate is then subjected to deep UV irradiation through a photomask with the desired cell adhesion pattern, reducing the PEG component and leaving behind a surface that promotes protein attachment. Finally, the surface is coated with fibronectin, a cell adhesion promoter. The fibronectin will only bind to the irradiated sections of the substrate. When cells are seeded onto the substrate they will be repelled from the PEG coated areas and form protein bonds to the fibronectin coated areas. This is shown in the microscope image in Figure 2-24.

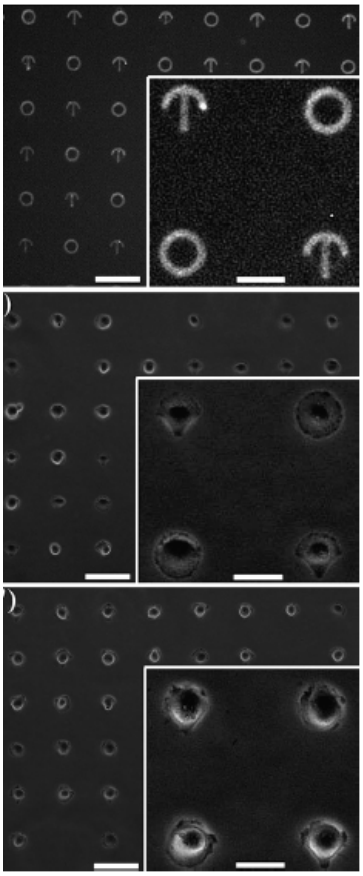

Figure 2-24: Patterned glass coverslips. Scale bars = 100 μm for main images, 34 μm for insets. Figure adapted from [54].

Images from top to bottom: Patterned coverslip, coverslip with cells seeded on it for 4 hours, same sample after 24 hours.

Azioune *et al* report approximately 88% of patterned areas were covered in cells, with 20% containing a single cell. Whilst not optimal for a single cell contact device, surface modification is a useful tool for cell confinement to a certain area.

2.3.8 Confinement traps

Confinement traps are cell traps that restrain cells by physically holding them in place. An example of this is the micropipette MHC-CD8 interaction experiment conducted by Huang *et al* [55]. The authors studied the receptor-ligand adhesion between a T Lymphocyte and a Red Blood Cell (RBC) coated with MHC by aspirating the cells onto the end of micropipettes and bringing the cells into contact; Figure 2-25.

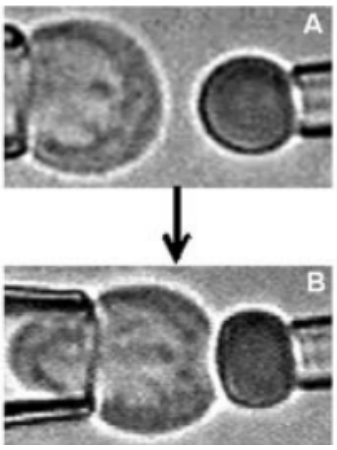

Figure 2-25: A) A T Lymphocyte (left) and RBC (right) are aspirated onto the end of micropipettes. B) The cells are brought into contact on the end of the micropipettes. Adapted from [55].

Using this method it is possible to study single cell-cell interactions, however doing so in a high-throughput manner would require additional infrastructure as undertaking the experiment for one cell pair at a time would be very time consuming.

SlipChip

The SlipChip was developed in 2009 by Du *et al* [56] and showed multiplexed experiments on a single microfluidic chip. The design is detailed in Figure 2-26. Although shown in cell culture applications [57], it has never been used to cause single-cell interactions.

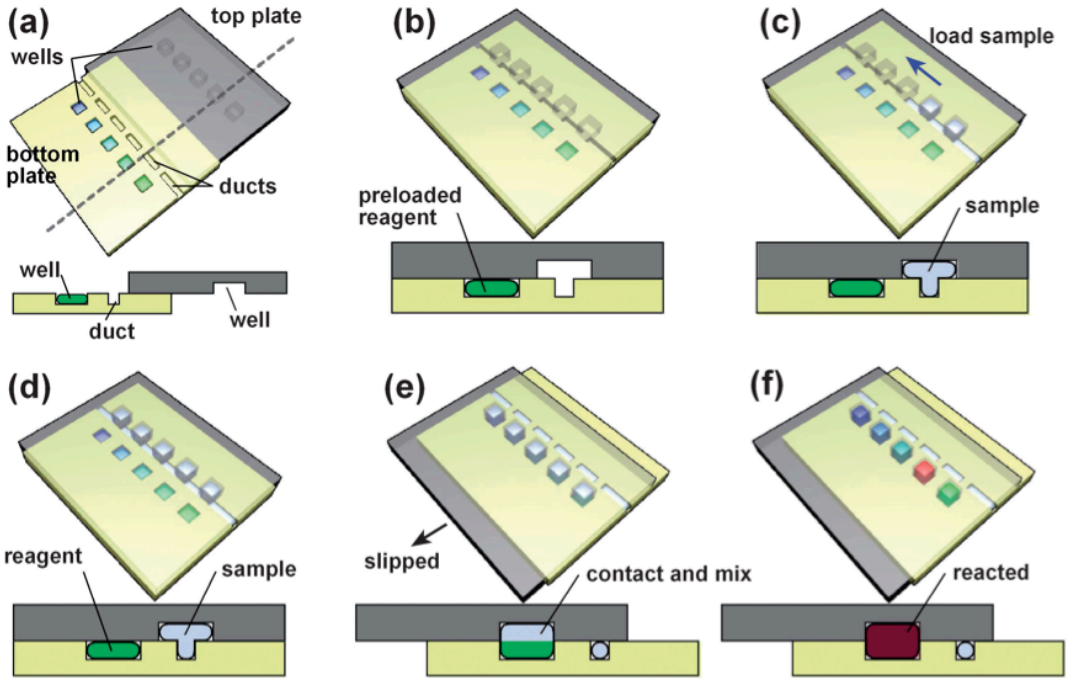

Figure 2-26: Illustration showing how the SlipChip is used to mix various samples with a reagent. Adapted from [56].

The SlipChip is operated as follows:

a) The wells of the bottom plate are filled with a reagent.

b) The top plate is translated ('slipped') relative to the bottom plate, covering the bottom wells (preventing the liquid from evaporating) and aligning the top wells with the ducts on the bottom plate to form a continuous channel.

c & d) The sample liquid is loaded into the top plate wells.

e) The top plate is slipped relative to the bottom plate, again causing the top and bottom wells to overlap, allowing the liquids to mix.

f) The reaction between the top and bottom wells has taken place.

The SlipChip could be altered to work with cells by placing one type of cell in the bottom wells and loading different cells in the top wells (in cell culture media) and slipping the device so that they interact. It presents a very promising technology for observing cell-cell interactions if it was constructed from transparent material and modified to have cell-dimensions.

For this project, the bottom cells would be APCs and the top cells would be T lymphocytes. The cells are then in individual compartments so they could be easily separated by slipping the device (giving control over the reaction time), and individual cells could be removed from their known well positions. Prevention of the T lymphocytes falling into the bottom APC well (and not being disassociated by slipping) could be accomplished by restricting the well size of the APC trap to have the capacity of just the APC, so there would be no room for the T lymphocyte.

The SlipChip could be manufactured out of a transparent plastic such as Polymethyl Methacrylate (PMMA) so that T lymphocyte activation through calcium imaging could be viewed using a microscope. The innate containment of the SlipChip means the device is portable, allowing the analysis to take place using any available microscope. Furthermore, the extra-cellular fluid would be contained in the well with the cell, allowing examination of this too, if required.

As with droplet technologies, single cell loading in the SlipChip is likely to be an issue. This could be improved by designing the well sizes to fit only one cell, but it is expected that this will be a flaw with the technology that cannot be fully overcome.

Microwell arrays

Trapping cells in microwells

Microwell arrays are wells that trap individual cells by sedimentation. Trapping more than one cell in a well is prevented by controlling the well dimensions for the cells under investigation, so that more than one cell cannot fit in a single well. The concept is displayed in Figure 2-27.

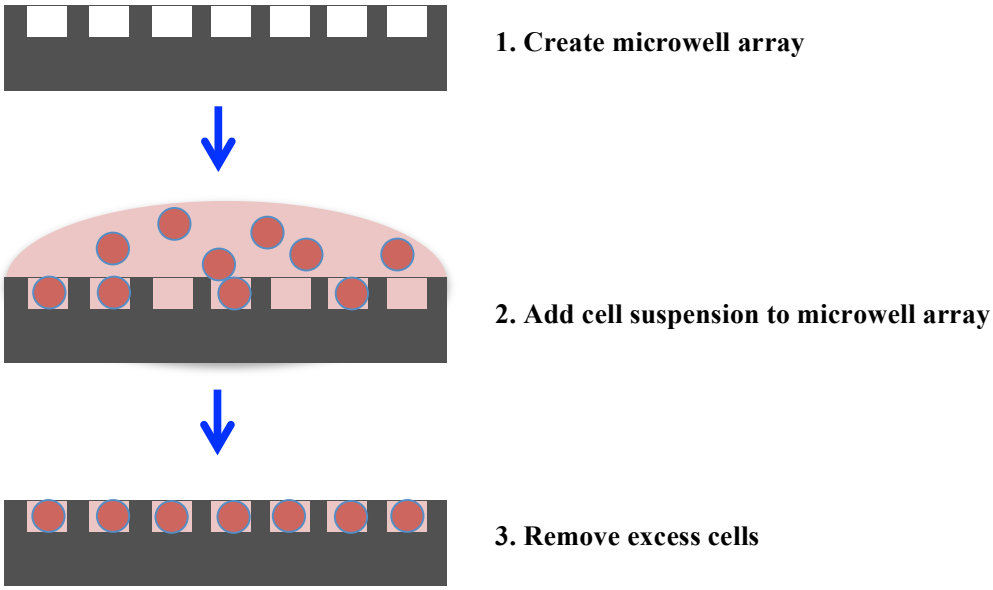

Figure 2-27: Microwell array cell capture concept. Microwell size exclusion prevents multiple cell loading in a single well.

Numerous examples of microwell array trapping of cells are available in the literature [58 - 61], for experiments ranging from antibody detection [62], to DNA analysis [63].

Often a combination of microwell confinement trapping with surface modification is utilised to prevent cell adhesion to unwanted areas, and create more biocompatible wells for the cells [64 - 67]. As an example, Ochsner *et al* [64] tested cell loading in a variety of well geometries and imaged intracellular features using confocal microscopy; Figure 2-28. The microwells were fabricated using soft lithography of PDMS from a silicon master that was created with photolithography and inductively coupled plasma etching. The microwell device was stamped with a PLL-g-PEG coating to prevent cell adhesion outside of the microwells, and coated with fibronectin to promote adhesion inside the wells.

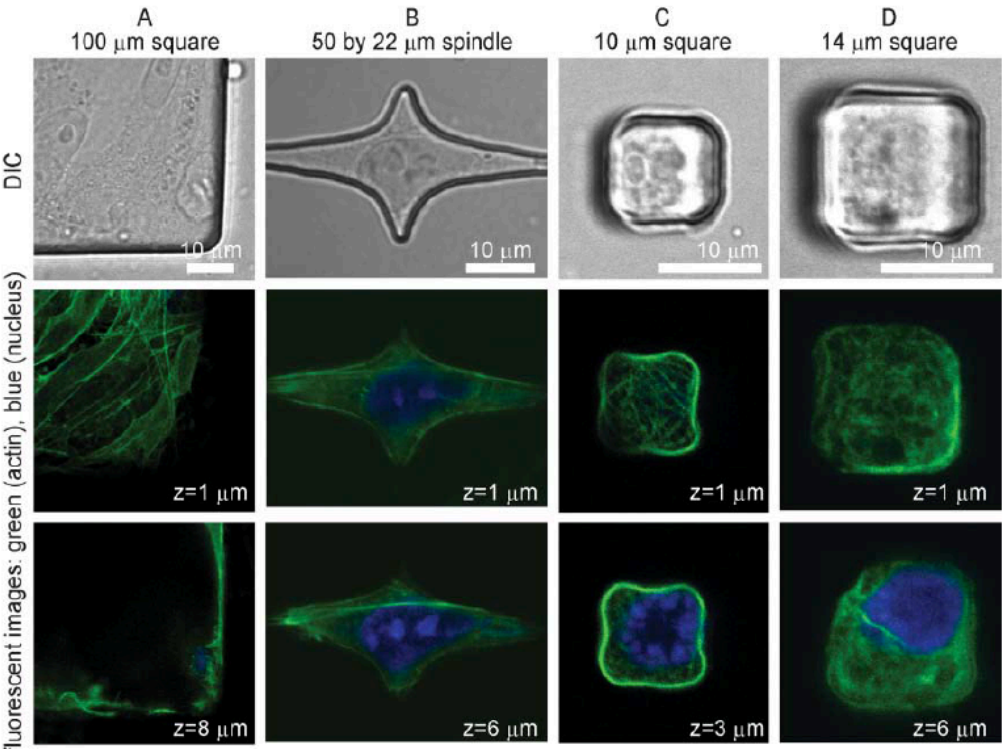

Figure 2-28: Differential interference contrast images (top) and fluorescent confocal images of cells cultured in microwells for 24 hours. Image adapted from [64]. Scale bars and confocal image slice height shown on images.

A: 100 μm square. B: Spindle. C: 10 μm square. D: 14 μm square. Nucleus cell staining (ethidium homodimer; blue) and actin cytoskeletal network staining (Alexa 488-phalloidin; green).

Microwells have been used to drive cell-interactions; the Önfelt group in Stockholm described immune interactions (Natural Killer (NK) cells interacting with target cells) that they observed through use of microwells [65, 66].

Briefly, 50 x 50 x 300 μm (width x width x height) wells were etched in a silicon-glass substrate. The cells were then seeded into the wells by sedimentation from a cell suspension; the device was continuously imaged using an inverted microscope. Due to the size of the wells (50 x 50 μm), multiple cells could be trapped inside a single well and the distance between them is small. Cells were seeded at low concentrations to prevent more than a couple of cells in each well. The device operation is diagrammatically explained in Figure 2-29.

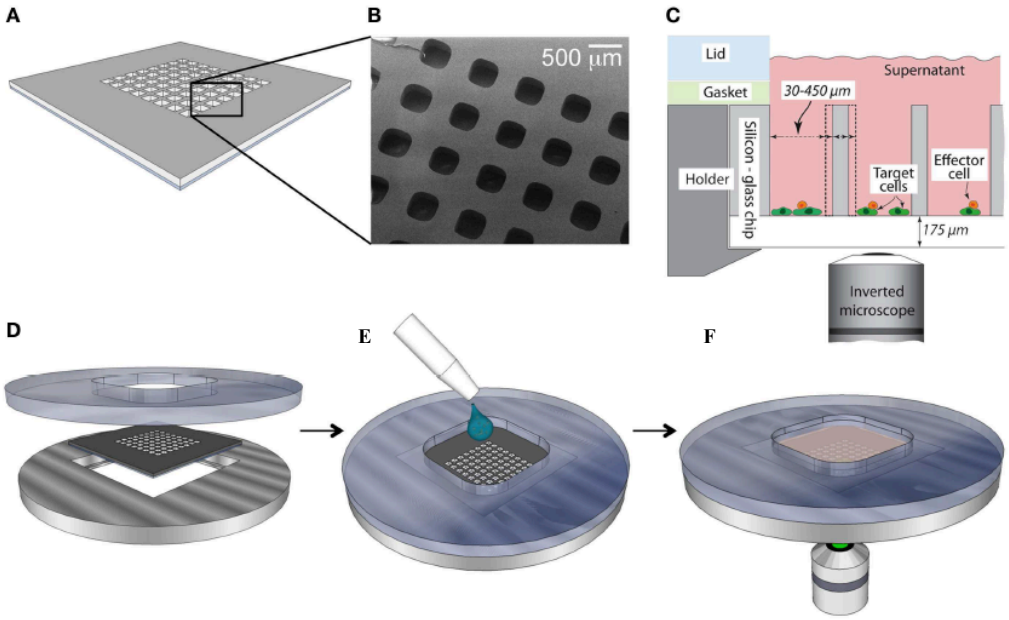

Figure 2-29: Diagrammatic explanation of device operation. Figure adapted from [65].

A/B: Microwells etched in silicon-glass. C: Well dimensions. D: Integration of microwell plate into microscope set-up. E: Addition of cell suspension. F: Visualisation of cells using an inverted microscope.

The entire device was then scanned to look for wells with a NK cell and a target cell seeded inside. To encourage cell-cell contact, an ultrasonic standing wave was applied to the device, forcing cell-cell contact as the cells move into the anti-node of the standing wave (as discussed in Chapter 2.3.6). The authors claim that at the wavelengths necessary to cause cell-cell contact in the device (around 2.5 MHz), there is minimal negative impact on cell viability.

This method does drive cell-cell interaction, but it is a disorganised way of bringing two cells into contact and there is no control over timing. Device scanning is necessary because the probability of having a NK cell and a target cell in the same well is low, so a large number of cells are wasted which would be a significant issue if the cells being investigated were a limited, precious cell sample.

A notable method of creating microwell arrays capable of selectively capturing a range of cell sizes was demonstrated by Wang *et al* [68]. A PDMS microwell device was created with soft lithography from a glass master patterned with SU-8 using photolithography.

The PDMS microwell device was then stretched during cell seeding, before being allowed to relax, effectively capturing cells; Figure 2-30.

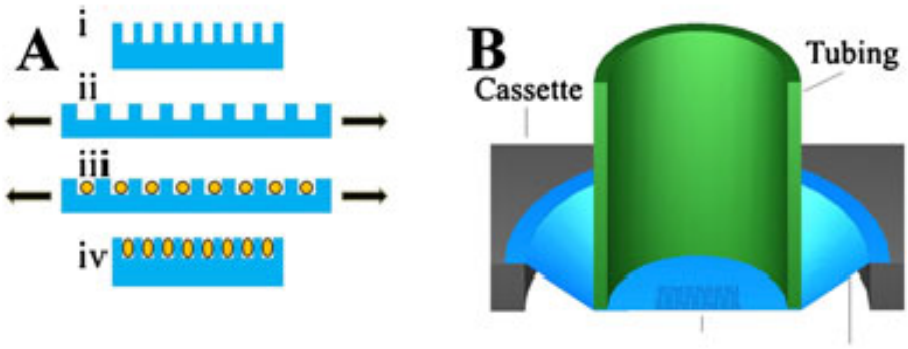

Figure 2-30: Diagram depicting stretchable microwells. Image adapted from [68].

A: i) Microwell dimensions when PDMS is 'at rest'. ii) Increased microwell width when PDMS is stretched. iii) Cell seeding. iv) PDMS is returned to its rest position; cells are subsequently trapped. B: PDMS microwells are stretched using a plastic tube attached to a micromanipulator.

Using this microwell array method, cells can be seeded inside microwells and repeatedly washed or dyed without being dislodged.

Retrieving cells from microwells

This project calls for cell recovery of interesting cells, so that they can undergo further analysis. Cell removal from microwells has been shown in a variety of ways and is described briefly below.

Wang *et al* [68] use the micromanipulator to selectively remove desired cells by locally deforming the PDMS under the chosen cell with a needle. Another method of cell retrieval is accomplished using a micromanipulator-driven micropipette to extract specific cells; described by Yamamura *et al* in 2005 [69] and Ozawa *et al* in 2009 [70]. Revzin *et al* [67] selectively remove cells from their microwells by laser capture microdissection and Sun, Kovax and Voldman [71] use a dual-photopolymerisation method to encapsulate undesired cells, allowing the retrieval of selected cells by washing.

In summary, microwells present a simple way of capturing single cells and recovery of cells should be possible, as has been widely documented in the literature. If there was a way to bring two microwell plates into contact then it could be possible to interact two

cells (in a time-controlled manner) trapped inside microwells. Therefore, microwells also present a very promising method of cell-cell contact that could be explored.

2.4 Conclusions

This review has examined possible technologies, including droplet microfluidics, DEP, hydrodynamic traps and confinement traps, and discussed their applicability to studying cell-cell interactions through single-cell trapping and manipulation.

It can be concluded that there are multiple technologies that can drive the interaction of two cells, but only a small subset can do this in high-throughput, for a specific amount of time and then allow the extraction of certain cells, without causing any injury to the cells.

For the experimental question posed: causing a timed interaction between a T lymphocyte and an APC that can be viewed using fluorescent light microscopy, possible routes for doing this include SlipChip and Microwell arrays.

With modifications, such as manufacture from a biocompatible material and selecting the right well dimensions for cells, the SlipChip provides a way to trap individual cells in arrays and interact them in a timed and controlled fashion without influencing normal cell behaviour.

Microwells are also an interesting method of trapping single cells. As long as the microwell array is fabricated in a transparent material, it too could be observed using bright field and fluorescent microscopy. If two microwells could be brought into contact and correctly aligned, then cell-cell contact could occur between cells trapped in wells in the two plates (not unlike the concept for cell-cell interaction with a SlipChip) and the reaction could be timed. Subsequent cell removal is also possible, making further analysis feasible.

Chapter 3: Design and Fabrication of Single-Cell Arrays for the Time-Resolved Measurement of T Lymphocyte Activation

As discussed in Chapter 1.3, the fundamental requirements of this project were to observe variation in cell activation of T lymphocytes at the single cell level, simultaneously for thousands of cells following cell-cell contact.

3.1 Introduction

After a detailed literature review (Chapter 2), it was concluded that the SlipChip technology could be adapted to work with single cells. The work undertaken to investigate this is detailed below.

3.1.1 Concept: SlipChip

As discussed in Chapter 2, the SlipChip was first published in 2009 [56] by the Ismagilov group, who described its use for liquid handling. The Ismagilov group have since shown the SlipChip to have applications in areas including immunoassays, digital PCR and protein crystallisation [72 - 74].

The inherent characteristics of the SlipChip such as containment, time-controlled interactions and optical transparency, make it an ideal platform to investigate for cell-cell interaction studies. The concept is detailed in Figure 3-1.

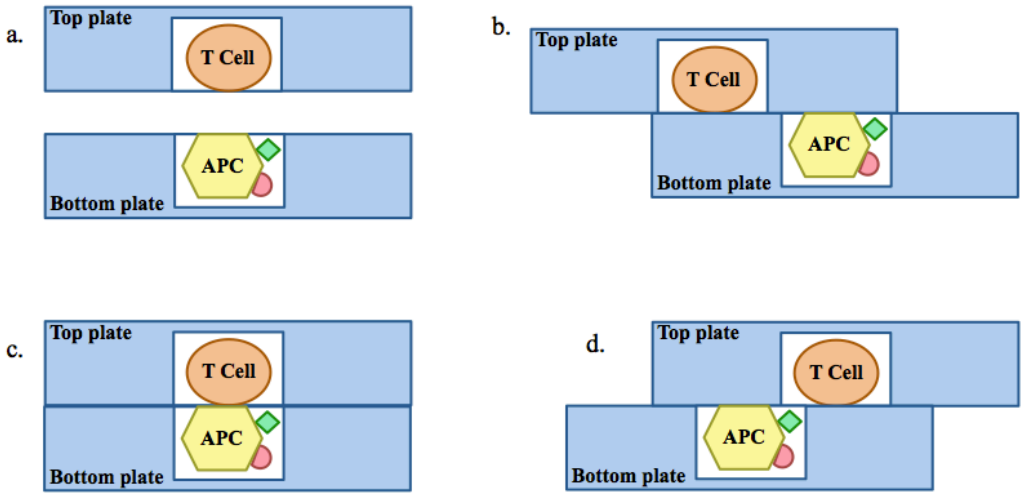

Figure 3-1: Diagram depicting how the SlipChip could be used with cells.

Device operation with cells:

a. The wells in the top and bottom plates are fabricated to be the correct dimension to contain a single cell per well.
b. The top plate of the SlipChip is placed over the bottom plate.
c. The top plate is 'slipped' over the bottom plate, allowing the cells in the top and bottom wells to make contact.
d. Continuing to slip the top plate causes the cells to be dissociated. Cells could then be extracted or be translated further to cause subsequent interactions.

3.2 Materials and methods

3.2.1 Fabrication

To create the microstructures necessary for working with single cells, a number of different fabrication methods were employed, described below. These methods are essential due to the dimensions of the features required for trapping single cells (10s of microns).

Photolithography with SU-8

Background

A widely used method for creating micron-sized structures is photolithography; the process of patterning photoresist. In photolithography, a layer of photoresist is spun onto a substrate wafer (glass/silicon) to the desired height, before being exposed to Ultraviolet (UV) light through a mask. Figure 3-2 diagrammatically shows the process with the negative photoresist 'SU-8' [75]. Where the photoresist is exposed to the UV light, a chemical reaction occurs which results in the photoresist crosslinking and hardening when it is heated.

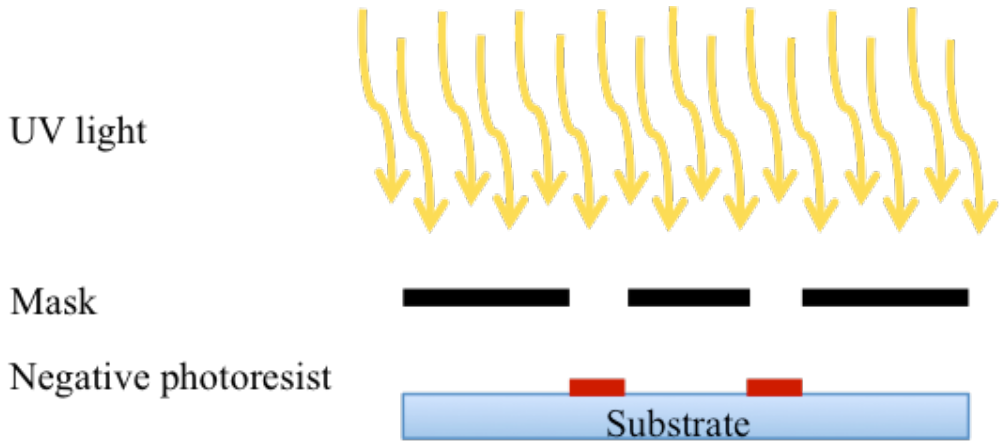

Figure 3-2: Diagram depicting photolithography using a negative photoresist, such as SU-8.

Protocol

The protocol for creating microstructures using photolithography is detailed in Appendix A.1.1. An example of SU-8 features is shown in Figure 3-3.

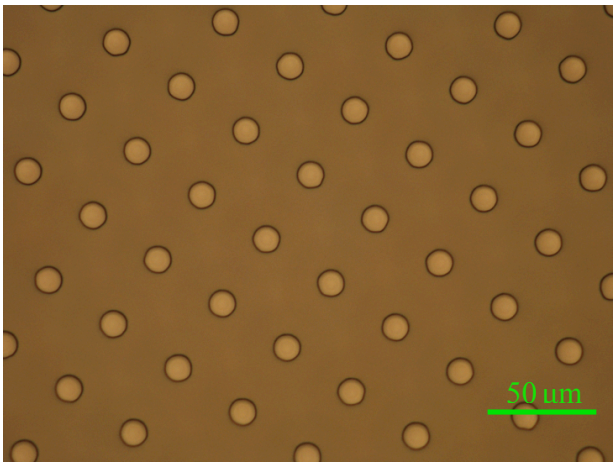

Figure 3-3: SU-8 3025 patterned layer on glass substrate, structures are 10 µm in diameter and 20 µm deep. Scale bar = 50 µm.

Soft lithography

Once microstructures have been created using photolithography with a photoresist, these structures can then be imprinted into elastomeric (soft) materials such as PDMS or agarose. This process, depicted in Figure 3-4, yields structures complementary to the original SU-8 'master'. Figure 3-5 shows a soft lithography master and the resulting imprinted microstructures in PDMS.

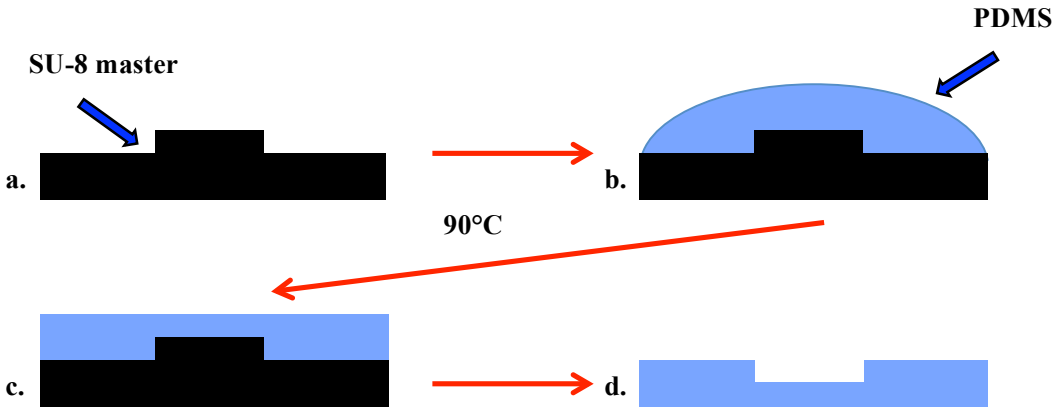

Figure 3-4: Soft lithography with PDMS.

a. SU-8 master.
b. Apply liquid PDMS to master, cure at 90°C for 2 hours.
c. Fully cured PDMS.

d. Remove PDMS with microstructure imprinted.

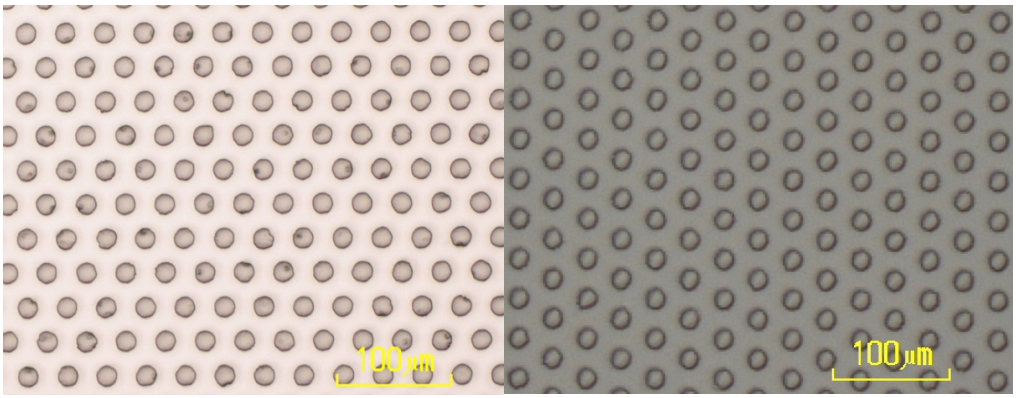

Figure 3-5: Microscope images showing a soft lithography master (left) of SU-8 pillars and the resultant PDMS well array (right). Scale bars = 100 µm.

Hot embossing

Hot embossing is the transfer of structures into hard materials such as acrylic by heating the material to above its glass transition temperature and then stamping it with a master. The master can be a variety of materials, but it must have a higher glass transition temperature than the material being embossed, and cannot be brittle at the temperature required to emboss. Figure 3-6 diagrammatically explains how Polymethyl Methacrylate (PMMA) is embossed using a soft PDMS master.

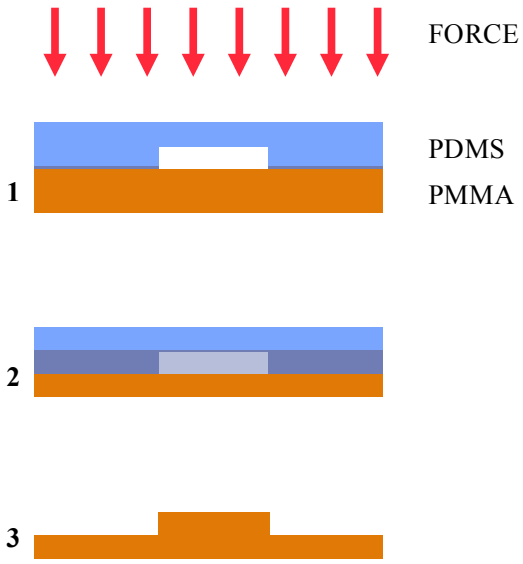

Figure 3-6: Hot embossing PDMS structures into PMMA.

1. PDMS is placed on top of the PMMA and a constant force pushes the PDMS into the PMMA (PMMA is soft, it has been heated to 40°C above its glass transition temperature).
2. PDMS is fully pushed into the PMMA and the assembly is allowed to cool to room temperature.
3. The PDMS is peeled off of the PMMA. The resulting PMMA has microstructures embossed in it.

Figure 3-7 shows the results of the replication steps when patterning PMMA using hot embossing. The PMMA was embossed using a bench-top EVG 501 bonder with force 4.5 kN for 15 minutes at 146°C. The glass transition temperature of PMMA is 110°C, and hot embossing was performed just under 40°C above this, following a protocol published by Narasimhan and Papautsky in 2004 [76]. Becker and Heim published another notable paper explaining the creation of high aspect ratio structures using hot embossing in 1999 [77].

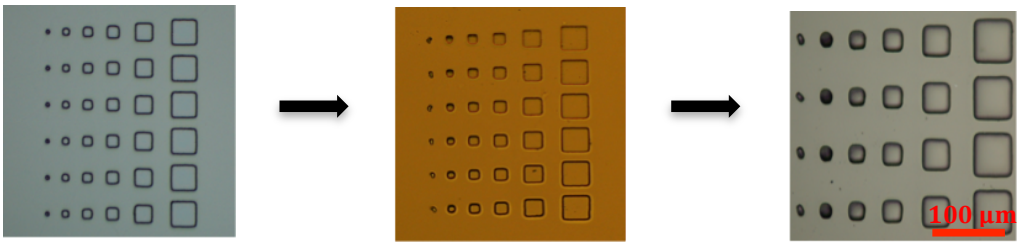

a. SU-8 wafer **b. PDMS mould** **c. Embossed PMMA**

Figure 3-7: Hot embossing microstructures into PMMA using a soft PDMS master. Scale bar = 100 µm.

a. Microstructures created in SU-8 using photolithography.
b. PDMS is cast from the SU-8 master (features are the exact opposite to the SU-8 features).
c. The PDMS is stamped into the PMMA, creating microstructures that are the same as the SU-8 master.

Fabrication summary

The fabrication methods detailed above are useful for creating structures that are of the same size as human cells (10s of microns) in a variety of materials. Once the microstructures have been created, surface modifications can be performed to alter the

characteristics of the materials, to complement the function of the micro-device. For example, native PDMS is hydrophobic (contact angle = 105°), but after exposure to oxygen plasma the PDMS surface will be covered in silanol (SiOH) groups, rendering the surface hydrophilic. This therefore makes it easier to load cells in liquid suspension into the microfluidic device. Other surface coatings such as fibronectin and collagen increase cell adherence, whereas PEG prevents it.

3.2.2 Selection of material

Conventionally, a SlipChip is fabricated by etching microstructures into glass; however this is a time-consuming procedure, so it was decided that the cell interaction SlipChip would be fabricated from another material that is easier to handle.

The material from which the SlipChip was created needs to have the following characteristics:

- Optical transparency;
- Possible to cut;
- Biocompatibility;
- Replicable;
- Slip-able.

Transparent material

The intercellular calcium level of T lymphocyte cells provides a measure of T lymphocyte activation against an APC. Calcium levels were determined using a calcium fluorescent dye called Fluo-8AM, see Chapter 4.1.2. The absorption wavelength of Fluo-8AM is around 490 nm and the emission wavelength is 520 nm. Hence, to view the activation of T lymphocytes using Fluo-8AM the SlipChip needs to be transparent between 490 nm and 520 nm.

The most common plastics used for microfluidic device replication are Cyclic Olefin Copolymer (COC), Cyclic Olefin Polymer (COP) and PMMA. All are transparent at the wavelengths necessary for Fluo-8AM; therefore it is possible to create a SlipChip from any material, using techniques such as hot embossing.

Material processing

Once patterned, the plastic needs to be cut to an exact size so that accurate 'slipping' can occur. As mechanical cutting of plastics can lead to cracking, the plastic was cut using a Carbon Dioxide (CO_2) laser. Figure 3-8 shows COC, COP and PMMA after cutting with the laser. The CO_2 laser causes both COC and COP to melt along the cutting edge, which would impede slipping. PMMA does not deform when cut with the laser and is transparent at the wavelengths necessary (490 nm to 520 nm). For these reasons, PMMA was selected for this work.

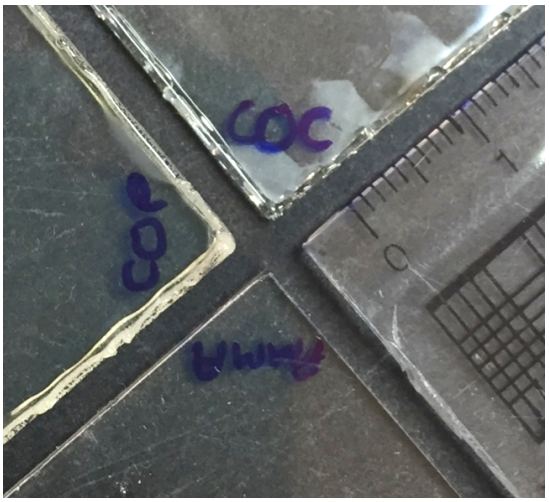

Figure 3-8: CO_2 laser cut COC, COP and PMMA.

Biocompatibility

It was important to construct the SlipChip from a biocompatible material, to ensure cells remain viable for the complete duration of the experiment. As the cells will not be cultured in the SlipChip, they are only in contact with the plastic for the duration of the experiment (less than an hour). For this, the biocompatibility of PMMA is adequate (PMMA is commonly used in orthopaedics as 'bone cement' as well as in dentistry [78]).

The other concern with trapping cells in a SlipChip is that, although PMMA is biocompatible, it is not gas-permeable. The following calculations were performed to determine the oxygen consumption rate of mammalian cells:

1. Well size = 20 µm x 20 µm x 20 µm (W x W x H), volume = 8 pL.
2. At 37°C the solubility of oxygen in water ≈ 6.72 mg/L [79]; therefore in 8pL there is 53.8 fg of oxygen.
3. Molecular mass of oxygen = 15.9994, number of moles of oxygen at 37°C in 8 pL = $[(53.8 \times 10^{-15}) / (15.9994)] = 3.36$ fmol.
4. At 37°C, the rate of oxygen consumption of mammalian cell lines ≈ 0.3 pmol/cell/hr [80]. For one cell = 0.3 pmol/hr = 0.083 fmol/sec.
   The oxygen will be depleted after $[(3.36 \times 10^{-15}) / (0.083 \times 10^{-15})]$ = **40.32 seconds**

Therefore, if the SlipChip is constructed from two PMMA plates, the cells will not remain viable for the duration of the experiment, which will exceed 40 seconds. The cell lifetime in a PMMA well was verified by trapping the cell line 'P815' in embossed wells on a PMMA plate. The plate was then covered with another plate of PMMA. The vital dye Trypan Blue was added to the cells after 1 minute to assess cell health (the cell membrane of a dead cell is permeable to Trypan Blue). All the cells were dead as predicted; hence creating a SlipChip completely from PMMA is unsuitable for cell processing. In conclusion, at least one plate of the SlipChip needs to be fabricated from a gas-permeable substrate (such as PDMS) to maintain cell viability for the duration of the experiment.

Slippable material

For the SlipChip device to function correctly, it must be constructed using a rigid material so that it can be slipped accurately without deforming. However, as discussed above, one plate needs to be made from a material that is not only transparent and biocompatible, but also gas permeable. The obvious solution is the silicon elastomer PDMS. PDMS is easy to replicate with high precision using soft lithography, transparent, and allows ample gas diffusion to sustain the oxygen consumption of the cells [81].

To verify that cells trapped in PDMS wells and covered with PMMA would survive, the following experiment was conducted: P815 suspension cells were trapped in PDMS wells and then covered with PMMA. After 5 minutes, Trypan Blue was added to the cells to test vitality; the majority (> 80%) survived (data not shown). Hence a SlipChip made with one plate PDMS and one plate PMMA would allow the cells to live for the duration of the experiment.

PDMS is a type of silicone and therefore is not slippable against PMMA, deforming when translated across the surface. Consequently, surface modification of the PDMS was explored. Surface modifications included silanisation (using Trichloro (1H, 1H, 2H, 2H-perfluorooctyl) silane), DuxBack coating, and plasma exposure multiple times. Changing the composition ratio of silicone elastomer to curing agent from the conventional 10:1 to 3:1 -making the PDMS more rigid- was also investigated.

It was concluded that to allow PDMS to slip against PMMA, the following treatments need to be applied:

1. Oxygen plasma activate the PDMS.

2. Silanise the oxygen plasma treated PDMS with Trichloro (1H, 1H, 2H, 2H-perfluorooctyl) silane.
3. Include a layer of the fluorinated lubricating fluid FC-40 between the PDMS and PMMA.
4. Apply uniform pressure to the plate in the direction of slip (not point pressure).

Replicable material

As discussed above (Chapter 3: Biocompatibility) the SlipChip needs to be constructed from one plate of PMMA and one plate of PDMS. PDMS microstructures can be fabricated using soft lithography with a SU-8 master, as detailed previously. The PMMA plate microstructures can be created using Hot embossing. Figure 3-9 and Figure 3-10 are examples of a bottom (hot embossed PMMA) and top (PDMS) SlipChip plate.

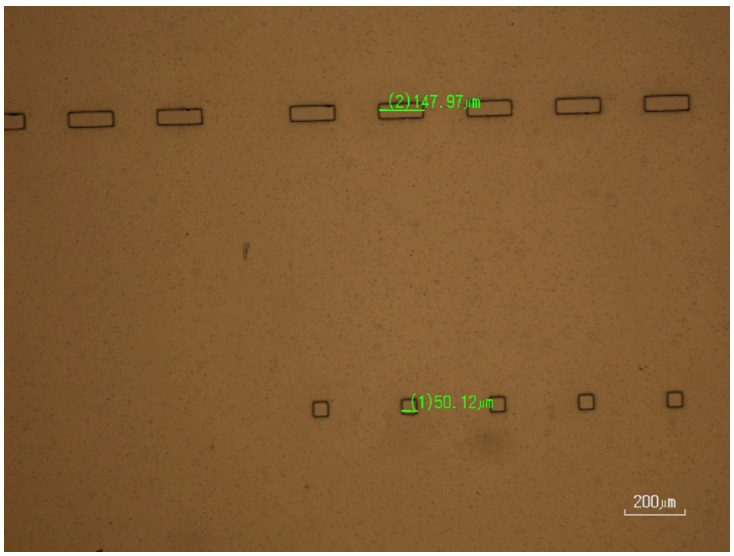

Figure 3-9: SlipChip bottom plate, consisting of 50 μm x 50 μm x 45 μm (W x W x H) wells and 50 μm x 150 μm x 45 μm (W x W x H) wells. Hot-embossed in PMMA. Scale bar = 200 μm.

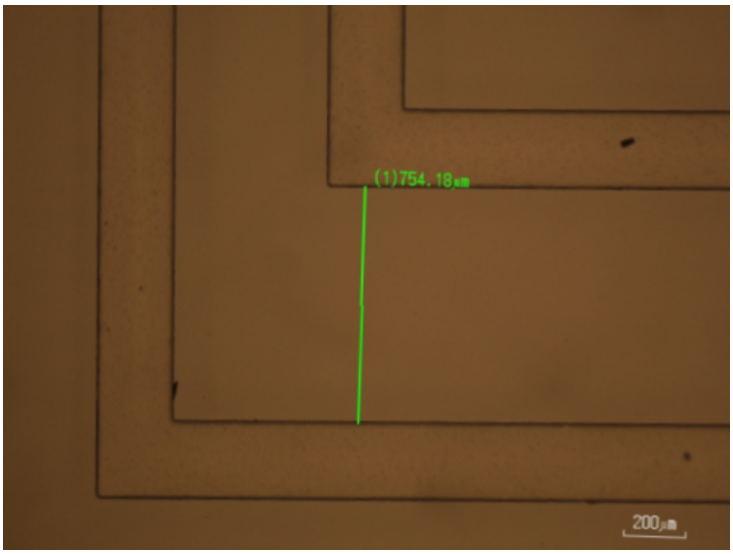

Figure 3-10: 250 μm x 45 μm (W x H) channels, replicated using soft lithography in PDMS to make SlipChip top plate. Scale bar = 200 μm.

3.2.3 Cell seeding

Cell size

In order to prevent trapping of multiple cells inside a single well and ensure single-cell occupancy, it is important to design the well dimension to be capable of housing only one cell. To establish suitable well sizes, the cells under investigation were imaged using an inverted IX81 Olympus microscope, and their cross-sectional dimensions measured. The results are presented below.

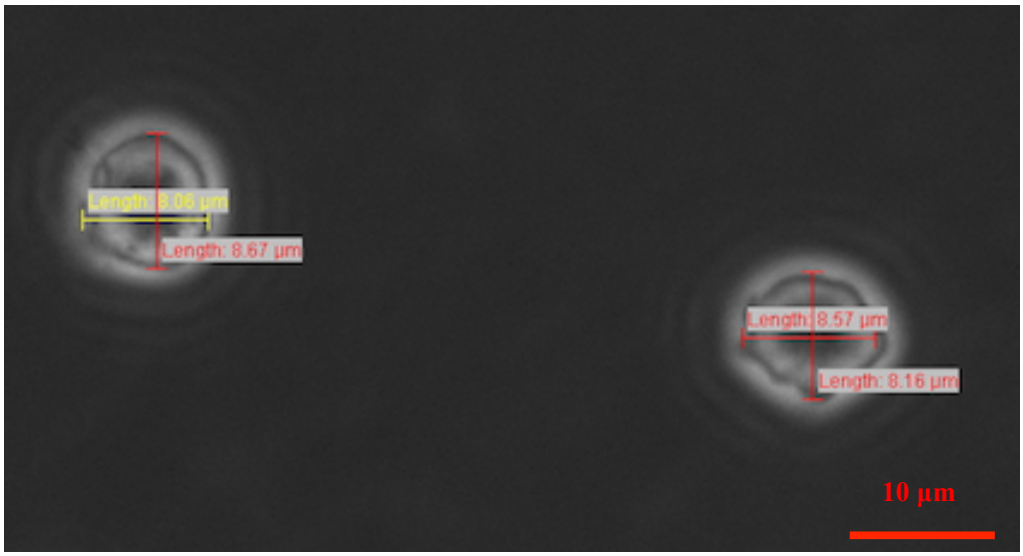

Figure 3-11: Brightfield microscope image of P815 cells, showing cross-sectional measurements. Image taken using an IX81 inverted microscope with 40x magnification. Scale bar = 10 µm.

The average cell size was determined by taking two perpendicular cross-sectional measurements of cell diameter and averaging them; repeated for approximately 100 cells. P815s are Mastocytoma cells (APCs) with a mean cell size of 9.3 µm, Standard Deviation (SD) of 0.9 µm (for 98 cells). Size data is shown in Figure 3-12.

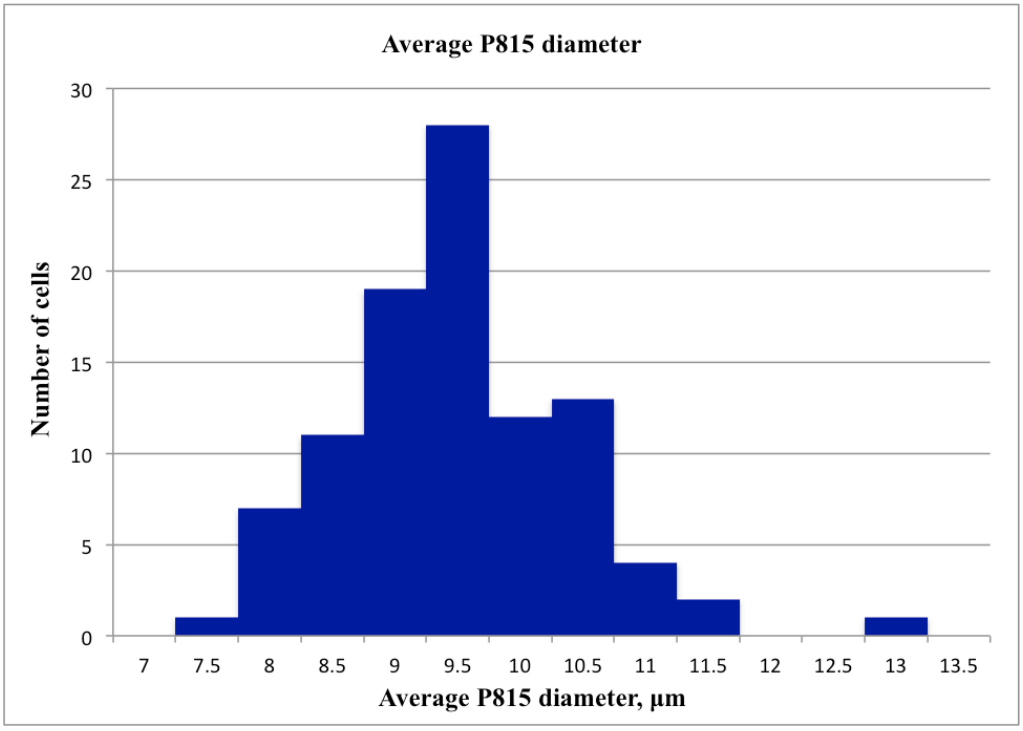

Figure 3-12: Histogram of individual cell size for P815 cells.

The average diameter of the cell line is therefore approximately 10 µm, hence the well size that is likely to trap only one cell is slightly greater than 10 µm in diameter.

Well traps

To trap the cells in the wells, a high concentration of cells in suspension medium were deposited on the surface and then the substrate was shaken to move cells into empty wells. The protocol is detailed in Appendix A.1.2.

This method was tested using 10 µm beads with mass density of 1.05 kg/m^3, the same approximate density as a cell (lymphocyte average density = 1.07 kg/ m^3 [82]), using microwells hot embossed into PMMA. Results are shown in Figure 3-13.

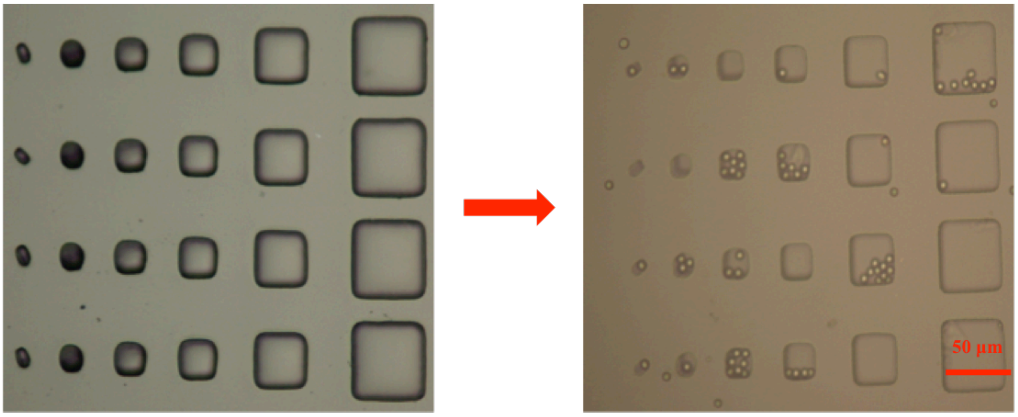

Empty wells in PMMA, size range 5 µm to 50 µm, depth 15 µm.

10 µm polystyrene beads trapped in PMMA wells.

Figure 3-13: Microscope images of PMMA wells before and after 10 µm polystyrene beads have been added. Scale bars = 50 µm.

The experiment was repeated three times and the number of beads trapped in each well was recorded. The data is presented in Figure 3-14.

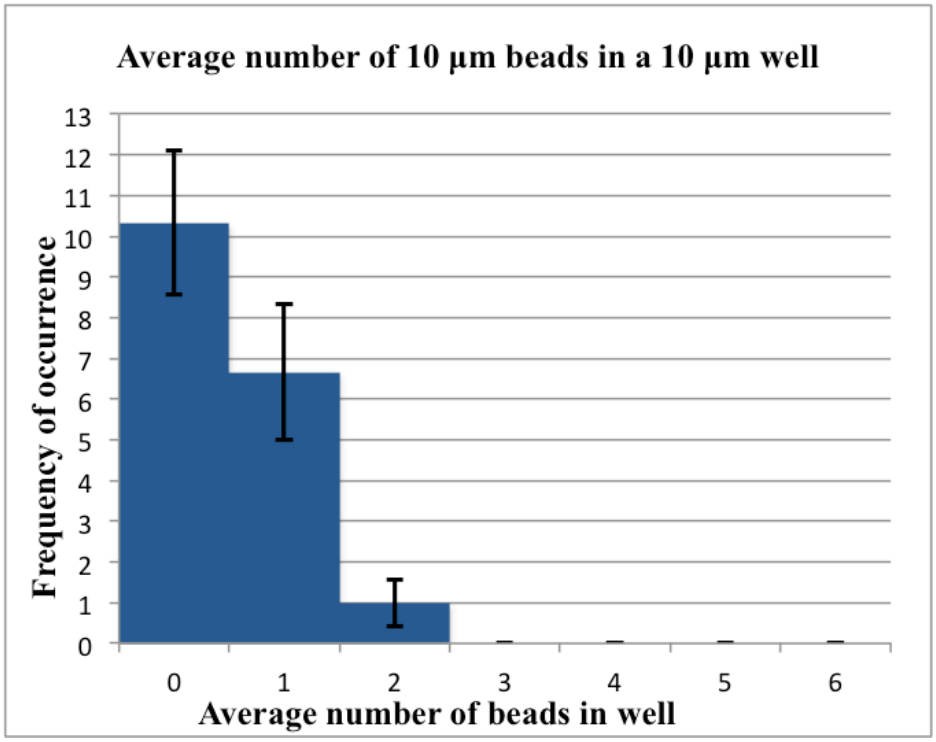

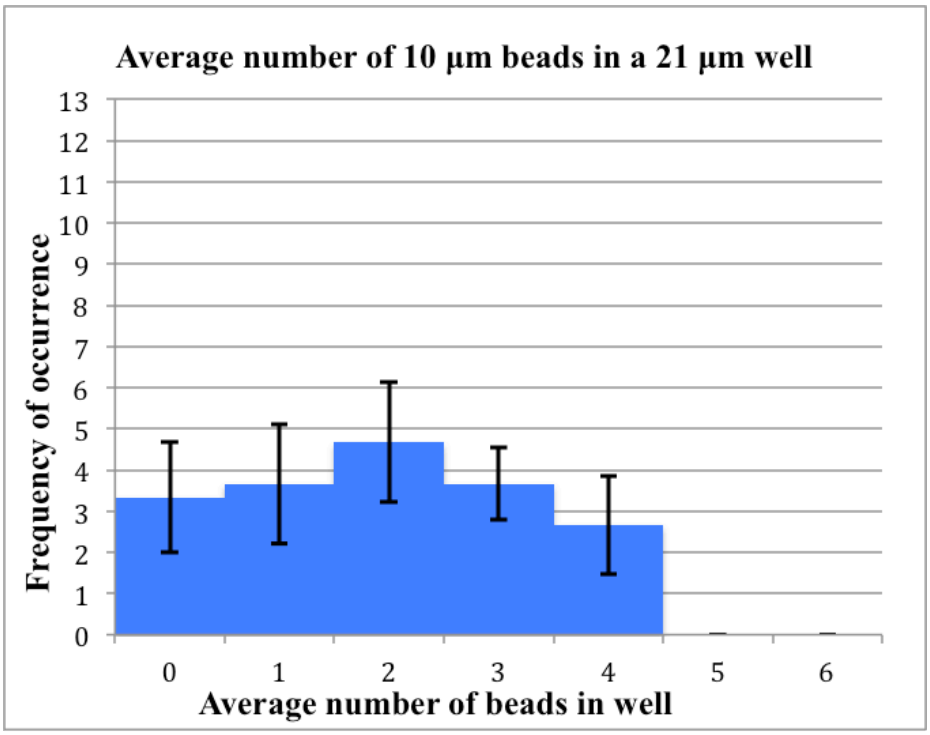

Figure 3-14: Histograms showing the number of 10 µm beads in 10 µm and 21 µm wells, data averaged across three experiments (Standard Error of the Mean (SEM) bars shown).

Multiple beads were trapped in wells with a diameter of 30 μm or more. No beads were trapped in the 5 μm wells. It can be seen from Figure 3-14 that both well sizes (10 μm and 21 μm) appear to have a Poisson distribution of beads in the well. In terms of single-cell occupancy, the 10 μm well was most effective, rarely trapping more than one cell. However, the majority of the 10 μm wells remained unoccupied, resulting in a low cell capture efficiency. This presents a significant drawback to this method of bead capture. The wells must be small enough to only capture one bead, but this could lead to no beads being captured.

The same protocol was repeated with cells. P815 cells (9.3 μm average diameter) were added to the microwells embossed in PMMA. 100 μL of cells at a concentration of $2x10^6$ cells/mL were deposited on the PMMA, leading to trapping in the PMMA wells. The results are shown in Figure 3-15.

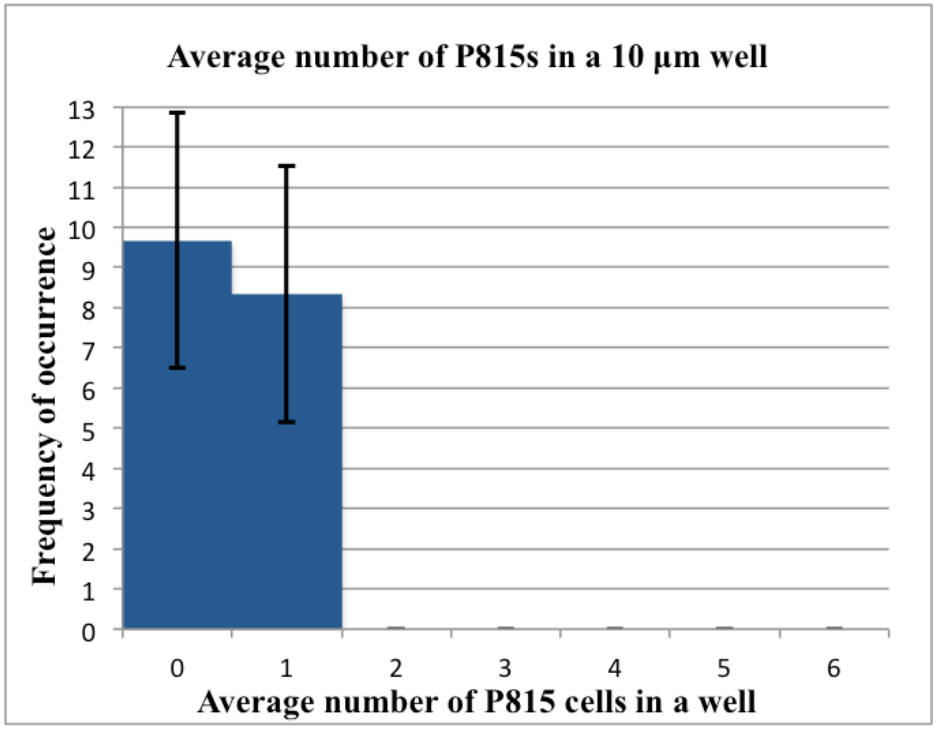

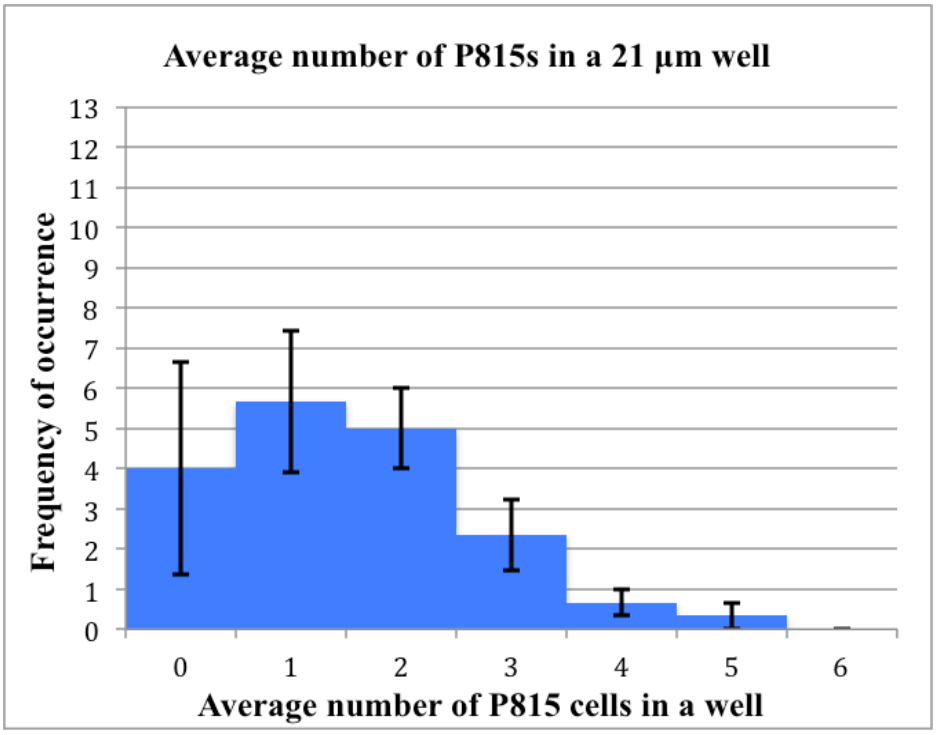

Figure 3-15: Histograms showing the number of P815 cells in 10 µm and a 21 µm wells, data averaged across three experiments (SEM bars shown).

Figure 3-15 confirms that the distribution of cells in wells is very similar to the distribution of beads, indicating that the best well size (for the proof-of-concept experiment performed) is 10 μm x 10 μm (W x W).

3.2.4 Summary

It is anticipated that the SlipChip could be used to trap individual cells and allow interactions in a controlled manner, provided the wells are sized appropriately to allow only one cell to dock. It has been shown that the SlipChip could be fabricated using one half made of PMMA using hot embossing, and the other half of PDMS, using soft lithography. Proof of concept tests were undertaken to verify that cells would remain viable in the device for the duration of the experiment. PDMS and PMMA are both optically transparent at the wavelengths necessary for calcium imaging, so T lymphocyte activation against an APC could be monitored using the calcium fluorophore Fluo-8AM.

3.3 Results

The cell trapping SlipChip concept is depicted in Figure 3-1. It was intended that the microwells would be fabricated in PDMS and PMMA plates to trap T lymphocytes and APCs respectively. The wells-containing-cells would then be sandwich-assembled and translated so that they overlap, allowing cell-cell interactions to take place.

3.3.1 Mask designs

Proof of concept: Ionomycin SlipChip

Ionomycin is a calcium ionophore that causes calcium channels to open in the cell membrane, allowing calcium from the media to diffuse into the cell. (Further discussed in Chapter 4: Activation with ionomycin.) Prior to use it is diluted in Dimethyl Sulfoxide (DMSO), a water miscible solvent that permeates through cell membranes and acts as a carrier for other substances. Ionomycin can be used to force a T lymphocyte calcium response [83]; it is a useful positive control. The ionomycin SlipChip was designed as a precursor experiment before the cell-cell interaction SlipChip was created; as such, the wells are larger than the optimum size concluded in Chapter 3.2.3.

A photolithography mask was designed to allow the minimum concentration of ionomycin required to induce a calcium response in T lymphocytes (fluorescently

labelled with Fluo-8AM) to be investigated. This was achieved by creating a series of wells containing varying levels of ionomycin concentration ('titration wells').

A schematic of the top and bottom plates is displayed in Figure 3-16. The top plate wells are loaded with ionomycin (and a control: PBS). The bottom plate wells are loaded with a diluent (PBS), and B3Z T lymphocytes (labelled with Fluo-8AM).

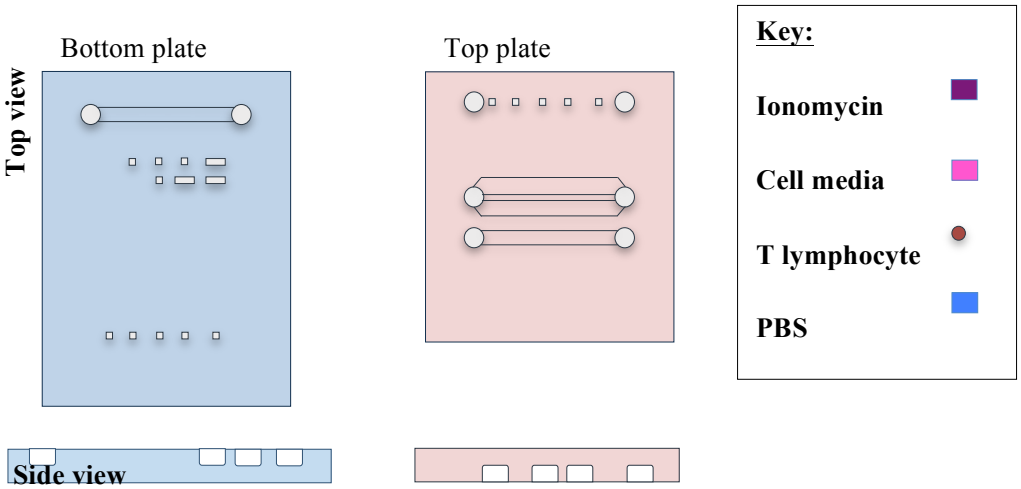

Figure 3-16: Schematic of ionomycin SlipChip top and bottom plate designs.

The top plate wells that are loaded with ionomycin (or the control) are 20 microns by 20 microns in size, shown in Figure 3-17.

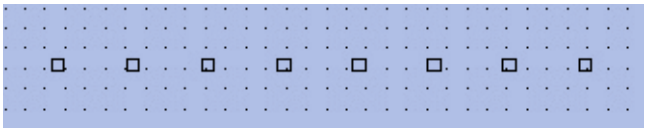

Figure 3-17: Section of a mask design of top plate wells, 20 µm by 20 µm in size.

The bottom plate titration wells were loaded with a diluent to dilute the ionomycin in the top wells. These are either the same size as the top plate wells (20 microns by 20 microns), and hence dilute the ionomycin by 50%, or three times the volume of the top plate wells (20 microns by 60 microns), and dilute the top plate ionomycin to 25% of its original concentration.

When the top plate is slipped over the bottom plate, the top plate wells overlap the bottom plate titration wells and the ionomycin is diluted (from left well to right well) to a final concentration of 1, $\frac{1}{2}$, $\frac{1}{4}$, $\frac{1}{8}$, $\frac{1}{16}$, $\frac{1}{32}$ and $\frac{1}{64}$. For example, if the top plate wells are loaded with 1 µg/mL ionomycin, the final titration profile will be:

1 µg/mL, 0.5 µg/mL, 0.25 µg/mL, 125 ng/mL, 62.5 ng/mL, 31.25 ng/mL and 15.625 ng/mL.

The operating procedure is shown diagrammatically in Figure 3-18.

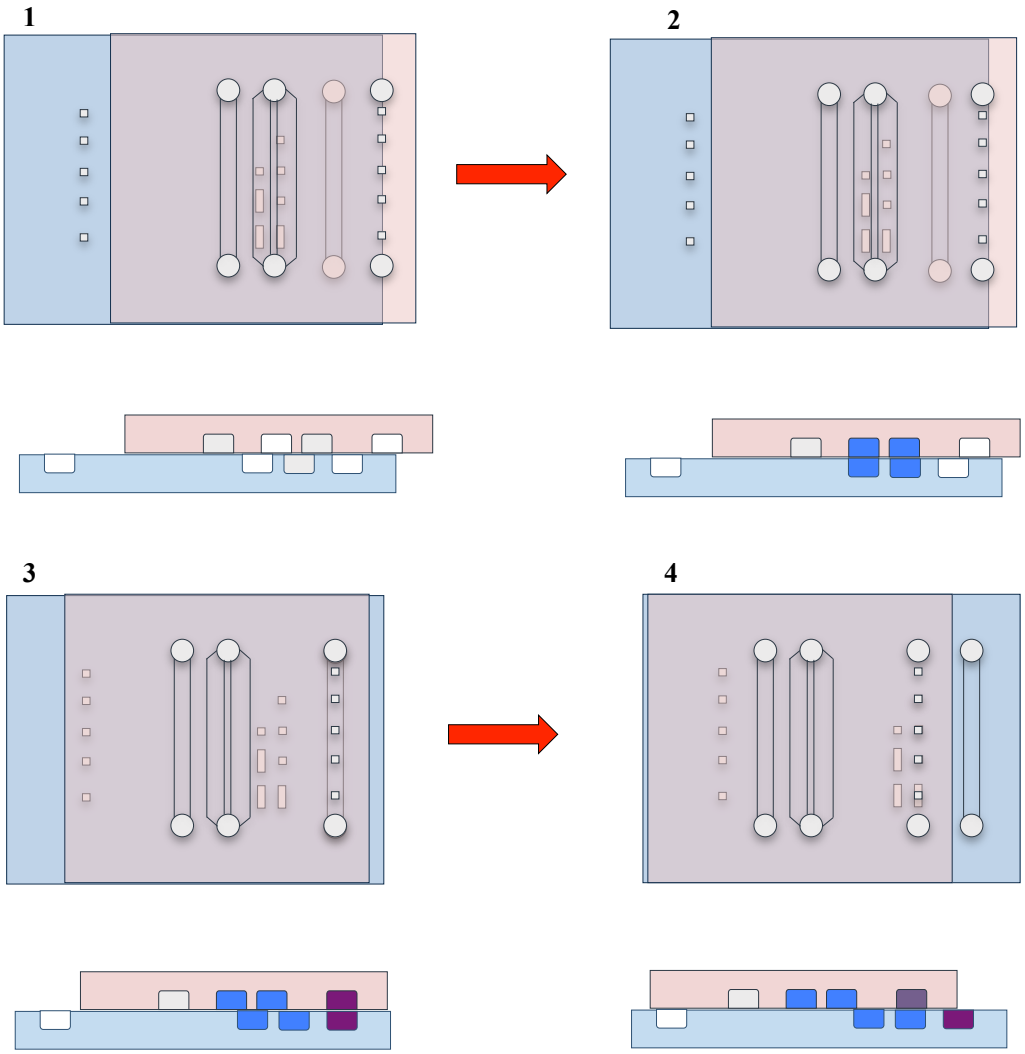

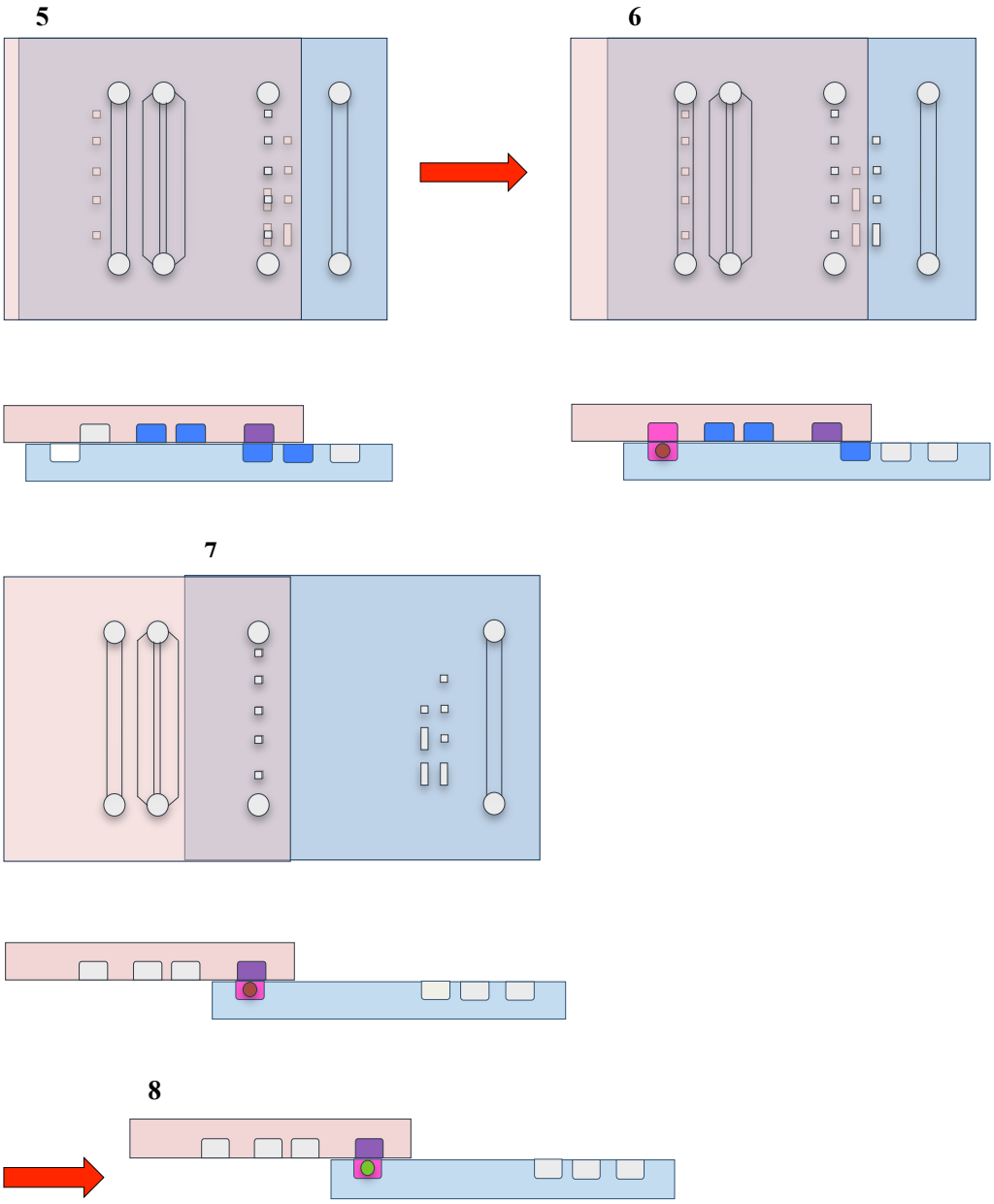

Figure 3-18: Ionomycin SlipChip operating procedure.

The step-by-step operating procedure is as follows:

1. Place top plate over bottom plate and align so the wells are parallel.
2. Slide by 2 mm, fill titration wells with PBS.
3. Slide another 2 mm (4 mm in total); fill top wells with ionomycin (or control).
4. (& 5) Slide 5 mm (9 mm in total); dilute ionomycin in top wells.
6. Slide 1 mm (10 mm in total); fill bottom wells with B3Z T lymphocytes.
7. Slide 10 mm (20 mm in total); expose T lymphocytes to ionomycin.

8. T lymphocyte activation can be seen by calcium response with Fluo-8AM.

Cell-Cell interaction SlipChip

A cell-cell interaction SlipChip was also designed. The titration wells on the bottom plate were replaced with two rows of cell wells for loading T lymphocytes. An APC line would be loaded in the top plate wells and slipped over the T lymphocytes in the bottom plate. A secondary row of T lymphocytes is included in the bottom plate to allow for the study of subsequent interactions between a single APC and two T lymphocytes.

3.3.2 Alignment and leakage

In order for the top plate wells to overlap the bottom plate wells, the two plates must be perfectly aligned at the micro-metre scale. To do this a rig was manufactured from PMMA that would hold the bottom plate stationary and allow the top plate to be slipped across the bottom plate using a micrometer screw, Figure 3-19. A PMMA holder that overlaps the top plate by 1 cm on all sides, and is mechanically pushed down with screws and wing nuts, clamps the top plate against the bottom plate.

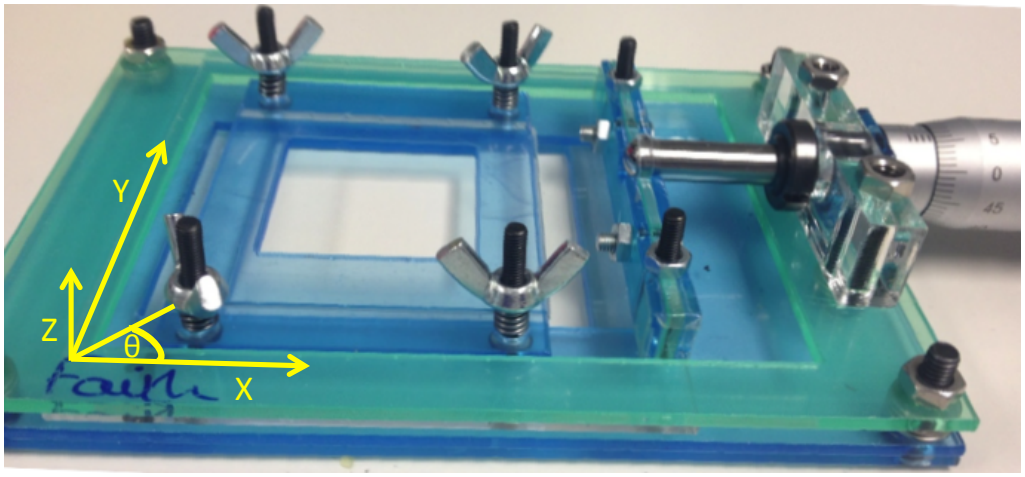

Figure 3-19: Initial rig design. Size: 12.5 cm x 9 cm (L x W). Top plate: 5 cm x 5 cm (L x W), bottom plate: 7 cm x 5 cm (L x W). Slipping distance = 2 cm.

The wells are loaded with liquid or cells by a syringe pump through capillary tubing connected to the top PDMS plate. The top and bottom plate inlet and outlet reservoirs are designed to overlap during loading; however it proved very difficult to achieve alignment using the rig shown in Figure 3-19, as movement was only possible in the X direction and not Y, Z or theta. If the top plate was at an angle to the bottom plate, or displaced in the Y

direction, then it was impossible to correct for this. An example of alignment in the X direction, but not in the Y direction, is presented in Figure 3-20.

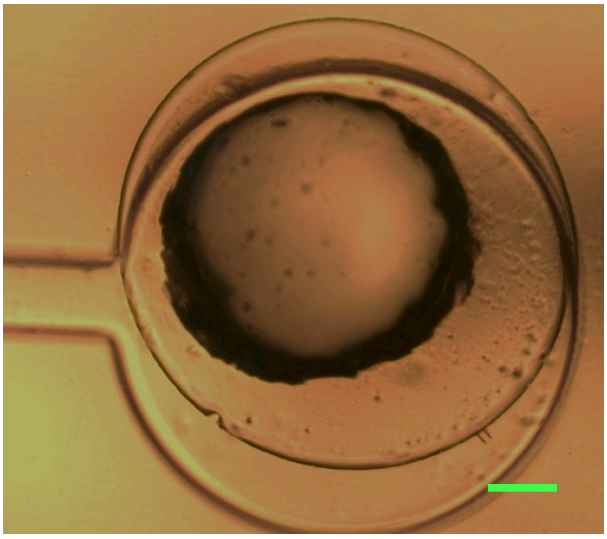

Figure 3-20: Alignment of top and bottom plate using initial rig design. Top plate is misaligned in the Y direction. Scale bar = 250 µm.

Furthermore, the top plate is only clamped against the bottom plate at the edges. As liquid is pushed into the channel with the syringe pump, air that is inside the tubing is pushed through the channel; Figure 3-21. This air can push outside of the channel boundaries as seen in the yellow box of Figure 3-21.

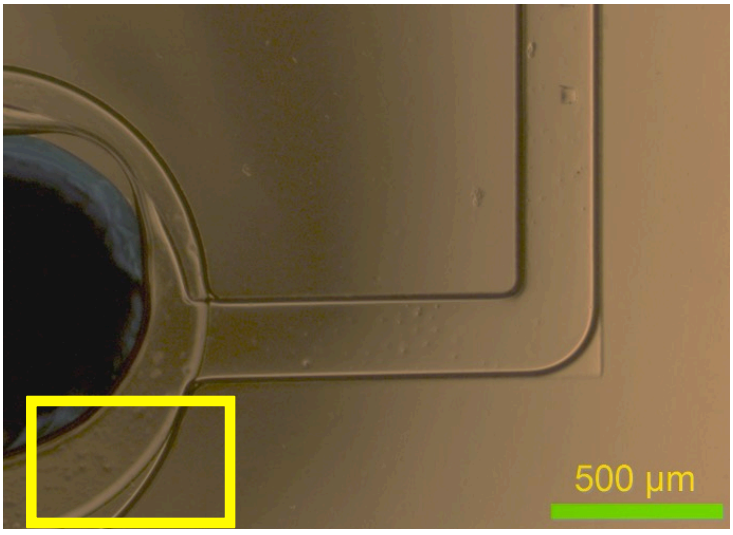

Figure 3-21: Air in channel. Yellow box shows air pushing outside of channel boundaries. Scale bar = 500 µm.

Once the seal between the top plate PDMS and the bottom plate PMMA is compromised, any liquid that is subsequently pushed into the device leaks out of the channel boundaries, filling the air pocket; Figure 3-22. It then continues to leak across the device; Figure 3-23.

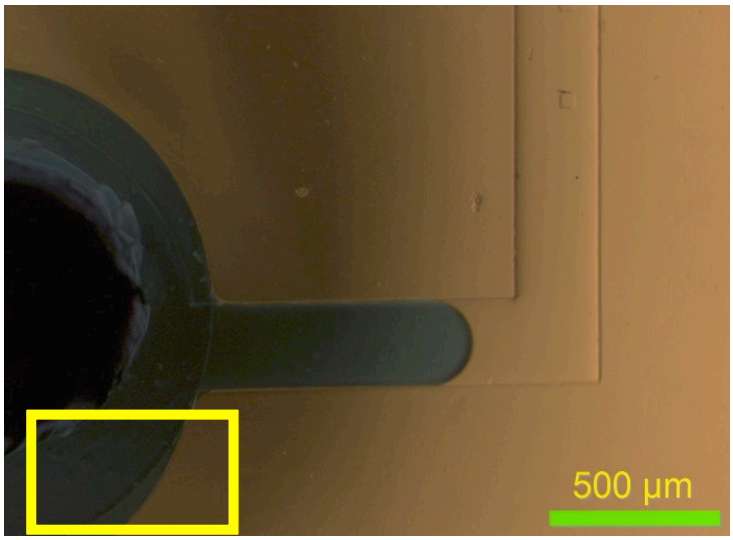

Figure 3-22: Liquid leaking after air has compromised the PDMS:PMMA seal. Scale bar = 500 µm.

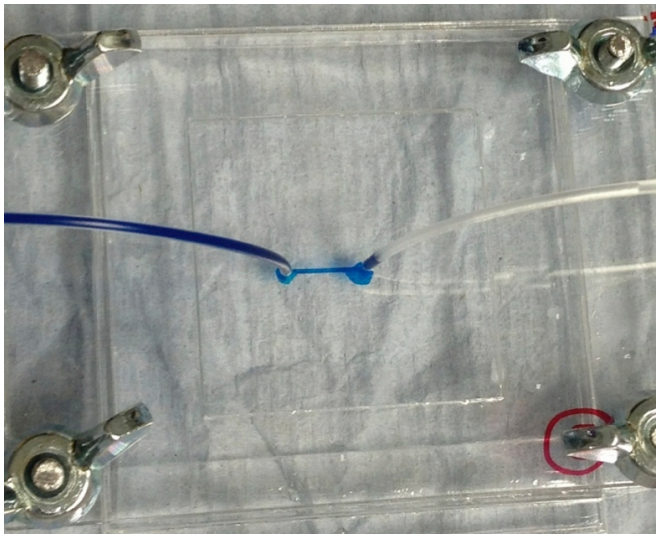

Figure 3-23: Liquid leaking between top and bottom plates.

Reducing the liquid flow rate (down to 2 µL/min) and flooding the inlet tubing with liquid before inserting it into the top plate (evacuating air from the channel) was tried to prevent liquid leaking. Unfortunately it was impossible to eliminate all the air inside the tubing, as the action of pushing the tubing into the PDMS forces the liquid back up the tubing slightly. The tubing can be inserted before the liquid is flowed through, but then

the liquid must be pushed almost to the inlet hole before the top plate is clamped against the bottom plate, and this action often causes some liquid to be released in-between the plates. The reduced flow rate decreased the likelihood of air breaking the seal, but the success rate was still only around 1 in 10.

As such, a new top ‘clamp plate’ was created from 5 mm thick PMMA which clamped the whole top plate to the bottom plate, except for inlet holes for the tubing to push through, Figure 3-24 and Figure 3-25.

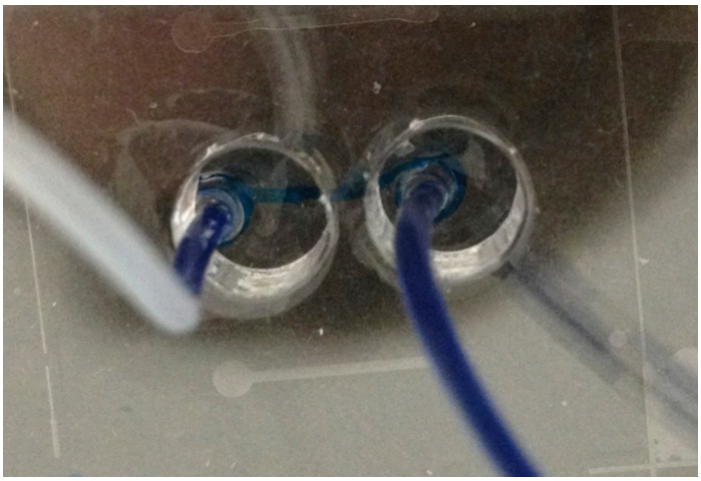

Figure 3-24: Magnified image of top plate clamp with holes for inlet and outlet tubing.

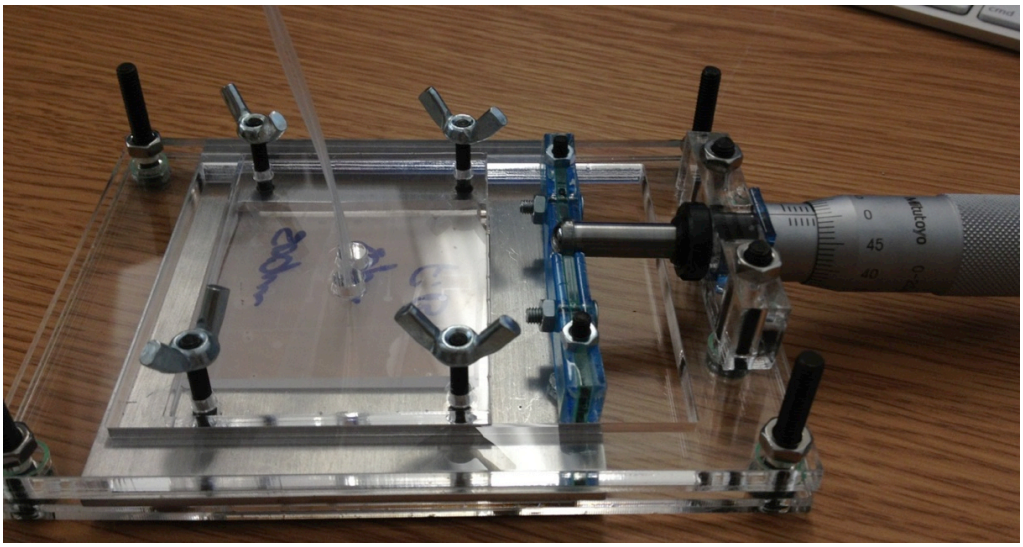

Figure 3-25: Image of rig with top plate clamp, showing inlet tubing attached to top plate through clamp.

Using this new clamping method reduced the liquid leakage. However only approximately 1 in 5 devices did not leak. Additionally, this rig still did not allow alignment in the Y, Z or theta directions. Therefore, a new top plate clamp was designed which allowed both Y and theta translation. The entire rig was made from aluminium so that it was more solid and did not bend under pressure. The new top plate clamp design is presented in Figure 3-26, with a magnified image of the clamp (yellow box) shown in Figure 3-27.

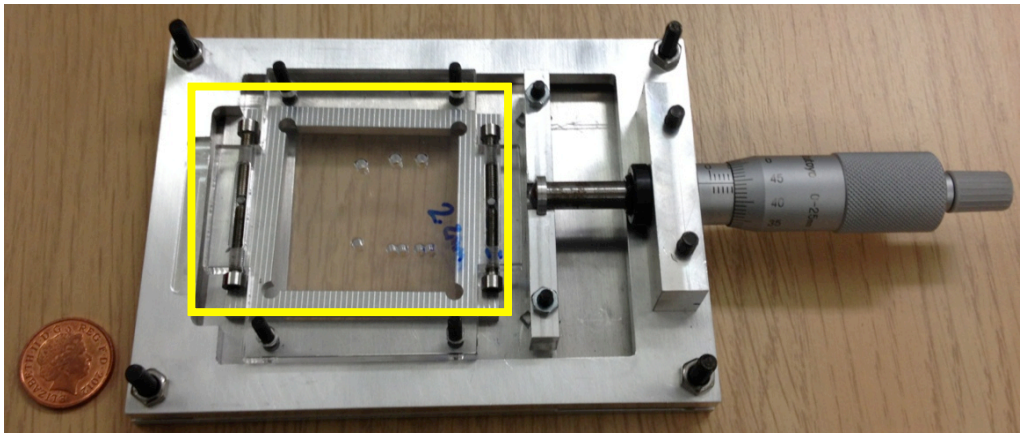

Figure 3-26: Rig made from aluminium with additional top plate clamp that allows Y and theta translation (yellow box).

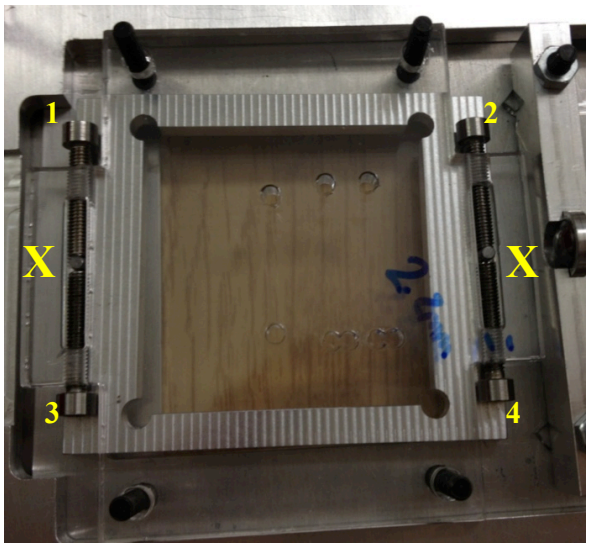

Figure 3-27: Yellow box from Figure 3-26.

The top plate is 4 cm by 4 cm, positioned inside the aluminium support, and clamped down using four screws and wing nuts, as in the previous rig. It can then be translated in

the Y direction, or rotated using the four side screws (1-4) that push on the pins seen next to the 'X's. For example, unscrewing screws 1 and 2 and screwing-in screws 3 and 4 moves the entire top plate to the left (i.e. 'up' in Figure 3-27), or releasing screws 3 and 2 and screwing-in screws 1 and 4 rotates the plate counter-clockwise. Using this clamp it was possible to align the top and bottom plates correctly (Figure 3-28); however this proved difficult as the alignment clamp does not allow fine-tuning, and requires multiple screw adjustments, which is time-consuming.

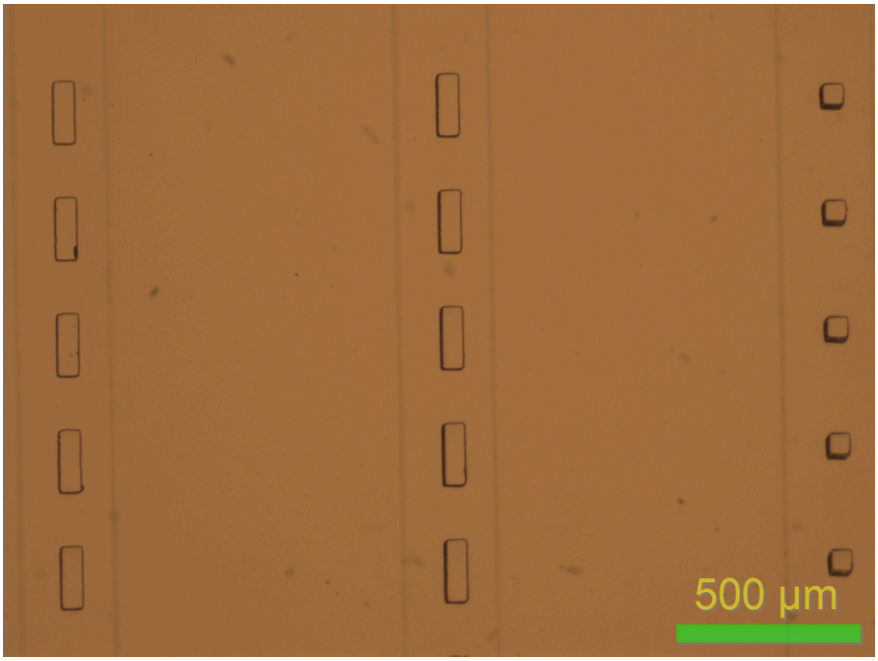

Figure 3-28: Top plate channels correctly aligned over bottom plate wells. Scale bar = 500 µm.

3.3.3 Cell docking

Once the top and bottom plates are clamped together and aligned correctly, it was expected that a cell suspension would be loaded into the channel above the wells and cells would dock inside the wells by gravitational force; one per well due to size exclusion, see Chapter 3.2.3.

However, for PDMS to be slipped over the PMMA bottom plate a thin layer of perfluorocarbon lubricating fluid (FC-40) was used (Figure 3-29). Unfortunately, the FC-40 filled the bottom plate wells preventing the cells from docking; FC-40 has a higher density (1.85×10^3 kg/m^3 [84]) than the suspending medium (PBS: 1.0×10^3 kg/m^3 [85]). As

FC-40 is a dense medium, only a medium with a higher density would displace it from the wells; however most liquids do not fulfil this requirement.

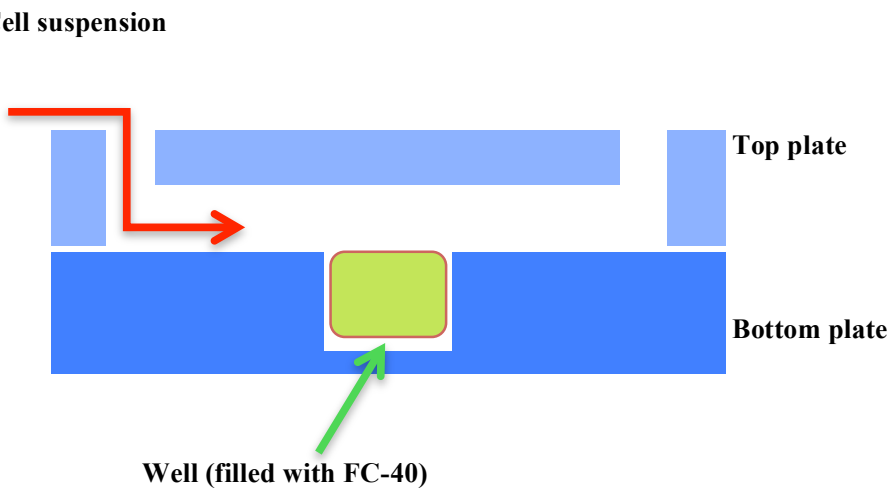

Figure 3-29: Issue with cell loading: well is filled with FC-40, so subsequent liquid flows over the well, preventing cell docking.

3.3.4 Magnetic bead transfer

To test the concept of the movement of cells from top to bottom plate wells (or vice-versa), and hence ensure interaction could take place between two plates, magnetic beads were seeded into the bottom PMMA plate manually. The SlipChip top and bottom plates were then brought into contact, and the magnetic beads were pulled up into the top PDMS plate using a magnet. The magnetic beads used in this work were monodisperse polystyrene iron oxide particles, average diameter 10.31 µm, purchased from Microparticles GmbH.

Translation of magnetic beads: Proof of concept

To ensure that the magnetic beads could be translated using stationary magnets, and determine the strength of magnet needed, the following proof of concept experiment was conducted. See Figure 3-30.

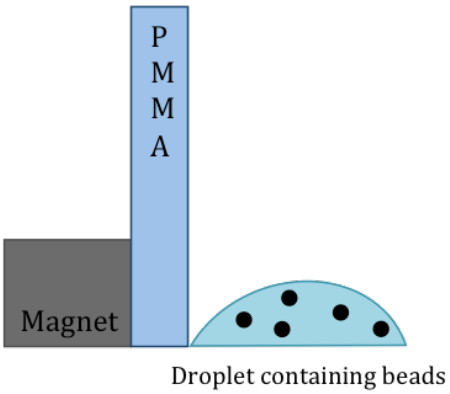

Figure 3-30: Diagram depicting magnetic bead translation experiment.

The procedure was as follows:

1. A droplet of PBS containing magnetic beads was deposited on a non-stick surface. The droplet spanned 2 mm.
2. The magnetic beads were pulled to the right edge of the droplet, furthest away from a 2 mm wide sheet of PMMA. (The PMMA was included to prevent the beads from making direct contact with the magnet, and also as a possible barrier that would exist between the beads and the magnet in the actual experimental set-up.)
3. The magnet was placed on the opposite side of the PMMA and the time taken for the magnetic beads to move across the width of the droplet was measured.

Results are presented in Table 1

Quoted Magnet Pull Force / kg	**Time / seconds**
4	0 (Instant)
1	0 (Instant)
0.5	1 ➔ 3
0.3	15 ➔ 60

Table 1: Results of magnetic bead translation experiment.

It can be concluded that the magnetic beads could be translated using stationary magnets.

Magnetic bead transfer in device

A PMMA bottom plate with 11 µm wells (created by hot embossing) was seeded with 10 µm magnetic beads and assembled as a SlipChip, with FC-40 lubricating fluid and a PDMS top plate with 20 µm wells. Using a Nikon inverted microscope, translation of magnetic beads from the bottom to the top plate of the SlipChip was imaged (Figure 3-31).

A) Bottom plate (PMMA) well with two magnetic beads as focal point.
B) As 'A', top plate (PDMS) empty wells as focal point.
C) Top plate is translated over the bottom plate to align the top and bottom wells.
D) A 1kg magnet is applied to the top plate for 10 minutes before the top plate is translated again; a magnetic bead is now seen in the well of the top plate.

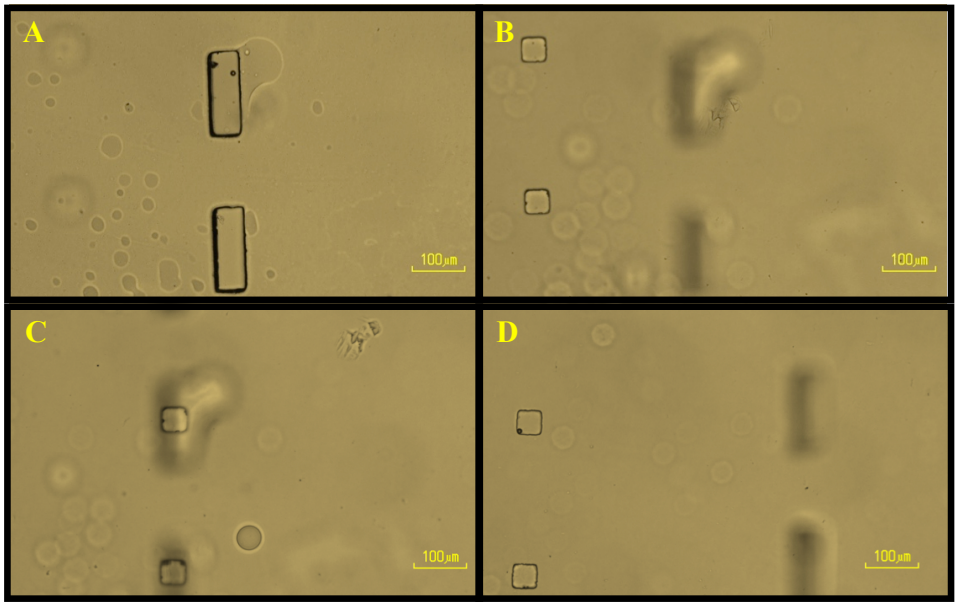

Figure 3-31: PMMA:PDMS SlipChip showing magnetic bead transfer. Scale bars = 100 µm. A) Bottom plate (PMMA) well with two magnetic beads as focal point. B) As 'A', top plate (PDMS) empty wells as focal point. C) Top plate is translated over the bottom plate to align the top and bottom wells. D) A 1kg magnet is applied to the top plate for 10 minutes before the top plate is translated again; a magnetic bead is now seen in the well of the top plate.

Although Figure 3-31 demonstrates that it is possible for magnetic beads to be transferred from bottom to top plate using a stationary magnet, in the majority of cases the transfer

was unsuccessful. The bottom plate bead would either remain in the bottom well, or move into the space between the plates and subsequently end up in an adjacent well.

In Figure 3-31, the plates used are the ionomycin SlipChip design with small wells of 50 µm x 50 µm (W x W) and large wells of 50 µm x 150 µm, hence multiple 10 µm magnetic beads could become trapped in a single well. As such, a plate was designed with 20 µm diameter wells so that the majority of wells would only contain one bead (see Chapter 4: Microwell array design). Proof of concept trials were undertaken to ensure that the magnetic beads could be removed from these smaller wells, see Figure 3-32, Figure 3-33 and Figure 3-34. The protocol is described below.

1. Beads were seeded in 18 µm diameter wells at a ratio of 2.5:1 beads:wells by depositing bead suspension in PBS on the surface of PDMS. See Figure 3-32.

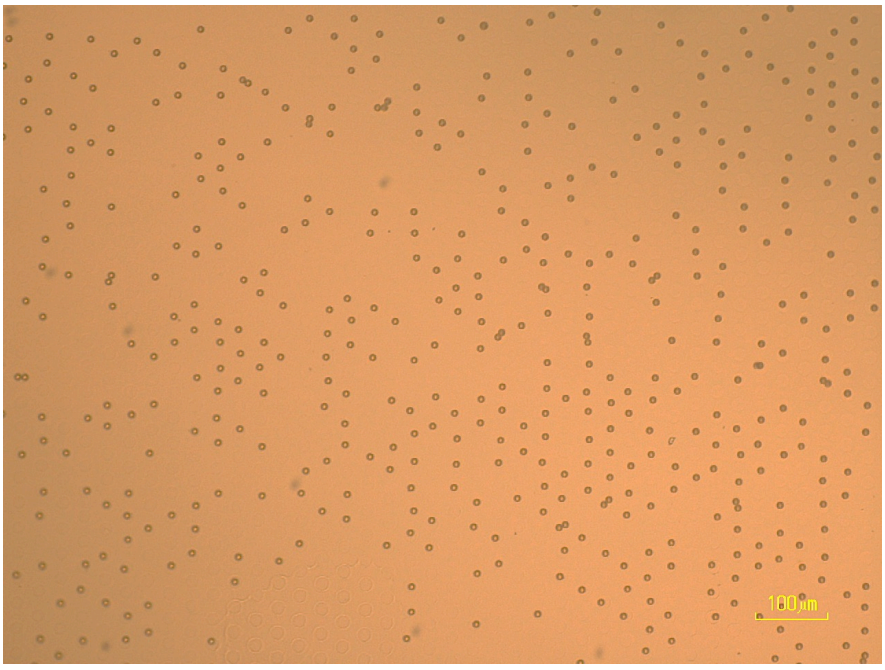

Figure 3-32: Image of 10 µm magnetic beads trapped in 18 µm x 16 µm (W x H) wells in PDMS. Image taken using a Nikon inverted microscope. Scale bar = 100 µm.

2. PDMS plate with magnetic beads was turned over for 10 minutes to test whether the beads would fall out of the wells under the force of gravity; Figure 3-33.

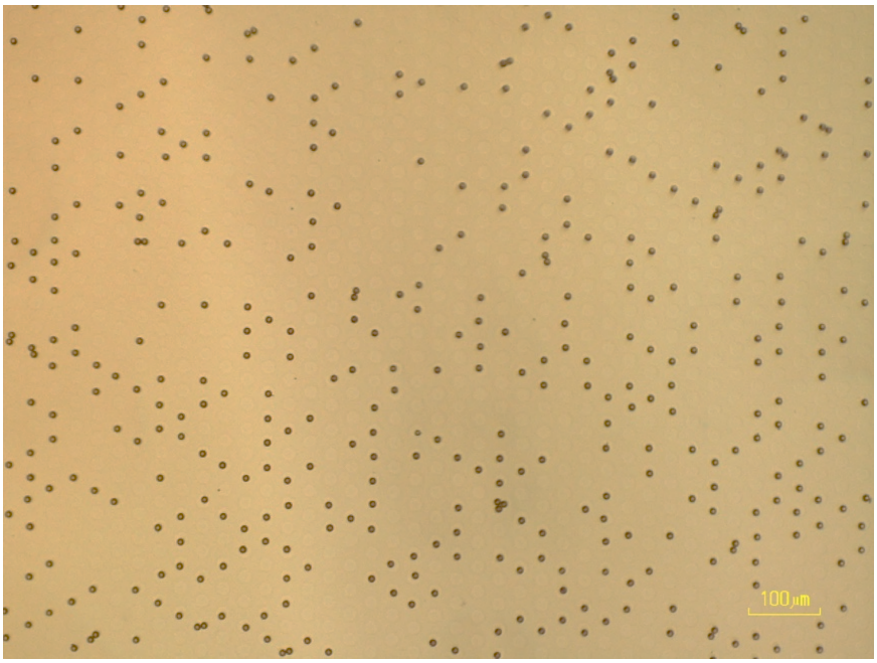

Figure 3-33: Image of PDMS plate with 10 µm magnetic beads, after 10 minutes inverted. Scale bar = 100 µm.

Note: The imaged section is of the same wafer, but not the exact same region as Figure 3-32.

It can be seen from Figure 3-33 that the magnetic beads do not fall out of the wells under the influence of gravity.

3. A standard refrigerator magnet (approximate strength – 5 mT) was placed under the PDMS when it was turned over for 10 seconds, so that the magnet would attract the magnetic beads out of the wells. See Figure 3-34.

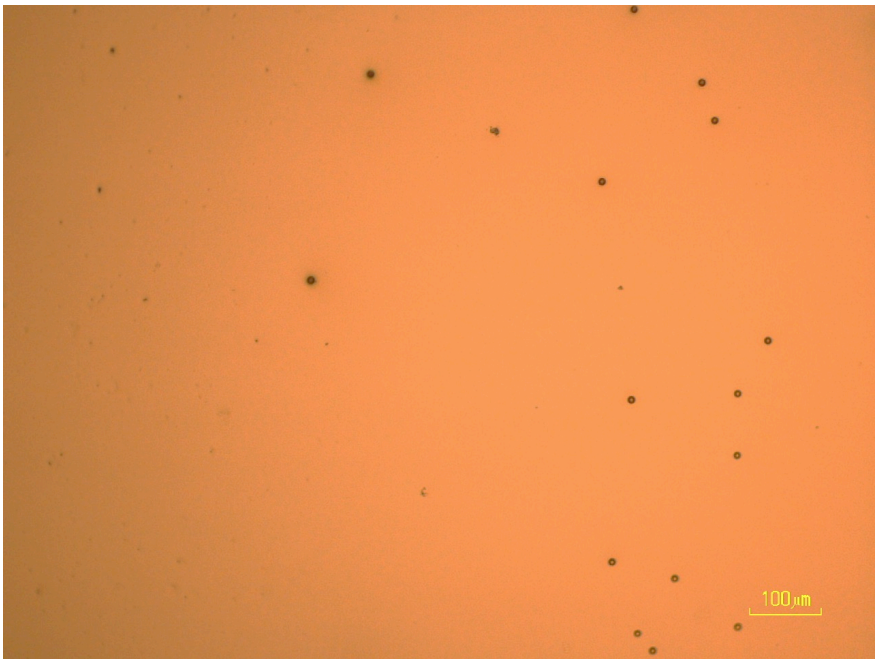

Figure 3-34: Image of PDMS plate with 10 µm magnetic beads, after 10 seconds inverted with a refrigerator magnet. Scale bar = 100 µm.

Note: The imaged section is of the same wafer, but not the exact same region as Figure 3-32 or Figure 3-33. It can be seen that the inclusion of a low-strength magnet caused the majority of magnetic beads to be pulled out of the wells.

Transfer of magnetic beads from bottom plate to top plate wells was then undertaken. See Figure 3-35. The experiment was conducted as follows:

A) 10 µm magnetic beads were seeded into 16 µm deep wells, in 4.5 mm deep PDMS.
B) A top plate (made from the same PDMS array) was placed on top of the bottom array and aligned as accurately as possible. Subsequently, a 1 kg pull force magnet was placed on top of the two plates to pull the beads into the top plate wells.
C) After 10 minutes, the top plate and magnet were removed and inverted. Beads are seen in the top plate wells.
D) Image of the bottom plate after bead transfer. No beads remain in the bottom plate.

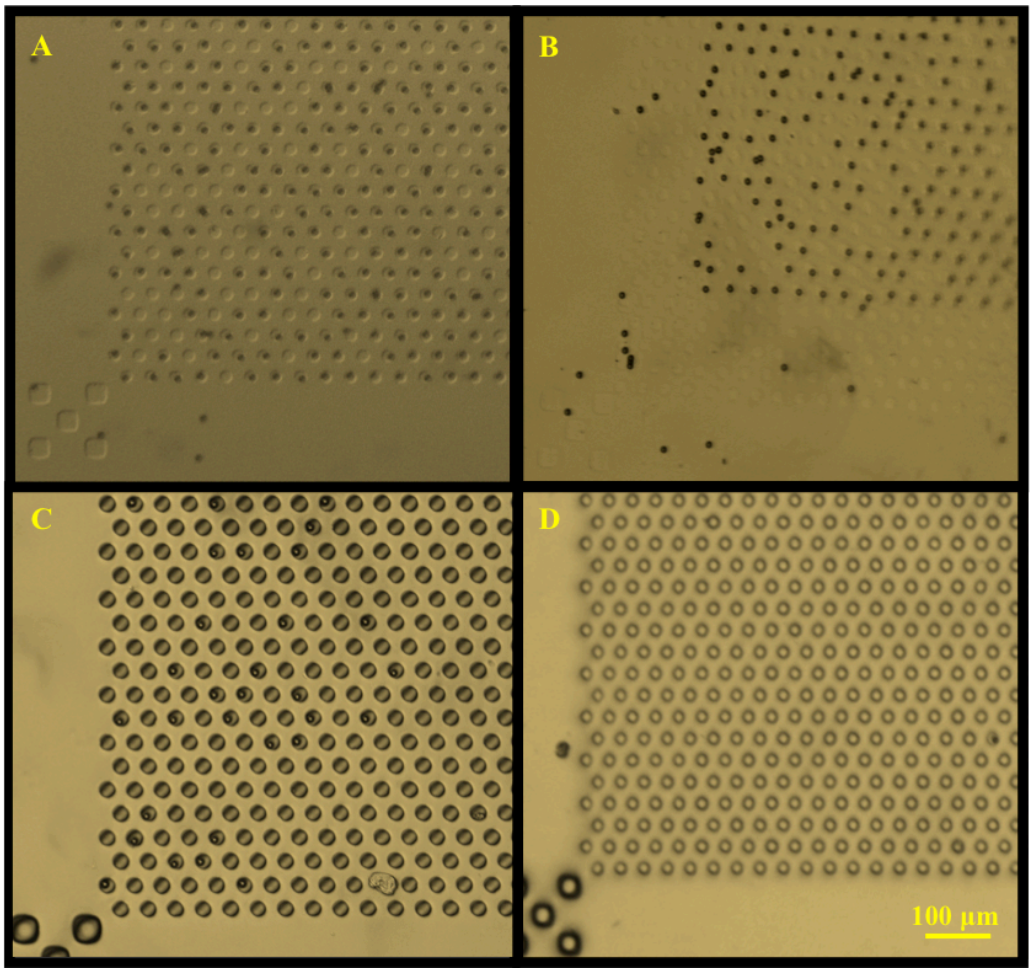

Figure 3-35: Microscope images of the transfer of 10 µm magnetic beads from bottom plate wells (A) into top plate wells (C) using a 1 kg stationary magnet. Wells are 18 µm x 16 µm (W x H). Scale bar = 100 µm.

Figure 3-35 provides proof of concept evidence that magnetic beads can be transferred from 18 µm diameter wells in a bottom plate, to equal sized wells in a top plate using a stationary magnet. It should be noted that the experiment is not ideal as alignment is difficult using the current rig, which does not allow very accurate alignment in the theta direction. Some beads are pulled out of the bottom wells and do not translate into a top plate well, as seen in image 'D'. This is most likely due to the absence of a top plate well directly above the bottom plate well, so the bead enters into the space between the plates and is then pulled into a different top plate well.

3.3.5 Results summary

In summary, a number of issues arose during testing of the SlipChip with cells, including alignment, leakage and cell loading. Problem solving for the alignment and leakage issues pointed to the requirement for a stronger rig with a top plate alignment clamp, which improved the issues, but was not ideal. The main issue of cell docking inside the wells could not be overcome with this design; however, proof of concept that magnetic beads could be moved from bottom to top plate wells was successful and pointed towards a modified design using two plates with no inlet/outlets as a possible route for exploring cell-cell interaction.

3.4 Conclusions

Initially the SlipChip seemed like a useful architecture that could be adapted to operate with cells. However after testing it was concluded that it was not the best solution. The initial SlipChip design [56] required liquid loading prior to device assembly (i.e. the plates were loaded with reagents before they were brought together), so that the volumes could be manipulated using a pipette, or liquid plugs in Teflon tubing. The Ismagilov group then showed additional sample/reagent loading on the device using the SlipChip overlapping duct/well design depicted in Figure 3-36; the fluid channel is created by overlapping discontinuous ducts with the sample wells, as such the FC-40 in the wells is displaced by the sample fluid [56, 72, 73, 86, 87, 88].

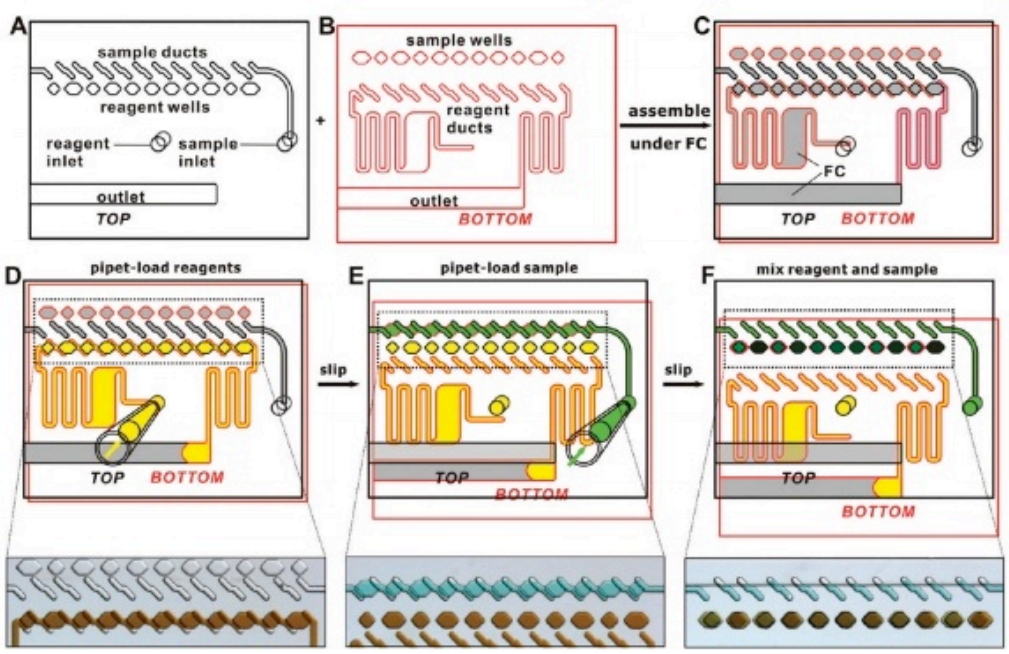

Figure 3-36: Diagram depicting pipette loading of an assembled SlipChip through overlapping ducts and sample wells. Diagram copied from [87].

A) Top plate. B) Bottom plate. C) Top and bottom plate are brought into contact under FC-40, which floods into all the wells. D) Reagent wells are loaded using a pipette (reagents wells and ducts are overlapping). E) Top plate is slipped relative to bottom plate so that the sample ducts and wells overlap, forming a continuous fluid path. Sample is loaded using a pipette. F) Top plate is slipped again, allowing sample and reagent wells to interact.

When driven with a syringe, the liquid is pushed into the device at 1 µL/min [72], but the authors report difficulties in filling without leakage. Hence they developed a method of 'dead-end filling' of the SlipChip [89, 90], which involves loading the SlipChip by firstly filling a reservoir which connects to the fluidic path. The fluidic path is created by overlapping sample wells/ducts; it does not have an outlet. The liquid spontaneously fills the fluidic path from the reservoir and stops when the chamber is full. In this instance the user must calculate the volume of liquid required to fill the chamber and not over-fill it, so leakage does not occur. This example indicates how the Ismagilov group also had to address issues with leakage.

Nevertheless, filling using the Teflon plug method would be difficult with cells, as cells would first need to be seeded into plugs, one cell per plug, and then transferred to the

device. This would take additional time and may disrupt normal cell behaviour. Additionally, the method of creating a fluidic path by overlapping wells and ducts could not be used for a cell capture SlipChip. The well would need to be larger than a single cell so that the fluidic path was not blocked when a cell was docked, but this would lead to multiple cells docking inside each well.

In conclusion, it was decided that the SlipChip, although a simple and elegant way of interacting two liquids, was not the best architecture for a cell-cell interaction device. However, investigation of the application of the SlipChip to study cell-cell interactions led to the concept of an alternative architecture, further detailed in Chapter 4: Microwell Arrays.

Chapter 4: Microwell Array Cell Traps for Single Cell Activation

4.1 Introduction

One method of capturing single cells is to trap them in microwells that are of a similar dimension to the cells, as discussed in Chapter 2. If the material used to trap the cells is biocompatible and optically transparent, then this architecture could be used to trap individual cells in a high-throughput manner. The concept is detailed below in Figure 4-1.

4.1.1 Concept

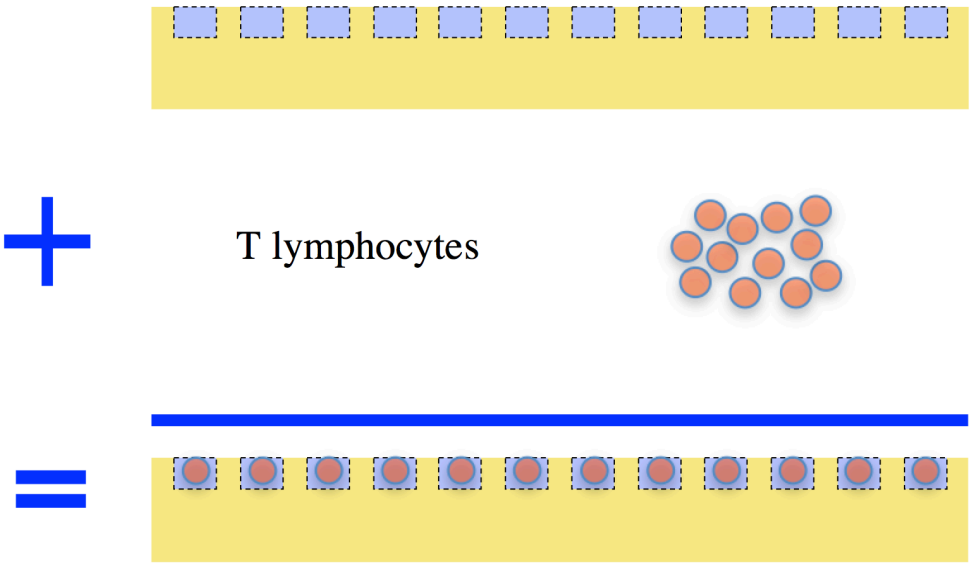

Figure 4-1: Concept schematic for the use of microwells to capture T lymphocyte activation. Microwells that are of a similar dimension to the T lymphocytes allow single cells to sediment into the wells.

As detailed in Chapter 1.3, the objectives of this project are as follows:

- **Single cell capture.** As discussed in Chapter 3.2.3, by designing the optimum size microwell, it is possible to achieve single cell-per-well capture.
- **Enable high-throughput data acquisition.** Using microwells of cell size (approximately 10-20 microns) it is possible to have thousands of microwells in

the field of view of a standard objective (approximately 2 mm x 2 mm (W x W) for a 10x objective).

- **Ability to bring two cells into contact for a defined period of time, after which it is possible to dissociate them.** See Chapter 5.1.1 for a detailed description of how microwells can be used for this.
- **Allow recovery of specific cells.** This could be possible through extraction techniques such as a micropipette, or laser removal.
- **Optically transparent to permit observation of cell-cell interaction with microscopy.** This is possible as long as the material used to create the device is optically transparent.

In summary, the use of the microwell array could be a viable solution to address the project objectives.

4.1.2 Capturing cell activation data

T lymphocyte activation: Calcium channels

When a T lymphocyte is activated via antigen receptor ligation a cascade reaction is induced within the cell, marking the beginning of an immune response. An early indicator of T lymphocyte activation is an increase in intracellular Ca^{2+}, which can be measured using a calcium-dependant fluorophore such as Fluo-8AM [4].

Activation with ionomycin

Ionomycin, a Ca^{2+} ionophore, can reversibly bind Ca^{2+}. It is lipid-soluble and is able to transport Ca^{2+} across the cell membrane. Hence, ionomycin can bind extracellular Ca^{2+} in the cell media (RPMI Ca^{2+} concentration = 0.42 mM [91]) and transport it into the cell. This is aided by its dilution in DMSO, which increases cell membrane permeability [92].

Ionomycin is classed as a mitogenic substance [83] because it has been found to induce cell proliferation, and the activation and generation of secondary messengers such as IP_3. Hence, ionomycin increases the intracellular Ca^{2+} concentration through two pathways:

1. Ionomycin transports extracellular Ca^{2+} across the cell membrane, increasing the Ca^{2+} level inside the cell.
2. Ionomycin triggers the generation of IP_3, which in turn prompts the release of Ca^{2+} from the ER and RER through IP_3R channels (as detailed in Chapter 1).

Activation with anti-CD3

T lymphocyte activation in-vivo requires not only TCR:pMHC engagement, but also the association of a number of co-stimulatory molecules on the T lymphocyte to induce an activation signal in the cell. CD3 is an important co-stimulatory molecule, very closely linked to the TCR; on the cell surface, CD3 and the TCR form a TCR-CD3 membrane complex. When the TCR engages with pMHC, the CD3 -if correctly stimulated- then begins signal transduction [93].

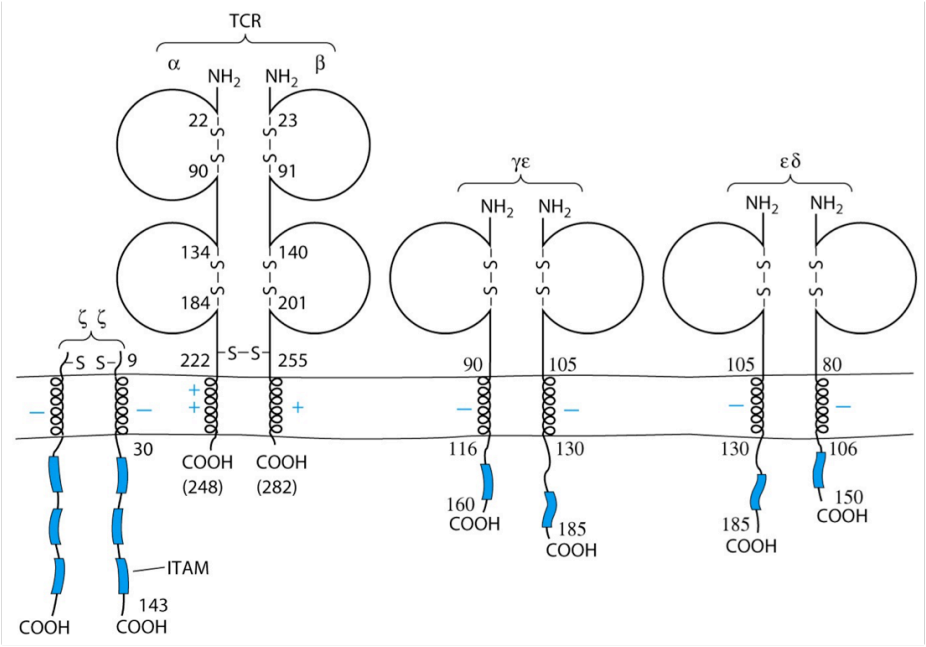

Figure 4-2: Diagram of the TCR-CD3 complex on the cell surface, showing cytoplasmic tails. Adapted from reference [1].

CD3 has 'cytoplasmic tails' (see Figure 4-2) that form the Immunoreceptor Tyrosine-based Activation Motif (ITAM); it is this that causes T lymphocyte activation by signal transduction [1] in the form of a phosphorylation cascade, resulting in the production of IP_3. Phosphorylation of ITAMs causes ZAP-70 (protein kinase) to bind and become active, ZAP-70 catalyses the phosphorylation of other membrane associated molecules, ultimately resulting in the activation of Phospholipase Cγ (PLCγ). PLCγ then hydrolyses Phosphoinositol Biophosphate (PIP_2), which produces IP_3.

Monoclonal anti-CD3 has been shown to cause T lymphocyte activation through the antigen-receptor complex by inducing the production of IP_3, which in turn mobilises intracellular Ca^{2+} [83, 94, 95, 96] as explained in Chapter 1.

Fluo-8AM

The change in calcium levels inside T lymphocytes was monitored using the 'Fluo-8AM', available from abcam [4]. Fluo-8AM has an excitation wavelength of 490 nm and a calcium-bound emission wavelength of 520 nm. Excitation is achieved using an argon laser (488 nm), and is observable with a Fluorescein isothiocyanate (FITC) filter. Figure 4-3 shows the excitation and emission profile of Fluo-4AM, the previous derivation of Fluo-8AM, which has the same excitation and emission profile. Fluo-8AM was developed to allow cell loading at lower temperatures and is 1.5x – 2x brighter than Fluo-4AM.

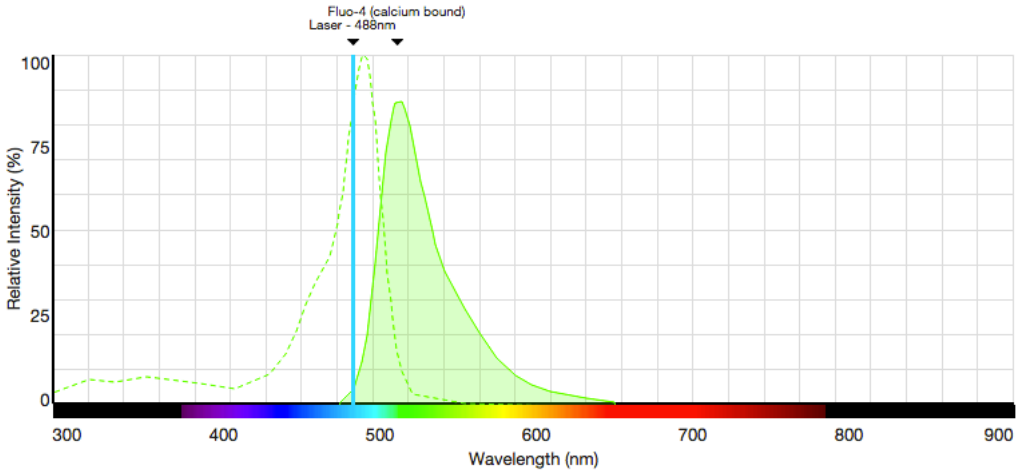

Figure 4-3: Excitation and emission profile of Fluo4-AM with 488 nm (argon) laser excitation. Image taken from [97].

As an Acetoxymethyl (AM) ester, Fluo-8AM is hydrophobic and uncharged, allowing it to permeate cell membranes. Once in the cell cytoplasm, intracellular esterases free a carboxyl group from the AM ester, hydrolyzing the Fluo-8AM, and preventing it from leaving the cell. Fluo-8AM is a calcium chelator and will bind to free calcium in the cytoplasm, allowing the amount of calcium in the cell to be observed using a fluorescent microscope.

4.2 Materials and methods

4.2.1 Microwell array fabrication

As previously discussed, the material from which the device is constructed must be biocompatible, so that the cells remain viable in the device for the duration of the experiment. Wood *et al* demonstrated fabrication of microwells in agarose gel [63], a material that is biocompatible, permeable and can slip against itself and other materials. This is due to agarose being a hydrogel. Agarose undergoes syneresis -the expulsion of liquid through its surface- which lubricates the slipping interface; an important characteristic if the microwell arrays are to be developed for cell-cell contact (Chapter 5).

To test the functionality of agarose as a microwell material, a photolithography mask was designed to create pillars in SU-8 that would in turn be used to create wells in agarose using soft lithography. The mask was printed on acetate.

Microwell array design

The mask is divided into 324 individually numbered squares of wells, each containing 4200 cell traps. (The whole 4" wafer has 1,360,800 cell traps.) Each square of cell traps is 2 mm x 2 mm (W x W), the size of the field of view for a 10x objective. A section of the photolithography mask is shown in Figure 4-4, showing the packing arrangement of the cell trapping wells.

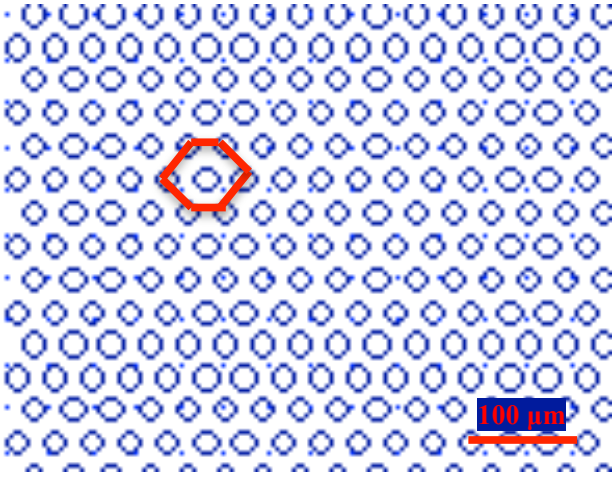

Figure 4-4: Agarose well mask; wells are organised in a HCP arrangement (red hexagon). Scale bar = 100 µm.

Each cell trap is 20 µm in diameter (large enough to trap a single 15 µm cell, but too small to trap multiple cells) and spaced in a Hexagonal Close Packed (HCP) arrangement, the most space efficient way to organise circles in a square. Figure 4-5 shows the well array pitch and dimensions.

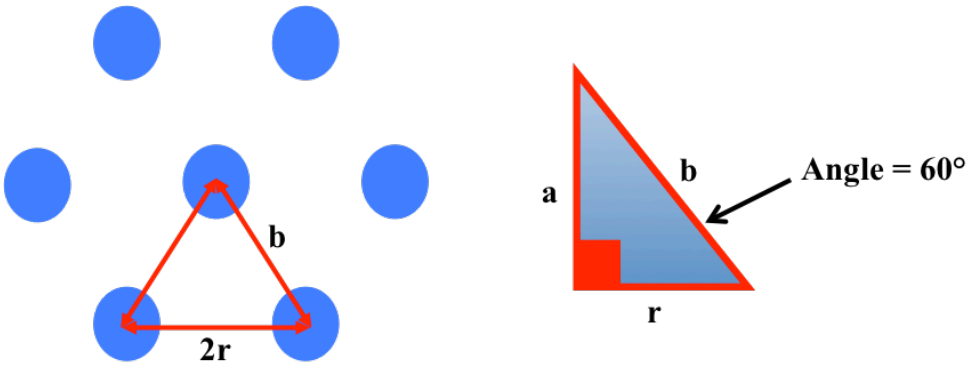

Figure 4-5: Diagrammatic representation of agarose mask trap arrangement.

The horizontal space between each well is 15 µm and the size of each well is 20 µm; hence,

$$2r = 15 + 10 + 10 \qquad (4\text{-}1)$$

$$r = 17.5\mu m$$

$$a = b.\sin(60°) = 2.r.\sin(60°) = \sqrt{3}.r \qquad (4\text{-}2)$$

$$a = 30.31\mu m$$

$$b = \frac{r}{\cos(60°)} = 2.r \qquad (4\text{-}3)$$

$$b = 35.0\mu m$$

SU-8 fabrication of agarose mask

SU-8 patterning on a substrate is detailed in Chapter 3.

Master fabrication on silicon

SU-8 pillars were fabricated on a silicon wafer; Figure 4-6.

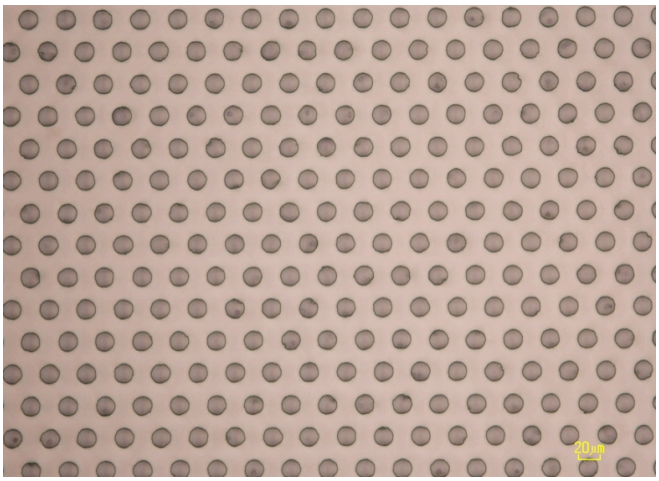

Figure 4-6: Nikon image of 30 µm x 20 µm (H x W) SU-8 pillars on silicon. Scale bar = 20 µm.

Agarose microwell soft lithography

The SU-8 microarray pillars were imprinted into 2% agarose -1 g per 50 mL Tris-acetate-EDTA (TAE) buffer- using soft lithography. Molten agarose was poured onto the SU-8 master wafer and allowed to cool for 30 minutes at room temperature, before being peeled off. The results are presented in Figure 4-7.

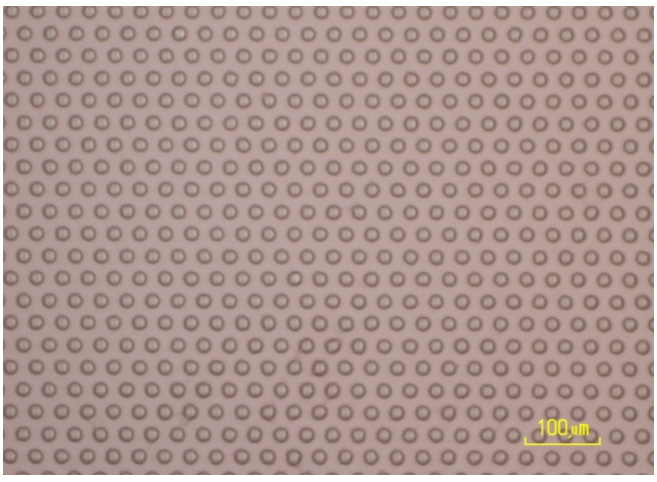

Figure 4-7: Nikon image of 18 µm x 30 µm (W x H) wells in 2% agarose. Scale bar = 100 µm.

It is imperative that the molten agarose is as close to the gelling temperature (≤ 36°C [98]) as possible before it is poured over the SU-8 master. This is to minimise condensation forming on the master as the hot liquid is poured over it. Condensation

creates a barrier between the SU-8 master and the agarose, preventing microwell formation. It was found that the optimum pouring temperature of the agarose was 45°C; this allowed a uniform layer of agarose to be applied to the mask before it began to cool, and reduced the occurrence of condensation as the temperature difference between the SU-8 master (room temperature ≤ 22°C) and the molten agarose was small.

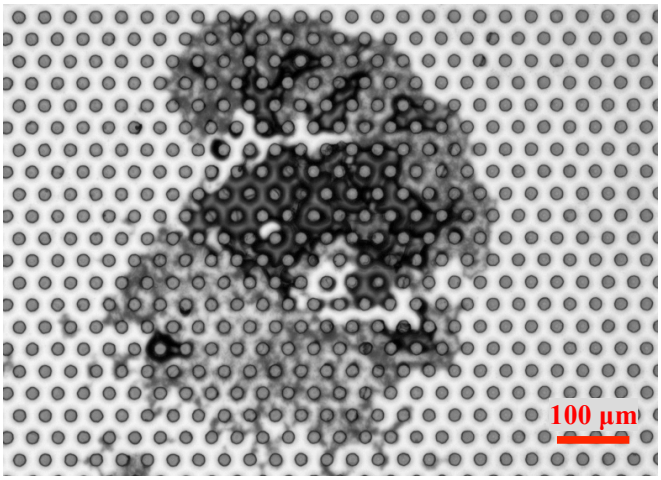

Figure 4-8: Residue on SU-8 master due to agarose condensation. Image taken using a Zeiss LSM 5 microscope. Scale bar = 100 µm.

An additional problem with condensation is that it damages the SU-8 layer and destroys the wafer, preventing further use; Figure 4-8. In general, it was found that a single SU-8 master could be used to create approximately eight agarose microarrays through soft lithography, before a new SU-8 master was required. Using a condensation-damaged SU-8 master resulted in poor microwell development; Figure 4-9.

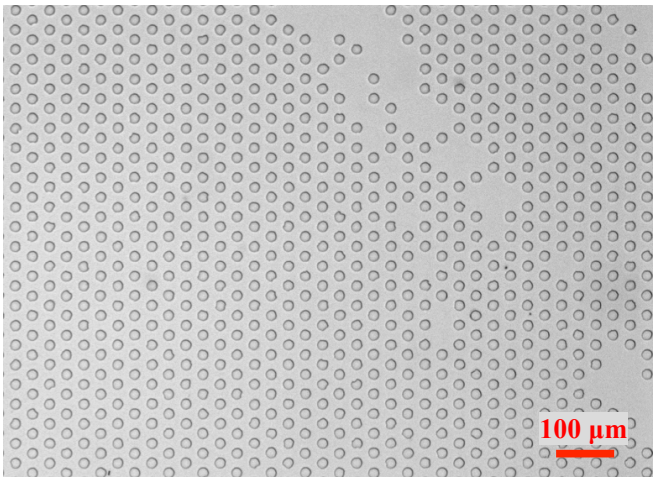

Figure 4-9: Agarose microwell array made using a damaged SU-8 master. Image taken using a Zeiss LSM 5 microscope. Scale bar = 100 µm.

4.2.2 Cell seeding

Cell size

As discussed in Chapter 3.2.3, it is important to know the size of the cells being seeded in the device, so that the correct microwell dimensions can be designed to ensure single cell occupancy. For the microwell array work, a suspension T lymphocyte cell line called 'B3Z' was used; hence, measurements were taken of this cell line.

The B3Z cells were measured by two methods. Firstly, the cells were measured in a similar way to the P815 cell line in Chapter 3. See Figure 4-10.

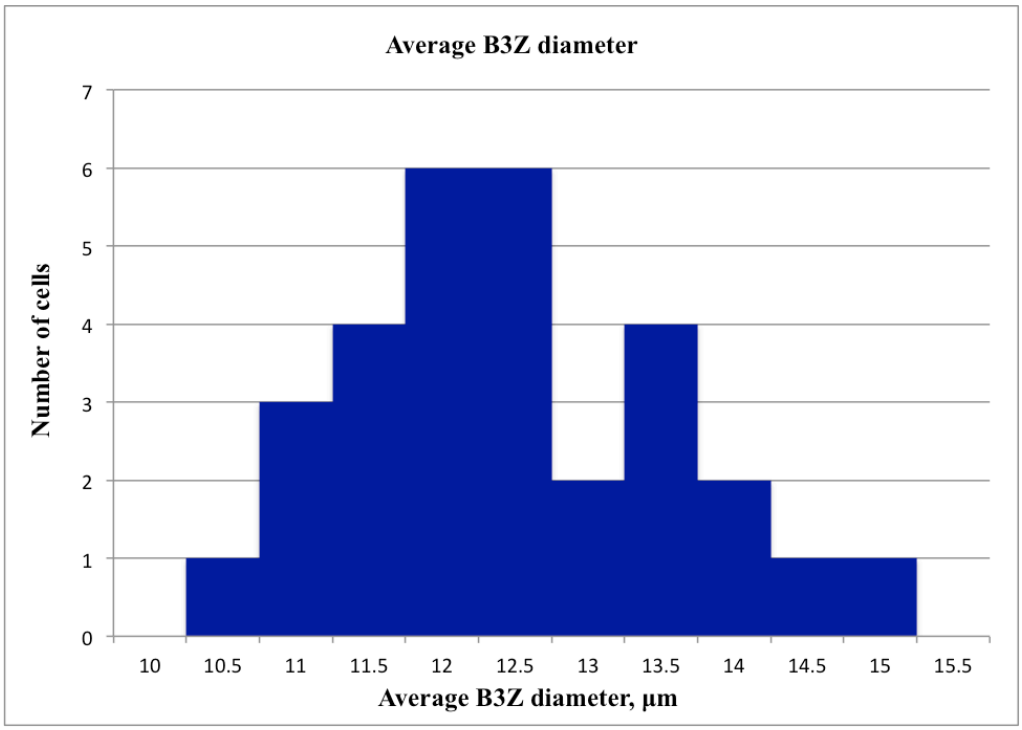

Figure 4-10: Histogram showing average B3Z cell size.

Measured mean cell size using this method was 12.2 µm, with a SD of 1.1 µm.

Additionally, the cells were measured using a LUNA™ Automated Cell Counter [99] which automatically counts a cell population, as well as determining average cell size and cell viability. The data from the LUNA™ is given in Table 2 and Figure 4-11.

Cell count results
Total cell concentration: 2.67 x 10^6 cells/mL
Live cell concentration: 2.59 x 10^6 cells/mL
Dead cell concentration: 8.37 x 10^4 cells/mL
Viabillity: 96.9 %
Average cell size: 14.0 µm
Total cell number: 638
Live cell number: 618
Dead cell number: 20

Table 2: Data output after measuring a B3Z cell population on the LUNA™ Automated Cell Counter.

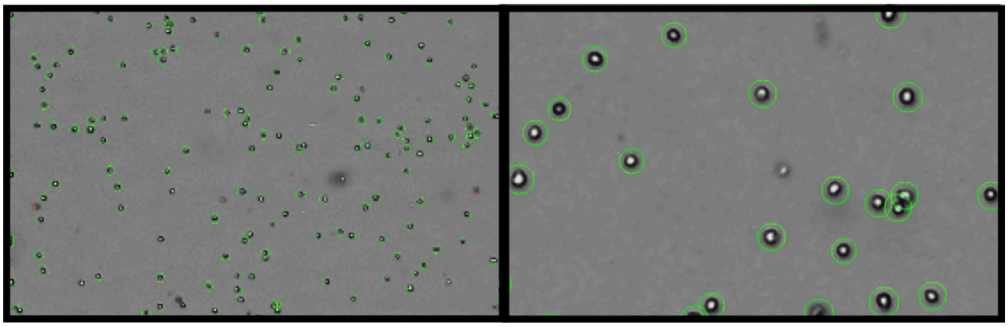

Figure 4-11: Image of B3Z cell population measured on the LUNA™ Automated Cell Counter.

The B3Z cell population was measured using the LUNA™ six times on different days, and at varying times, to encompass fluctuations in cell size depending on cell cycle at the time of measurement. The average size was found to be 12.9 µm.

It can be concluded that the B3Z cell line has an approximate size of 12 µm to 13 µm and, as both methods agree on the cell size, both cell size measurement techniques yield reliable results; however it should be noted that using the LUNA™ Automated Cell Counter is substantially less time consuming.

Figure 4-12 shows the loading density after B3Z cells have been allowed to settle in the wells for 30 minutes at 37°C and then washed with PBS. Loading efficiency is approximately 87%. It was found that loading efficiency varied between experiments despite the loading protocol remaining the same. Sometimes the loading procedure was repeated to increase efficiency, whereas at other times this was not necessary. It is postulated that this is an effect of changes in average cell size when passaging took place. As mentioned previously, at a certain point in the cell growth cycle, the cells are an optimum size for loading in the microwells.

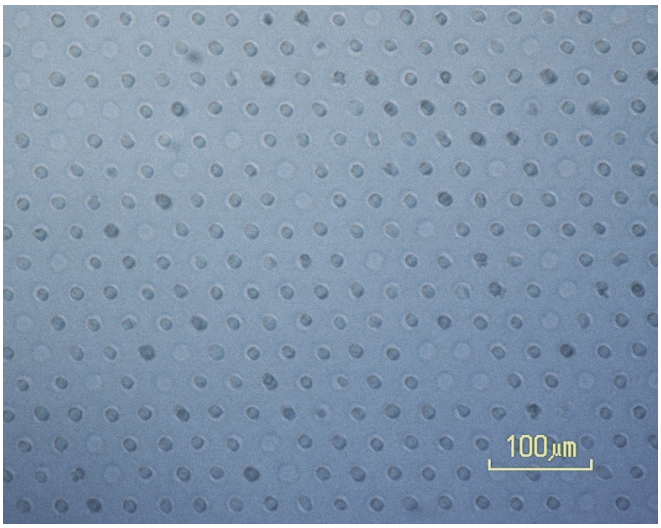

Figure 4-12: B3Z loaded for 30 minutes in 37°C incubator at a concentration of 10:1 (cells:wells). Microwell size is 29 µm x 18 µm (H x W). Loading efficiency approximately 87%. Image taken using a Nikon microscope. Scale bar = 100 µm.

To find the optimum well width and height for the B3Z cells, multiple micropillar array wafers were fabricated with varying SU-8 height and pillar widths. B3Z cells were seeded into the different sized wells at the same loading density (10:1 cells:wells), using the same protocol described in Appendix A.2.1; the results are presented in Figure 4-13 and Figure 4-14.

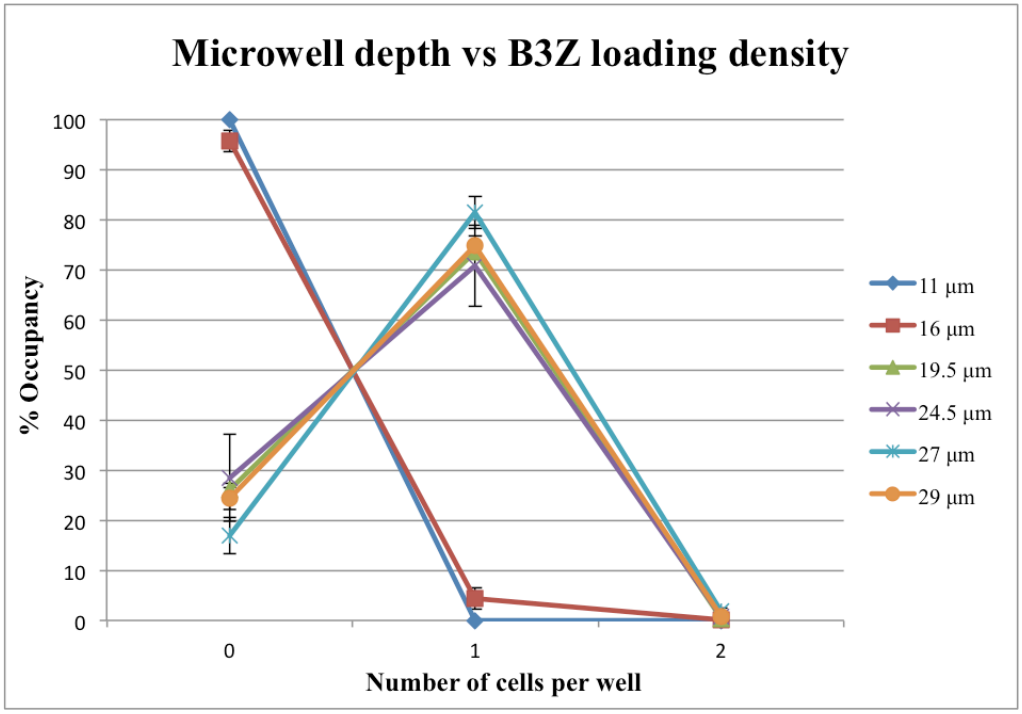

Figure 4-13: Graph showing B3Z loading density in various depths of microwell (microwell width = 18 µm). Error bars = SD.

Figure 4-13 shows that microwells of depth 19.5 µm and above achieve between 70-80% loading efficiency; the optimum depth is 27 µm. It is believed that this is the case because 27 µm is approximately double the B3Z average cell diameter; making the microwells deep enough to capture single cells and protect captured cells from the sheer force of the PBS wash. The wash will cause any secondary cells to be displaced out of the wells.
16 µm deep microwells are too shallow to protect the single captured cells from the sheer force of the PBS wash, and it is anticipated that wells of depth greater than 29 µm would show an increase in the number of multiple cells being captured. However, micropillars of over 30 µm are difficult to fabricate due to the aspect ratio of the SU-8 required; hence data for deeper wells is not shown here.

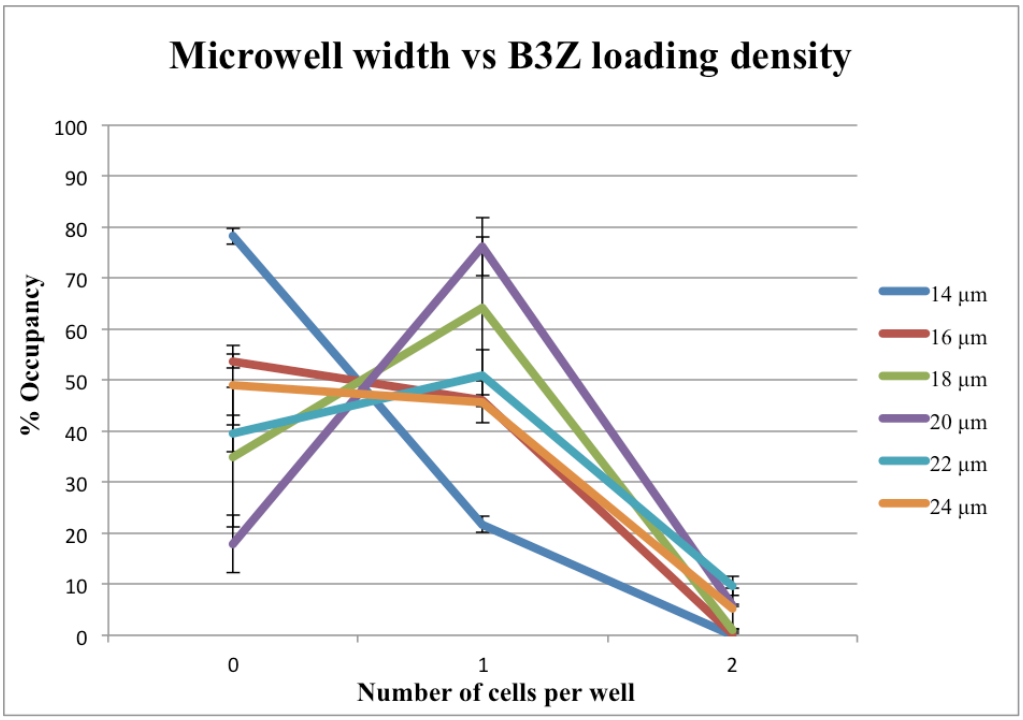

Figure 4-14: Graph showing B3Z loading density in various widths of microwell (microwell depth = 22 µm). Error bars = SD.

Figure 4-14 shows that the best microwell diameter for single cell capture is 20 µm. This size allows single cells (around 12 µm - 13 µm) to dock, but is too small for multiple cells to sediment into the microwells side-by-side. It should be noted that the cell capture efficiency seen in Figure 4-14 is less than if the microwells were the optimum depth of 27 µm; however, it proved difficult to fabricate an SU-8 master with micropillars taller than 22 µm in height because of the small microwell widths required for the experiment (14 µm and 16 µm). The mask design used for this experiment also contained microwells with diameters of 10 µm and 12 µm; however, these were so poorly fabricated that they were omitted from the experiment.

It was found that 27 µm x 20 µm (H x W) microwells were the optimum dimensions for high-density cell loading. Trapping of multiple cells per well was infrequent owing to well size exclusion (more than one cell would not fit in a well).

4.2.3 Cell viability

Agarose is a polysaccharide extracted from algae, formed of repeating units of D-galactose and 3,6-anhydro-L-galactopyranose, that form a matrix when they gel together with glycosidic bonds 'α-(1-3)' and 'β-(1-4)' [100].

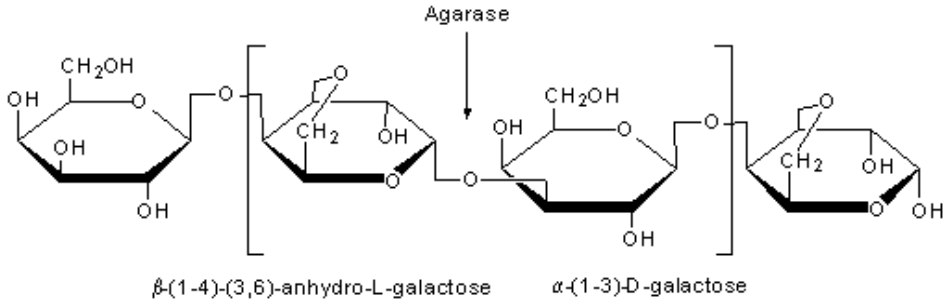

Figure 4-15: Molecular structure of agarose: repeating units of α-(1-3)-D-galactosyl-β-(1-4)-anhydro-L-galactosyl (agarase). Image taken from [100].

Agarose is classed as a 'hydrogel' because it is formed of repeating hydrophilic units; hence, it retains liquid for long durations. This results in an important characteristic of agarose that allows cells to survive in the microwells - the ability of macromolecules to diffuse through the agarose matrix. Diffusion of macromolecules permits the transfer of necessary nutrients to the cells from the media (such as oxygen and L glutamine) and the removal of waste products.

The time for macromolecules to diffuse through the matrix depends on the macromolecule size. The matrix will impede macromolecules that are large enough to interact with the gel matrix; this forms the basis of gel electrophoresis. However, macromolecules of hydrodynamic radius 'R_H' of 30 nm or less will not interact with the matrix of a 2% agarose gel, and hence travel through the matrix as if they were simply diffusing through PBS [101]. The Stokes-Einstein relation can describe this diffusion process:

$$D_0 = \frac{k_B.T}{6.\pi.\eta.R_H} \qquad (4\text{-}4)$$

Where:

D_0 = Diffusion coefficient

k_B = Boltzmann constant = 1.38×10^{-23} m^2 kg s^{-2} K^{-1}

T = Temperature (in Kelvin); 0°C = 273.15 K

η = Solvent viscosity

e.g. The macromolecule ionomycin, diluted in DMSO at 20°C has the following hydrodynamic radius:

$$R_H = \frac{k_B.T}{6.\pi.\eta.D_0} \quad (4\text{-}5)$$

The dynamic viscosity of DMSO at 25°C = η = 1.991×10^{-3} Pa.s (= $kg.m^{-1}.s^{-1}$) [102]

The diffusion coefficient of ionomycin = $D_0 = 2.7 \times 10^{-10}$ $m^2.s^{-1}$ [103]

$$R_H = [(1.38 \times 10^{-23})(293.15)] / [6\pi(1.991 \times 10^{-3})(2.7 \times 10^{-10})]$$

$$R_H = 0.4 \text{ nm}$$

Using the diffusion coefficient of macromolecules it is also possible to determine the time it would take for the macromolecules to diffuse through 1 mm of agarose, using Einstein's mean free path in 3D calculation:

$$x^2 = 6.D_0.t \quad (4\text{-}6)$$

$$t = \frac{x^2}{6.D_0} \quad (4\text{-}7)$$

The diffusion coefficient of oxygen in liquid at 20°C is 19.7×10^{-10} $m^2.s^{-1}$ [104]

$$t = (1 \times 10^{-3})^2 / 6(19.7 \times 10^{-10})$$

$$t = 85 \text{ seconds}$$

The following molecules needed to keep the cells alive: glutamine, pyruvate and oxygen. All are less than 30 nm in hydrodynamic radius, so will diffuse through agarose at approximately the same rate as they would in PBS. This means that replenishment of the macromolecules in the microwells around the cells will occur within a few minutes.

However, that would be the extreme condition of a molecule travelling 1 mm from the cell media to the microwell. As agarose is a hydrogel, it will be saturated with media, so initial macromolecule uptake will deplete the store of molecules in the agarose first, which will be much closer.

To ensure that the cells would remain viable in agarose for the duration of the experiment (up to 4 hours maximum), a proof of concept experiment was conducted. B3Z cells were seeded into agarose microwells at a 10:1 (cell:well) concentration using the protocol in Appendix A.2.1. The 2.4 mm thick agarose microwell arrays were then balanced on top of fresh cell media (RPMI 1640, Sigma-Aldrich) inside petri dishes, and placed into the 37°C incubator for 2 hours, 4 hours, 6 hours, 8 hours or 24 hours. This is explained in Figure 4-16.

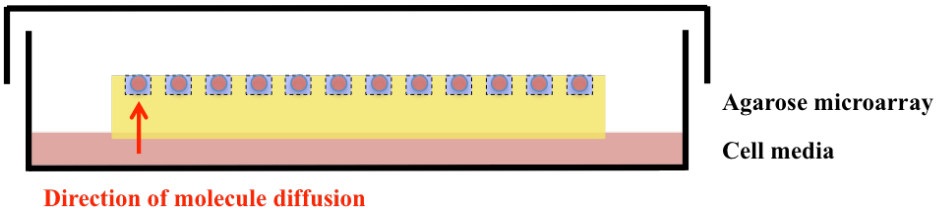

Figure 4-16: Diagram explaining cell viability experimental set-up.

Note: Extreme care was taken to ensure that the agarose did not submerge into the cell media; otherwise the cells would migrate out of the microwells. As such, the experiment would not be testing the viability of cells in agarose, as they would have free access to the cell media. The results are presented in Figure 4-17.

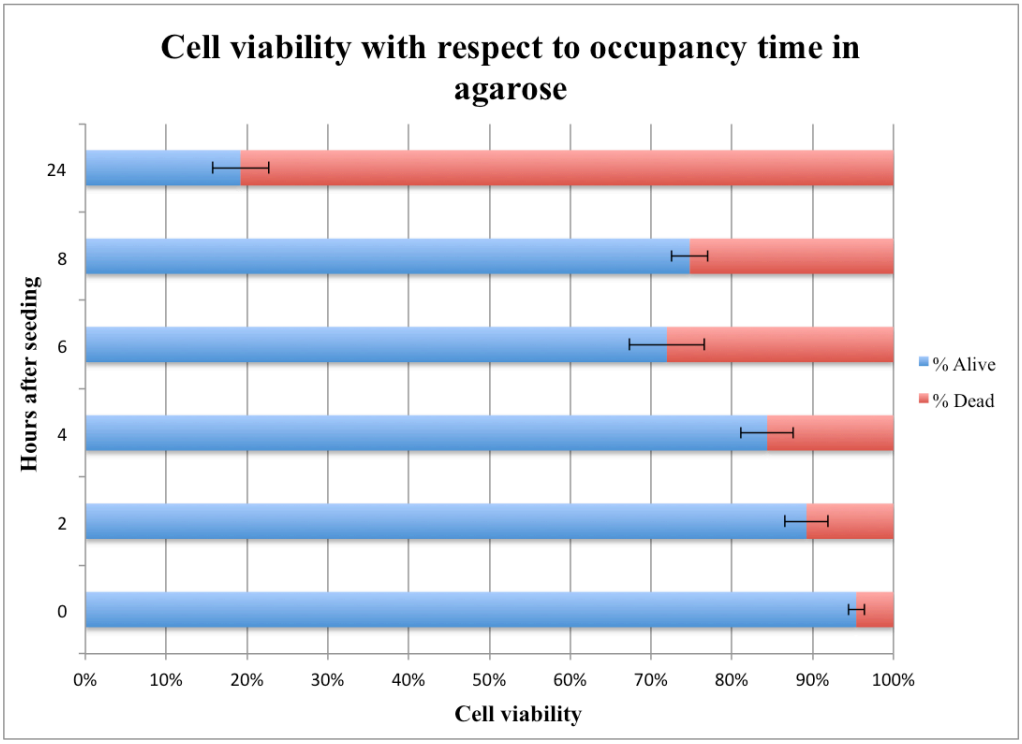

Figure 4-17: Split bar chart showing B3Z cell viability in agarose at various time points. Error bars = SD.

Figure 4-17 demonstrates that cells can survive in agarose microwells at a viability of over 80% for up to 4 hours.

4.2.4 Data collection

Cell activation was induced using either the calcium ionophore, ionomycin, or using the co-stimulatory molecule, anti-CD3.

Fluo-8AM cell staining

The protocol describing how Fluo-8AM is loaded into the B3Z T lymphocytes prior to stimulation is detailed in Appendix A.2.2.

Flow cytometry

Chapter 2.2 details the basic principles of flow cytometry, the current state-of-the-art method of bulk single cell analysis. B3Z activation data was collected using flow cytometry, as well as microwell arrays, so that the two techniques could be compared.

The ionomycin stimulation protocol and the anti-CD3 stimulation protocol are in Appendices A.2.3 and A.2.4 respectively.

Fluorescent microscopy

Microwell array data was collected using a DeltaVision (DV) Elite Imaging System with environmental control chamber; an inverted microscope that was able to keep the cells in a temperature (37°C) controlled environment for the duration of the experiments [105].

With its motorised stage, the DV has the capability to recall position 'points', allowing multiple arrays to be processed at once. A custom-designed PMMA stage attachment was created using a CO_2 laser to enable a 30 mm x 30 mm (W x W) section of agarose microarrays to be attached to the DV. It could then be moved using the motorised stage into controlled positions that could be returned to; Figure 4-18. The agarose holder has an additional PMMA lattice that divides the agarose into nine working sections, enabling stimulant to be added to the nine sections separately, increasing the throughput of a single experiment.

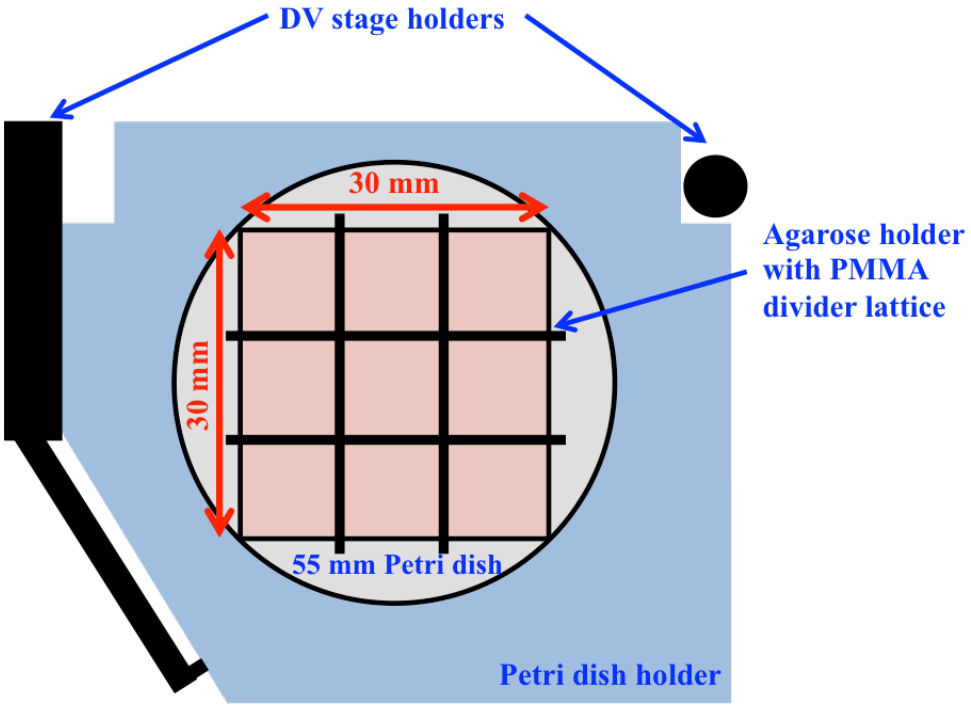

Figure 4-18: Custom-made 55 mm petri dish holder to insert into DV stage attachments, including PMMA divider lattice.

The protocol for stimulating cells and viewing their activation using the DV is detailed in Appendix A.2.5.

Data analysis

To analyse the fluorescent data collected using microscopy, a custom-made MATLAB program was written. The basic run-sequence is detailed in the flow chart presented in Figure 4-19; for a more detailed explanation with images, see Appendix B: MATLAB Cell Analysis.

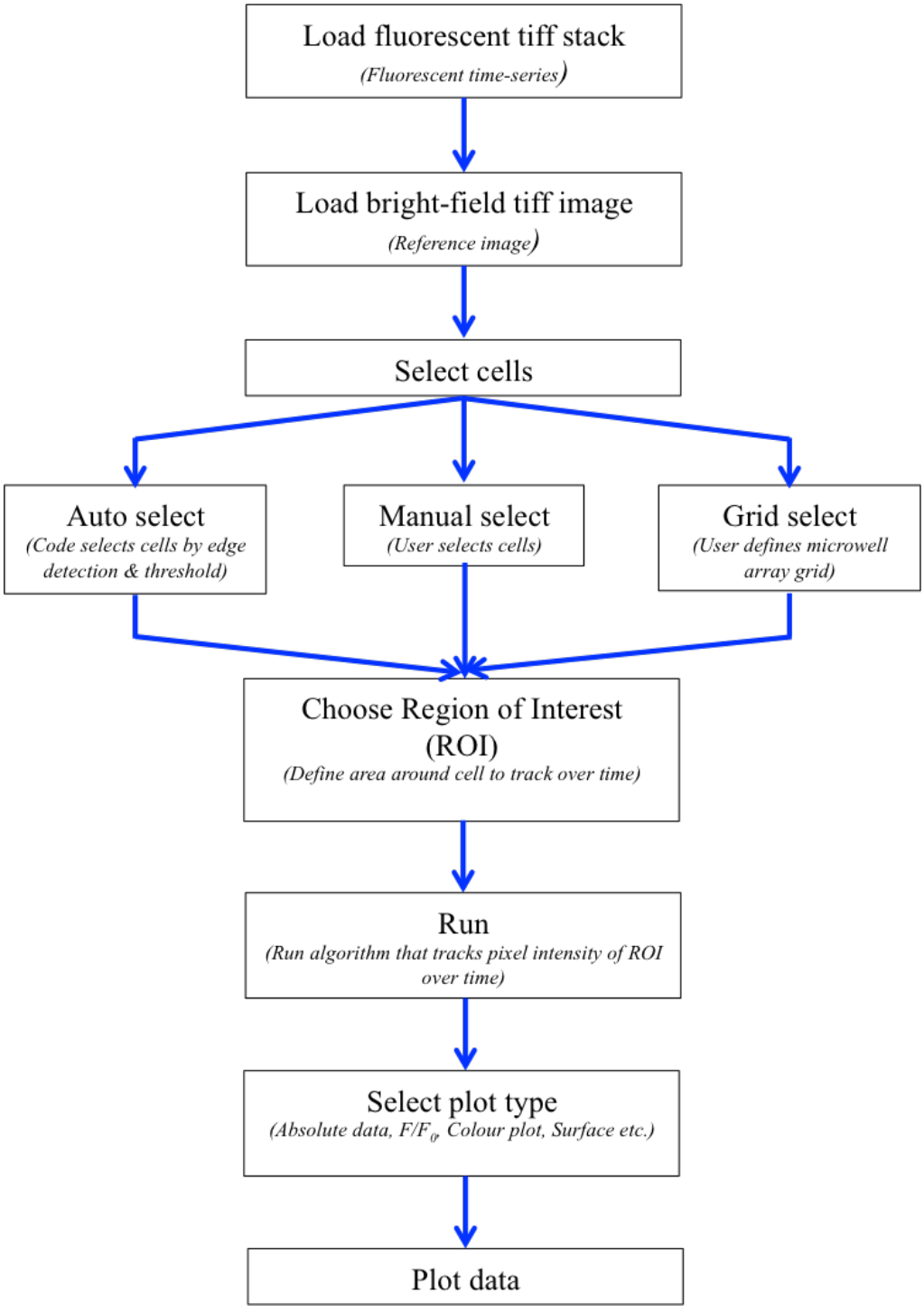

Figure 4-19: Flow chart depicting MATLAB program to monitor cell activation over time.

4.3 Results

4.3.1 B3Z activation with stimulants

B3Z T lymphocytes were stimulated with ionomycin or anti-CD3, and the subsequent increase in Ca^{2+} was tracked using Fluo-8AM, flow cytometry and microwell arrays.

Flow cytometry

The protocols for examining fluorescently labelled B3Z on the BD LSRFortessa™ are detailed in Appendices A.2.3 and A.2.4.

Figure 4-20 shows the typical data output from the flow cytometer after capturing B3Z fluorescence for 1 minute before adding ionomycin (as described in Appendix A.2.3), and then returning the cells to the flow cytometer for a further 2 minutes. The data is analysed with the software package 'FlowJo'.

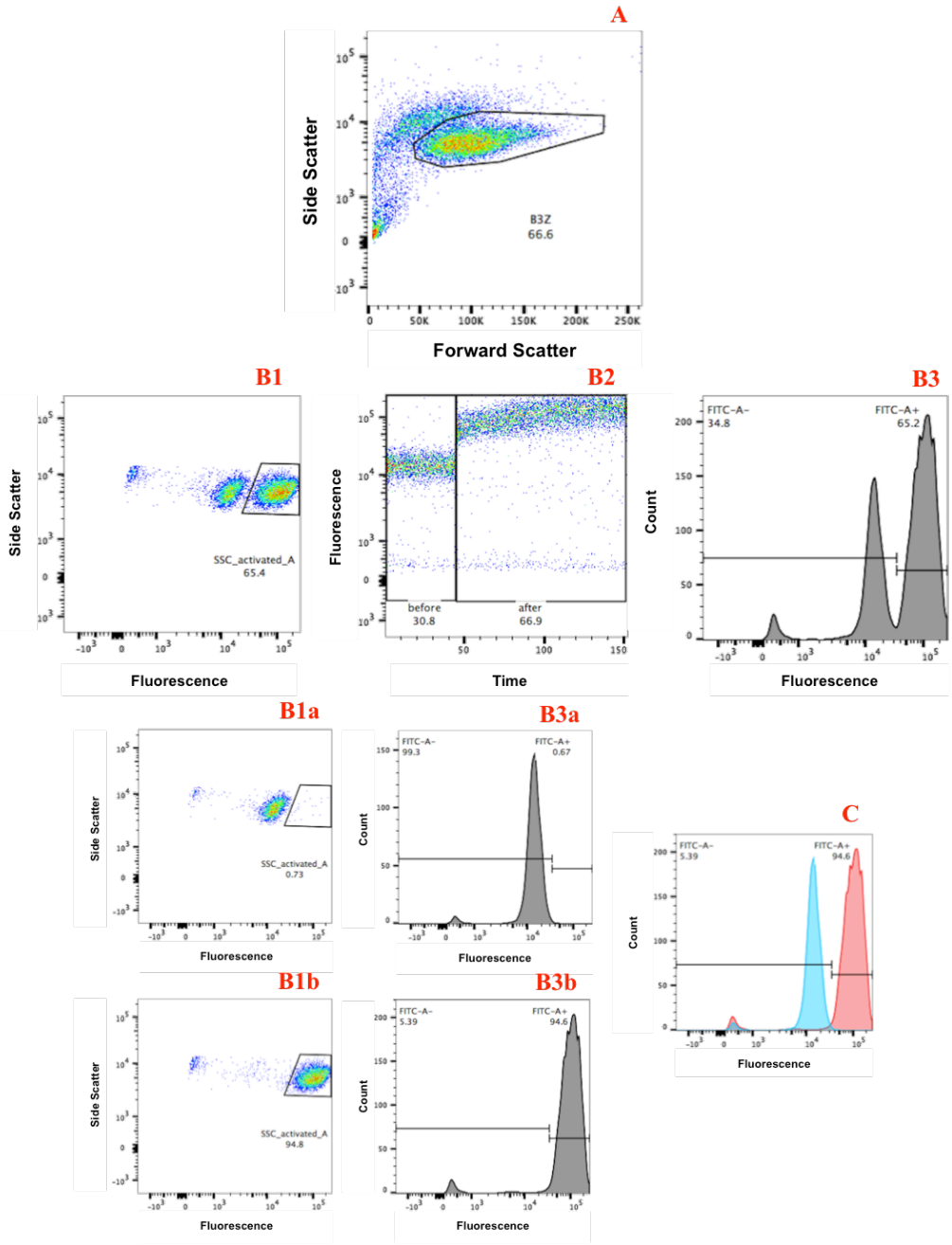

Figure 4-20: Typical data output from the BD LSRFortessa™ after stimulation of B3Z T lymphocytes with ionomycin. Data analysed using FlowJo.

A. Density plot of all cells recorded during experiment. The gated area is of B3Z cells, selected by their size and granularity profile. Axes = Forward Scatter (FSC):Side Scatter (SSC) (X:Y).
   FSC indicates cell size, SSC shows granularity.
B. All 'B' plots are of the B3Z selected in 'A'.

B1: B3Z density plot (FITC:SSC). Two populations are clearly seen; the left population are the unstimulated B3Z cells -fluorescence level is basal fluorescence- and the right population are the stimulated cells with increased intracellular Ca^{2+} and therefore higher Fluo-8AM fluorescence.

B1a/b: 'B1' divided into populations of before and after stimulation, respectively.

B2: B3Z density plot showing fluorescence level against time (Time:FITC). The B3Z were measured for one minute, showing basal fluorescence, before ionomycin was added. The cells were then measured for a further 2.5 minutes. The increase in intracellular Ca^{2+} is clearly seen by the increased fluorescence of the B3Z cells. The Mean Fluorescent Intensity (MFI) of the unstimulated cells is 14440; whereas the MFI of the stimulated cells is 105731. F/F_0 (fluorescence over basal fluorescence) = 7.3.

B3: Histogram of cell fluorescence. B3 shows the same data as B1.

B3a/b: 'B3' divided into populations of before and after stimulation, respectively. B3b shows that the percentage of B3Z cells activated after ionomycin stimulation is 94.6%.

C. Combination of B3a and B3b, showing overlap of activated and non-activated cell populations.

Figure 4-21 displays the same experimental data, but for anti-CD3 stimulation using the protocol described in Appendix A.2.4.

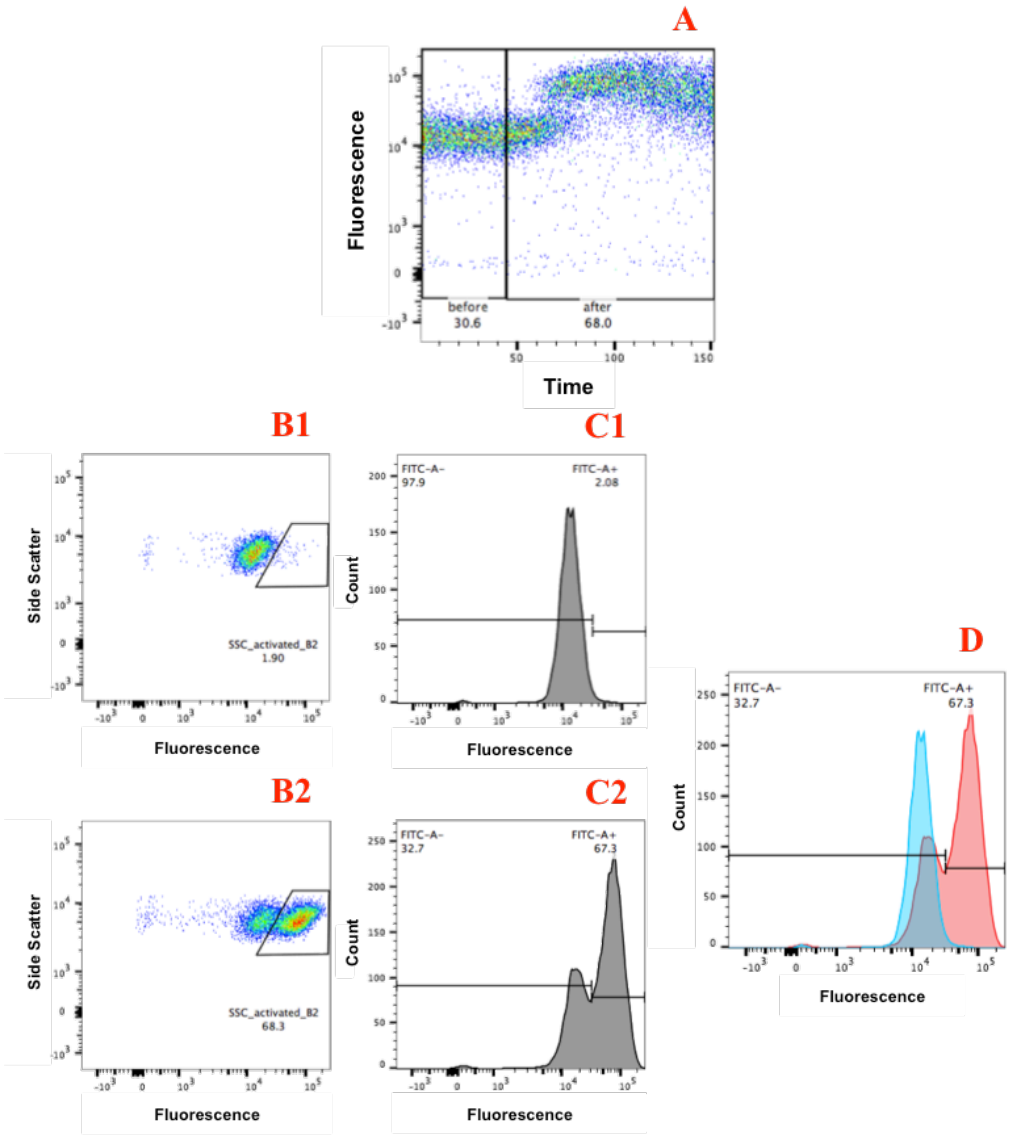

Figure 4-21: Typical data output from the BD LSRFortessa™ after stimulation of B3Z T lymphocytes with anti-CD3. Data analysed using FlowJo.

All plots are of B3Z cells that have been gated on.

A. B3Z density plot showing fluorescence level against time. The B3Z were measured for one minute, showing basal fluorescence, before anti-CD3 was added and the cells were measured for a further 2.5 minutes. The increase in intracellular Ca^{2+} is clearly seen by the increased fluorescence of the B3Z cells after approximately 30 seconds. The Mean Fluorescent Intensity (MFI) of the unstimulated cells is 14358; whereas the MFI of the stimulated cells is 57843. F/F_0 (fluorescence over basal fluorescence) = 4.

B. B3Z density plots. Two populations are visible; the left population is the unstimulated B3Z cells -fluorescence level is basal fluorescence- and the right population is the stimulated cells with increased intracellular Ca^{2+} and therefore higher Fluo-8AM fluorescence.
   B1/2: Populations of before and after stimulation respectively.
C. Histogram of cell fluorescence. C shows the same data as B.
   C1/2: Populations before and after stimulation respectively. C2 shows that the percentage of B3Z cells activated after anti-CD3 stimulation is 67.3%.
D. Combination of C1 and C2, showing overlap of activated and non-activated cell populations.

Using data such as that displayed in Figure 4-20 and Figure 4-21, it is possible to determine the Ca^{2+} store recovery time of B3Z T lymphocyte cells after stimulation, with either ionomycin or anti-CD3.

Briefly, the protocol was as follows:

1. The entire B3Z population is stimulated with ionomycin or anti-CD3.
   T=0 minutes.
2. The cells are pelleted, re-suspended in fresh cell media and incubated at 37°C in a cell incubator.
3. At T=20/30/60 minutes, an aliquot (50,000 B3Z cells) was taken from the population and re-stimulated with the same stimulant.

The results are presented in Figure 4-22.

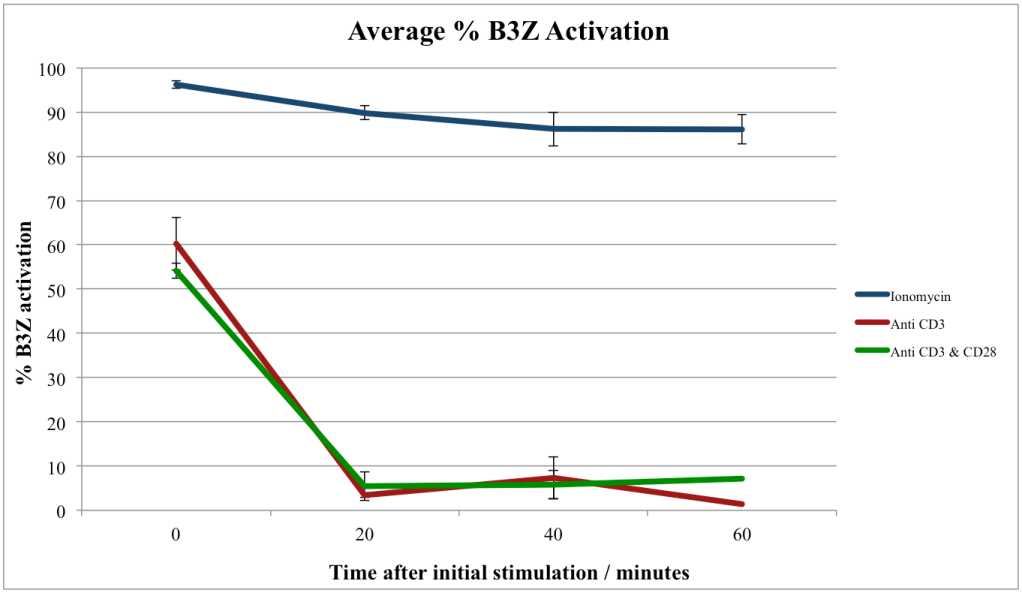

Figure 4-22: Average % B3Z activation and Ca^{2+} store recovery time of B3Z T lymphocytes after ionomycin, anti-CD3 or anti-CD3 and anti-CD28 stimulation. Triplicate data taken from the same cell population on separate days. Error bars = SEM.

CD28 is another co-receptor on the cell surface of T lymphocytes, situated close to the TCR. Subsequent activation using a combination of anti-CD3 and anti-CD28 (clone 37.51 at concentration 10 µg/mL, from affymetrix eBioscience) was also investigated. It has been widely reported that a combination of CD3 and CD28 co-receptor binding can result in high activation of T lymphocytes (in proliferation and interleukin-2 production characteristics) without the requirement of TCR:pMHC ligation [106].

It can be seen from Figure 4-22 that the inclusion of anti-CD28 had no effect on initial Ca^{2+} concentration, nor on the speed of recovery of Ca^{2+} internal stores after cell activation; hence it was not investigated further. This result was not unexpected as CD28 is thought to provide a regulatory signal to the T lymphocyte, to aid proliferation, and act upon a different pathway to CD3 [107]. Increases in intracellular Ca^{2+} during activation due to the co-stimulation of CD28 have been shown in $CD4^+$ T lymphocytes, but not $CD8^+$.

It can be seen from Figure 4-22 that initial ionomycin stimulation activates 95% of B3Z T lymphocytes. Subsequent activation is possible as soon as 20 minutes after the first activation took place; over 85% of B3Z cells activated at T = 20, 40 and 60 minutes.

Anti-CD3 initial stimulation activates approximately 60% of B3Z cells, but once the cells have been stimulated, they show very low subsequent activation levels. From the data presented in Figure 4-22, it is evident that B3Z T lymphocytes require longer than one hour between stimulations using anti-CD3.

As previously discussed, ionomycin and anti-CD3 increase intracellular Ca^{2+} through the same pathway; IP_3 production leads to Ca^{2+} channels in the ER, RER and cell membrane opening. To analyse the data fairly, Ca^{2+} levels are recorded from the moment that the stimulant is added.

Ionomycin activation, as shown in Figure 4-20, occurs within seconds of the stimulant being added to the cells; whereas, stimulation with anti-CD3 takes between 30 - 60 seconds; Figure 4-21. Ionomycin stimulation is instant because Ca^{2+} is transported into the cell by the ionophore; therefore the secondary release of Ca^{2+} from the internal stores, after IP_3 production has taken place, does little to increase the fluorescence because the Ca^{2+} concentration inside the cell is already so high. For anti-CD3, the Ca^{2+} increase is a result of Ca^{2+} being released from internal stores due to CD3 engagement initiating a phosphorylation cascade in the cell.

The delay in Ca^{2+} increase for anti-CD3 stimulation is seen in Figure 4-21 A. It appears from Figure 4-22 that only approximately 60% of B3Z cells are activated; however this may not be the case because is clear from Figure 4-21 A, that once the Ca^{2+} level begins to rise, the entire population increases to a higher Ca^{2+} level. This may suggest that the majority of cells are activated by anti-CD3.

Hence, the difference in % B3Z activation between ionomycin and anti-CD3 stimulation can be attributed to the additional Ca^{2+} that ionomycin, as an ionophore, will transport into the cell rapidly. This increases the percentage of cells with a fluorescence that is high enough to be considered active within the time frame.

Ionomycin forces a Ca^{2+} response by transferring external Ca^{2+} from the cell media into the cytoplasm. The same amount of extracellular Ca^{2+} is available to the ionophore to transport into the cell at each time point. Hence, it stands to reason that the decreased Ca^{2+} levels seen in subsequent activations are attributable to the reduction of Ca^{2+}available from internal stores.

The ability of anti-CD3 to stimulate T lymphocytes, but prevent activation with secondary stimulation has been reported [108]. It is thought that stimulation with soluble

anti-CD3 results in the modulation of the TCR-CD3 complex, internalising it, and hence preventing subsequent activations through the same pathway. In Figure 4-22, subsequent activation of B3Z T lymphocytes at T = 20, 40 and 60 minutes showed very low Ca^{2+} levels. This could be due to the recovery time of the cells replenishing their Ca^{2+} stores; however, more likely is that the TCR is internalised after the initial stimulation. Therefore, the cells cannot be re-activated in the same way because the CD3 is not available for anti-CD3 to bind to. It has been reported that it can take days to replenish the TCR-CD3 complex on the cell surface and allow subsequent activation of the T lymphocytes [109]. As such, the results displayed in Figure 4-22 are to be expected, as the TCR-CD3 will be internalised during the secondary stimulus.

It can be concluded from the flow cytometry data presented above, that a drawback of this method is the inability to see individual cell activation over time. It appears that a lower percentage of B3Z are activated by anti-CD3 than by ionomycin using the MFI threshold method of determining cell activation. In reality, it is possible that all the cells recorded after the anti-CD3 stimulus was added will eventually reach the threshold MFI to be considered as activated. However, at the instant at which the cell crossed the laser, the phosphorylation cascade (release of Ca^{2+} from internal stores) had not yet completed.

The ability to monitor the Ca^{2+} increase in individual cells with respect to time is a major advantage of the microwell arrays developed in this project; as discussed below.

Microwell array

The protocol for measuring fluorescently labelled B3Z cells that are trapped in microwell arrays using the DV Elite Imaging System is detailed in Appendix A.2.5.

Figure 4-23 and Figure 4-25 show the data output of a triplicate microwell experiment, using the same cells as those analysed in Figure 4-22. The B3Z cells have been stimulated twice with ionomycin or anti-CD3 respectively.

Ionomycin double stimulation

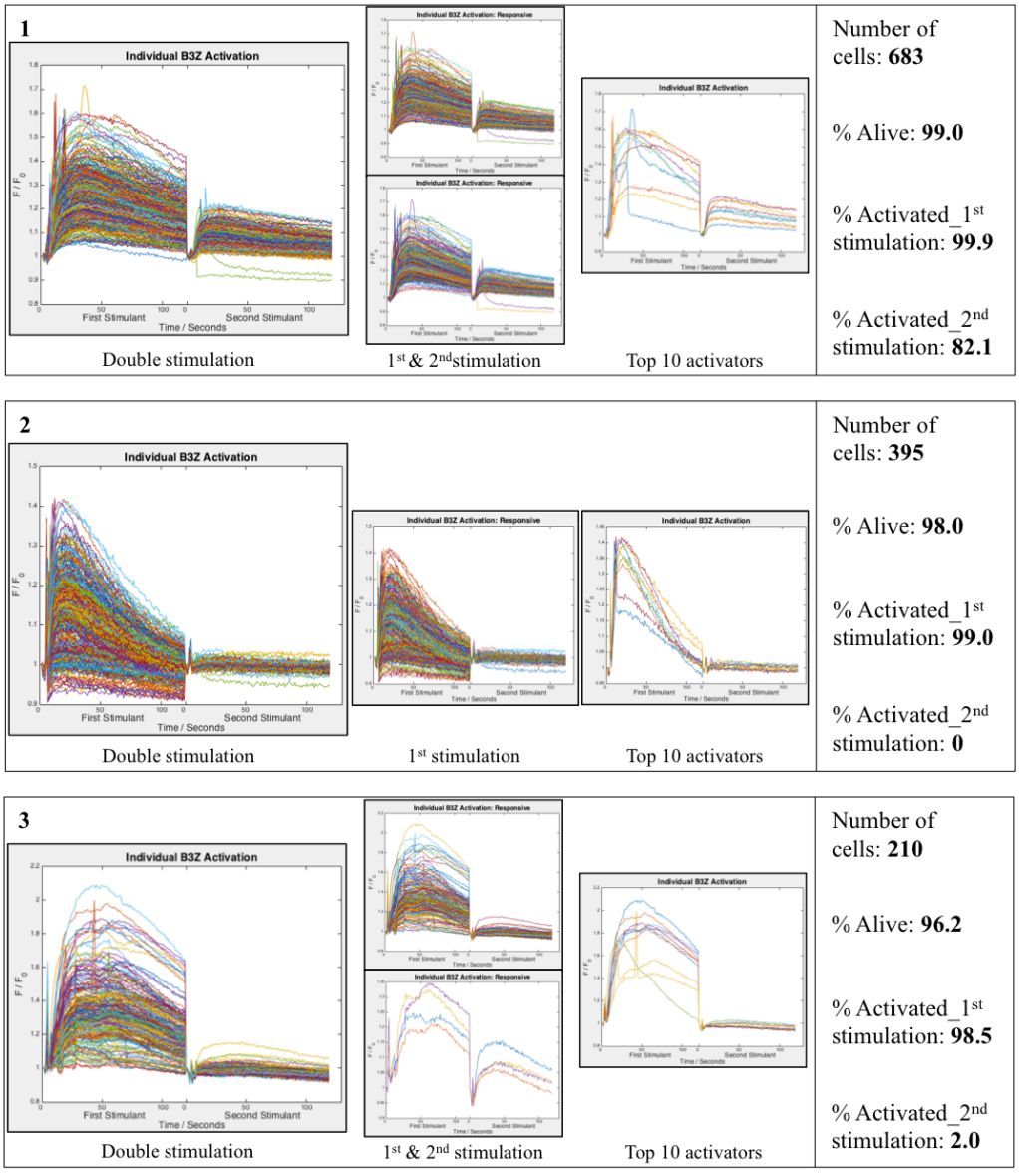

Figure 4-23: Triplicate experiment showing double ionomycin stimulation of B3Z T lymphocytes with experimental statistics. B3Z T lymphocytes are the same as those displayed in the flow cytometry data, Figure 4-22.

Figure 4-24 shows the first experiment of Figure 4-23 in more detail.

Ionomycin double stimulation

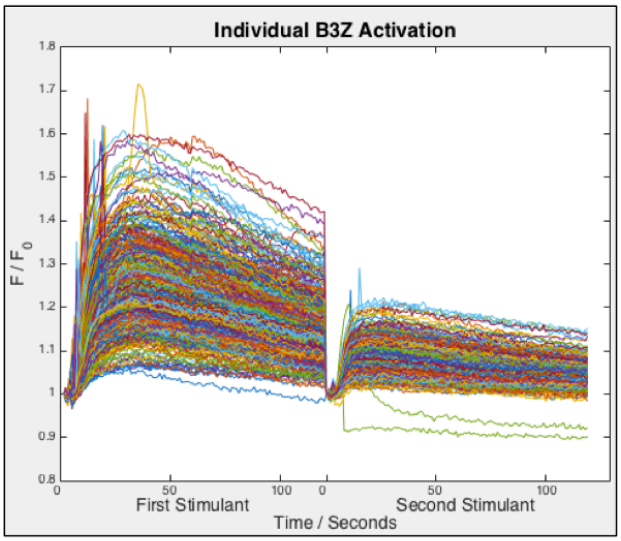

STATISTICS

Number of cells: **683**

% Alive: **99.0**

% Activated_1st stimulation: **99.9**

% Activated_2nd stimulation: **82.1**

Double stimulation

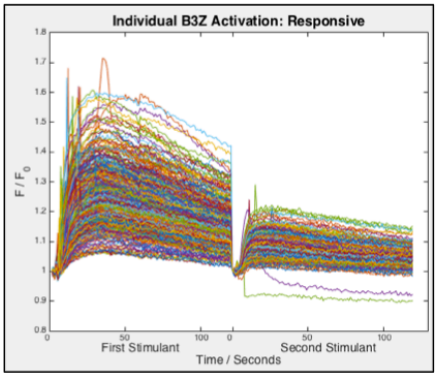

1st stimulation

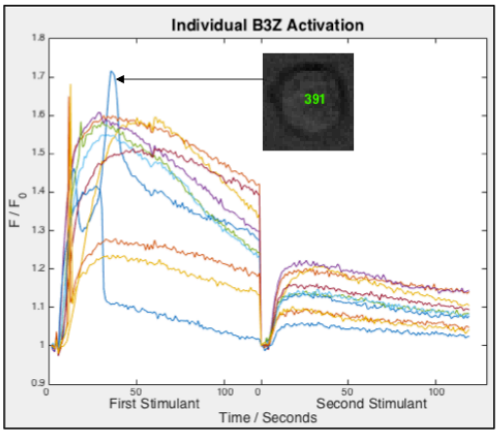

Top 10 activators

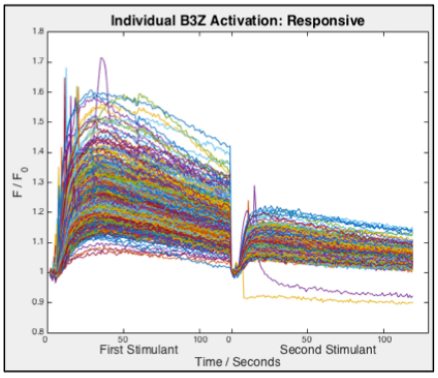

2nd stimulation

Figure 4-24: Experiment 1 of Figure 4-23.

AntiCD3 double stimulation

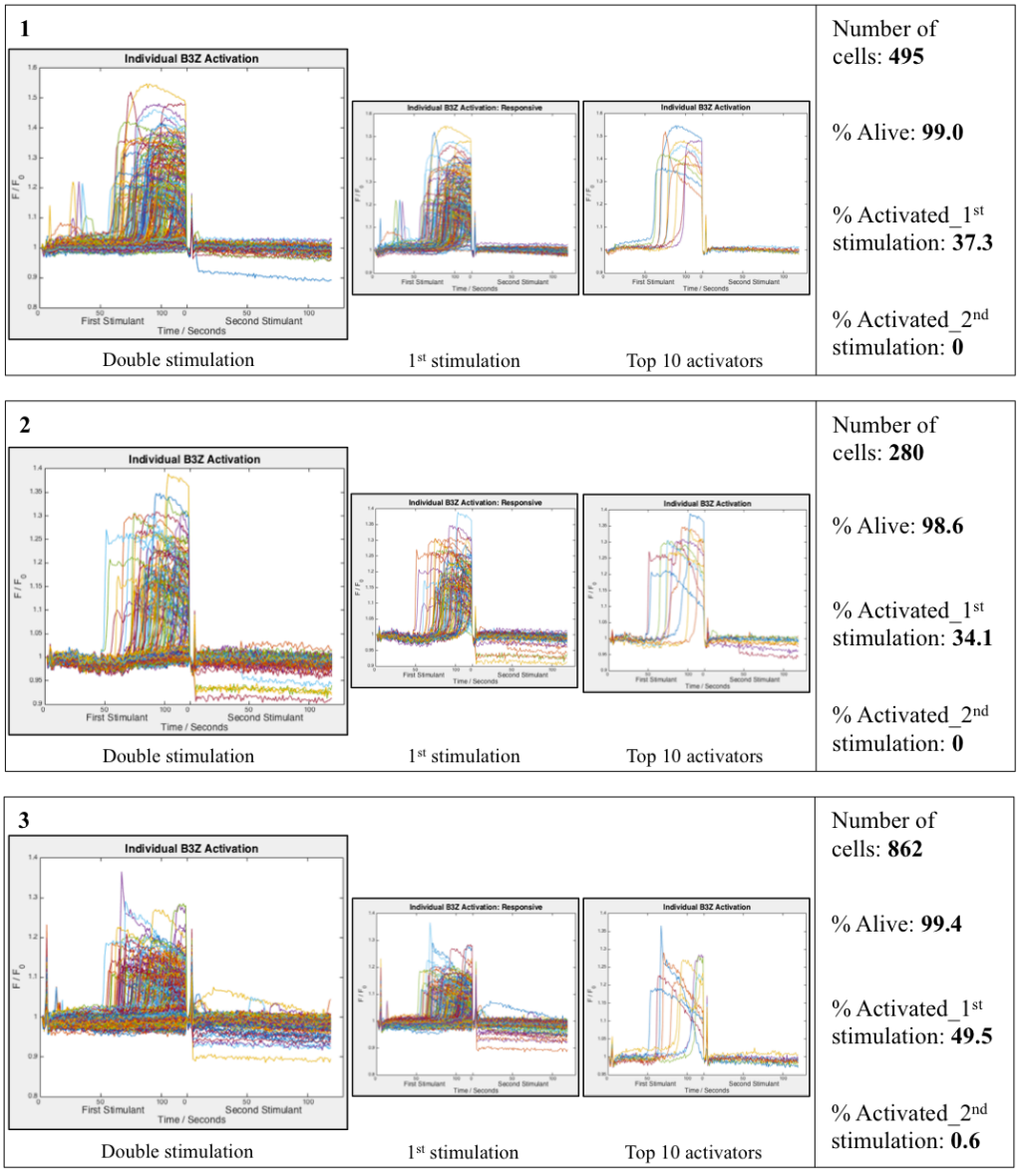

Figure 4-25: Triplicate experiment showing double anti-CD3 stimulation of B3Z T lymphocytes with experimental statistics. B3Z T lymphocytes are the same as those for the flow cytometry data, Figure 4-22.

Figure 4-26 shows the first experiment of Figure 4-25 in more detail.

AntiCD3 double stimulation

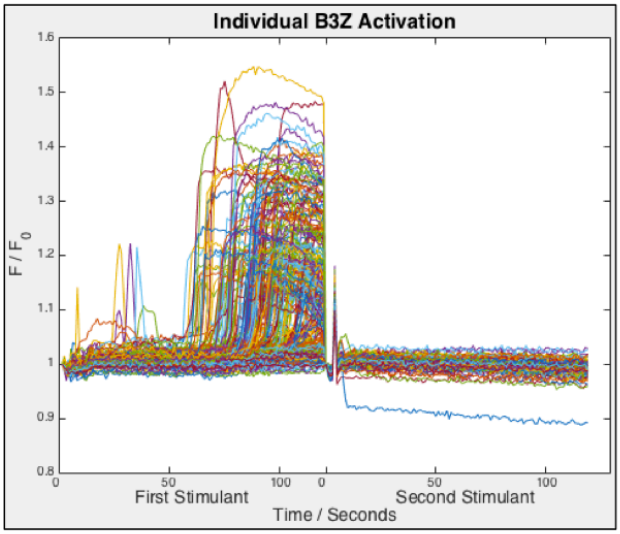

STATISTICS

Number of cells: **495**

% Alive: **99.0**

% Activated_1st stimulation: **37.3**

% Activated_2nd stimulation: **0**

Double stimulation

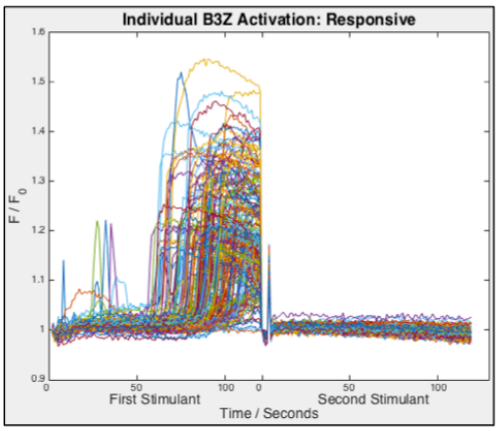

1st stimulation

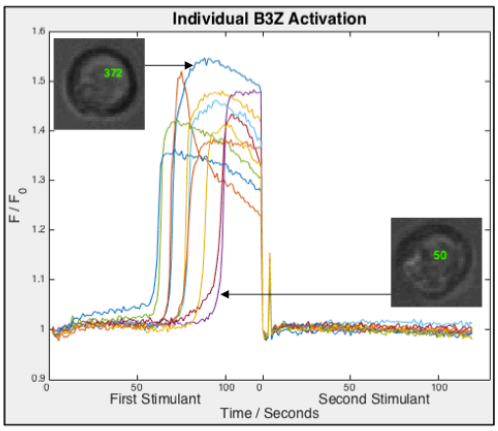

Top 10 activators

Figure 4-26: Experiment 1 of Figure 4-25.

The 'Top 10 activators' shown in Figure 4-26 again highlight the difference in activation characteristics between cells, which is only possible with time-resolved data.

The flow cytometry data presented in Figure 4-22 indicated that B3Z T lymphocytes could be re-stimulated with ionomycin every 20 minutes; however the data shown in Figure 4-23 does not fully agree with this assessment. Experiment 1 differs from Experiments 2 and 3 in that it does show subsequent activation with ionomycin; whereas the other two experiments do not follow the same pattern.

There may be a number of reasons for this:

- The cells used in Experiment 1 were freshly thawed; whereas in Experiments 2 and 3 they were a few days old. Cell lines such as B3Z lose sensitivity over time, so they are regularly replaced by freshly thawed stocks. Hence, it is to be expected that Experiment 1 would show the highest activation characteristics.
- After stimulation the cells are 'washed' with PBS and then supplemented with 50 µL of cell media, to replenish the cell Ca^{2+} internal stores and provide external Ca^{2+} for ionomycin to transport into the cell. It is possible that the cells in Experiments 2 and 3 did not receive enough external Ca^{2+} in the cell media to replace the Ca^{2+} expended in the first stimulation. Also, not enough external Ca^{2+} may have been available for ionomycin to transport into the cells. It was not possible to add more cell media, as an excess of liquid on the surface of the microwell array could cause the cells to be washed out of the wells.

Although as a population, the secondary response to ionomycin has a lower MFI than the initial stimulation, the cells follow the same activation order as for the first stimulation. That is to say, the highest activators in the first stimulation are the highest activators in the second stimulation. The reason for this phenomenon is unknown; however one explanation could be that cell surface area plays a key role in determining how much Ca^{2+} can be transported into the cell. Cell surface area will not change between subsequent stimulations. Therefore the cell with the largest surface area could have the highest amount of Ca^{2+} transported into the cell, and so have the greatest Fluo-8AM output. This type of data could not be collected using flow cytometry, as the cells analysed during the first stimulation are disposed of, so their secondary characteristics could not be evaluated (unless the cells were sorted, which requires additional cell markers and would be very time consuming).

Another characteristic of activation that is not observable with flow cytometry is the difference in activation profiles, shown in Figure 4-24. Three profiles can be seen:

1. Fast increase in Ca^{2+}, followed by a fast decrease.
2. Fast increase in Ca^{2+}, followed by a slow decrease.
3. Double peaking increase in Ca^{2+}, followed by a mid-region extended level (e.g. Cell 391).

This type of transient data cannot be collected using standard techniques such as flow cytometry. Microwells allow transient data for 100's of cells in parallel to be monitored simultaneously.

Additionally, as shown in Figure 4-24, individual cells can be selected from the microarray data for imaging. This allows cell size and health to be assessed, and also the individual fluorescent activation data to be examined. Specific cells can be located and could be removed, as discussed in Chapter 6.2.

The data presented in Figure 4-25 agrees with that presented in Figure 4-21; B3Z T lymphocyte activation against anti-CD3 takes between 30 to 60 seconds. The level of fluorescence is equal to that achieved using ionomycin (fluorescent intensity), with around 40% of the cells activating for the first stimulation (average B3Z activation from triplicate experiment = 40.3%), and none activating for the second stimulation. This is useful data to obtain as it shows that 100% B3Z activation is not possible through anti-CD3 stimulation, so the flow cytometry results are giving an accurate portrayal of anti-CD3 B3Z activation.

4.3.2 Stimulation of B3Z cells with multiple stimulants

Double stimulation with multiple stimulants was also investigated, yielding the following results.

Ionomycin-anti-CD3

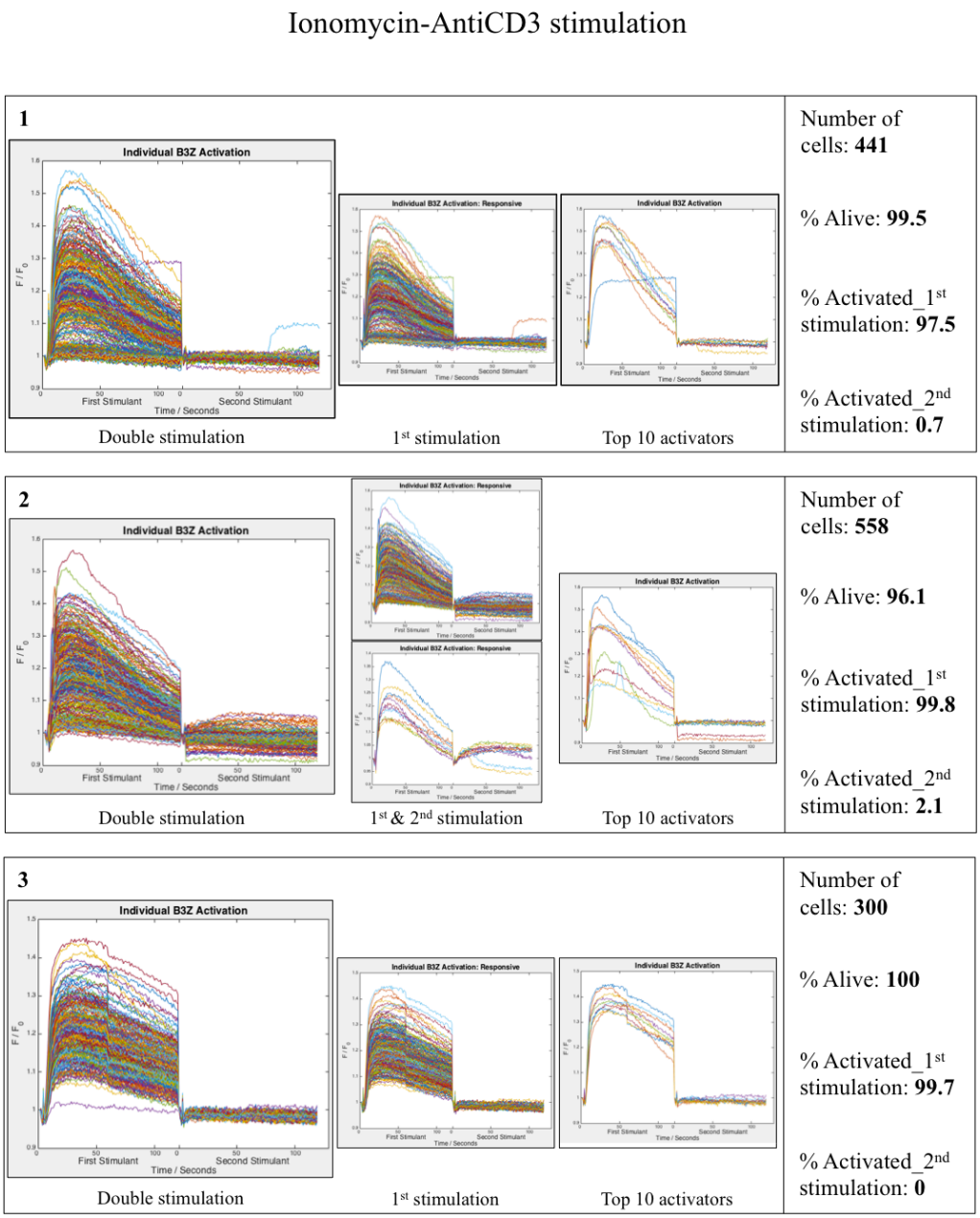

Figure 4-27: Triplicate experiment showing ionomycin and anti-CD3 stimulation of B3Z T lymphocytes with experimental statistics.

Figure 4-28 presents the first experiment of Figure 4-27 in more detail.

Ionomycin-AntiCD3 stimulation

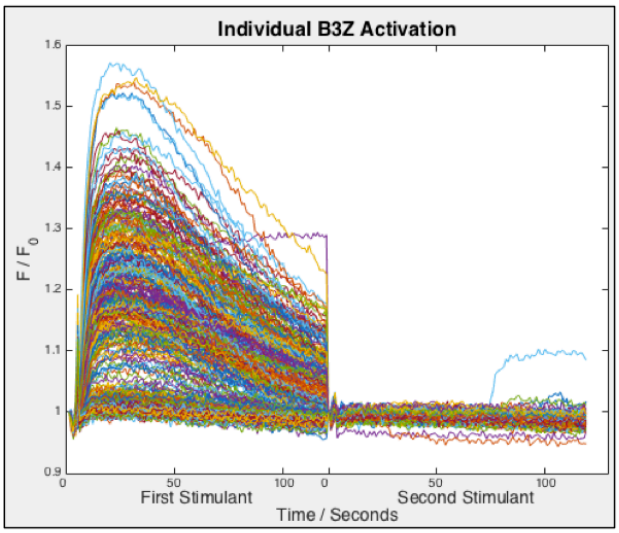

STATISTICS

Number of cells: **441**

% Alive: **99.5**

% Activated_1st stimulation: **97.5**

% Activated_2nd stimulation: **0.7**

Double stimulation

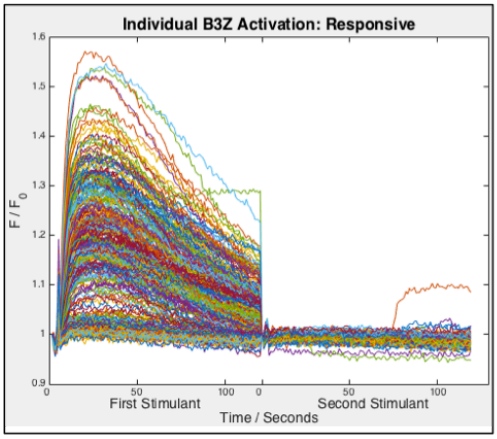

1st stimulation

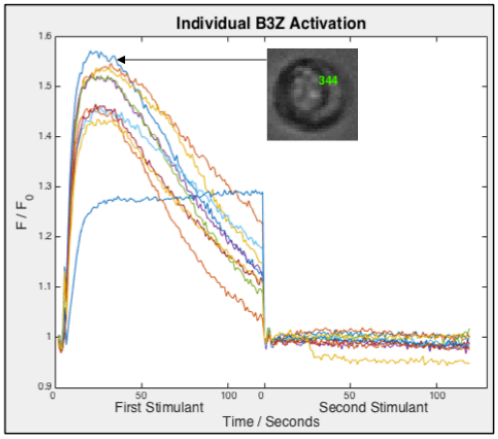

Top 10 activators

Figure 4-28: Experiment 1 of Figure 4-27.

Flow cytometry data of the same experiment, using the same cells as those in Figure 4-27 is shown in Figure 4-29.

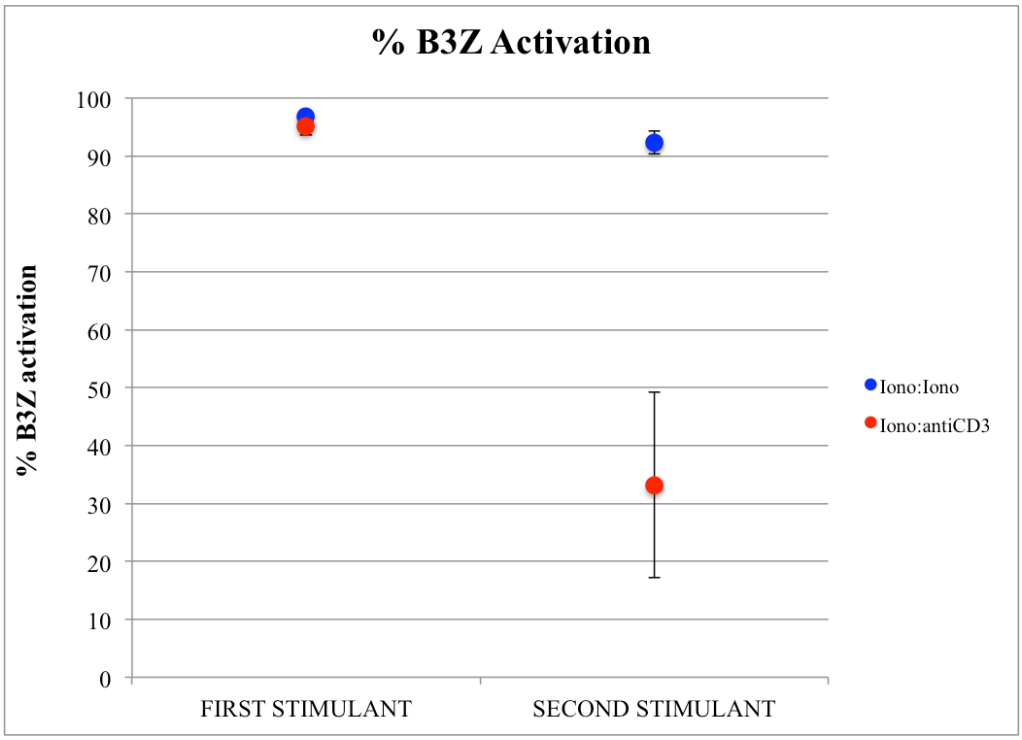

Figure 4-29: % B3Z activation of cells stimulated with ionomycin (T = 0 minutes) and then ionomycin or anti-CD3 (T = 30 minutes). Flow cytometry triplicate data taken from the same cell population on separate days. Error bars = SEM.

The ionomycin double stimulation data in Figure 4-29 agrees with the previous flow cytometry simulation data collected; Figure 4-22. Again, a slight reduction is seen for the secondary ionomycin activation, which is attributed to the reduction in Ca^{2+} available from internal stores after the initial stimulation.

Interestingly, in Figure 4-29, 30% B3Z secondary activation occurs with anti-CD3 stimulation when ionomycin is used as the first stimulant. This indicates that either ionomycin does not fully deplete the internal Ca^{2+} stores, or it is unable to access a Ca^{2+} store that CD3 engagement can. Hence, Ca^{2+} remains available inside the cell for the anti-CD3 pathway to release, or, the Ca^{2+} stores have regained some Ca^{2+} in the time between stimulations. It is possible that the additional Ca^{2+} available in the cytoplasm due to ionomycin aids this. This could not be investigated through multiple anti-CD3 stimulations because, after the first stimulation, the TCR-CD3 complex is internalised.

This is in disagreement with the data in Figure 4-27, which indicates B3Z cells cannot be activated with anti-CD3, if they have previously been stimulated with ionomycin.

There are two possible reasons why secondary activation is not possible with the microwell arrays:

1. Lack of external Ca^{2+} available after stimulation (as explained above), so the cells cannot replenish their internal stores.
2. When the first stimulant is washed away from the cells (PBS deposition on the surface of the microwell array and then aspirated away), some stimulant remains and therefore continually stimulates the cells so they are not able to rejuvenate during the rest period.

The few B3Z T lymphocytes that did activate against anti-CD3 as a secondary stimulant in Figure 4-27: Experiment 2, showed only middle-range stimulation against ionomycin. It is possible that these cells retained some of their internal Ca^{2+} stores and thus had reserves available for the second activation.

Anti-CD3-Ionomycin

AntiCD3-Ionomycin stimulation

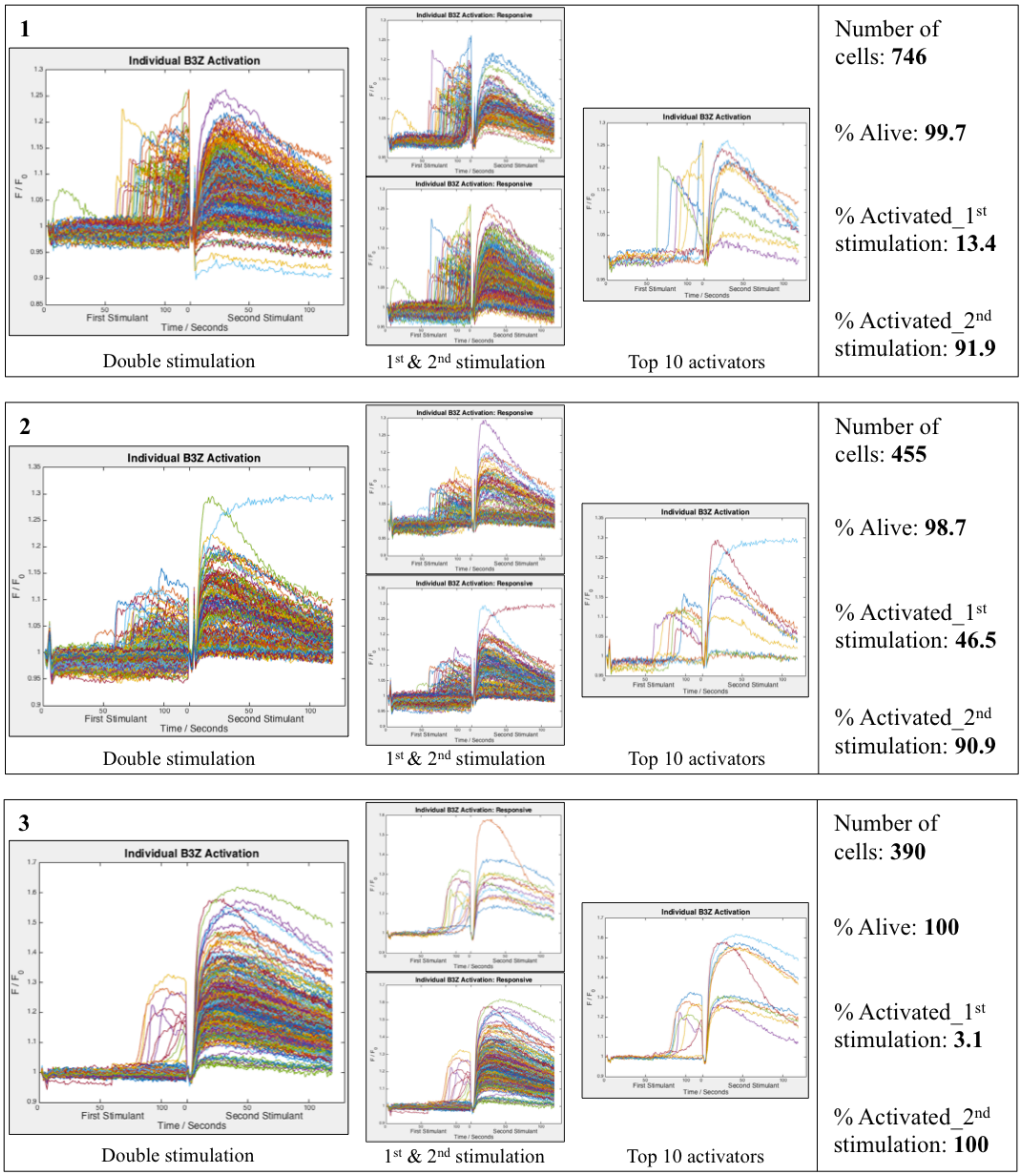

Figure 4-30: Triplicate experiment showing anti-CD3 and ionomycin stimulation of B3Z T lymphocytes with experimental statistics.

Figure 4-31 presents the first experiment of Figure 4-30 in more detail.

AntiCD3-Ionomycin stimulation

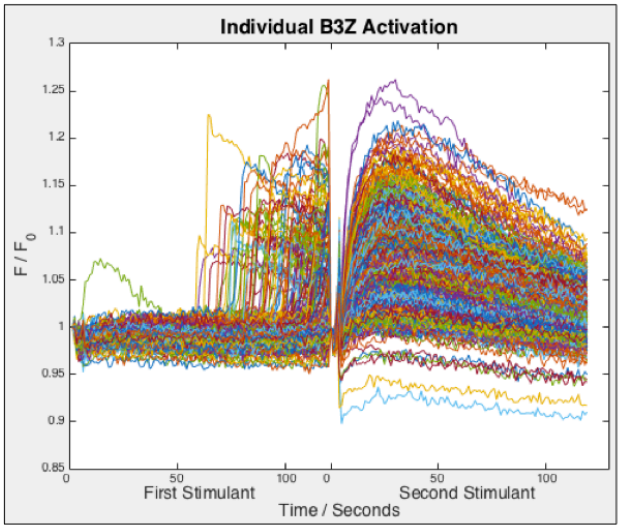

STATISTICS

Number of cells: **746**

% Alive: **99.7**

% Activated_1st stimulation: **13.4**

% Activated_2nd stimulation: **91.9**

Double stimulation

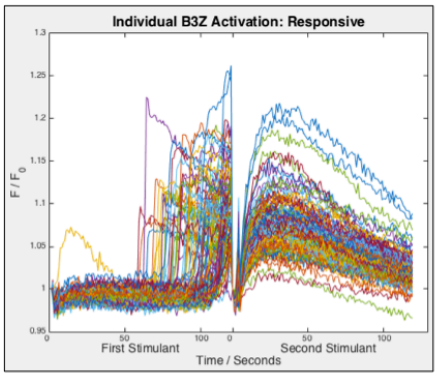

1st stimulation

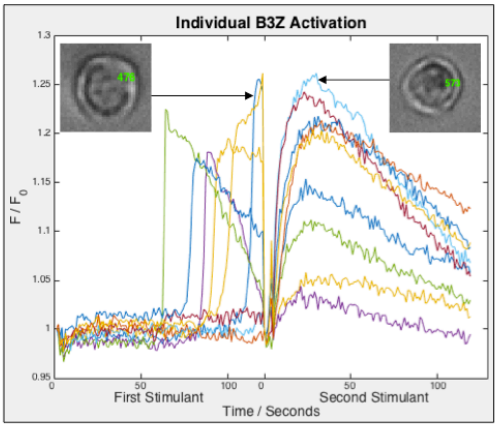

Top 10 activators

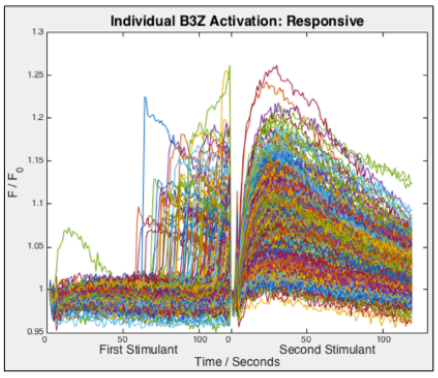

2nd stimulation

Figure 4-31: Experiment 1 of Figure 4-30.

Flow cytometry data of the same experiment, using the same cells as those in Figure 4-30 is shown in Figure 4-32.

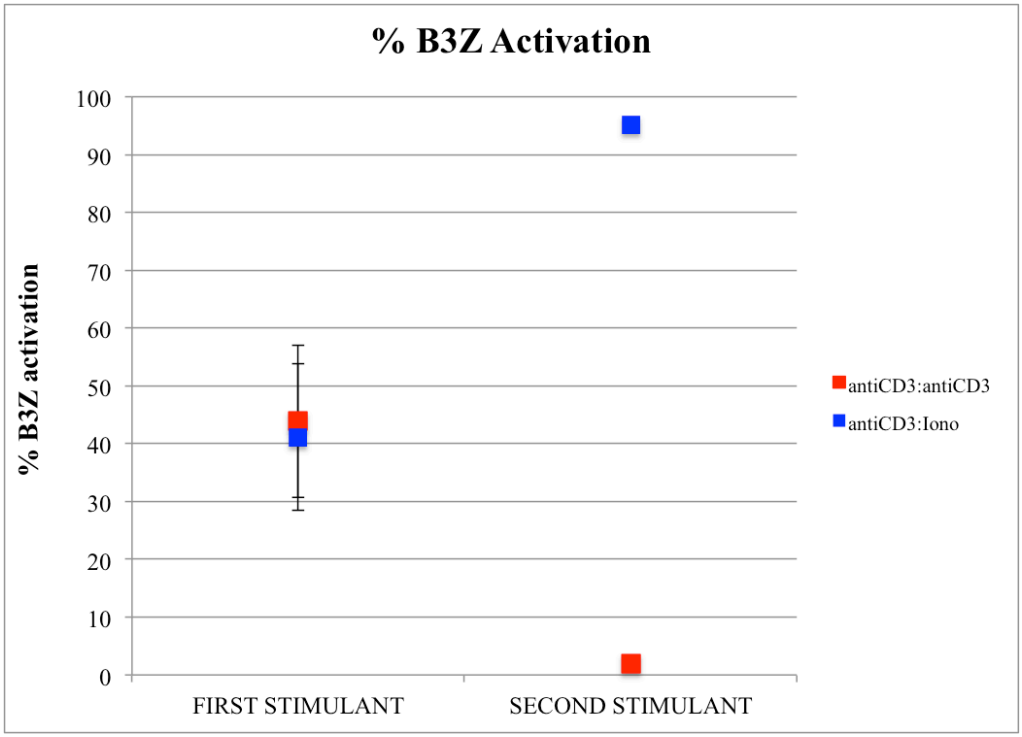

Figure 4-32: % B3Z activation of cells stimulated with anti-CD3 (T = 0 minutes) and then ionomycin or anti-CD3 (T = 30 minutes). Flow cytometry triplicate data taken from the same cell population on separate days. Error bars = SEM.

The data presented in Figure 4-32 agrees with the previous flow cytometry data for subsequent anti-CD3 activations shown in Figure 4-22; secondary activation with anti-CD3 is not possible. The anti-CD3 followed by ionomycin stimulation data is as expected; subsequent activation with ionomycin is possible because the ionophore is able to transport extracellular Ca^{2+} into the cell. Any reduction in available intracellular Ca^{2+} from internal stores is negated by the magnitude of extracellular Ca^{2+} being transported into the cell. The microwell array data displayed in Figure 4-30 corroborates these findings.

The following are noteworthy findings from the microwell investigations, which were not possible to deduce from the flow cytometry data:

- The cells that show the highest fluorescence for the initial anti-CD3 stimulation subsequently have only a mid-range fluorescence level for ionomycin stimulation, Figure 4-31. As previously discussed, in microwell arrays it is difficult to fully wash away stimulus and replenish Ca^{2+} stores, so this finding indicates that secondary ionomycin stimulation is possible because anti-CD3

stimulation of the B3Z T lymphocytes results in very little external Ca^{2+} being used. Hence sufficient external Ca^{2+} is available for subsequent ionomycin stimulation. However, because internal Ca^{2+} stores have been depleted, the overall fluorescent magnitude is reduced.

- Ionomycin fully depletes internal Ca^{2+} stores. This is evident because when the first stimulant is ionomycin (Figure 4-23 and Figure 4-27) in microwells, secondary stimulation cannot be achieved. Secondary stimulation is possible in the flow cytometry experiments (Figure 4-22 and Figure 4-29), because the internal stores can be restored from external Ca^{2+}.

4.4 Conclusions

In conclusion, the microwell array is an efficient way to trap multiple (1000s) of cells in a reliable way. Adjusting the lithography mask to have greater or fewer cells per unit area can vary the pitch of the cell traps, and hence the number available in a single microscope objective field of view. This provides a very high-throughput, parallel method of observing temporal cell activation. Using agarose as the construction material means that device fabrication (once a master has been created) takes just 30 minutes, a very fast turn-around time. Additionally, agarose is biocompatible so the cells remain viable inside the wells for extended periods of time; as verified by the very high cell viability in all the results presented.

The activation profile of an individual cell over time can be observed -data that is not obtainable using flow cytometry- can be measured through the use of microwell arrays. Individual cell activation characteristics over time can be analysed; presenting the opportunity to study the range of cell activation characteristics within a single population that are not possible with standard bulk analysis. The significance of this has been demonstrated through the improved understanding of the Ca^{2+} response characteristics of individual cells against multiple stimulations, discussed in Chapter 4.3.

Another valuable characteristic of microwell arrays is the opportunity they present for subsequent cell removal after activation, allowing cells of interest to be extracted for downstream analysis (further discussed in Chapter 6.2).

Interacting two microwell plates is a promising route for single cell-cell contact. Agarose alignment is possible as it is easily slipped against itself, and is optically transparent so fluorescent microscopy can be used to track cell activation. This is described and discussed in Chapter 5.

Chapter 5: Measurement of Physiologically Relevant T Lymphocyte Activation Following Cell-Cell Contact in Microwell Array Cell Traps

5.1 Introduction

As discussed in Chapter 2, microwell arrays provide a means of trapping single cells in high-density arrays, allowing cell activation characteristics to be temporally monitored. It was anticipated that microwell arrays could also be utilised to monitor cell-cell contact, so that T lymphocyte activation against an APC could be investigated.

5.1.1 Concept

The concept is illustrated in Figure 5-1 and described below.

1. Two microwell plates are loaded with cells, one with T lymphocytes (fluorescently labelled with Fluo-8AM) and one with APCs.

2. The plates are brought into contact and aligned.

3. Fluorescent activation of the T lymphocytes is viewed with respect to time using a microscope.

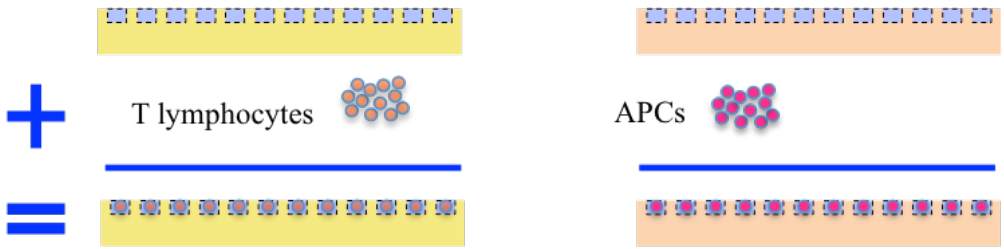

Figure 5-1: Concept schematic for the use of microwells to assess T lymphocyte activation.

As detailed in Chapter 1.3, the objectives of this project are as follows:

- **Single cell capture.** Discussed in Chapter 4; microwells allow single cells to be individually captured in wells.
- **Enable high-throughput data acquisition.** Using microwells at cell size (approximately 15 microns) it is possible to have thousands of microwells in the field of view of a standard objective; approximately 2 mm x 2 mm (W x W) for a 10x objective.

- **Functionality to bring two cells into contact for a defined period of time, after which it is possible to dissociate them.** If the microwells are correctly aligned, the cells in the top plate should drop (due to gravity) down to contact the cells in the bottom plate wells. Dissociation is possible if the bottom plate wells are not large enough to house two cells. Sliding the top plate off the bottom plate would break cell-cell contact.
- **Allow recovery of specific cells.** This could be possible through extraction techniques described in Chapter 6.2, such as use of a micropipette, or laser removal.
- **The device has to be optically transparent to permit observation of cell-cell interaction with microscopy.** This is possible by fabricating the device from an appropriate material, as discussed in Chapter 3: Transparent material.

In summary, the use of the microwell design could be a viable solution to address the project objectives.

5.1.2 T lymphocyte activation with pMHC

The T lymphocyte cells used in this work are the B3Z T cell hybridomas, discussed in Chapter 4. B3Z T lymphocytes can be activated using the APC mouse fibroblast cell line 'K89'. K89 is an adherent cell line that can activate B3Z cells through the TCR:pMHC pathway, when K89 has bound the antigen 'SIINFEKL' to its MHC complex. SIINFEKL is derived from Ovalbumin (a protein in egg white) and has a MHC bound half-life of approximately 5 hours.

When B3Z cells are activated through the TCR:pMHC pathway, the resulting Ca^{2+} flux is via the same route as the TCR:CD3 pathway discussed in Chapter 1.

5.2 Materials and methods

The material from which the device was constructed needed to be biocompatible and slip-able. This permitted one plate to be translated with respect to the other, for alignment, and allowed the cells to survive for the duration of the experiment. As in Chapter 4, the device was constructed from agarose, a highly biocompatible hydrogel which is translatable with respect to itself.

5.2.1 Plate alignment

Once the agarose microwell arrays had been fabricated, they needed to be brought into contact and aligned. Microstructure alignment is impossible by eye. Generally the maximum translation required to achieve full alignment, after macro-scale alignment had been conducted by hand, was 2 mm left-right/up-down and 15° rotational. Figure 5-2 shows an example of misalignment.

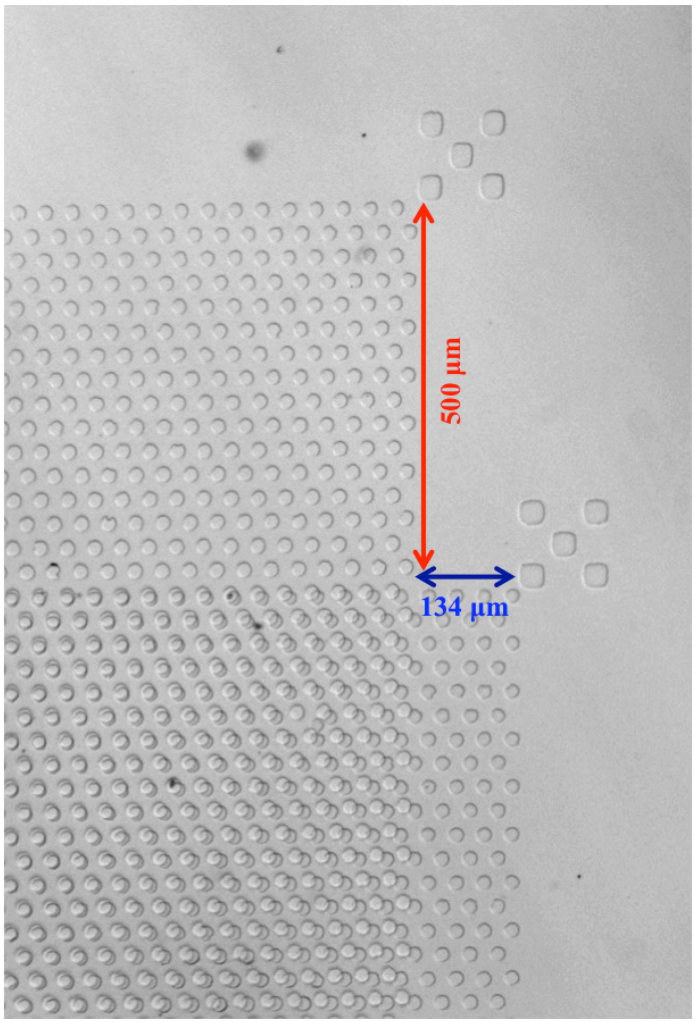

Figure 5-2: Agarose microwell array top and bottom plate initial position, prior to fine-alignment. Arrows with measurements show alignment necessary.

Experimental system

To achieve full alignment, an alignment rig was designed and manufactured to enable translation in the X, Y, Z and theta directions. As part of this, an optical stage was purchased from Newport Optics [110]; Figure 5-3.

Figure 5-3: Photograph of the New Focus Kinematic All-In-One Alignment Stage 9082M from Newport Optics. Image taken from [110].

The stage was capable of 3 mm travel in the X, Y and Z directions and 8° rotational alignment. Crude alignment was conducted by eye when the plates were brought together, to ensure that the rotational alignment necessary was as small as possible.

To align the plates, they must firstly be clamped in place, before one is translated with respect to the other. The alignment rig created translates the bottom plate with respect to a stationary top plate. An attachment was constructed to clamp the bottom plate to the movable stage, and the top plate in place above the stage. A cross-section of the attachment is depicted in Figure 5-4, with the full assembly shown in Figure 5-5.

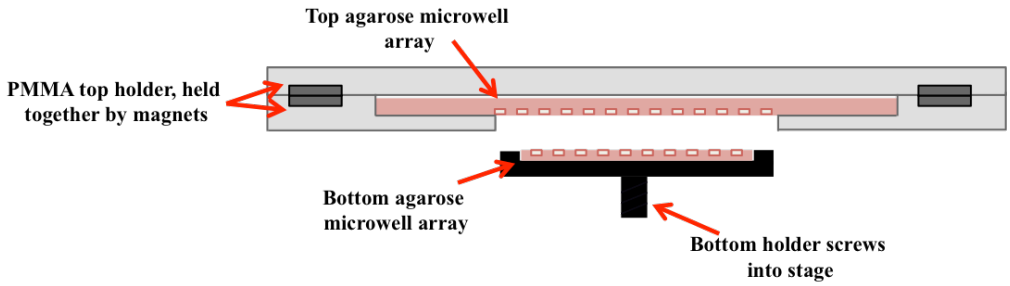

Figure 5-4: Cross-section of stage attachment to clamp top and bottom plates. Actual dimensions: bottom plate = 48 mm diameter, top plate = 65 mm diameter.

Additional stage attachments were made with the following dimensions:

Top plate = 50 mm diameter, bottom plate = 20 mm x 20 mm (W x W).

Top plate = 30 mm diameter, bottom plate = 5 mm x 5 mm (W x W).

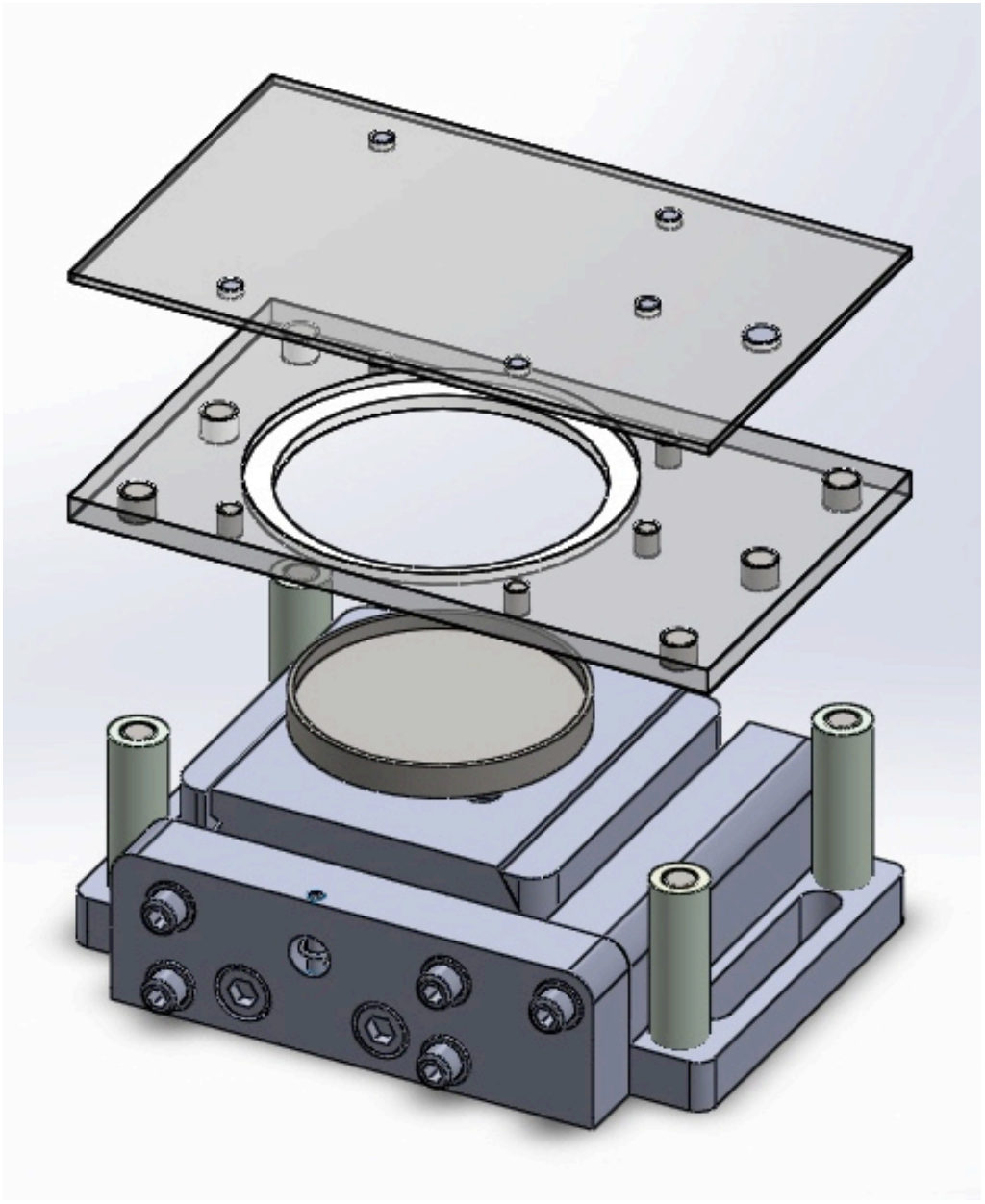

Figure 5-5: SolidWorks diagram of alignment rig including all attachments. Dimension of full assembly = 117 mm x 72 mm x 45.5 mm (W x L x H).

The final rig assembly is shown in Figure 5-6, with the top plate stage attachment in Figure 5-7.

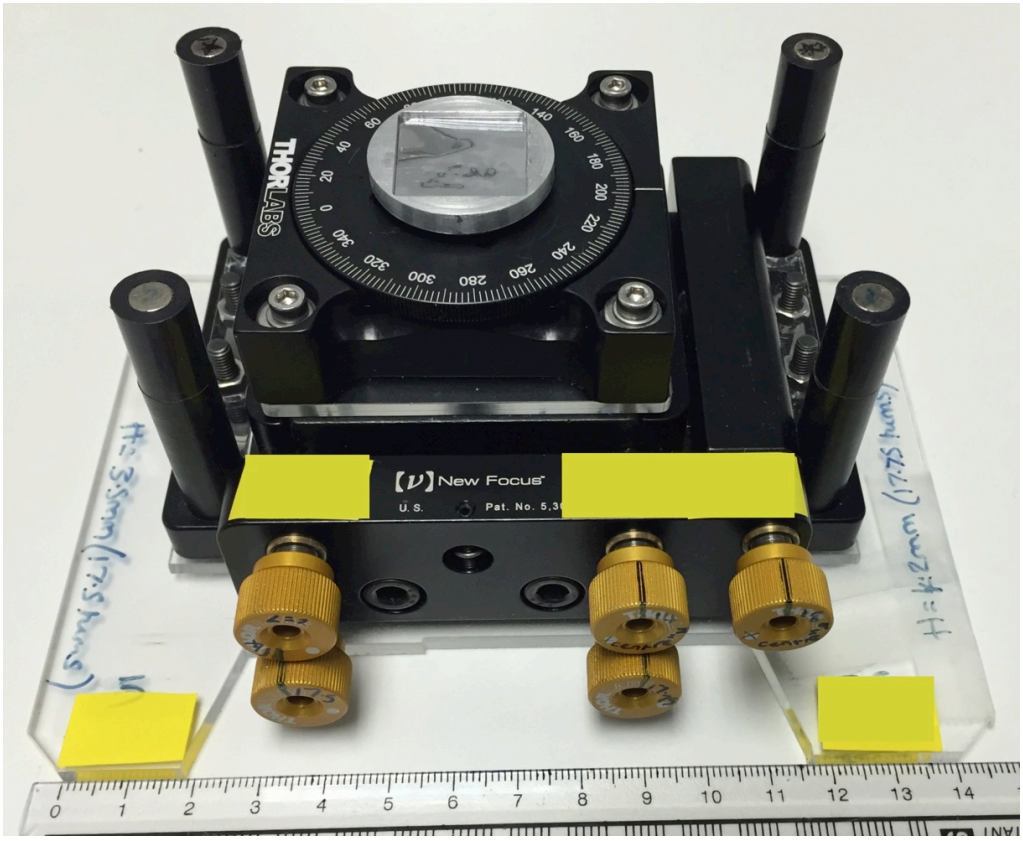

Figure 5-6: Photograph of alignment rig with 20 mm x 20 mm (W x W) bottom plate holder.

As seen in Figure 5-6, screw grips were added to the adjustment screws to make alignment easier. Additionally, a 360° rotational stage was added to the rig so that full theta control was possible.

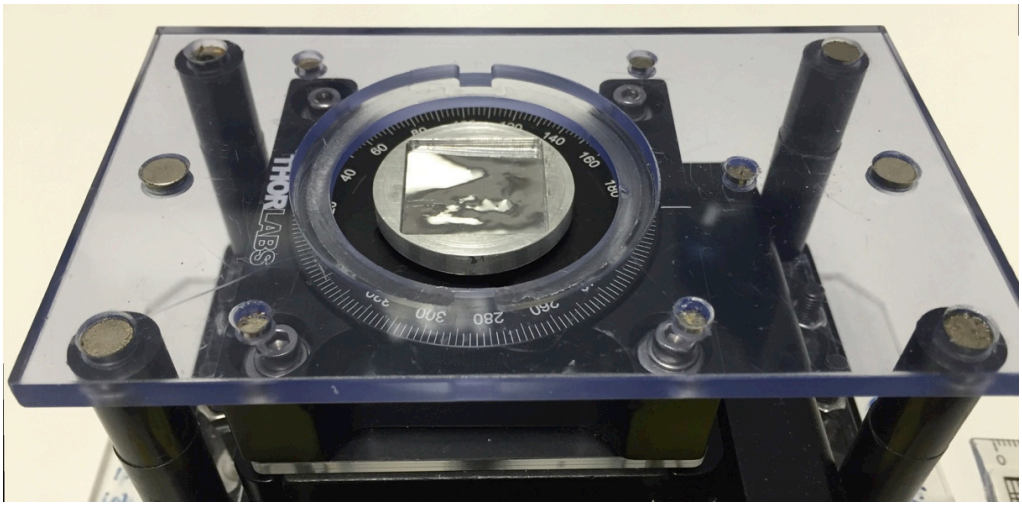

Figure 5-7: Top plate attachment, showing position of bottom plate relative to top plate.

Figure 5-8 shows the microwell array alignment possible using the alignment rig. In the image, 1369 x 20 µm wells are in perfect alignment. No lubricant is required to translate the agarose arrays with respect to each other.

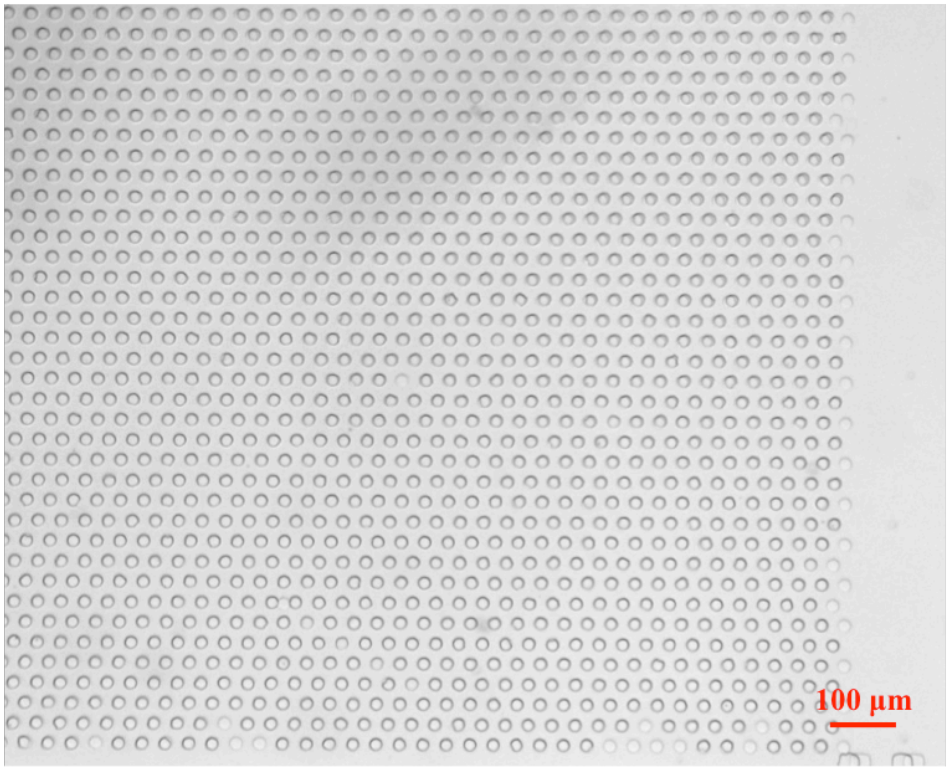

Figure 5-8: Top and bottom microwell array alignment. Well diameter is 20 µm; microwell arrays are fabricated from agarose. Scale bar = 100 µm.

Once the plates are aligned, the bottom plate is moved upwards into the top plate, to ensure good contact between the agarose plates. This prevents cells from flowing out of the wells into the cavity between the plates.

It should be noted that the depth of the agarose plates is important to ensure that good contact is possible. If the plates are too thick, or not uniform in thickness, then the microwells can become deformed and alignment is not possible (Figure 5-9).

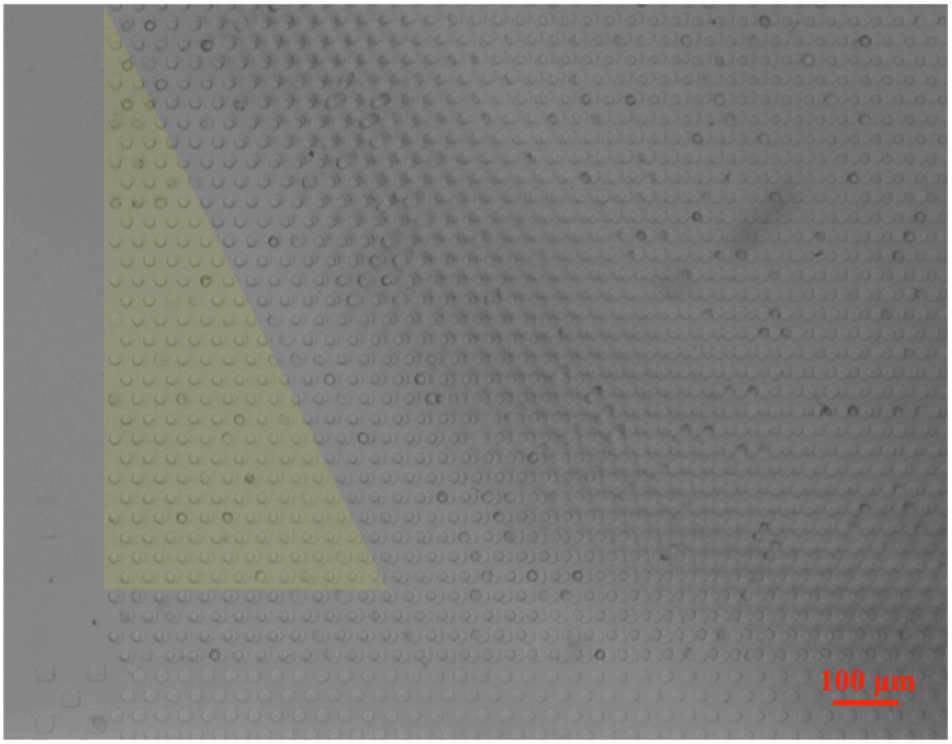

Figure 5-9: Misalignment of microwell arrays caused by non-uniform agarose plate thickness. Yellow triangle = aligned wells. Scale bar = 100 µm.

5.2.2 Cell capture

K89 loading

The K89 APC was used to stimulate the B3Z T lymphocytes in the following experiments. Accordingly, the size of K89 cells was investigated in the same manner as B3Z cells in Chapter 4: Cell size. A histogram showing the range of K89 size is presented in Figure 5-10.

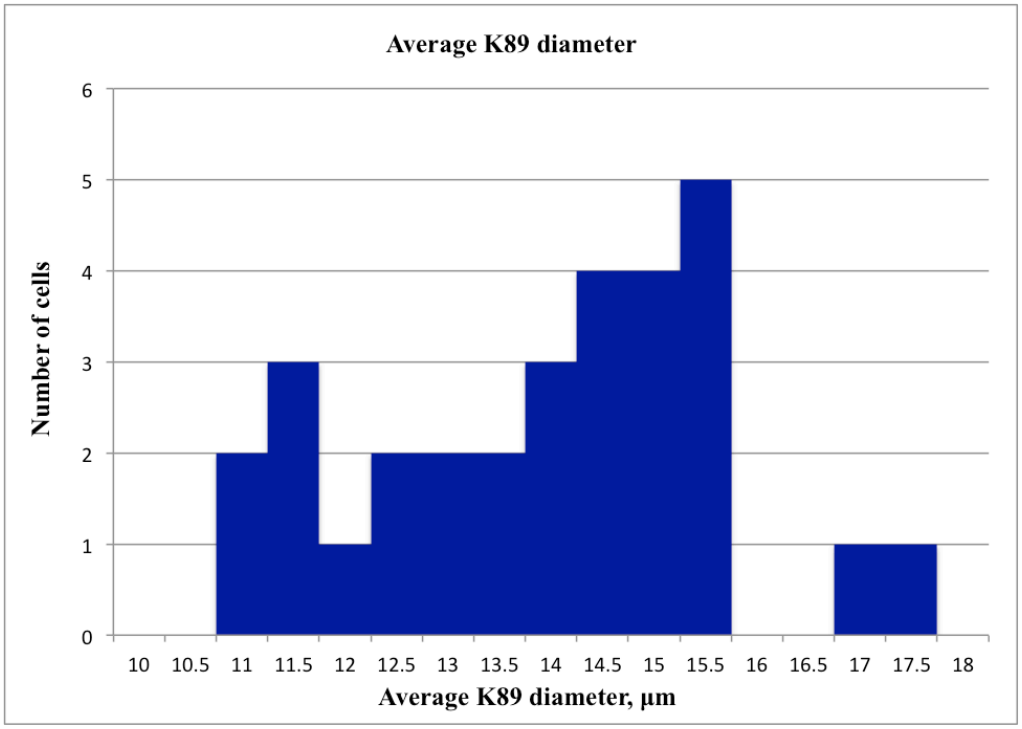

Figure 5-10: Histogram showing average K89 cell size.

Mean cell size using the manual microscope method was 13.7 µm, with a SD of 1.7 µm. The cells were also measured using the LUNA™ Automated Cell Counter, which yielded an average size of 14.6 µm.

Although K89 cells are not much larger than B3Z cells (12-13 µm in diameter), they did not load as efficiently into the wells. Figure 5-11 shows K89 loading in agarose, using the optimal protocol discussed in Chapter 4 (Appendix A.2.1). Loading density of K89 cells is a maximum of 30%.

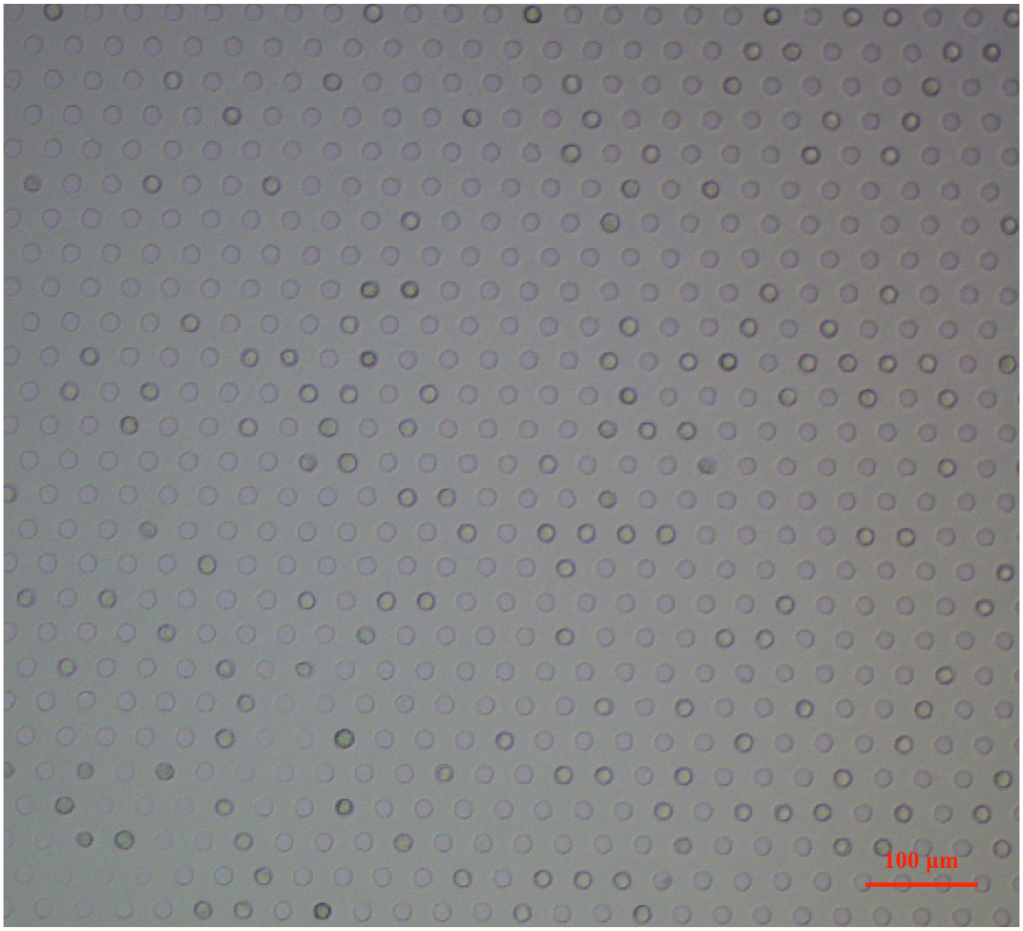

Figure 5-11: K89 loading in 20 µm x 27 µm (W x H) agarose microwells using optimum protocol. Loading density = 22%. Scale bar = 100 µm.

To ensure that the increased size of K89 cells was not the reason for reduced loading efficiency, the cells were seeded into wells of varying width to determine the optimum diameter; Figure 5-12.

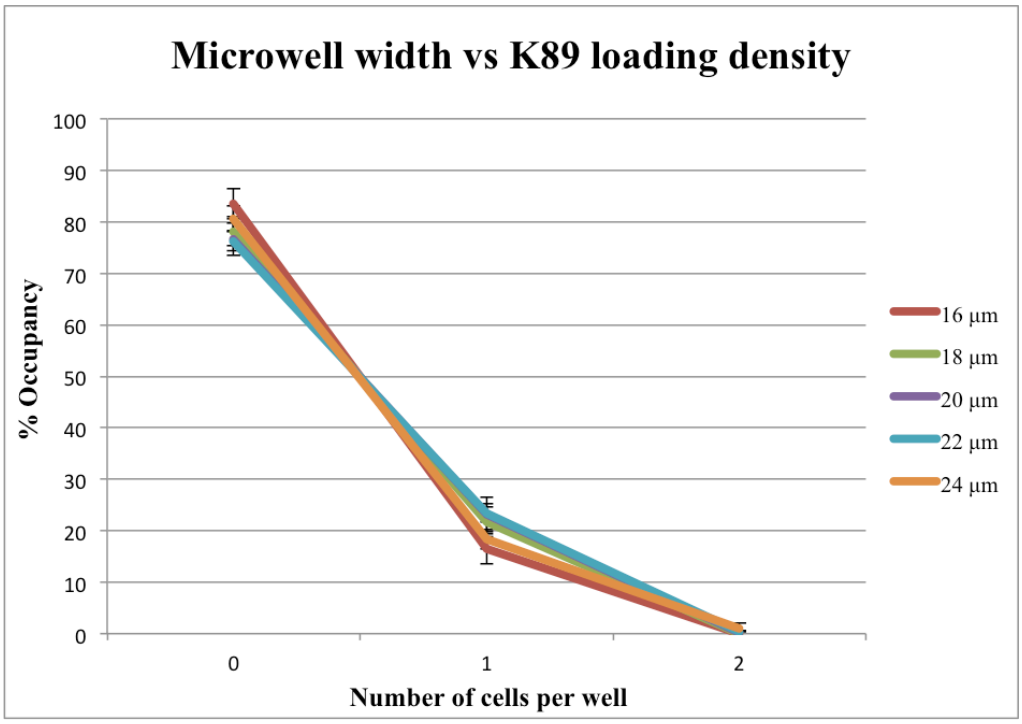

Figure 5-12: Graph showing K89 loading density in various widths of microwell (microwell depth = 22 µm). Error bars = SD.

It can be concluded from Figure 5-12 that the reason for the low K89 loading density in the 20 µm (W) microwells used for this project was not due to the cells being too large for the well. A possible reason for the reduced loading efficiency with K89 cells is that they are an adherent cell line and would normally adhere to the surface of their container. The K89 cannot adhere to agarose, hence, are not loading as efficiently as the B3Z suspension cell line.

Despite the low loading density of K89, as long as the B3Z microwell array had a loading density of 80% or higher, with a K89 loading efficiency of 30%, there would still be approximately 1008 cell-cell interactions for every array.

5.2.3 Cell-cell interaction

A concern that has not been addressed is the contact time of the cells, as it is not possible to know exactly when cell-cell interaction will take place inside microwells. Calculations were performed to estimate the time it would take for a cell in the top plate to fall into the bottom plate well. However, in reality, other factors influence the length of time, such as where the cells are residing in the wells, and if the top cell has formed any peptide bonds

to the agarose. The time taken for the cells to fall out of the wells was calculated from Stokes' drag below, however in practice the cells did not fall out of the wells due to gravity.

The Stokes' drag ($\boldsymbol{F_d}$) on a particle suspended in a liquid [111]:

$$\boldsymbol{F_d} = 6\pi\mu R v \qquad (5\text{-}1)$$

Where:

μ = dynamic viscosity (kg/m.s)

R = radius of particle (m)

v = velocity (m/s)

At terminal velocity, the force acting on a particle due to gravity ($\boldsymbol{F_g}$) is a combination of the buoyancy of the particle, counteracted by its weight and is equal to the Stokes' drag, hence $\boldsymbol{F_g} = \boldsymbol{F_d}$.

$$\boldsymbol{F_g} = (\rho_p - \rho_f) g \frac{4}{3}\pi R^3 \qquad (5\text{-}2)$$

Where:

$4/3\pi R^3$ = volume of the particle, where R = radius (m)

ρ_p = mass density of the particle (kg/m^3)

ρ_f = mass density of the suspension medium (kg/m^3)

g = gravitational acceleration constant = 9.81 m/s^2

Solving for $\boldsymbol{v}$ with $\boldsymbol{F_g} = \boldsymbol{F_d}$:

$$6\pi\mu R v = (\rho_p - \rho_f) g \frac{4}{3}\pi R^3$$

$$6\mu v = (\rho_p - \rho_f) g \frac{4}{3} R^2$$

$$v = \frac{2}{9\mu}(\rho_p - \rho_f) g R^2$$

Hence, the settling velocity of a cell in a suspension of PBS:

ρ_p = 1070 kg/m^3 (approximate average density of a lymphocyte [82])

ρ_f = 993.4 kg/m^3 (average density of PBS, as measured)

μ = 10^{-3} kg/ms (dynamic viscosity of water at room temperature [112])

R = 6.5x10^{-6} m (as measured)

$$v = \frac{2}{9(10^{-3})}(1070 - 993.4) \times 9.81 \times (6.5\times10^{-6})^2$$

$$v = 7.06\mu m/s$$

If the cells are loaded in 30 μm deep wells, and there is a 13 μm (average) diameter cell in each well, the maximum distance (d) the cell must move from the top well to the bottom cell = (30+30-13-13) μm = 34 μm.

The time (t) for a cell to move this distance is calculated as:

$$t = \frac{d}{v} \qquad (5\text{-}3)$$

$$t = \frac{34\times10^{-6}}{7.06\times10^{-6}}$$

$$t = 4.82\ seconds$$

As mentioned above, the cells did not fall out of the microwells at all. It is presumed that this is due to the cells interacting with the agarose traps and forming weak bonds to the agarose matrix. As such, techniques to prevent cell adhesion to the agarose were investigated, such as PEG coating of the agarose surface to prevent cell adhesion, and Pluronic (non-ionic surfactant) coating of the cells. These methods proved unreliable, so it was decided that the top plate cells (B3Z) should remain in the wells, and the bottom plate cells (K89) would be pulled up to cause cell-cell contact instead.

Magnetic nanoparticles

Magnetic nanoparticles (MNPs) can be used to magnetise cells, allowing manipulation of cells with a magnetic field [113]. The uptake of MNPs of 10 nm, or less, does not affect

cell viability [52] and they have been shown to enter cells via the endocytosis pathway [114].

The MNPs used in this work are 10 nm, carboxylic acid functionalised, iron oxide MNPs, acquired from Sigma-Aldrich [115]. The carboxylic acid functionalisation of the MNPs provides them with an overall negative net charge, which promotes their electrostatic adhesion to the cell surface membrane. The plasma membrane then undergoes invagination and the MNPs are enclosed in vesicles that then fuse with endosome and lysosomes inside the cell [114]. Figure 5-13 shows MNPs inside K89 cells at 40x magnification. The left and right images are of the same cells, with changed focus, showing the various locations of MNPs at different positions in the cell.

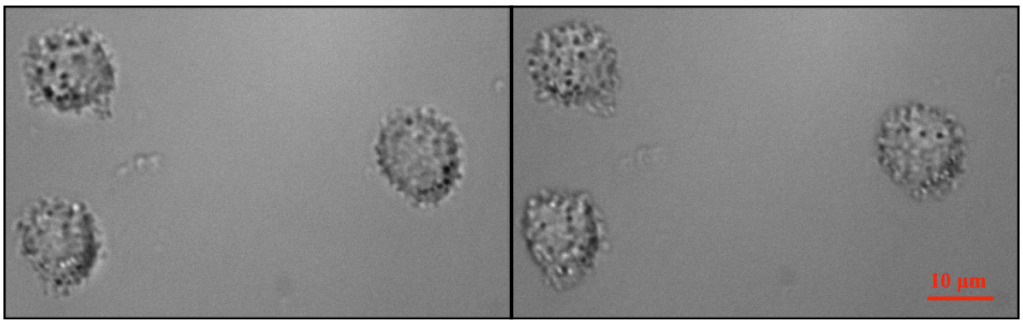

Figure 5-13: MNPs inside K89 cells. Scale bar = 10 µm.

In agreement with the protocol published by Kolosnjaj-Tabi *et al* in 2013 [52], the MNPs were loaded by incubating the cells with 0.5 mM of MNPs in serum-free media for 60 minutes at 37°C. The following calculation shows the amount of MNPs used for $1x10^6$ cells suspended in 1 ml RPMI cell media.

$$C = \frac{n}{V} \qquad (5\text{-}4)$$

where, $n = \frac{m}{Mr}$

C = concentration (M)

n = number of moles

V = volume (m^3)

m = mass (kg)

Mr = molecular mass ($g.mol^{-1}$)

MNP Mr = 231.53 $g.mol^{-1}$ [115]

For a volume of 1 ml:

$$n = CV = (0.5x10^{-3})(1x10^{-3}) = 500x10^{-9}$$

$$m = nMr = (500x10^{-9})(231.53) = 116x10^{-6}\ g$$

Nanoparticle concentration = 5 $mg.ml^{-1}$

For 116 µg = $\frac{V}{43} = \frac{1000}{43}$ = 23.2 µl

This yields an iron loading per cell of approximately 1 - 2 pg [114].

To test the manipulation of MNP loaded K89 cells, the movement of the cells in suspension was imaged when a 4 kg pull force neodymium magnet was placed next to the cell suspension. The data is not shown, but the experiment showed the movement of MNP loaded K89 cells towards a stationary magnet.

The magnetic force experienced per cell can be calculated using the following equation [114]:

$$F_m = M_c.gradB \qquad (5\text{-}5)$$

Where:

F_m = Force per cell

M_c = Magnetic moment of a cell = 6.6 x 10^{-14} A m^2 for 1 pg of iron [113].

$gradB$ = Field gradient = 17 $T.m^{-1}$ [113]

Therefore,

$$F_m = (6.6 \times 10^{-14})(17) = 1.1x10^{-12}\ N = 1.1\ pN$$

To test whether K89 cell transfer from bottom into top microwell plate wells was possible, the following experiment was conducted, shown in Figure 5-14.

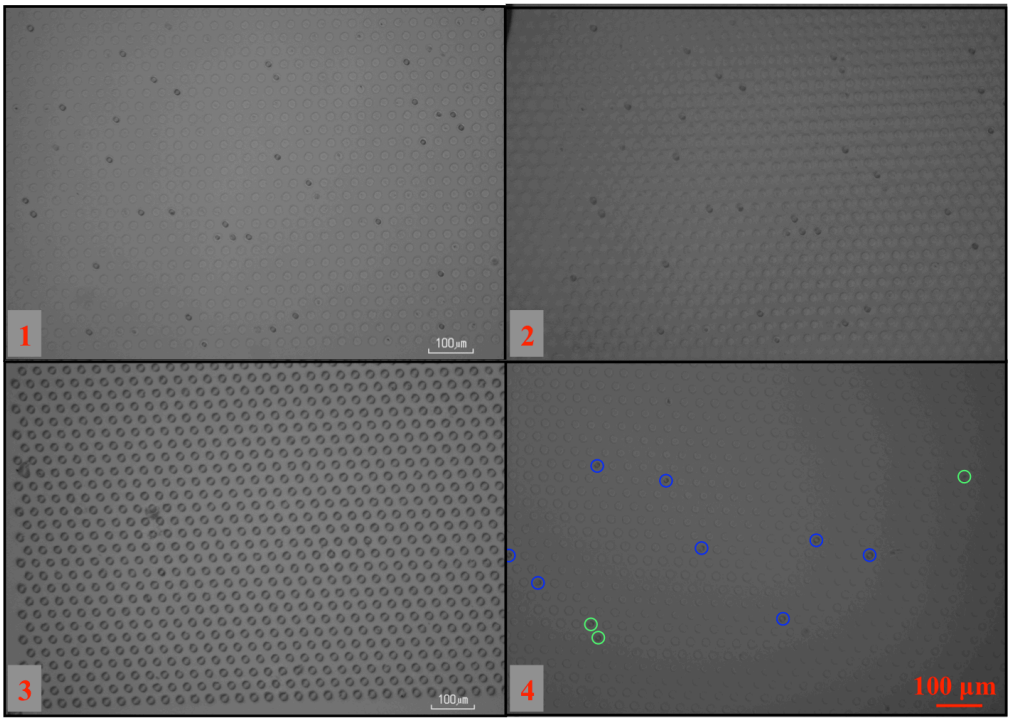

Figure 5-14: Transfer of K89 cells (loaded with MNPs) from bottom to top plate agarose microwells. Well dimensions = 20 µm x 29 µm (W x H). Scale bar = 100 µm.

1. K89 cells (loaded with MNPs) were seeded into a bottom plate agarose microwell array.
2. An empty top plate agarose microwell array was placed on top of the K89 loaded microwell array and manually aligned (approximately, by eye). A 4 kg pull force, neodymium magnet was then placed over the two microwell arrays for 10 minutes.
3. The top plate microwell array was removed, leaving no K89 cells in the bottom plate.
4. The top microwell array was turned over, and the transferred cells were analysed. Green circles = cells transferred correctly. Blue circles = cells that have been pulled into the incorrect wells.
   % Transferred correctly = 9.3
   % Not transferred correctly = 90.6
   % In incorrect wells = 25

It should be noted from Figure 5-14 that 100% of the K89 cells were pulled out of the bottom plate wells, demonstrating that K89 cells in microwells can be manipulated using a magnet. When using the alignment rig discussed in Chapter 5.2.1, the plate

cannot be removed quickly when accurate alignment is conducted. Hence, for the experiment shown in Figure 5-14, the top plate was placed and aligned by eye on the bottom plate. For this reason, incorrect transfer is not unprecedented, as some of the wells may not be perfectly aligned. Also, in the actual alignment rig, the bottom plate is pushed into the top plate, eliminating any gap between the plates. In the above experiment this was not possible. As a result, cells have been pulled out of the microwells by the magnet, and have then flowed into the space between the plates. This accounts for the 'lost' cells and the cells that have appeared in incorrect wells. Nevertheless, this experiment still provides proof of concept that the cells can be translated using a stationary magnet.

5.3 Results

5.3.1 Cell-Cell activation

B3Z T lymphocytes were activated against the APC K89, via TCR:pMHC recognition with the peptide SIINFEKL. Cell-cell contact was achieved by pulling the K89 cells into the B3Z T lymphocytes with a neodymium magnet. Following B3Z activation, the Ca^{2+} flux of the cells was recorded using the fluorophore Fluo-8AM and a Zeiss LSM 5 upright microscope. An overview of the experimental protocol is depicted in Figure 5-15.

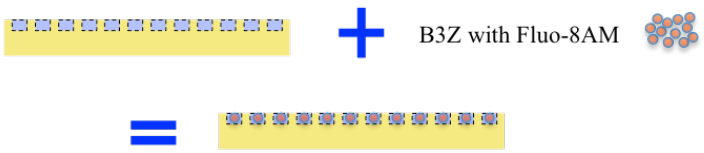

1. Load T lymphocytes into top plate microwells

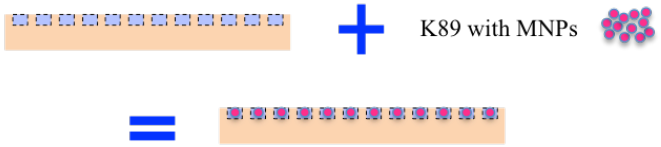

2. Load APCs into bottom plate microwells

3. Connect and align microwell plates

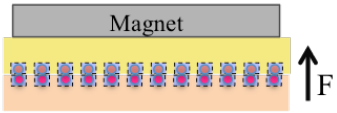

4. Apply stationary magnet above top plate for 10 minutes, to pull APCs into T lymphocytes

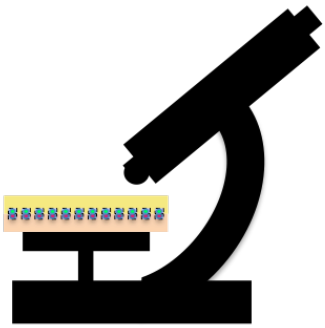

5. View T lymphocyte activation using a fluorescent microscope

Figure 5-15: Diagram of the experimental protocol for T lymphocyte activation through cell-cell contact with an APC.

Microwell array Cell-Cell contact

The bottom plate is seeded with the APC line, K89, and imaged to locate the K89 cells; Figure 5-16.

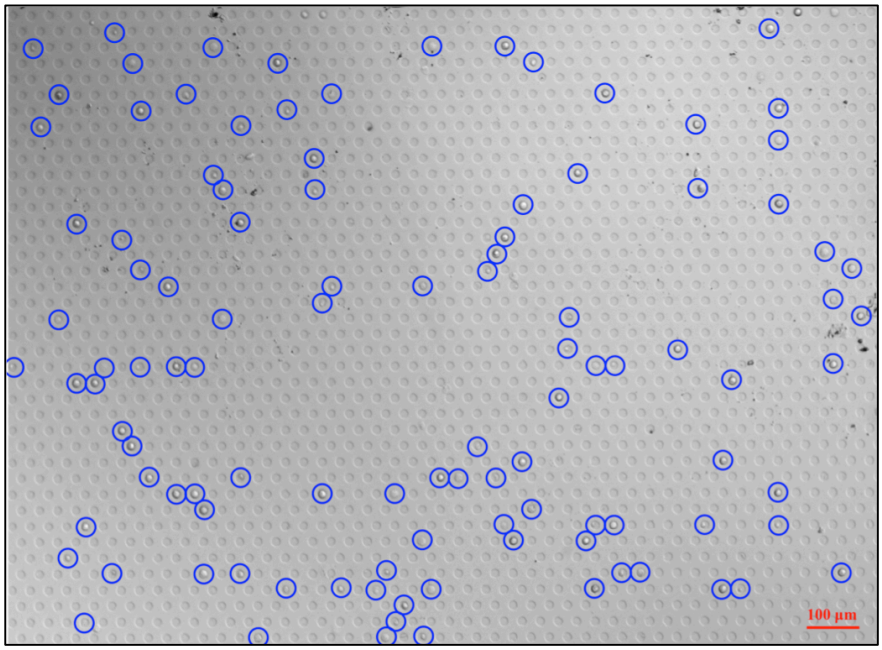

Figure 5-16: Bottom microwell array plate, seeded with 107 K89 cells (incubated with MNPs and SIINFEKL). Blue circles show K89 cells. Scale bar = 100 µm.

The top microwell array plate that has been seeded with B3Z T lymphocytes is then assembled in the alignment rig, and aligned; Figure 5-17.

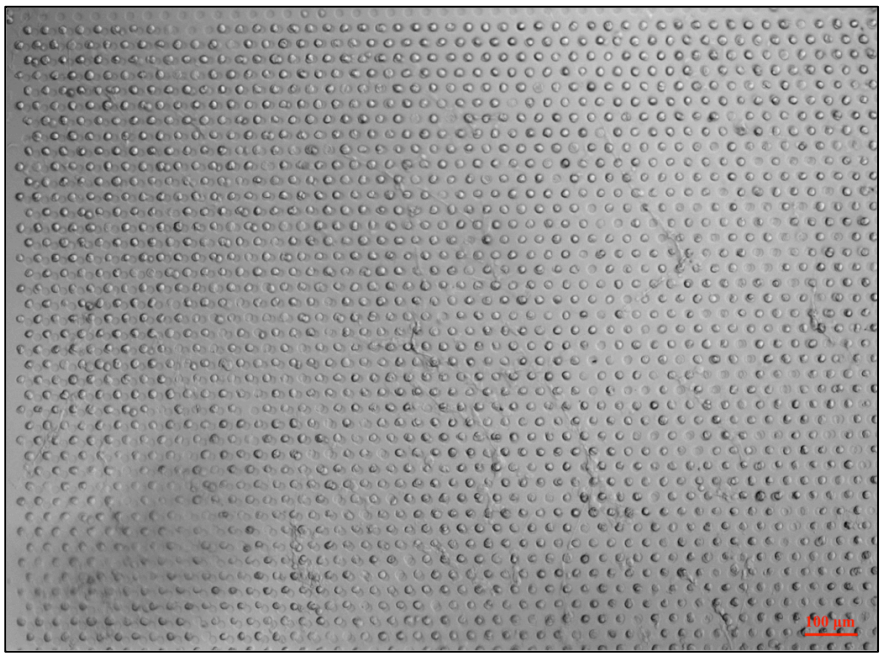

Figure 5-17: Alignment of bottom microwell array plate (Figure 5-16) and top plate, containing B3Z T lymphocytes. Scale bar = 100 µm.

The Ca^{2+} flux of the B3Z cells is shown in Figure 5-18.

B3Z activation against K89 APCs

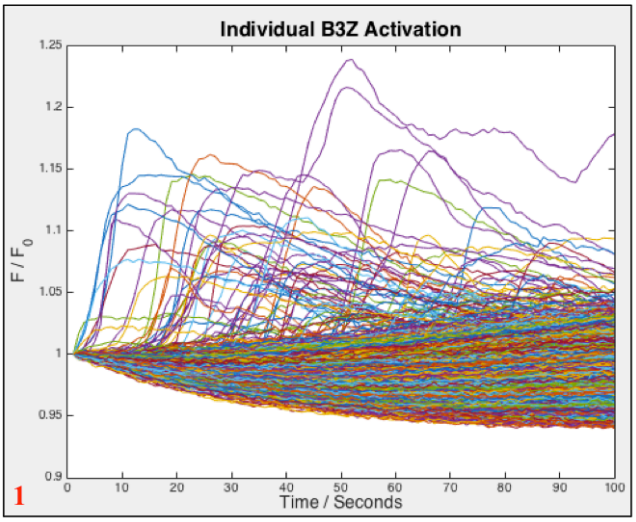

STATISTICS

Number of B3Z: 1899

Number of K89: 107

Number of B3Z activated: 92

% Activated: 86.0

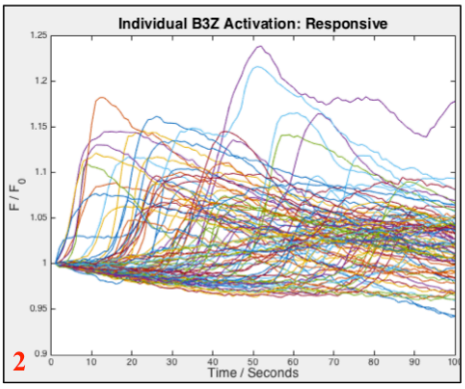

Activated B3Z

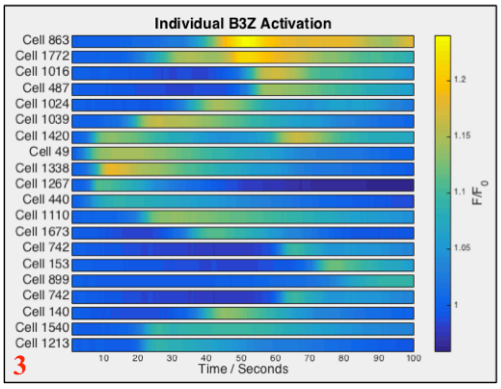

Top 20 activators

Figure 5-18: Ca^{2+} flux in B3Z T lymphocytes after contact with K89 APCs, pulsed with SIINFEKL.

1: Ca^{2+} response of all B3Z cells.

2: Ca^{2+} response of activated B3Z cells.

3: Ca^{2+} response of the top 20 activating B3Z cells.

107 K89 cells were counted on the bottom microwell array plate, and 92 B3Z cells reached the threshold to be considered as activated; this is an activation level of 86 %.

The advantage of using microwell arrays to cause cell-cell contact is the ability to view single cells of interest after the experiment has been conducted. Figure 5-19 shows the individual activation characteristics of three separate cells.

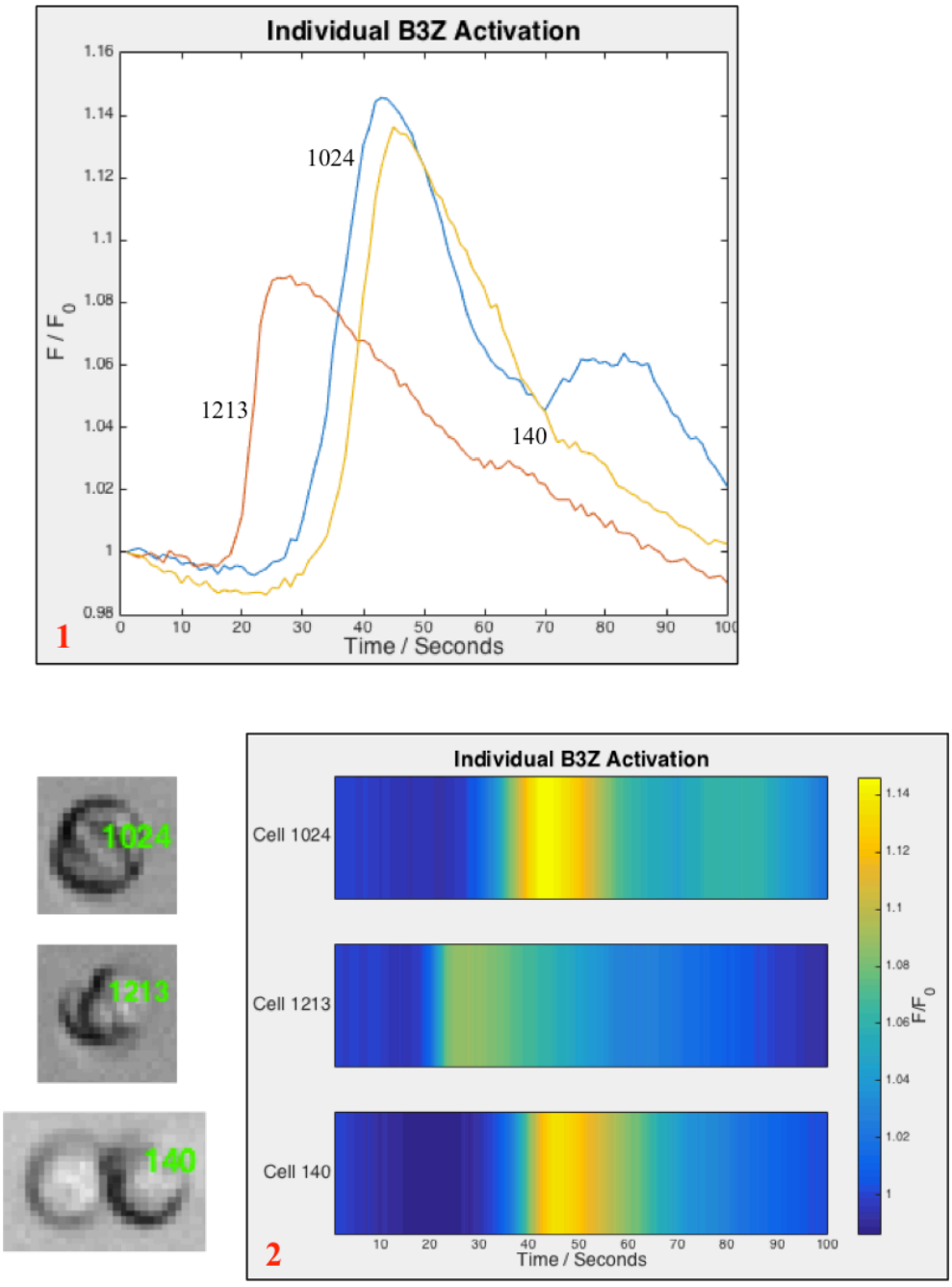

Figure 5-19: Individual activation characteristics of cells 1024, 1213 and 140.

1: F/F_0 line plot.

2: F/F_0 p-colour plot.

Interestingly, as shown in Figure 5-19, the alignment of the top and bottom plate wells does vary slightly across the array. It is thought that this is due to slight variations in agarose depth across the plate. Cell 1024 is perfectly aligned with the bottom plate, meaning the APC underneath cannot be viewed. Cell 1213 shows minor misalignment, allowing the APC in the bottom well to be seen. Cell 140 is almost completely misaligned, so the whole bottom plate well, including APC can be observed. Despite this, B3Z Cell 140 still shows high Ca^{2+} activation, greater than B3Z Cell 1213, which is better aligned.

The experiment discussed was repeated ten times to ensure validity; three data sets from the experiments are presented in Figure 5-20.

The following control experiments were also conducted, each showing no B3Z activation:

- B3Z T lymphocyte activation against K89 cells, incubated with MNPs but no SIINFEKL;
- B3Z T lymphocyte activation when the bottom microwell array contained no cells;
- B3Z T lymphocyte activation against K89 cells, incubated with MNPs and SIINFEKL, but without the inclusion of a magnet for 10 minutes.

This confirms that it is the K89 cells with SIINFEKL activating the B3Z T lymphocytes (through the TCR:pMHC pathway), as the removal of the peptide results in no activation. Also, the need for MNPs is highlighted by the experiment where no magnet was used, as the B3Z cells did not activate in this instance, hence cell-cell contact was not achieved.

Intriguingly, despite B3Z cells being a clone population, and therefore expected to show the same Ca^{2+} responses to the same antagonist, again it can be seen from the data collected using microwell arrays that individual cell responses vary greatly. For example, if B3Z Cells 1024, 1213 and 140 had been recorded by flow cytometry, at t = 25 seconds, Cell 1213 would be shown as the highest activator and the increased activation of Cells 1024 and 140 at t = 40 seconds would not have been observed. This type of information cannot be obtained using traditional bulk cell analysis techniques such as flow cytometry. The temporal resolution of Ca^{2+} flux provided by microwell arrays, allows the variation in single T lymphocyte activation within a population to be located.

This will allow cells of interest to be located; further investigation into why these cells differ from the main population can be explored with downstream analysis.

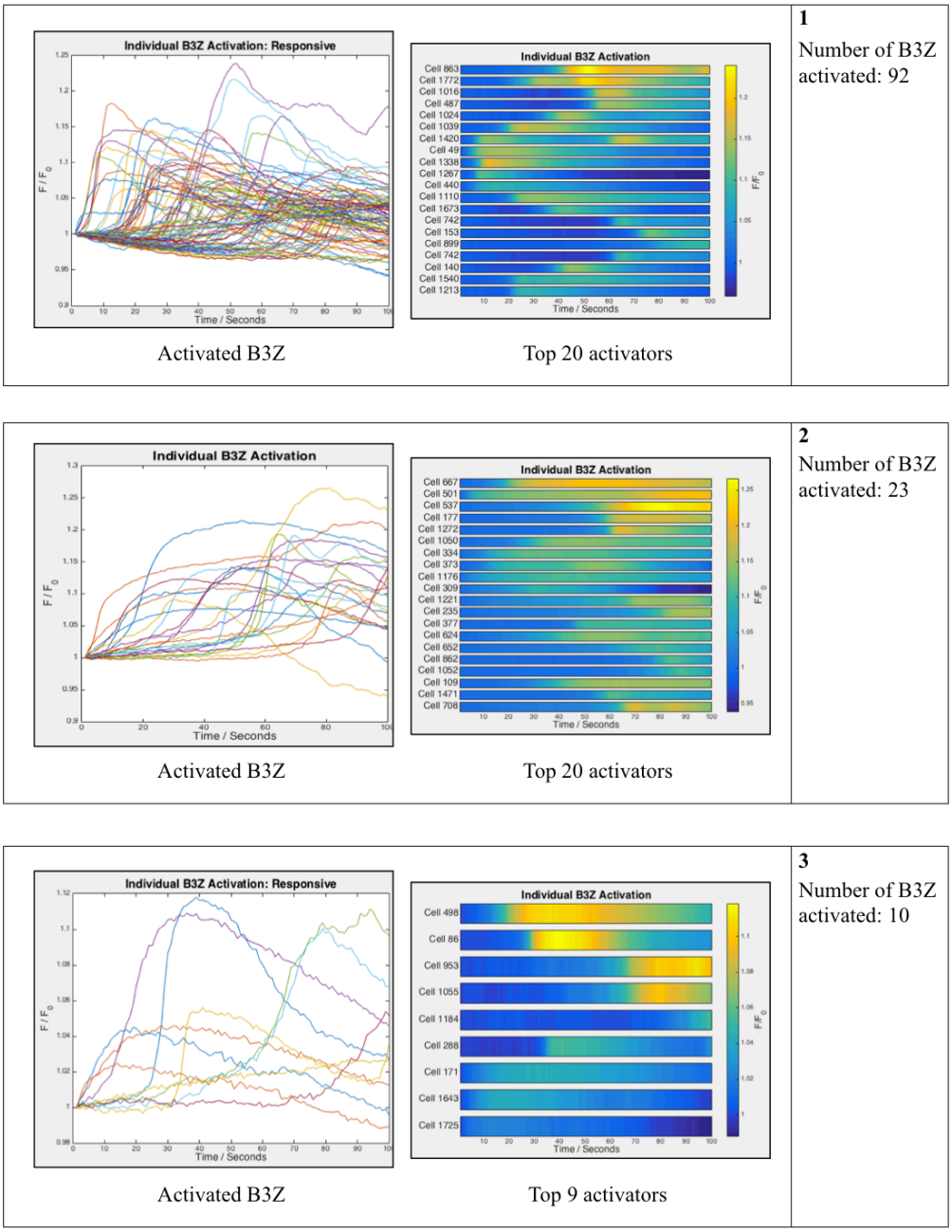

Figure 5-20: Data from three separate experiments, using the same B3Z cell population, showing Ca^{2+} flux in B3Z T lymphocytes after contact with K89 APCs, pulsed with SIINFEKL.

Figure 5-21 shows the bottom plate, seeded with K89, before and after an experiment. It can be seen that the majority of K89 cells remain in their wells. The top plate wells are

not large enough to accommodate two cells, and the top and bottom microwell array plates are forced together so that there is no space in-between the plates for cells to occupy. Hence, the K89 cells are not removed from their original wells. This means that they can be extracted for future analysis (described in Chapter 6.2), or used to activate a secondary population of B3Z T lymphocytes. This would allow sequential contact with the same APC to be investigated.

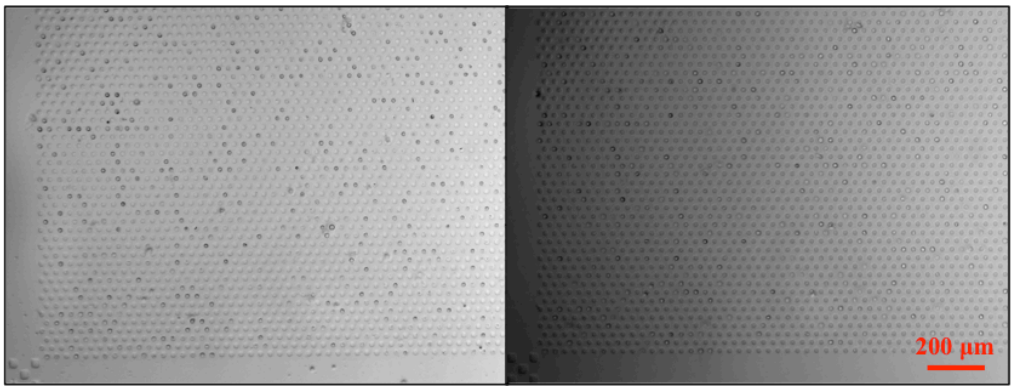

Figure 5-21: K89 cells seeded in the bottom microwell array plate, before (left) and after (right) an experiment. Scale bar = 200 µm.

Flow cytometry

As a comparison, the same experiment (B3Z activation against K89 cells pulsed with SIINFEKL) was conducted with flow cytometry. The results are displayed in Figure 5-22.

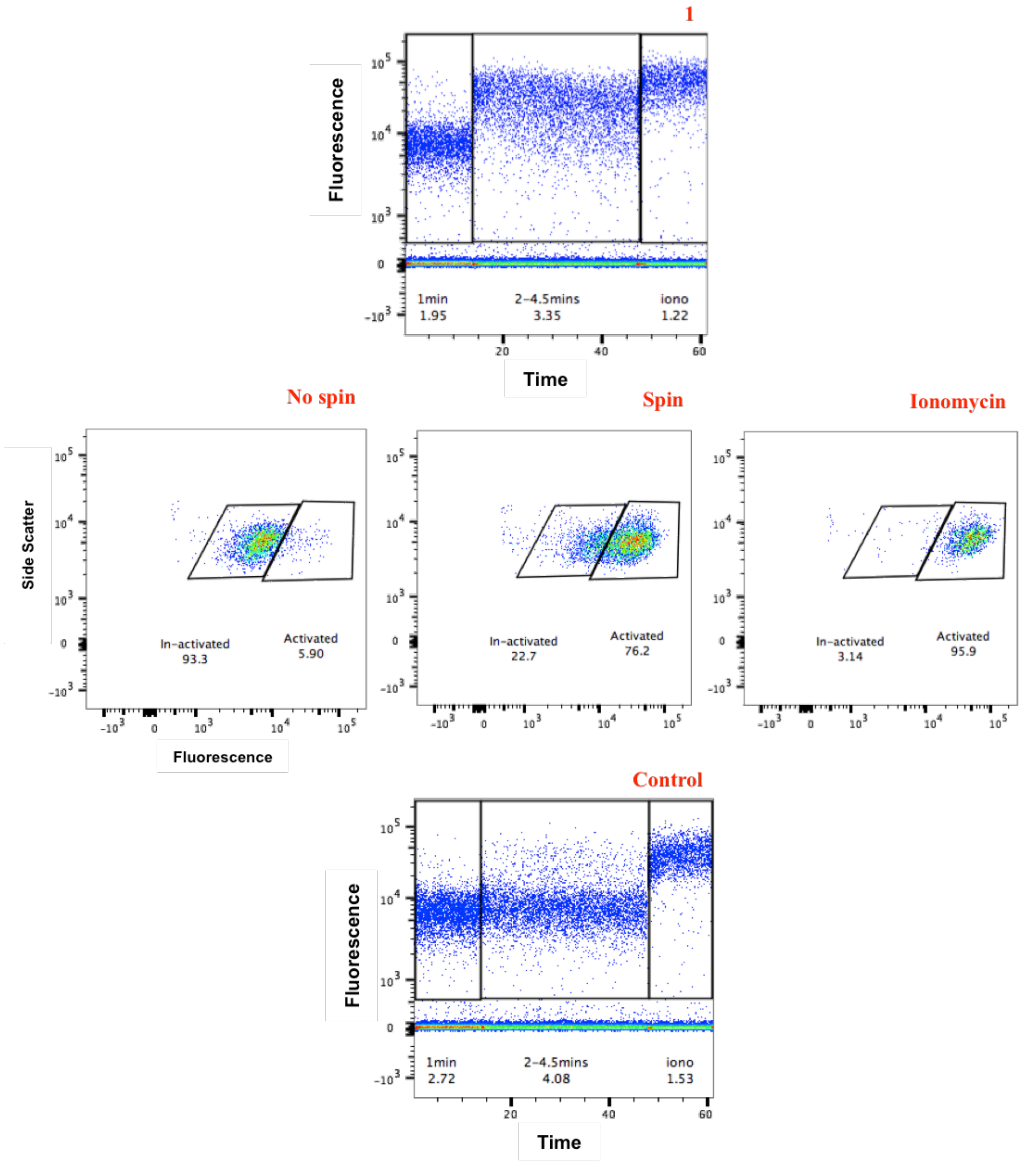

Figure 5-22: Typical data output from the BD LSRFortessa™ after stimulation of B3Z T lymphocytes with p:K89 cells.

1. B3Z density plot showing fluorescence level against time (Time:FITC). B3Z and K89 cells (pulsed with 10 μM SIINFEKL) were run for one minute at a concentration of 1:10 B3Z:K89, before being centrifuged at 900 rpm for 3 minutes at 4°C to force cell contact, and run for a further 2.5 minutes. Finally 2 μM ionomycin was added to force a Ca^{2+} increase and the cells were run for a further minute.

No spin: B3Z density plot (FITC:SSC) of B3Z:K89 (1:10) cells.

Spin: B3Z density plot (FITC:SSC) of B3Z:K89 (1:10) cells after centrifuging.

Ionomycin: B3Z density plot (FITC:SSC) of B3Z:K89 (1:10) cells after 2 μM ionomycin was added.

The increase in intracellular Ca^{2+} is clearly seen by the increased fluorescence of the B3Z cells after centrifuging. Centrifuging increases the likelihood of TCR:pMHC engagement.

Control. B3Z density plot showing fluorescence level against time (Time:FITC). B3Z and K89 cells (not pulsed with SIINFEKL) were run for one minute at a concentration of 1:10 B3Z:K89, before being centrifuged at 900 rpm for 3 minutes at 4°C to force cell contact, and run for a further 2.5 minutes. Finally 2 μM ionomycin was added to force a Ca^{2+} increase and the cells were run for a further minute.

For the control experiment there is no Ca^{2+}increase after centrifuging because there is no peptide (SIINFEKL) available for TCR:pMHC engagement.

Comparing the control to the peptide inclusive experiment:

- No spin MFI F/F_c (fluorescence over control fluorescence) = 7946/6904 = 1.15
- Spin MFI F/F_c = 27013/9728 = 2.78

Four repeats of the experiment displayed in Figure 5-22 were conducted with the same cells on the same day. % B3Z activation against K89 cells that have been pulsed with SIINFEKL is shown in Figure 5-23, with average response presented in Figure 5-24.

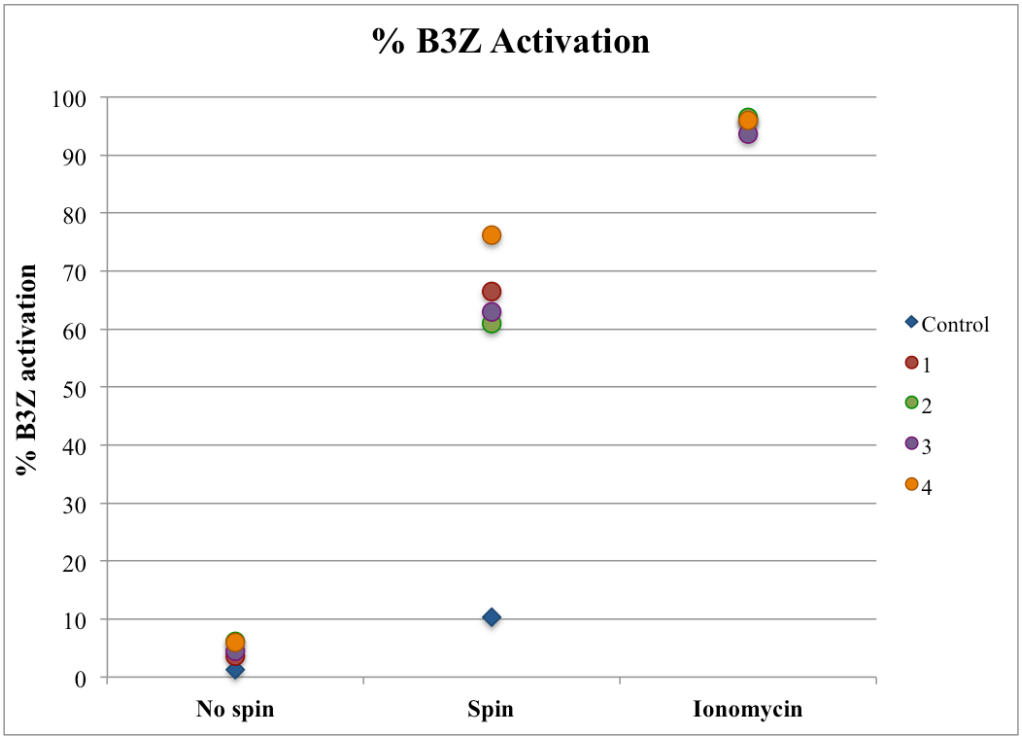

Figure 5-23: % B3Z activation after stimulation with K89 cells pulsed with SIINFEKL and ionomycin. Data taken from the same cell population on the same day.

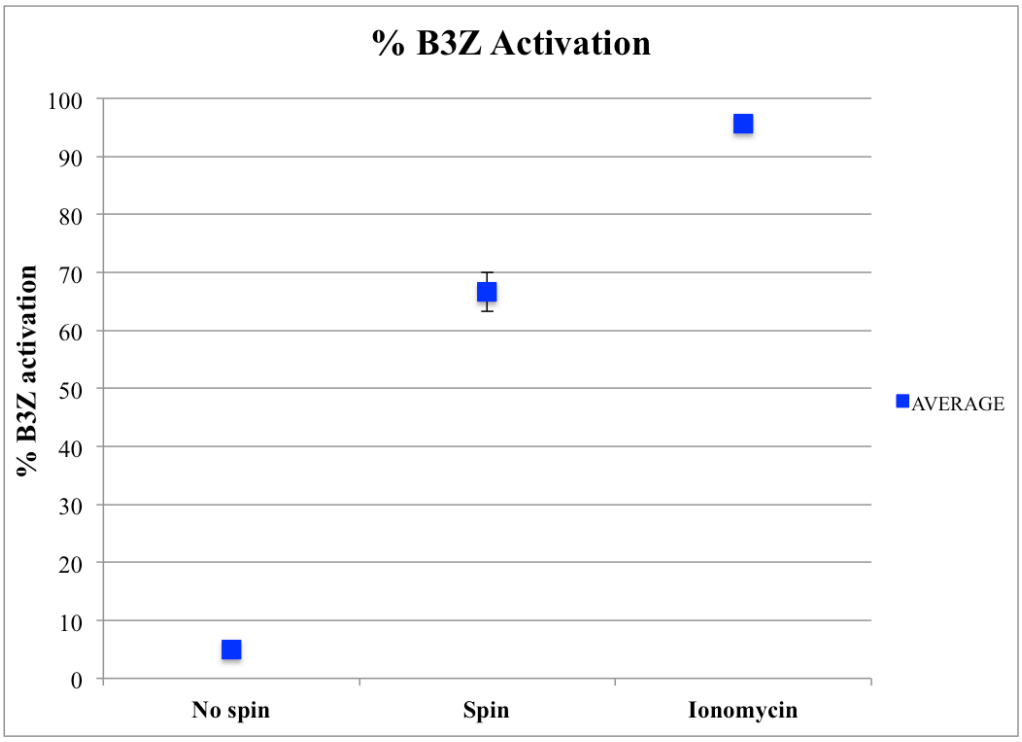

Figure 5-24: Average % B3Z activation from data shown in Figure 5-23. Error bars = SEM.

It can be seen from Figure 5-24 that there is an average of 67 % B3Z activation against K89 cells that have been pulsed with SIINFEKL. It should be noted that the ratio of APC to T lymphocyte is 10:1 in the flow cytometry experiments; if the ratio is 1:1 no Ca^{2+} increase is seen.

An advantage of microwell arrays, in comparison to flow cytometry, is the confinement of individual cells in wells. Each APC can be magnetically translated to cause cell-cell contact. In comparison, flow cytometry requires the use of a centrifuge to elicit activation through cell-cell contact. Even then cell contact is not guaranteed, highlighted by the 67% B3Z activation in Figure 5-24. Conversely for microwell arrays, the B3Z activation against APCs is 86%.

5.4 Conclusions

In conclusion, it has been shown that microwell arrays can be used to create a high-throughput, cell-cell interaction architecture that can cause T lymphocytes to be activated against APCs through the TCR:pMHC pathway. Now that cell-cell interaction has been observed, possible routes to remove cells of interest can be explored; discussed in Chapter 6.2.

Cell contact through magnetic translation of APCs was demonstrated, and the variation in Ca^{2+} flux after TCR:pMHC within a clone cell population has been shown. This data is unavailable through the state-of-the-art bulk single cell analysis technique, flow cytometry. Using microwell arrays, single cell-cell contact and subsequent T lymphocyte activation can be monitored with respect to time, for 1000s of cells in parallel.

In the future this architecture could be further developed to allow sequential cell-cell contact between a single T lymphocyte and multiple APCs, by sliding the T lymphocyte microwell array over different APC microwell arrays. By assessing the differences in T lymphocyte activation against different peptides, and in different sequences, interesting peptides or cells could be discovered and then extracted for further downstream analysis. Additionally, the impact of TCR:pMHC contact time could be investigated, to determine whether the period of contact impacts the level and duration of T lymphocyte activation.

Chapter 6: Conclusions and Future Recommendations

6.1 Conclusions

A detailed review of microfluidic device technologies was conducted in order to identify suitable techniques for single cell analysis. The SlipChip and Microwell array architectures were found to have the potential to implement controlled cell-cell interactions. Further investigations into these techniques were undertaken, specifically their application to temporal resolution of T lymphocyte activation. In addition, work was conducted into the use of serpentine cell traps; however the details of this particular investigation were outside the scope of this thesis.

After detailed analysis, it was concluded that the serpentine and SlipChip architectures were not suitable due to inherent issues that could not be overcome. For serpentines, this was the inability to remove cells after analysis, and that interaction times could not be measured. For SlipChip, the predominant issue was being able to construct a device for use with living cells, with non-permeable materials. This led on to investigations of different materials, but ultimately it was decided that the SlipChip was not an optimal solution due to the complications involved with cell seeding.

Microwell arrays were identified as the technology most suited to addressing the project objectives, and were discussed in detail in Chapter 4. Microwell array traps are able to divide cell colonies into single cells, separated by a defined distance according to the designed lithography mask. Multiple cells (thousands) can be trapped in a single microscope field of view. A bespoke alignment rig was designed which allows two microwell array plates to be precisely aligned, enabling cell-cell interactions to take place. The bottom cell plate is loaded with APCs, pre-incubated with magnetic nanoparticles, allowing the cells to be manipulated using a stationary magnet. The APCs are pulled into contact with T lymphocytes (loaded in the top plate) using a magnet.

T lymphocyte activation was assessed through calcium response and was visualised using the fluorophore Fluo-8AM. Findings showed significant variation in the activation of individual T lymphocytes within a clone cell population.

All the project objectives (Chapter 1.3) were fulfilled, as summarised below:

- **Single cell capture** – Single T lymphocytes and APCs have been captured in individual wells of a microwell array, through sedimentation and design of wells that are comparable to cell size.
- **Enable high-throughput data acquisition** – The pitch of well spacing within an array was designed to contain the maximum number of individually addressable wells within the microscope field of view. In this work, 4200 cell traps were designed into a 2 mm x 2 mm (W x W) field of view; an area observable by a 10x microscope objective.
- **Functionality to bring two cells into contact for a defined period of time, after which it is possible to dissociate them, allowing sequential contact** – Activation of single T lymphocytes against single APCs was observed using the microwell array architecture developed in this work. To dissociate the cells, the top plate can either be translated to the side, or removed altogether from the rig. Sequential contact would be possible if the array was moved and then aligned with a different APC section of the bottom plate array.
- **Allow recovery of specific cells** – After cell contact has occurred, the cells remain in their individually addressable wells. Hence, removal would be possible through one of the methods discussed in the following future work section; Chapter 6.2.
- **The device has to be optically transparent to permit observation of cell-cell interaction with microscopy** – The trapping material used was agarose, which is optically transparent, allowing cell activation to be observed in real time through a microscope.

6.2 Future Work

The following recommendations are made for additional work that could be undertaken to further the research conducted in this thesis:

- Rig improvements: In the future it is recommended that the alignment rig be augmented by the inclusion of motorised actuators, so that the user can control stage translation with improved precision. Additionally, to allow higher magnification images to be taken of the cells when they are trapped in

microwells, the height of the rig needs to be reduced so that it can fit underneath higher magnification objectives.

- Single cell extraction: Post-experiment extraction of cells from their microwells would allow downstream analysis of interesting cells to be undertaken. This would be possible through use of a micromanipulator, to 'push' the cell out of the well from underneath [68], or a micropipette to aspirate selected cells out of wells [69, 70].
- Multiple cell extraction: Large-scale removal of cells would be possible by extracting an area of agarose with a scalpel, and then submerging the microwell array in cell media. When microwell arrays are submerged in liquid, the docked cells drift out of the wells within a few minutes.
- Downstream analysis in-well: Agarose is typically used in gel electrophoresis; the size separation of DNA. As such, if the cells were lysed in-well, they could be gel electrophoresed, providing DNA for further analysis, as shown by Wood *et al* [63]. Another possibility is sodium dodecyl sulfate polyacrylamide gel electrophoresis (SDS-PAGE) with microwells, so that post-experiment, the protein components of the cells can be analysed [116, 117].

It is anticipated that the functionality provided by the device developed in this project will allow the identification of specific cells of interest that have noteworthy characteristics. This is expected to have multiple applications in biological studies, including immunology and pharmacology to better understand the variation in individual cell responses to stimulants. A key application of this could be investigation into immunodominance. The next logical step is downstream analysis of these cells to better understand the observed characteristics and their impact on cell functionality.

Appendix A: Experimental Protocols

A.1 Chapter 3 Protocols

A.1.1 Photolithography with SU-8

Clean glass or silicon wafer (substrate)

1. Submerge wafer in fuming nitric acid for 2 minutes.
2. Remove wafer from acid and transfer into a 10 L flask of De-ionised (DI) water to dilute any remaining acid on the wafer.
3. Transfer wafer into another 10 L flask of DI water.
4. Place wafer into cassette holder and run 'Quick, Dump, Rinse' cycle in fume hood.
5. Rinse surface of wafer with acetone, swapping tweezer position during this step to ensure the whole wafer is flushed with acetone.
6. Rinse surface of wafer with Isopropanol (IPA), swapping tweezer position during this step to ensure the whole wafer is flushed with IPA.
7. Repeat acetone and IPA wash.
8. Dry wafer with nitrogen.
9. Place wafer in 210°C oven to dehydrate for $12 \leq \text{hours} \leq 24$.

Fabrication of SU-8 structures

1. Remove wafer from 210°C oven.
2. Spin Ti prime -an adhesion promoter- using spin recipe shown in Table 3.

Speed / rpm	Acceleration / $rpm.s^{-1}$	Time / s
500	5000	5
3000	5000	30
500	500	5

Table 3: Ti prime spin recipe

3. Bake wafer at 120°C for 2 minutes.
4. Spin SU-8 using spin recipe detailed in Appendix A.3.
5. Soft bake using recipe given in Appendix A.3.
6. Expose to UV at $\lambda = 365$ nm (optimum for SU-8), dosage required is shown in Appendix A.3.

7. Post expose bake, recipe detailed in Appendix A.3.
8. Leave to cool (to reduce stress in SU-8) for 30 minutes at room temperature.
9. Develop in EC solvent for the time specified in Appendix A.3.
10. Submerge in IPA for 1 minute.
11. Nitrogen dry.
12. Check structure development with a microscope.
13. Hard bake at 150°C for 2 minutes.
14. Surface profile to check SU-8 structure height.

A.1.2 Trapping cells/beads in wells

1) Plasma expose the PMMA surface to make it hydrophilic (contact angle changed from 59° to 37°).
2) Add 50 µL of beads at 0.13% (mass/volume) in PBS, put plate on shaker for 5 minutes.
3) Remove excess beads/liquid by wicking away with tissue.
4) Add 50 µL DI water to wash away any remaining beads.
5) Wick away DI water.
6) View with microscope.

A.2 Chapter 4 Protocols

A.2.1 Cell seeding

The following details the generic loading protocol used; however, incubation times and seeding amounts may differ depending on cell type.

1. Prior to loading, the cells are firstly passaged using Ethylenediaminetetraacetic acid (EDTA, an anti-coagulator), to prevent cell aggregation and to remove adherent cells from their container. Around 100,000 cells are re-plated to continue the cell line.
2. Passaged cells are passed through a 20 μm cell filter to remove any cell clusters or unusually large cells.
3. The cells are counted and suspended at the concentration which results in a redundancy of 10:1 (cells : available wells) and at the minimum volume that will allow the cell suspension to entirely cover the microwell array. For example, for a 20 mm x 20 mm (W x W) area of agarose, there are 20 cell arrays.

⇒ 20 arrays = 20 x 4200 = 84,000 wells.

⇒ 10:1 (cells:wells) = 840,000 cells.

⇒ To cover a 20 mm x 20 mm (W x W) area of agarose requires a minimum of 150 μL of cell suspension.

⇒ Therefore, cell concentration = 8.4×10^5 cells in 150 μL = 5.6×10^6 cells/mL.

4. The cell suspension is deposited on the surface of the agarose microwell arrays, taking care to ensure that the liquid does not spill over the sides of the agarose (otherwise the cells will move towards the edge of the liquid and not settle in the wells).
5. The agarose microwell array with cell suspension is placed in a 37°C incubator for a duration of $20 \leq$ minutes ≤ 40 to allow the cells to sediment into the wells.
6. The surface of the microwell array is rinsed with PBS from the side (not directly on the array) to remove excess cells.
7. The process may be repeated if necessary.

A.2.2 Fluo-8AM cell staining

The following protocol details how Fluo-8AM is loaded into the B3Z T lymphocytes prior to stimulation.

1. The suspension B3Z cells are removed from the flask and re-suspended at a concentration of $1x10^6$ cells/mL. 10 mL of fresh cell media (RPMI 1640) is added to the remaining B3Z cells that are partially attached to the bottom of the flask, and the flask is returned to the 37°C incubator to continue the culture.
2. 1 mL of cells are transferred to a light resistant Falcon tube and Fluo-8AM is added to the cells at a final concentration of 5 μM.
3. The Falcon is placed in a 37°C incubator for 30 minutes.
4. The Falcon is transferred to room temperature and incubated for 30 minutes.
5. 4 mL of fresh cell media is added to the cells, to increase the volume to 5 mL.
6. The cells are washed by centrifuging the Falcon at 1200 rpm for 5 minutes to pellet the cells, removing the supernatant and re-suspending the cells in 5 mL of fresh media.
7. Step 6 is repeated three times.
8. The cells are re-suspended at the desired concentration for stimulation.

A.2.3 Ionomycin stimulation protocol

The following protocol details the standard procedure for stimulating B3Z T lymphocytes with ionomycin.

1. B3Z cells that have been loaded with Fluo-8AM (see Appendix A.2.2) are re-suspended in 4 mL, so that 200 μL contains $5x10^5$ cells.
2. B3Z cells are loaded onto the flow cytometer (BD LSRFortessa™) and run for 30 seconds (to determine basal fluorescence).
3. Ionomycin is added to the cells at a final concentration of 2 μM (DMSO concentration of no more than 1%).
4. The cells are immediately run on the cytometer for approximately 2 minutes.

It should be noted that ionomycin stimulation of B3Z T lymphocytes occurs rapidly, so care should be taken to add the stimulant and return the tube to the cytometer to record the stimulation profile as fast as possible (within 5 seconds), so that the stimulation profile can be viewed.

A.2.4 Anti-CD3 stimulation protocol

1. B3Z cells that have been loaded with Fluo-8AM (see Appendix A.2.2) are re-suspended in 4 mL, so that 200 μL contains $5x10^5$ cells.
2. B3Z cells are loaded onto the flow cytometer (BD LSRFortessa™) and run for 30 seconds (to determine basal fluorescence).
3. Anti-CD3e (clone 500A2) -available from BD Pharmingen™- is added to the cells at a final concentration of 20 μg/mL.
4. The cells are immediately run on the cytometer for approximately 2 minutes.

Note: Anti-CD3 stimulation occurs more slowly than ionomycin stimulation.

A.2.5 Stimulating cells and viewing their activation on the DV

The protocol for stimulating cells and viewing their activation using the DV is detailed below:

1. B3Z cells that have been loaded with Fluo-8AM (see Appendix A.2.2) are re-suspended to a concentration of 10:1 (cells:wells), discussed in Appendix A.2.1.
2. Steps 4, 5 and 6 from the microwell array loading protocol detailed in Appendix A.2.1 are undertaken to seed cells in the microwells. The agarose section that is seeded has a volume of 35 mm x 35 mm x 2 mm (W x W x H).
3. The agarose section is placed inside a 55 mm petri dish fitted with the custom-designed holder, shown in Figure 4-18.
4. The entire assembly is slotted into the custom-made stage attachment shown in Figure 4-18, and then secured over the objective using the spring clamp on the DV.
5. The microwells are focussed on, and a time-series of images (in the FITC channel) is taken. 1 frame per second, for a duration of 2 minutes.
6. 10 μL of stimulant is added directly onto the microarray after the first two images of the times series have been acquired, to induce activation.
7. 50 μL of PBS is deposited on the microarray and subsequently aspirated off, to rinse away stimulant.
8. 50 μL of cell media is added to the microarray, to allow Ca^{2+} stores to replenish.
9. After a minimum of 30 minutes, steps 5 and 6 are repeated for the second stimulant.

A.3 SU-8 spin recipes

Feature depth / µm	Ti Prime spin recipe / rpm , $rpm.s^{-1}$, s	Bake / min , °C	SU8-3025 spin recipe / rpm , $rpm.s^{-1}$, s	Soft bake / min , °C	UV expose / $mJ.cm^{-2}$	Post bake / min , °C	Develop / min	IPA / min	Hard bake / min , °C
20	500 5000 5 3000 5000 30 500 500 5	2 , 120	500 500 5 3100 300 30 500 500 5	10 , 95	200	1 , 65 4 , 95	3	1	2 , 150
25	500 5000 5 3000 5000 30 500 500 5	2 , 120	500 500 5 2500 300 30 500 500 5	10 , 95	200	1 , 65 4 , 95	3	1	2 , 150
30	500 5000 5 3000 5000 30 500 500 5	2 , 120	500 500 5 2100 300 30 500 500 5	10 , 95	200	1 , 65 4 , 95	3	1	2 , 150

Appendix B: MATLAB Cell Analysis

B.1 Overview

A bespoke computer program was developed as part of this work for the analysis of fluorescent time series data. The numerical computation software package MATLAB was used as the basis for the program, as it is well suited for image analysis and the processing of large data sets.

For analysis of this work, the program requirements were as follows:

- Read and process fluorescent time series data contained within multi-image TIFF stacks.
- Track fluorescent intensity of individual cells and provide quantitative response data separately for each.
- Analyse cell responses from double stimulation experiments using two independent data sources.
- Identify and separate responses from dead/alive and unresponsive/responsive cells based on fluorescent intensity.
- Plot absolute and normalised responses for the entire cell population.
- Select specific cells of interest, plot corresponding responses and identify cell locations on bright-field image.

A flowchart describing the main program sequence and operation is given in Figure B-1. The program is divided into the following key stages:

1. Load first fluorescent image stack.
2. Load first bright-field image and select cells / regions of interest (ROIs).
3. Run first analysis algorithm.
4. Load second fluorescent image stack and bright-field image.
5. Run second analysis algorithm.
6. Plot results.
7. View individual cells of interest.

Details of each stage, including program screen-shots, are presented in the following section.

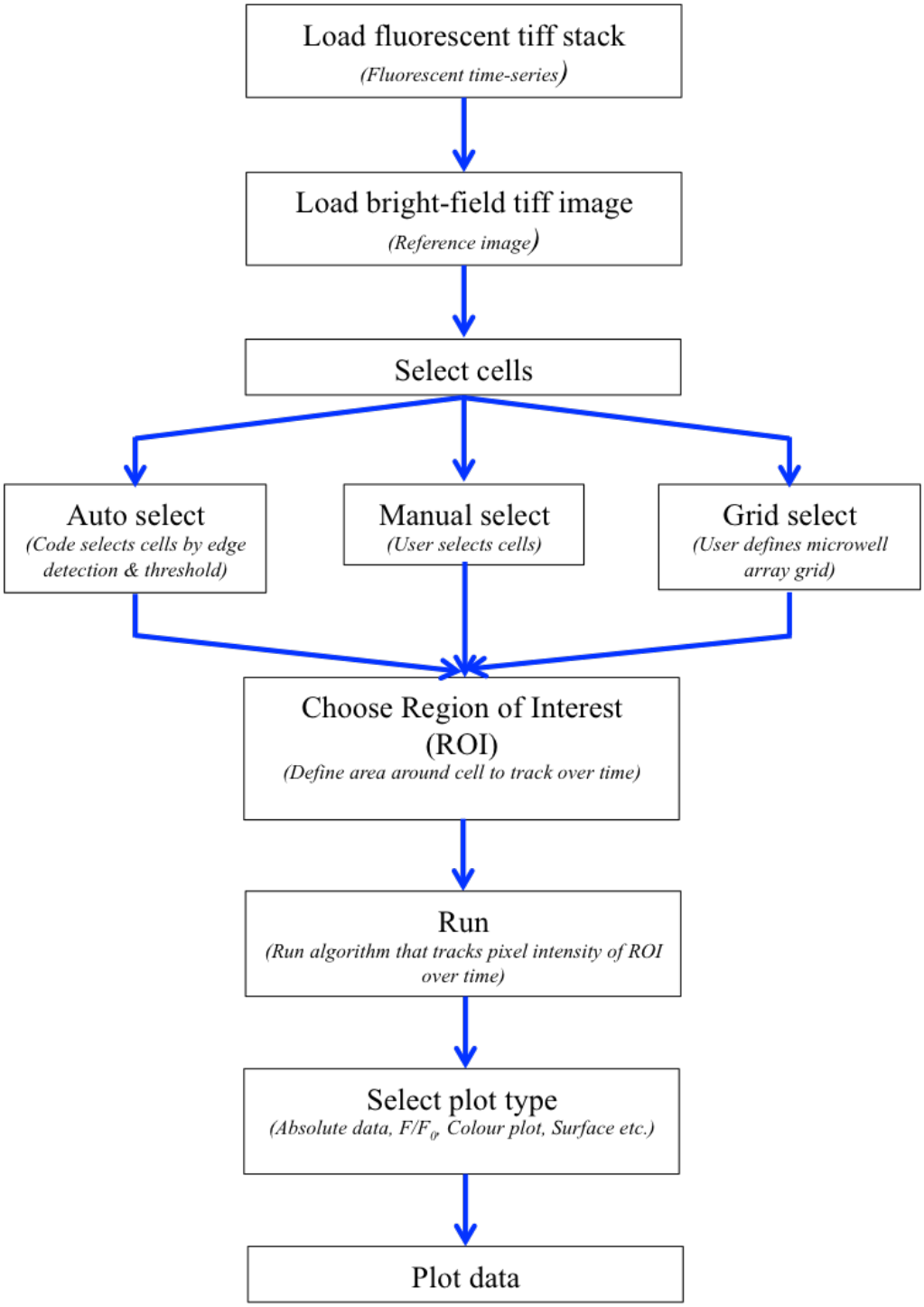

Figure B-1: Flowchart showing overview of main MATLAB program sequence.

B.2 Program Operation

On launch of the program, the main menu is displayed (Figure B-2). From here, all features of the program can be accessed.

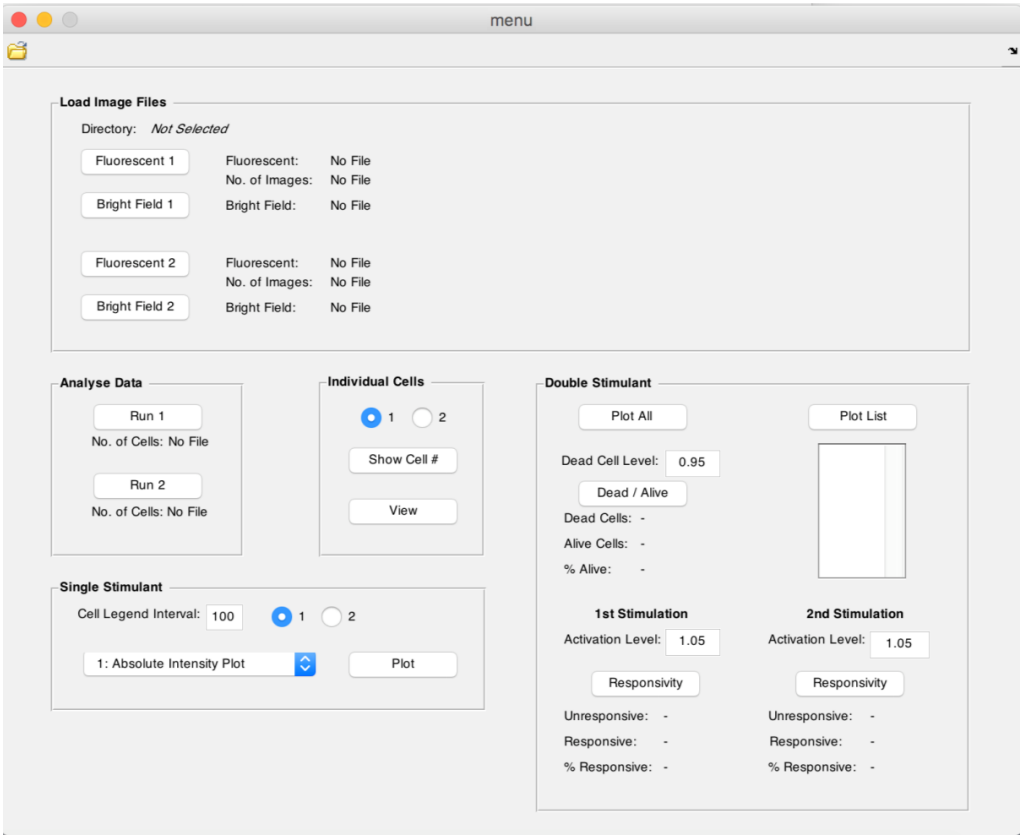

Figure B-2: MATLAB program – Main menu.

Stage 1: Load first fluorescent image stack

From the main menu (Figure B-2), the directory containing the fluorescent and bright-field images is set by clicking the 'open folder' icon at the top-left of the window. The button labelled 'Fluorescent 1' is then selected from the 'Load Image Files' panel; this opens a new window shown in Figure B-3.

The first fluorescent TIFF image stack is loaded by clicking the 'open file' icon at the top-left of the window. Once loaded, the first image of the stack will be displayed. The slider beneath the image can then be used to select and view the different images/frames within the file, as shown in Figure B-4.

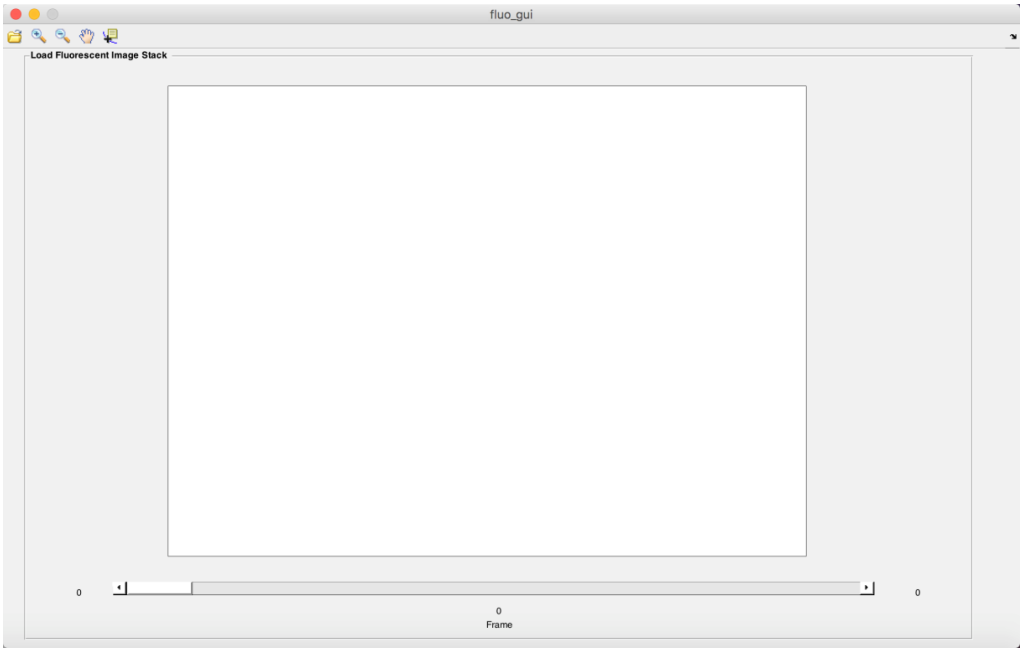

Figure B-3: MATLAB program – Blank fluorescent image window.

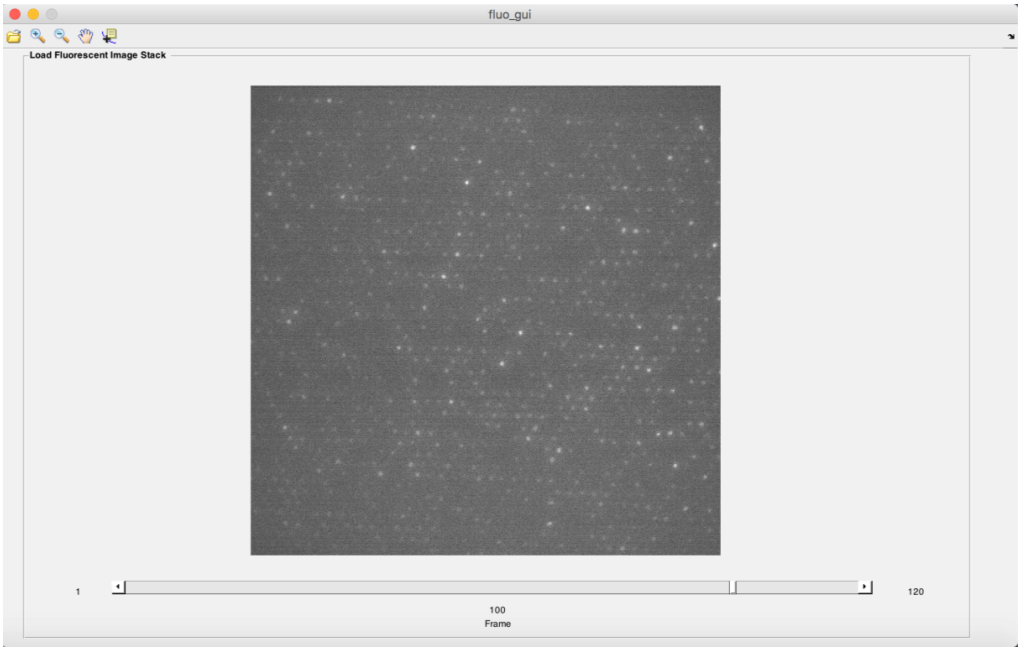

Figure B-4: MATLAB program – Loaded fluorescent image window.

Stage 2: Load first bright-field image and select cells / ROIs

Returning to the main menu, the button labelled 'Bright Field 1' is then selected from the 'Load Image Files' panel; this opens a new window shown in Figure B-5.

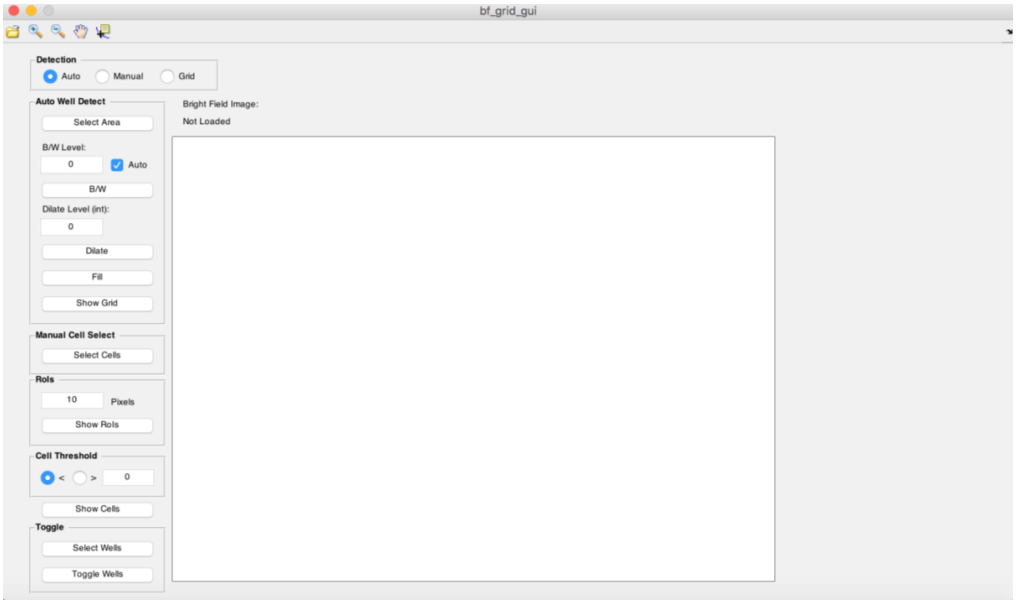

Figure B-5: MATLAB program – Blank first bright-field image window.

The bright-field image corresponding to the fluorescent image stack is loaded by clicking the 'open file' icon at the top-left of the window. Once loaded, the required method of cell selection is chosen, i.e. 'Auto', 'Manual', or 'Grid'. The three different selection methods are described below.

Auto

Automatic (Auto) cell selection determines the location of cells in the bright-field image using a series of functions included within the MATLAB Image Processing Toolbox; this method requires minimal input from the user.

Firstly, the 'Select Area' button on the 'Auto Well Detect' panel adds a selection rectangle to the bright-field image, as shown in Figure B-6. This rectangle can be moved and re-sized to define a specific area of the image to analyse.

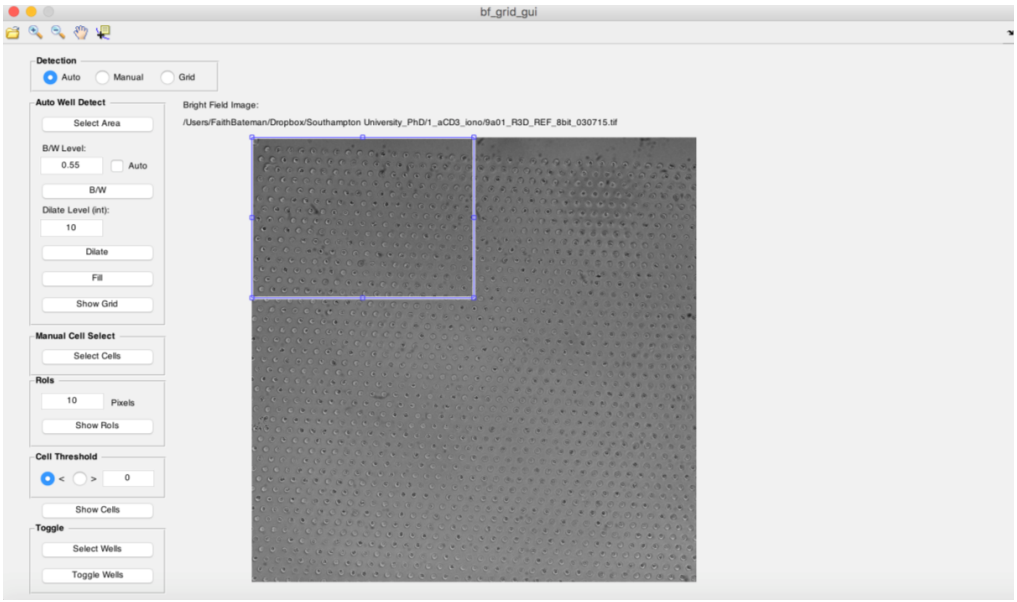

Figure B-6: MATLAB program – Bright-field image area selection.

The ‘B/W’ button converts the selected image area from greyscale to binary (black and white) using the MATLAB ‘im2bw’ function with the defined ‘B/W Level’ threshold, as shown in Figure B-7. Selecting the ‘Auto’ checkbox will compute the threshold automatically using the MATLAB ‘graythresh’ function; otherwise, a value between 0 and 1 may be input manually.

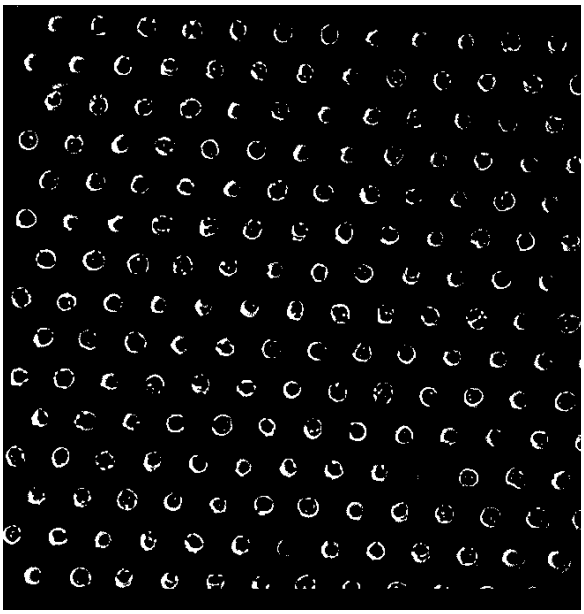

Figure B-7: MATLAB program – Bright-field image binary conversion.

The ‘Dilate’ button uses the MATLAB ‘imdilate’ function with the integer ‘Dilate Level’ to increase the size of the white areas in the image, making the well edges more prominent. This effect can be seen in Figure B-8 (a). The ‘Fill’ button uses the MATLAB ‘imfill’ function to fill regions/holes in the image with white. This process converts any completely closed well edges from rings to solid white shapes, as shown in Figure B-8 (b).

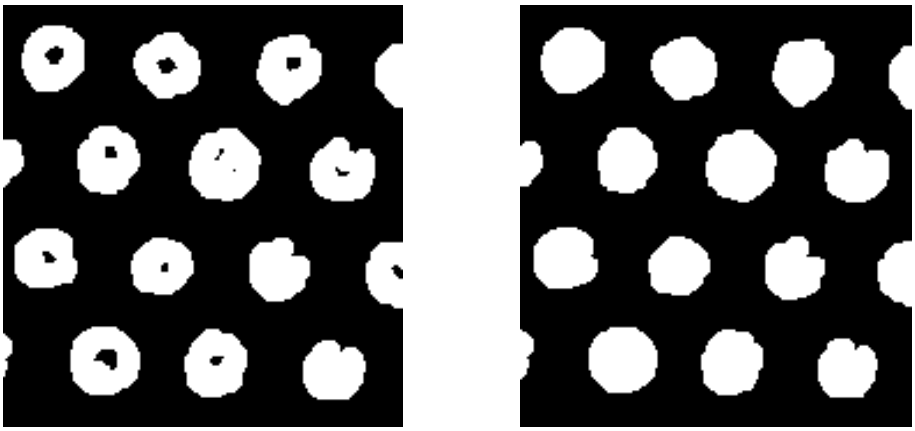

(a) (b)

Figure B-8: MATLAB program – Bright-field image dilation/fill examples.

Finally, the ‘Show Grid’ button uses the MATLAB ‘regionprops’ function to calculate the centroids (centre points) of all objects in the image, thereby giving the X:Y co-ordinates for each well centre. The calculated centre points (blue dots) are plotted over the bright-field image, as in Figure B-9.

Any wells missed by the automatic detection routine may be added manually using the ‘Select Cells’ button in the ‘Manual Cell Select’ panel. This adds a mouse cursor to the image, which is used to select missed wells and add them to the grid, as depicted in Figure B-10 and Figure B-11.

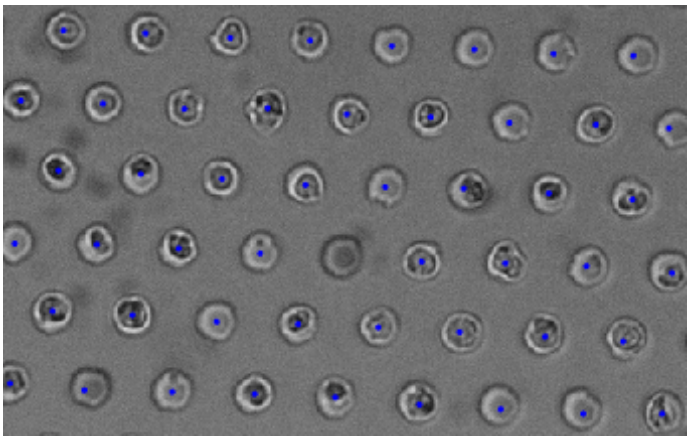

Figure B-9: MATLAB program – Bright-field image centre-points grid.

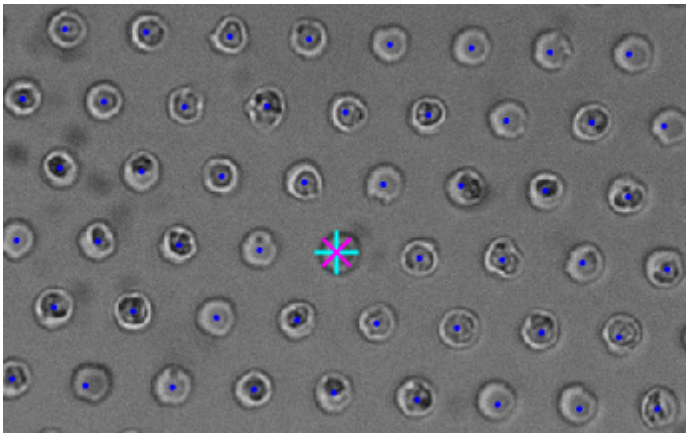

Figure B-10: MATLAB program – Bright-field image well selection.

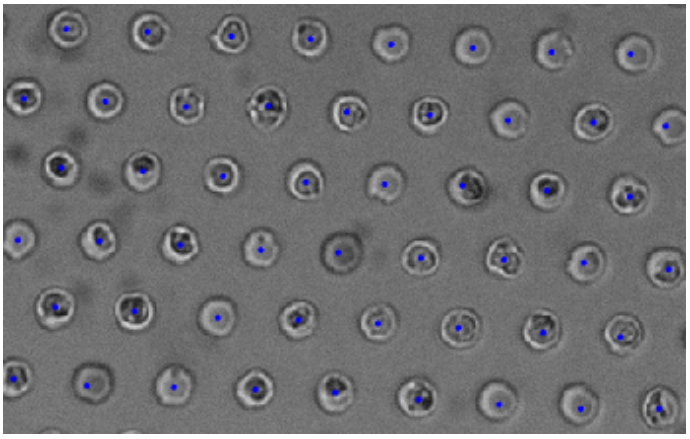

Figure B-11: MATLAB program – Bright-field image well added.

A square ROI is created around each well using the ‘Show ROI’ button in the ‘ROIs’ panel. The size of the ROI is defined in terms of pixels. Areas outside the ROIs are removed from the image, as shown in Figure B-12.

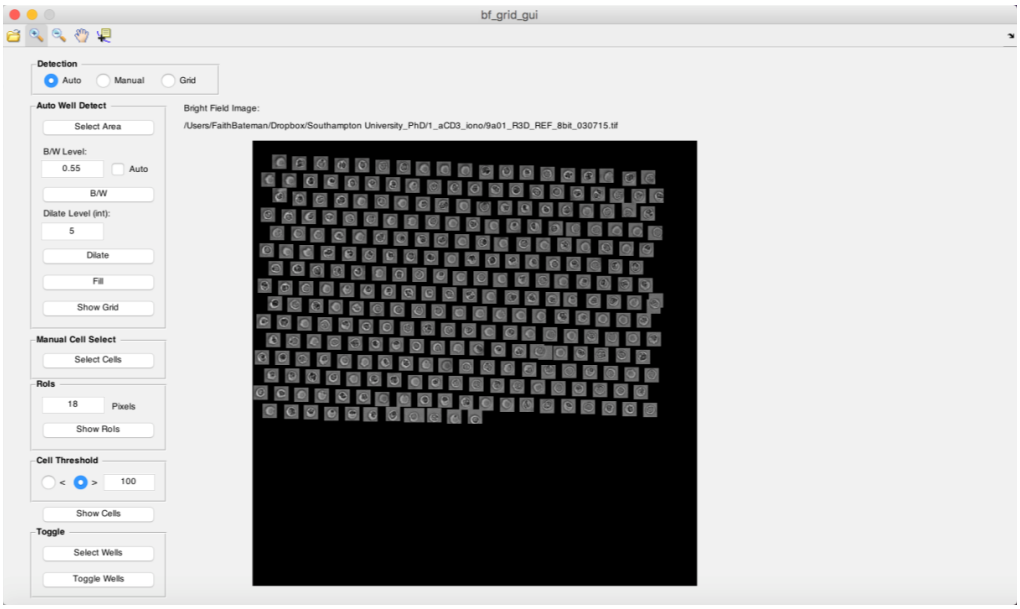

Figure B-12: MATLAB program – Bright-field ROIs.

Using the ‘Show Cells’ button, wells containing cells are detected based on the pixel intensity sum of each ROI. Depending on the defined ‘Cell Threshold’ (< / >), ROIs are marked as containing a cell (green dot), or empty (red cross), as shown in Figure B-13.

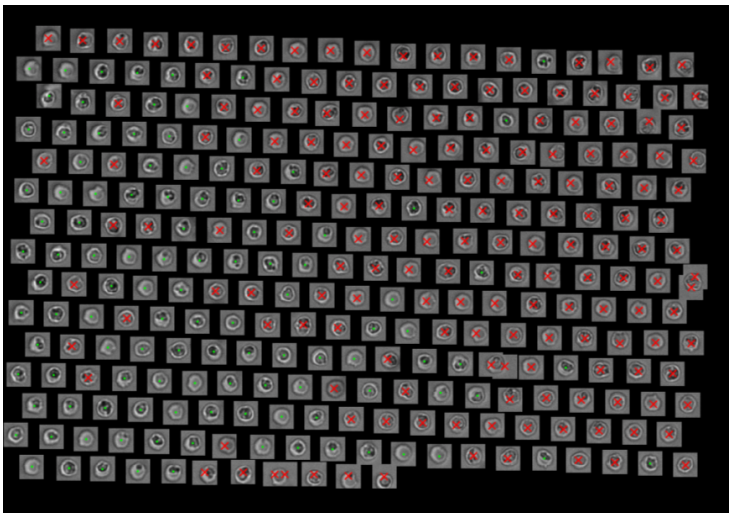

Figure B-13: MATLAB program – Cell threshold detection.

As can be seen in Figure B-13, using this simple threshold technique does not always identify 100% of cells correctly. In such cases, the marked state of a particular well may be manually toggled from 'empty' to 'cell-containing' (or vice-versa), using the 'Select/Toggle Wells' buttons in the 'Toggle' panel. The toggled well states are shown in Figure B-14.

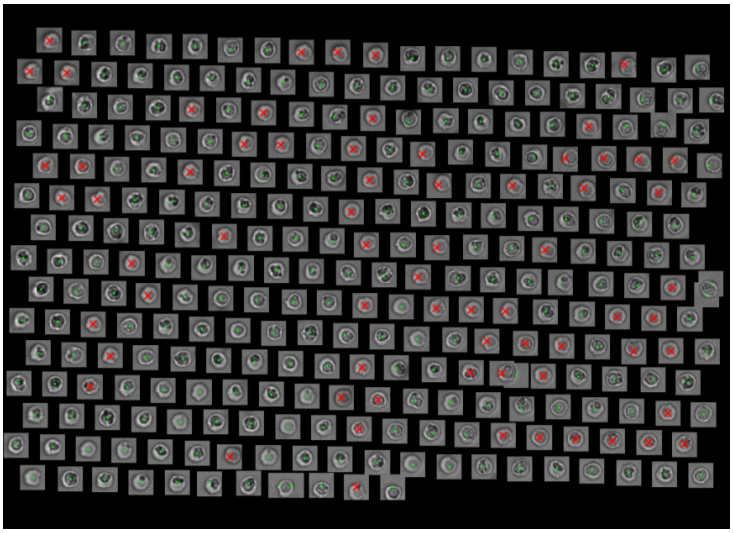

Figure B-14: MATLAB program – Toggled wells.

Manual

Manual cell selection determines the location of cells in the bright-field image entirely through input from the user. This cell selection technique is relatively time-consuming; nevertheless, it is the most reliable method for ensuring 100% of cells are selected correctly. For this reason, the manual cell selection method is used for all data analysis in this thesis.

Firstly, 'Manual' is selected from the 'Detection' panel. This changes the bright-field image window to appear as in Figure B-15. The 'Select Cells' button in the 'Manual Cell Select' panel adds a mouse cursor to the image, which is used to select the cells for analysis.

Square ROIs are then created around each well using the 'Show ROI' button in the 'ROIs' panel, as in the automatic detection method. The size of the ROI is defined in terms of pixels. Areas outside the ROIs are removed from the image, as shown in Figure B-16.

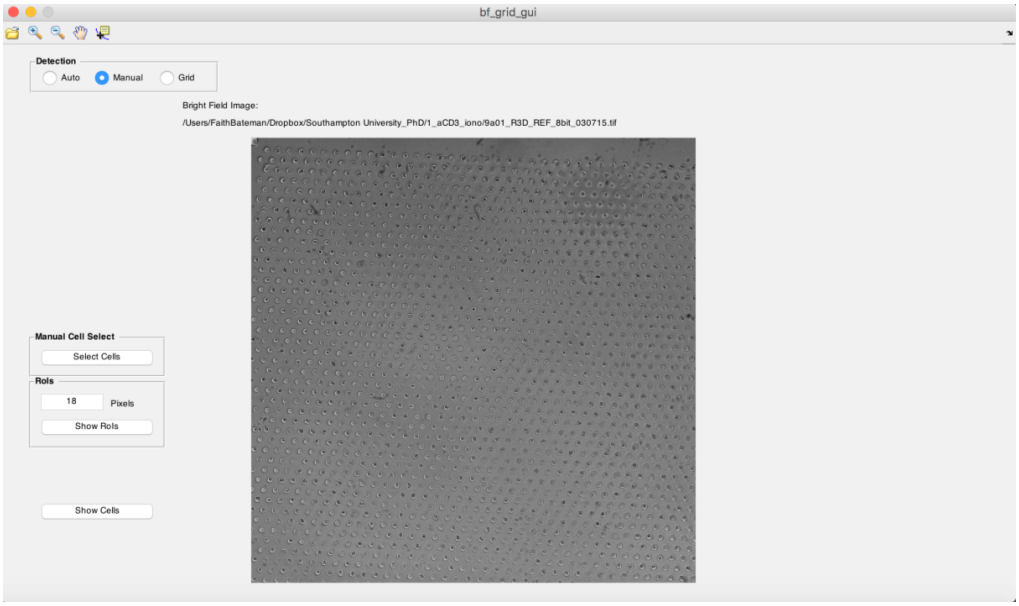

Figure B-15: MATLAB program – Manual bright-field window.

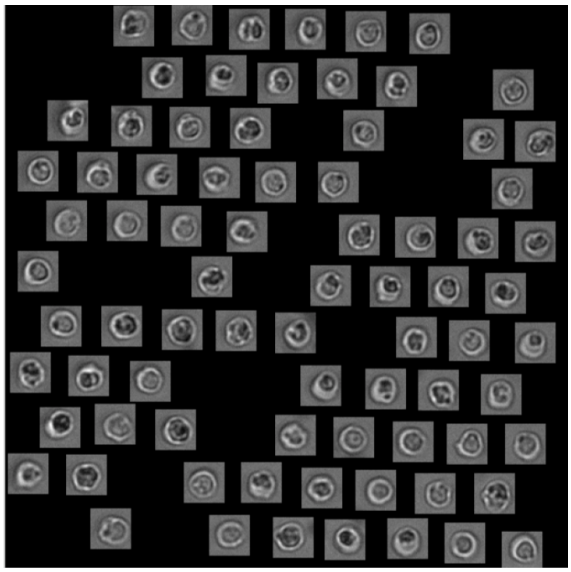

Figure B-16: MATLAB program – Manual ROI selection.

Finally, the 'Show Cells' button marks all the wells as containing a cell (green dot), and stores the ROIs ready for analysis.

Grid

Grid selection determines the location of wells in the bright-field image by over-laying a uniform grid defined by the user. Once the grid has been aligned correctly with the wells,

ROI and cell selection is performed in the same manner as the automatic detection method previously described.

Firstly, 'Grid' is selected from the 'Detection' panel. This changes the bright-field image window to appear as in Figure B-17.

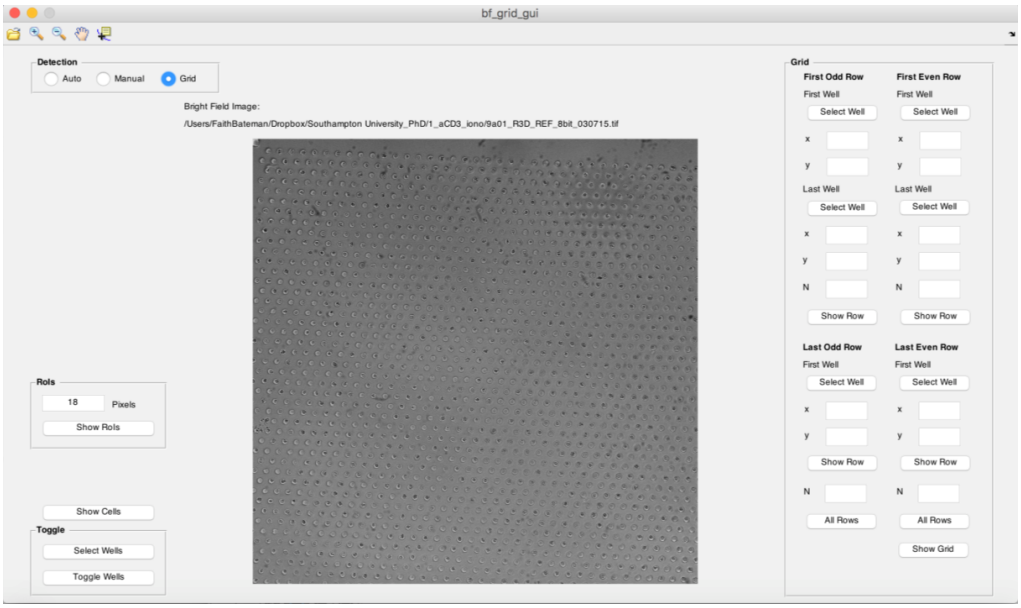

Figure B-17: MATLAB program – Grid selection window.

Definition of the uniform grid is performed in two stages: 1) odd rows, and 2) even rows. Firstly, the odd rows are defined by selecting the first and last wells in the top odd-numbered row using the corresponding 'Select Well' buttons in the 'Grid' panel. The X:Y co-ordinates of these wells are stored.

The number of wells in the top odd row is entered in the corresponding box 'N' and the 'Show Row' button is selected. Co-ordinates of evenly distributed intermediate wells are calculated and displayed on the bright-field image. The defined top odd row (blue dots) is shown in Figure B-18.

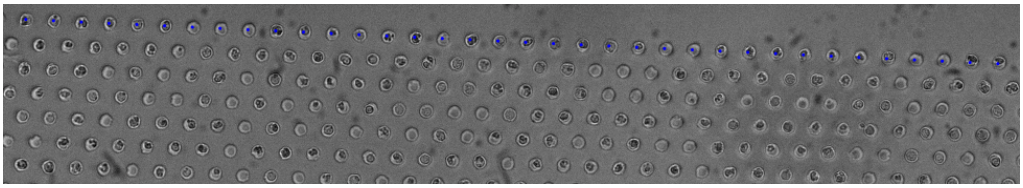

Figure B-18: MATLAB program – First odd row.

Next, the first well in the bottom odd-numbered row is selected using the corresponding 'Select Well' button and the X:Y co-ordinates of this well are stored. The 'Show Row' button is selected. Co-ordinates of wells at the same pitch as the top odd row are calculated and displayed on the bright-field image. The defined bottom odd row (blue dots) is shown in Figure B-19.

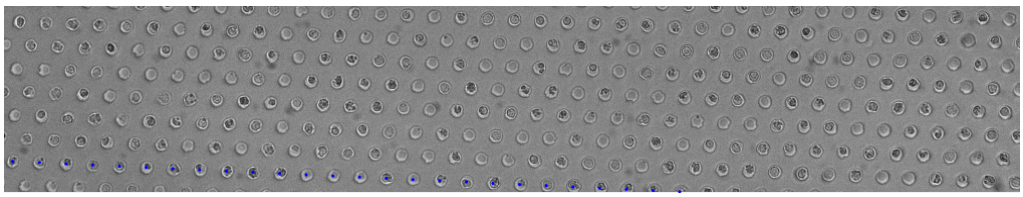

Figure B-19: MATLAB program – Last odd row.

The total number of odd rows is entered in the corresponding box 'N' and the 'All Rows' button is selected. Co-ordinates of evenly distributed intermediate rows are calculated and displayed on the bright-field image. A selection of the defined odds row (blue dots) is shown in Figure B-20.

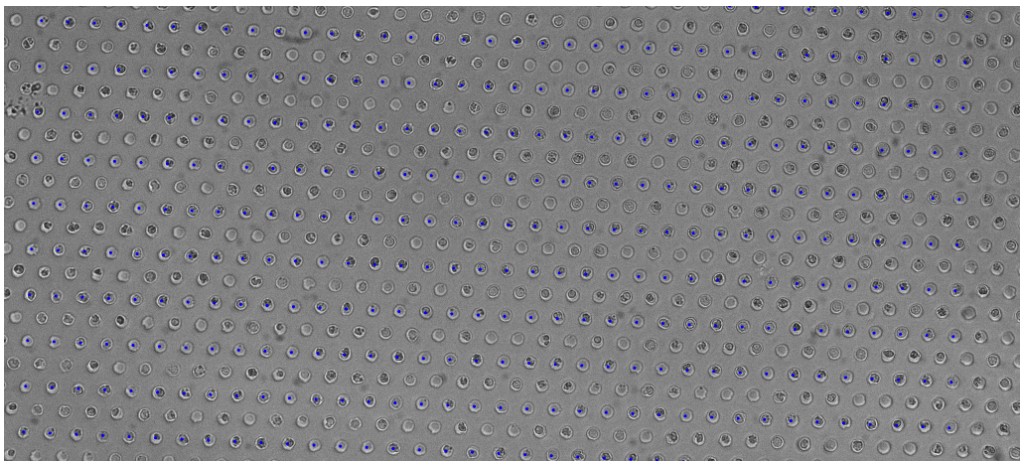

Figure B-20: MATLAB program – Odd rows.

The procedure is then repeated for the even-numbered rows. Once complete, the 'Show Grid' button is selected to display the defined grid on the bright-field image. Square ROIs are then created around each well using the 'Show ROI' button in the 'ROIs' panel, as in the previous methods. The size of the ROI is defined in terms of pixels. Areas outside the ROIs are removed from the image, as shown in Figure B-21.

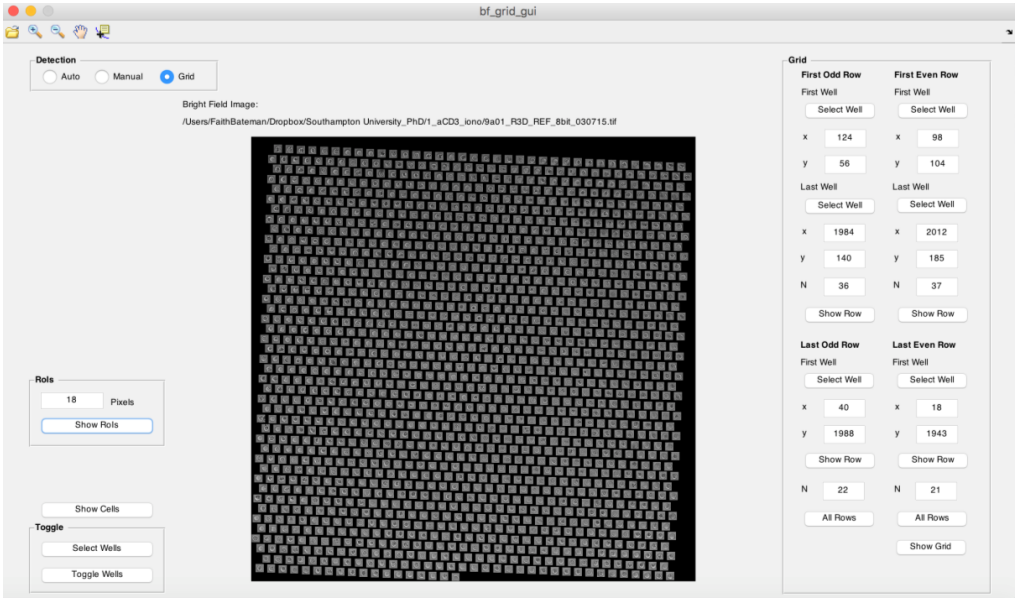

Figure B-21: MATLAB program – Defined grid.

In this mode, the 'Show Cells' button marks all the wells as cells. The user must then manually switch empty wells using the 'Select/Toggle Wells' buttons, as described in the previous methods.

Stage 3: Run first analysis algorithm

Once cell ROIs have been defined using the bright-field image, intensity analysis of the fluorescent time-series is performed.

The first fluorescent image is loaded from the TIFF stack using 8-bit grey-scale format (0-255, per pixel). For each cell defined in the bright-field image, the corresponding ROI pixels are selected in the fluorescent image. The sum of the pixel intensities is calculated and divided by the ROI area to obtain a mean fluorescent intensity (MFI) for the cell. For example, if the defined ROI area is 20 x 20 pixels, the intensity (0-255) of each pixel added to a cumulative sum, and then divided by 400.

The process is repeated for each frame contained within the fluorescent image stack to obtain a MFI time-series for each individual cell. This 'absolute' data is normalised with respect the first fluorescent image frame, such that the initial MFI for each cell is unity. This normalised data is referred to as 'F/F_0' and is used to analyse the cell responses.

Stage 4: Load second fluorescent image stack and bright-field image

For double stimulation experiments, two fluorescent time-series and two bright-field images are taken, one for each stimulant.

Firstly, the second fluorescent image stack is loaded by selecting the 'Fluorescent 2' button from the 'Load Image Files' panel on the main menu; this opens a new window, as in Stage 1 (Figure B-3). The TIFF image stack is loaded by clicking the 'open file' icon at the top-left of the window. Once loaded, the first image of the stack will be displayed. The slider beneath the image can then be used to select and view the different images/frames within the file, as in Stage 1 (Figure B-4).

Returning to the main menu, the button labelled 'Bright Field 2' is then selected from the 'Load Image Files' panel; this opens a new window shown in Figure B-22. The bright-field image corresponding to the second fluorescent image stack is loaded by clicking the 'open file' icon at the top-left of the window.

Once loaded, the cell locations previously defined in Stage 2 are overlaid on the image by selecting the 'Show BF 1 Grid' button. In most cases, the position of the device differs slightly between the first and second stimulations, as shown in Figure B-23 (a); therefore it is necessary to re-align the cell grid accordingly. Appropriate 'X' and 'Y' pixel shifts are set, and the 'Adjust' button is selected to show the re-positioned grid, as in Figure B-23 (b). The 'Show ROIs' button is used to display the defined ROIs on the image, as shown in Figure B-23 (c).

Any cells that are no longer present may be removed using the 'Select/Remove Cells' buttons; these cells will not be analysed. The displayed 'Total Cells' number will update accordingly.

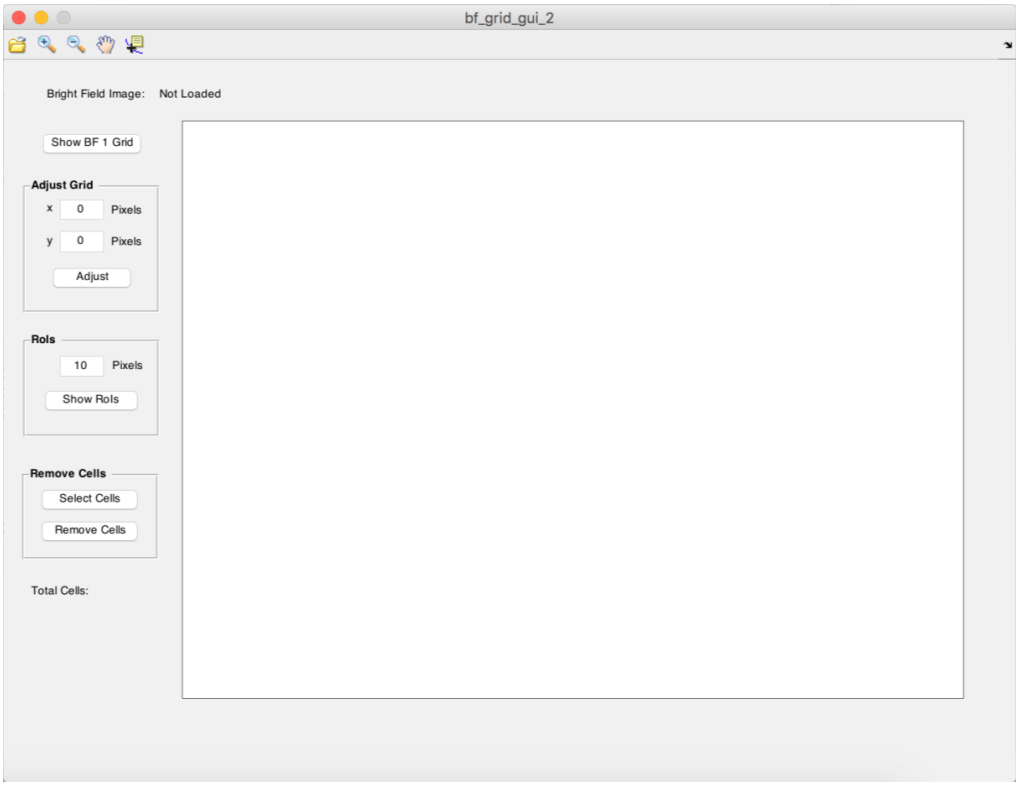

Figure B-22: MATLAB program – Blank second bright-field image window.

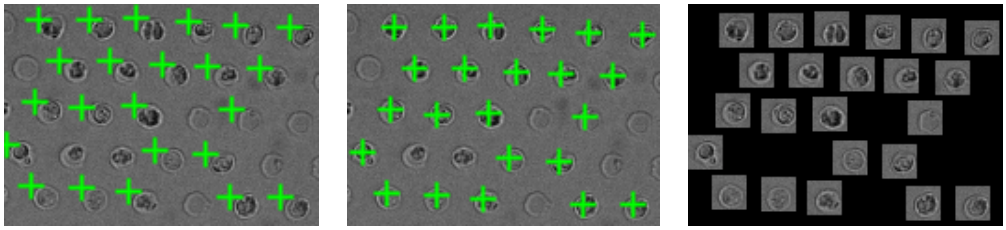

(a) (b) (c)

Figure B-23: MATLAB program – Second cell grid alignment and ROIs.

Stage 5: Run second analysis algorithm

Once cell ROIs have been defined, intensity analysis of the second fluorescent time-series is performed, using the same method as the first.

Stage 6: Plot results

From the 'Single Stimulant' panel on the main menu, MFI data for all cells from either time-series may be plotted. The first or second time-series is selected using buttons '1' and '2', and the required data plot is selected from the drop-down list. A 'Cell Legend

Interval' is defined to control the number of cells appearing in the plot legend, e.g. '100' creates legend entries for every 100th cell.

The 'Double Stimulant' panel allows combined MFI data from the two time-series to be plotted. Firstly, a minimum MFI threshold is defined to identify any dead cells. If at any point during the first time-series, the normalised MFI of a cell is beneath the minimum level, the cell is marked as dead. Plots and statistics are displayed for the separated alive and dead cells.

For the living cells, those that are responsive and unresponsive are then identified. For each time-series, activation MFI thresholds are defined. If at any point during the time-series, the normalised MFI of a cell exceeds the activation level, the cell is marked as responsive. Plots and statistics are displayed for the separated responsive and unresponsive cells.

Any cells of particular interest can be isolated and plotted separately. Once identified, cell numbers are entered in the plot list, and a plot type is chosen. Selecting the 'Plot List' button displays the plot showing only the cells of interest. A selection of different plots are shown in Figure B-24 to Figure B-27.

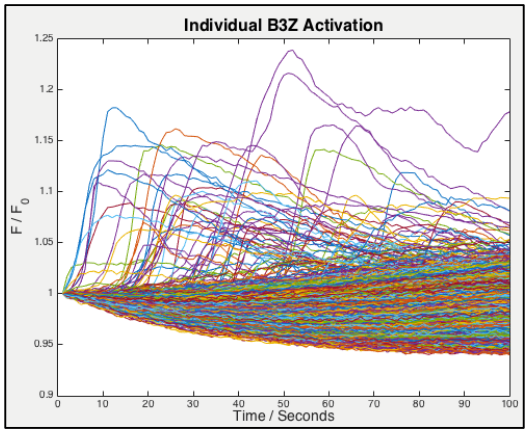

Figure B-24: MATLAB program – Normalised plot, all cells.

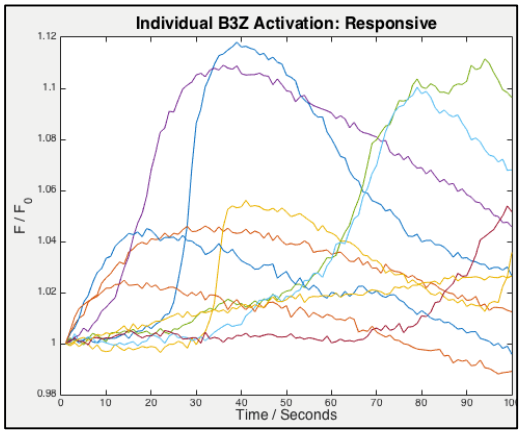

Figure B-25: MATLAB program – Normalised plot, responsive cells.

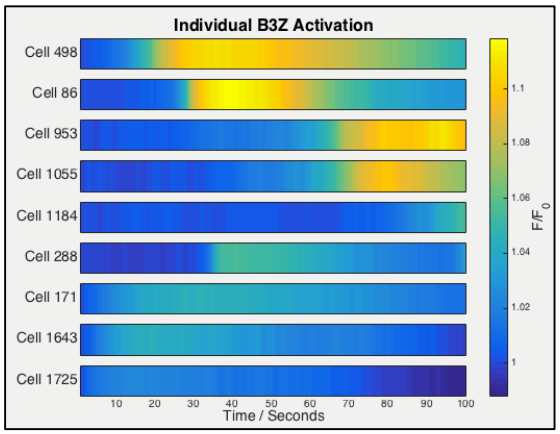

Figure B-26: MATLAB program – Normalised P-colour plot.

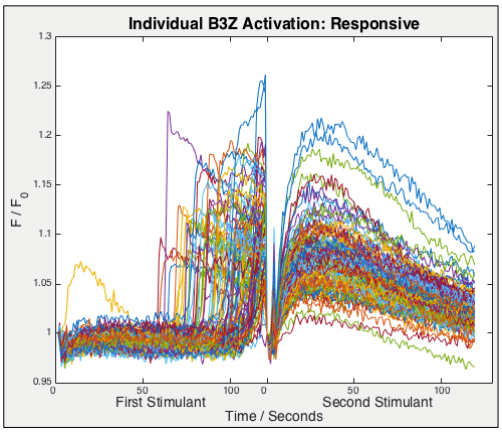

Figure B-27: MATLAB program – Double stimulation plot.

Stage 7: View individual cells of interest

The final feature of the MATLAB program allows the user to view individual cells of interest. Firstly, the number of the cell to be viewed is determined, either by selecting a specific response line within a plot window, or using the 'Show Cell #' window displayed in Figure B-28.

Once the cell number has been identified, the 'View' button within the 'Individual Cells' panel on the main menu (Figure B-2) is selected. This opens the single cell window, as shown in Figure B-29.

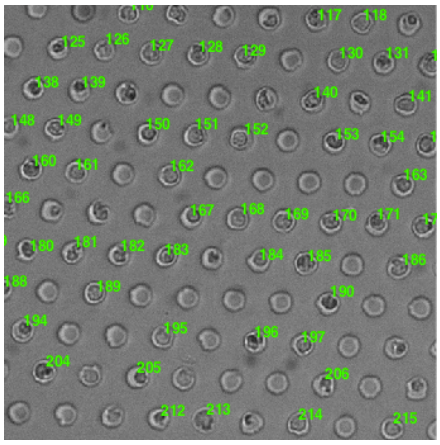

Figure B-28: MATLAB program – Cell numbers.

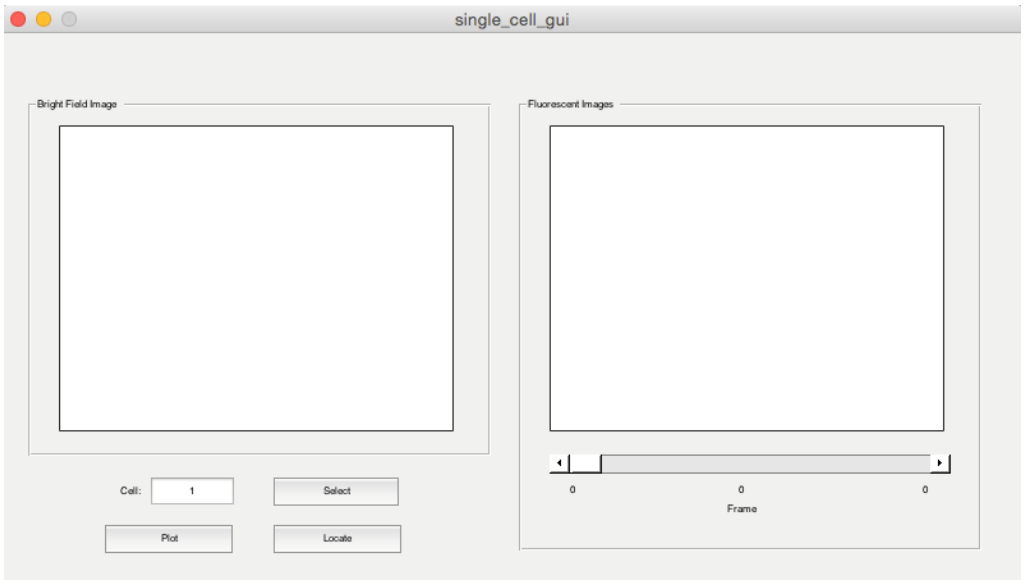

Figure B-29: MATLAB program – Single cell window.

From within the single cell window, the number of the cell of interest is entered, e.g. 94. Pressing the 'Select' button loads the bright-field and fluorescent images for the region of the chosen cell, as shown in Figure B-30. Individual frames of the fluorescent image stack are viewed by adjusting the horizontal slider.

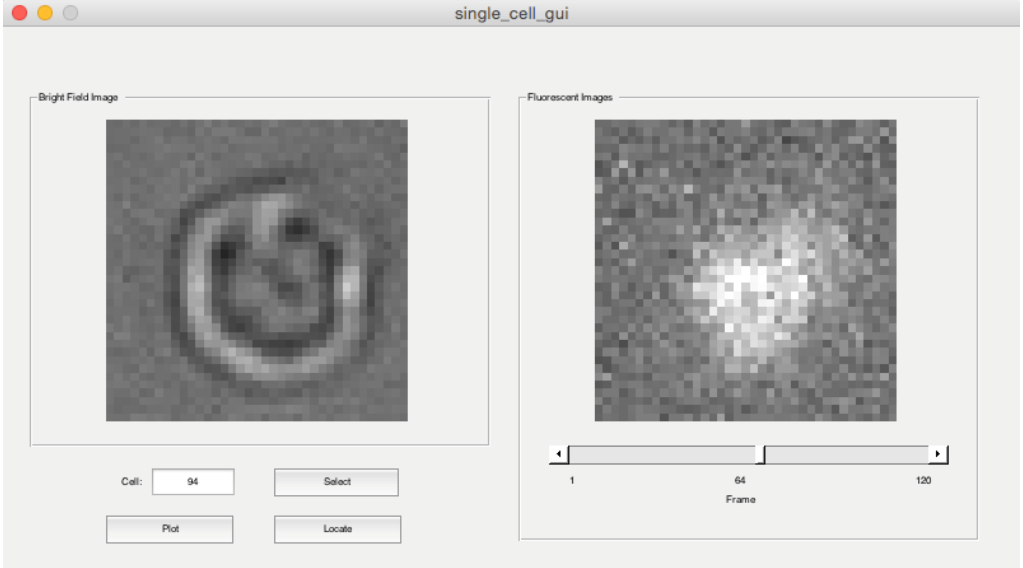

Figure B-30: MATLAB program – Single cell window with example cell selected.

Selecting the 'Plot' button displays the MFI data for the chosen cell, absolute and normalised (Figure B-31).

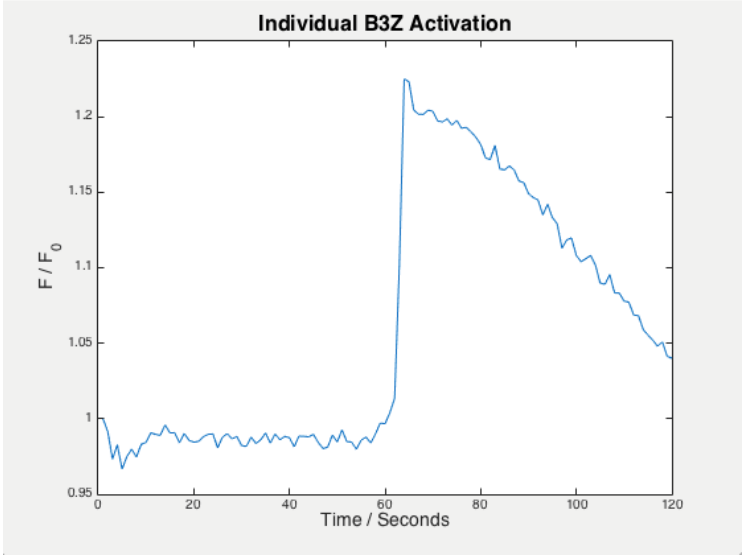

Figure B-31: MATLAB program – Single cell normalised response example.

The ‘Locate’ button highlights the cell location on the overall bright-field image, as shown in Figure B-32 for Cell 94.

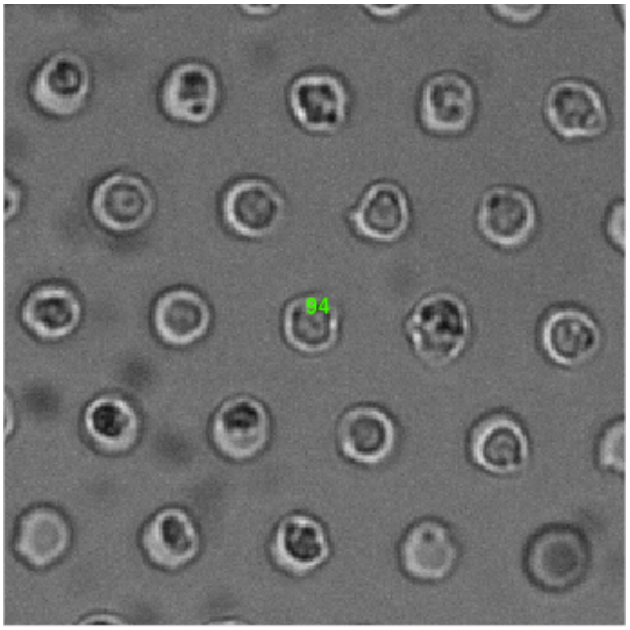

Figure B-32: MATLAB program – Single cell location example.

Bibliography

[1] T. J. Kindt, R. A. Goldsby, and B. A. Osborne, Kuby Immunology, Sixth ed. New York: W. H. Freeman and Company, 2007. Ch. 9, p. 235-236 & Ch. 10, p. 235-237, 254-259.

[2] STEMCELL technologies. (Accessed, 2016). “Frequencies of Cell Types in Human Peripheral Blood Wallchart”. [Online]. Available: http://www.stemcell.com/~/media/Files/wallchart_CellTypes_WEB.pdf?la=en

[3] QIAGEN. (Accessed, 2016). “Antigen Processing and Presentation by MHCs”. [Online]. Available: https://www.qiagen.com/gb/shop/genes-and-pathways/pathway-details/?pwid=33

[4] abcam. (Accessed, 2016). “Fluo-8 AM (ab142773)”. [Online]. Available: http://www.abcam.com/fluo-8-am-ab142773.htmL

[5] N. Joseph, B. Reicher, and M. Barda-Saad, "The calcium feedback loop and T cell activation: How cytoskeleton networks control intracellular calcium flux," Biochimica Et Biophysica Acta-Biomembranes, vol. 1838, pp. 557-568, Feb 2014.

[6] G. Grafton and L. Thwaite, "Calcium channels in lymphocytes," Immunology, vol. 104, pp. 119-126, Oct 2001.

[7] D. Di Carlo and L. P. Lee, "Dynamic single-cell analysis for quantitative biology," Analytical Chemistry, vol. 78, pp. 7918-7925, Dec 2006.

[8] M. Junkin and S. Tay, "Microfluidic single-cell analysis for systems immunology," Lab on a Chip,vol. 14, pp. 1246-1260, 2014.

[9] J. Avesar, T. B. Arye, and S. Levenberg, "Frontier microfluidic techniques for short and long-term single cell analysis," Lab on a chip, vol. 14, pp. 2161-7, Jul 2014.

[10] V. Chokkalingam, J. Tel, F. Wimmers, X. Liu, S. Semenov, J. Thiele, et al., "Probing cellular heterogeneity in cytokine-secreting immune cells using droplet-based microfluidics," Lab on a Chip, vol. 13, pp. 4740-4744, 2013.

[11] E. Delamarche, N. Tonna, R. D. Lovchik, F. Bianco, and M. Matteoli, "Pharmacology on microfluidics: multimodal analysis for studying cell-cell interaction," Current Opinion in Pharmacology, vol. 13, pp. 821-828, Oct 2013.

[12] W. Chen, N.-T. Huang, X. Li, Z. T. F. Yu, K. Kurabayashi, and J. Fu, "Emerging microfluidic tools for functional cellular immunophenotyping: a new potential paradigm for immune status characterization," Frontiers in oncology, vol. 3, pp. 98, 2013.

[13] P. S. Kim, P. P. Lee, and D. Levy, "A theory of immunodominance and adaptive regulation," Bull Math Biol, vol. 73, pp. 1645-65, Jul 2011.

[14] I. Galea, J. Stasakova, M. S. Dunscombe, C. H. Ottensmeier, T. Elliott, and S. M. Thirdborough, "CD8+T-cell cross-competition is governed by peptide-MHC class I stability," European Journal of Immunology, vol. 42, pp. 256-263, Jan 2012.

[15] S. Pion, G. J. Christianson, P. Fontaine, D. C. Roopenian, and C. Perreault, "Shaping the repertoire of cytotoxic T-Lymphocyte responses: Explanation for the

immunodominance effect whereby cytotoxic T lymphocytes specific for immunodominant antigens prevent recognition of nondominant antigens," Blood, vol. 93, pp. 952-962, Feb 1 1999.

[16] M. A. Nowak, “Immune responses against multiple epitopes: A theory for immunodominance and antigenic variation,” *Seminars in Virology*, vol. 7, pp. 83-92, Feb 1996.

[17] L. Adorini, E. Appella, G. Doria, and Z. A. Nagy, "Mechanisms Influencing the Immunodominance of T-Cell Determinants," Journal of Experimental Medicine, vol. 168, pp. 2091-2104, Dec 1 1988.

[18] J. T. W. Yewdell and J. R. Bennink, "Immunodominance in major histocompatibility complex class i-restricted t lymphocyte responses," Annual Review of Immunology, vol. 17, pp. 51-88, 1999.

[19] M. F. Kotturi, I. Scott, T. Wolfe, B. Peters, J. Sidney, H. Cheroutre, M. G. Von Herrath, M. J. Buchmeier, H. Grey, and A. Sette, "Naive precursor frequencies and mhc binding rather than the degree of epitope diversity shape cd8(+) T cell immunodominance," Journal of Immunology, vol. 181, pp. 2124-2133, Aug 1 2008.

[20] Y. Yoshimura, R. Yadav, G. J. Christianson, W. U. Ajayi, D. C. Roopenian, and S. Joyce, "Duration of alloantigen presentation and avidity of T cell antigen recognition correlate with immunodominance of ctl response to minor histocompatibility antigens," Journal of Immunology, vol. 172, pp. 6666-6674, Jun 1 2004.

[21] A. Brodovitch, P. Bongrand, and A. Pierres, "T Lymphocytes Sense Antigens within Seconds and Make a Decision within One Minute," Journal of Immunology, vol. 191, pp. 2064-2071, Sep 1 2013.

[22] S. Lindstrom and H. Andersson-Svahn, "Overview of single-cell analyses: microdevices and applications," Lab on a Chip, vol. 10, pp. 3363-3372, 2010.

[23] A. Schmid, H. Kortmann, P. S. Dittrich, and L. M. Blank, "Chemical and biological single cell analysis," Current Opinion in Biotechnology, vol. 21, pp. 12-20, Feb 2010.

[24] Y. Chen, P. Li, P.-H. Huang, Y. Xie, J. D. Mai, L. Wang, et al., "Rare cell isolation and analysis in microfluidics," Lab on a Chip, vol. 14, pp. 626-645, 2014.

[25] F. Lautenschlaeger and M. Piel, "Microfabricated devices for cell biology: all for one and one for all," Current Opinion in Cell Biology, vol. 25, pp. 116-124, Feb 2013.

[26] C. Ma, R. Fan, H. Ahmad, Q. Shi, B. Comin-Anduix, T. Chodon, et al., "A clinical microchip for evaluation of single immune cells reveals high functional heterogeneity in phenotypically similar T cells," Nature Medicine, vol. 17, pp. 738, Jun 2011.

[27] T. Thorsen, R. W. Roberts, F. H. Arnold, and S. R. Quake, "Dynamic pattern formation in a vesicle-generating microfluidic device," Phys Rev Lett, vol. 86, pp. 4163-4166, Apr 2001.

[28] J. F. Edd, D. Di Carlo, K. J. Humphry, S. Koster, D. Irimia, D. A. Weitz, et al., "Controlled encapsulation of single-cells into monodisperse picolitre drops," Lab on a Chip, vol. 8, pp. 1262-1264, Aug 2008.

[29] H. N. Joensson, M. L. Samuels, E. R. Brouzes, M. Medkova, M. Uhlen, D. R. Link, et al., "Detection and Analysis of Low-Abundance Cell-Surface Biomarkers Using

Enzymatic Amplification in Microfluidic Droplets," Angewandte Chemie-International Edition, vol. 48, pp. 2518-2521, 2009.

[30] X. Niu, S. Gulati, J. B. Edel, and A. J. deMello, "Pillar-induced droplet merging in microfluidic circuits," Lab on a Chip, vol. 8, pp. 1837-1841, 2008.

[31] E. Brouzes, M. Medkova, N. Savenelli, D. Marran, M. Twardowski, J. B. Hutchison, et al., "Droplet microfluidic technology for single-cell high-throughput screening," Proceedings of the National Academy of Sciences of the United States of America, vol. 106, pp. 14195-14200, Aug 2009.

[32] M. Sesen, T. Alan, and A. Neild, "Microfluidic on-demand droplet merging using surface acoustic waves," Lab on a chip, vol. 14, pp. 3325-33, Jul 2014.

[33] S. M. Frisch and R. A. Screaton, "Anoikis mechanisms," Current Opinion in Cell Biology, vol. 13, pp. 555-562, Oct 2001.

[34] P. J. Lee, P. J. Hung, R. Shaw, L. Jan, and L. P. Lee, "Microfluidic application-specific integrated device for monitoring direct cell-cell communication via gap junctions between individual cell pairs," Applied Physics Letters, vol. 86, May 30 2005.

[35] B. Sakmann and E. Neher, "Patch Clamp Techniques for Studying Ionic Channels in Excitable-Membranes," Annual Review of Physiology, vol. 46, pp. 455-472, 1984.

[36] D. Di Carlo, N. Aghdam, and L. P. Lee, "Single-cell enzyme concentrations, kinetics, and inhibition analysis using high-density hydrodynamic cell isolation arrays," Analytical Chemistry, vol. 78, pp. 4925-4930, Jul 2006.

[37] D. Di Carlo, L. Y. Wu, and L. P. Lee, "Dynamic single cell culture array," Lab on a Chip, vol. 6, pp. 1445-1449, 2006.

[38] A. M. Skelley, O. Kirak, H. Suh, R. Jaenisch, and J. Voldman, "Microfluidic control of cell pairing and fusion," Nature Methods, vol. 6, pp. 147-152, Feb 2009.

[39] B. Dura, Y. Liu, and J. Voldman, "Deformability-based microfluidic cell pairing and fusion," Lab on a chip, vol. 14, pp. 2783-90, Aug 2014.

[40] W. H. Tan and S. Takeuchi, "A trap-and-release integrated microfluidic system for dynamic microarray applications," Proceedings of the National Academy of Sciences of the United States of America, vol. 104, pp. 1146-1151, Jan 2007.

[41] J. P. Frimat, M. Becker, Y. Y. Chiang, U. Marggraf, D. Janasek, J. G. Hengstler, et al., "A microfluidic array with cellular valving for single cell co-culture," Lab on a Chip, vol. 11, pp. 231-237, 2011.

[42] J. Chung, Y.-J. Kim, and E. Yoon, "Highly-efficient single-cell capture in microfluidic array chips using differential hydrodynamic guiding structures," Applied Physics Letters, vol. 98, Mar 21 2011.

[43] Y.-C. Chen, Y.-H. Cheng, H. S. Kim, P. N. Ingram, J. E. Nor, and E. Yoon, "Paired single cell co-culture microenvironments isolated by two-phase flow with continuous nutrient renewal,"Lab on a chip, vol. 14, pp. 2941-7, Jul 2014.

[44] X. B. Wang, Y. Huang, J. P. H. Burt, G. H. Markx, and R. Pethig, "Selective Dielectrophoretic Confinement of Bioparticles in Potential-Energy Wells," Journal of Physics D-Applied Physics, vol. 26, pp. 1278-1285, Aug 1993.

[45] D. S. Gray, J. L. Tan, J. Voldman, and C. S. Chen, "Dielectrophoretic registration of living cells to a microelectrode array (vol 19, pg 771, 2004)," Biosens Bioelectron, vol. 19, pp. 1763, Jul 2004.

[46] M. Kirschbaum, M. S. Jaeger, T. Schenkel, T. Breinig, A. Meyerhans, and C. Duschl, "T cell activation on a single-cell level in dielectrophoresis-based microfluidic devices," Journal of Chromatography A, vol. 1202, pp. 83-89, Aug 15 2008.

[47] A. Ashkin, J. M. Dziedzic, and T. Yamane, "Optical Trapping and Manipulation of Single Cells Using Infrared-Laser Beams," Nature, vol. 330, pp. 769-771, Dec 1987.

[48] J. E. Molloy and M. J. Padgett, "Lights, action: optical tweezers," Contemporary Physics,vol. 43, pp. 241-258, Jul-Aug 2002.

[49] Gregory P. McNerney, Wolfgang Hübner, Benjamin K. Chen and Thomas Huser, “Manipulating CD4+ T cells by optical tweezers for the initiation of cell-cell transfer of HIV-1,” J Biophotonics, vol. 3, pp. 216-223, Apr 2010.

[50] Stephane Oddos, Christopher Dunsby, Marco A. Purbhoo, Anne Chauveau, Dylan M. Owen, Mark A. A. Neil, Daniel M. Davis, and Paul M. W. French, “High-Speed High-Resolution Imaging of Intercellular Immune Synapses Using Optical Tweezers,” Biophysical Journal, vol 95, pp. 66-68, Nov 2008.

[51] M. Werner, F. Merenda, J. Piguet, R. P. Salathe, and H. Vogel, "Microfluidic array cytometer based on refractive optical tweezers for parallel trapping, imaging and sorting of individual cells," Lab on a Chip, vol. 11, pp. 2432-2439, 2011.

[52] J. Kolosnjaj-Tabi, C. Wilhelm, O. Clement, and F. Gazeau, "Cell labeling with magnetic nanoparticles: Opportunity for magnetic cell imaging and cell manipulation," Journal of Nanobiotechnology, vol. 11, Dec 10 2013.

[53] H. M. Hertz, "Standing-Wave Acoustic Trap For Nonintrusive Positioning of Microparticles," Journal of Applied Physics, vol. 78, pp. 4845-4849, Oct 1995.

[54] A. Azioune, M. Storch, M. Bornens, M. Thery, and M. Piel, "Simple and rapid process for single cell micro-patterning," Lab on a Chip, vol. 9, pp. 1640-1642, 2009.

[55] Jun Huang, Lindsay J. Edwards, Brian D. Evavold, and Cheng Zhu, “Kinetics of MHC-CD8 Interaction at the T Cell Membrane,” Journal of Immunology, vol 179, pp. 7653-7662, 2007.

[56] W. B. Du, L. Li, K. P. Nichols, and R. F. Ismagilov, "SlipChip," Lab on a Chip, vol. 9, pp. 2286-2292, 2009.

[57] Chia-Wen Chang, Chien-Chung Peng, Wei-Hao Liao, and Yi-Chung Tung, “Polydimethylsiloxane SlipChip for mammalian cell culture applications,” Analyst, vol. 140, pp. 7355-7365, 2015.

[58] J. R. Rettig and A. Folch, "Large-scale single-cell trapping and imaging using microwell arrays," Analytical Chemistry, vol. 77, pp. 5628-5634, Sep 2005.

[59] M. P. Lutolf, R. Doyonnas, K. Havenstrite, K. Koleckar, and H. M. Blau, "Perturbation of single hematopoietic stem cell fates in artificial niches," Integrative Biology, vol. 1, pp. 59-69, Jan 2009.

[60] W. C. Lee, S. Rigante, A. P. Pisano, and F. A. Kuypers, "Large-scale arrays of picolitre chambers for single-cell analysis of large cell populations," Lab on a Chip, vol. 10, pp. 2952-2958, 2010.

[61] M. Charnley, M. Textor, A. Khademhosseini, and M. P. Lutolf, "Integration column: microwell arrays for mammalian cell culture," Integrative Biology, vol. 1, pp. 625-634, 2009.

[62] J. C. Love, J. L. Ronan, G. M. Grotenbreg, A. G. van der Veen, and H. L. Ploegh, "A microengraving method for rapid selection of single cells producing antigen-specific antibodies," Nat Biotechnol, vol. 24, pp. 703-707, Jun 2006.

[63] D. K. Wood, D. M. Weingeist, S. N. Bhatia, and B. P. Engelward, "Single cell trapping and DNA damage analysis using microwell arrays," Proceedings of the National Academy of Sciences of the United States of America, vol. 107, pp. 10008-10013, Jun 1 2010.

[64] M. Ochsner, M. R. Dusseiller, H. M. Grandin, S. Luna-Morris, M. Textor, V. Vogel, et al., "Micro-well arrays for 3D shape control and high resolution analysis of single cells," Lab on a Chip, vol. 7, pp. 1074-1077, 2007.

[65] E. Forslund, K. Guldevall, P. E. Olofsson, T. Frisk, A. E. Christakou, M. Wiklund, et al., "Novel Microchip-Based Tools Facilitating Live Cell Imaging and Assessment of Functional Heterogeneity within NK Cell Populations," Frontiers in immunology, vol. 3, pp. 300, 2012.

[66] K. Guldevall, B. Vanherberghen, T. Frisk, J. Hurtig, A. E. Christakou, O. Manneberg, et al., "Imaging Immune Surveillance of Individual Natural Killer Cells Confined in Microwell Arrays," Plos One, vol. 5, Nov 12 2010.

[67] A. Revzin, K. Sekine, A. Sin, R. G. Tompkins, and M. Toner, "Development of a microfabricated cytometry platform for characterization and sorting of individual leukocytes," Lab on a Chip, vol. 5, pp. 30-37, 2005.

[68] Y. Wang, P. Shah, C. Phillips, C. E. Sims, and N. L. Allbritton, "Trapping cells on a stretchable microwell array for single-cell analysis," Analytical and Bioanalytical Chemistry, vol. 402, pp. 1065-1072, Jan 2012.

[69] S. Yamamura, H. Kishi, Y. Tokimitsu, S. Kondo, R. Honda, S. R. Rao, et al., "Single-cell microarray for analyzing cellular response," Analytical Chemistry, vol. 77, pp. 8050-8056, Dec 15 2005.

[70] T. Ozawa, K. Kinoshita, S. Kadowaki, K. Tajiri, S. Kondo, R. Honda, et al., "MAC-CCD system: a novel lymphocyte microwell-array chip system equipped with CCD scanner to generate human monoclonal antibodies against influenza virus," Lab on a Chip, vol. 9, pp. 158-163, 2009.

[71] T. Sun, J. Kovac, and J. Voldman, "Image-Based Single-Cell Sorting via Dual-Photopolymerized Microwell Arrays," Analytical Chemistry, vol. 86, pp. 977-981, Jan 21 2014.

[72] W. Liu, D. Chen, W. Du, K. P. Nichols, and R. F. Ismagilov, "Slip Chip for Immunoassays in Nanoliter Volumes," Analytical Chemistry, vol. 82, pp. 3276-3282, Apr 15 2010.

[73] S. Feng, D. Wenbin, J. E. Kreutz, A. Fok, and R. F. Ismagilov, "Digital PCR on a SlipChip," Lab on a Chip, vol. 10, pp. 2666-2672, 2010.

[74] L. Liang and R. F. Ismagilov, "Protein Crystallization Using Microfluidic Technologies Based on Valves, Droplets, and SlipChip," Annual Review of Biophysics, vol. 39, pp. 139-58, 01 2010.

[75] Microchem. (Accessed, 2015). “SU-8 3000 Permanent Epoxy Negative Photoresist”. [Online]. Available: http://www.microchem.com/pdf/SU-8%203000%20Data%20Sheet.pdf

[76] J. Narasimhan and I. Papautsky, "Polymer embossing tools for rapid prototyping of plastic microfluidic devices," Journal of Micromechanics and Microengineering, vol.14, pp. 96-103, Jan 2004.

[77] H. Becker and U. Heim, "Hot embossing as a method for the fabrication of polymer high aspect ratio structures," Sensors and Actuators a-Physical, vol. 83, pp. 130-135, May 22 2000.

[78] R. Q. Frazer, R. T. Byron, P. B. Osborne, and K. P. West, "PMMA: an essential material in medicine and dentistry," Journal of long-term effects of medical implants, vol. 15, pp. 629-39, 2005.

[79] Fisheries and Aquaculture Department. (2013). “Dissolved Oxygen” [Online]. Available: http://www.fao.org/docrep/field/003/ac183e/ac183e04.htm

[80] P. Jorjani and S. S. Ozturk, "Effects of cell density and temperature on oxygen consumption rate for different mammalian cell lines," Biotechnology and Bioengineering, vol. 64, pp. 349-356, Aug 5 1999.

[81] P. Montoya. (Accessed, 2010). “Membrane Basics” [Online]. Available: http://www.permselect.com/membranes

[82] A. Zipursky, E. Bow, R. S. Seshadri, and E. J. Brown, "Leukocyte Density and Volume in Normal Subjects and in Patients with Acute Lymphoblastic Leukemia," Blood, vol. 48, pp. 361-371, 1976.

[83] T. Chatila, L. Silverman, R. Miller, and R. Geha, "Mechanisms of T-Cell Activation by the Calcium Ionophore Ionomycin," Journal of Immunology, vol. 143, pp. 1283-1289, Aug 15 1989.

[84] Sigma-Aldrich. (Accessed, 2014). “Fluorinert FC-40”. [Online]. Available: http://www.sigmaaldrich.com/catalog/product/sigma/f9755?lang=en&region=GB

[85] Santa Cruz Biotechnology. (Accessed, 2016). “Phosphate Buffered Saline: 500 ml of 10X”. [Online]. Available: http://www.scbt.com/datasheet-362298.html

[86] F. Shen, W. Du, E. K. Davydova, M. A. Karymov, J. Pandey, and R. F. Ismagilov, "Nanoliter Multiplex PCR Arrays on a SlipChip," Analytical Chemistry, vol. 82, pp. 4606-4612, Jun 1 2010.

[87] L. Li, W. Du, and R. F. Ismagilov, "User-Loaded SlipChip for Equipment-Free Multiplexed Nanoliter-Scale Experiments," Journal of the American Chemical Society, vol. 132, pp. 106-111, Jan 13 2010.

[88] L. Li, W. Du, and R. F. Ismagilov, "Multiparameter Screening on SlipChip Used for Nanoliter Protein Crystallization Combining Free Interface Diffusion and Microbatch Methods," Journal of the American Chemical Society, vol. 132, pp. 112-119, Jan 13 2010.

[89] L. Li, M. A. Karymov, K. P. Nichols, and R. F. Ismagilov, "Dead-End Filling of SlipChip Evaluated Theoretically and Experimentally as a Function of the Surface Chemistry and the Gap Size between the Plates for Lubricated and Dry SlipChips," Langmuir, vol. 26, pp. 12465-12471, Jul 20 2010.

[90] S. Begolo, F. Shen, and R. F. Ismagilov, "A microfluidic device for dry sample preservation in remote settings," Lab on a Chip, vol. 13, pp. 4331-4342, 2013.

[91] Sigma-Aldrich. (Accessed, 2016). “Calcium in Cell Culture”. [Online]. Available: http://www.sigmaaldrich.com/life-science/cell-culture/learning-center/media-expert/calcium.html

[92] F. He, W. Liu, S. Zheng, L. Zhou, B. Ye, and Z. Qi, "Ion transport through dimethyl sulfoxide (DMSO) induced transient water pores in cell membranes," Molecular Membrane Biology, vol. 29, pp. 107-113, May-Jun 2012.

[93] G. Kitchen and J. Griffin, Immunology AND Haematology, Third ed. Philadelphia: ELSEVIER, 2007. Ch. 1, p. 14-18.

[94] J. A. Ledbetter, L. E. Gentry, C. H. June, P. S. Rabinovitch, and A. F. Purchio, "Stimulation of T-Cells Through the CD3/T-Cell Receptor Complex - Role of Cytoplasmic Calcium, Protein-Kinase-C Translocation, and Phosphorylation of Pp60c-Src in the Activation Pathway," Molecular and Cellular Biology, vol. 7, pp. 650-656, Feb 1987.

[95] J. B. Imboden and J. D. Stobo, "Transmembrane Signaling by the T-Cell Antigen Receptor - Perturbation of the T3-Antigen Receptor Complex Generates Inositol Phosphates and Releases Calcium-Ions from Intracellular Stores," Journal of Experimental Medicine, vol. 161, pp. 446-456, 1985.

[96] J. B. Imboden and A. Weiss, "The T-Cell Antigen Receptor Regulates Sustained Increases in Cytoplasmic Free Ca-2+ Through Extracellular Ca-2+ Influx and Ongoing Intracellular Ca-2+ Mobilization," Biochemical Journal, vol. 247, pp. 695-700, Nov 1 1987.

[97] ThermoFisher Scientific. (Accessed, 2015). “Fluorescence SpectraViewer”. [Online]. Available: http://www.thermofisher.com/us/en/home/life-science/cell-analysis/labeling-chemistry/fluorescence-spectraviewer.html

[98] ThermoFisher Scientific. (Accessed, 2015). “UltraPureTM Agarose”. [Online]. Available: https://tools.thermofisher.com/content/sfs/manuals/ultrapure_agarose.pdf

[99] logos biosystems. (Accessed, 2012). “LUNA™ Automated Cell Counter”. [Online]. Available: http://logosbio.com/cell_counters/luna/features.php

[100] Sigma-Aldrich. (Accessed, 2016). “Agarase and Agarose”. [Online]. Available: http://www.sigmaaldrich.com/life-science/metabolomics/enzyme-explorer/learning-center/carbohydrate-analysis.html#Agarose

[101] A. Pluen, P. A. Netti, R. K. Jain, and D. A. Berk, "Diffusion of macromolecules in agarose gels: Comparison of linear and globular configurations," Biophysical Journal, vol. 77, pp. 542-552, Jul 1999.

[102] Viscopedia. (Accessed, 2016). “Dimethyl sulfoxide”. [Online]. Available: http://www.viscopedia.com/viscosity-tables/substances/dimethyl-sulfoxide/

[103] B. Kuczenski, W. C. Ruder, W. C. Messner, and P. R. LeDuc, "Probing Cellular Dynamics with a Chemical Signal Generator," Plos One, vol. 4, Mar 16 2009.

[104] Cornell Composting Science & Engineering. (1996). “Calculating the Oxygen Diffusion Coefficient in Water”. [Online]. Available: http://compost.css.cornell.edu/oxygen/oxygen.diff.water.html

[105] GE HealthCare Life Sciences. (Accessed, 2016). “DeltaVision Elite”. [Online]. Available: http://www.gelifesciences.com/webapp/wcs/stores/servlet/ProductDisplay?categoryId=493916&catalogId=10101&productId=112730&storeId=12751&langId=-1

[106] C. B. Thompson, T. Lindsten, J. A. Ledbetter, S. L. Kunkel, H. A. Young, S. G. Emerson, et al., "CD28 Activation Pathway Regulates the Production of Multiple T-Cell-Derived Lymphokines Cytokines," Proceedings of the National Academy of Sciences of the United States of America, vol. 86, pp. 1333-1337, Feb 1989.

[107] J. A. Ledbetter, J. B. Imboden, G. L. Schieven, L. S. Grosmaire, P. S. Rabinovitch, T. Lindsten, et al., "CD28 Ligation in T-Cell Activation - Evidence For 2 Signal Transduction Pathways," Blood, vol. 75, pp. 1531-1539, Apr 1 1990.

[108] J. A. Ledbetter, C. H. June, P. J. Martin, C. E. Spooner, J. A. Hansen, and K. E. Meier, "Valency Of CD3 Binding and Internalization of the CD3 Cell-Surface Complex Control T-Cell Responses to 2nd Signals - Distinction Between Effects on Protein-Kinase-C, Cytoplasmic Free Calcium, and Proliferation," Journal of Immunology, vol. 136, pp. 3945-3952, Jun 1 1986.

[109] A. G. Schrum, A. D. Wells, and L. A. Turka, "Enhanced surface TCR replenishment mediated by CD28 leads to greater TCR engagement during primary stimulation," International Immunology, vol. 12, pp. 833-842, Jun 2000.

[110] Newport Corporation. (Accessed, 2014). “Wide Five-Axis Aligner, 3 mm Travel, 8° Angular, M4 & M6”. [Online]. Available: http://search.newport.com/?q=*&x2=sku&q2=9082-M

[111] J. Berthier & P. Silberzan, “Microfluidics for Biotechnology,” Artech House, 2006, ch.3, sec.4, p.110.

[112] (Accessed, 2014). “Water Properties”. [Online]. Available: http://people.ucsc.edu/~bkdaniel/WaterProperties.html

[113] D. Robert, N. Pamme, H. Conjeaud, F. Gazeau, A. Iles, and C. Wilhelm, "Cell sorting by endocytotic capacity in a microfluidic magnetophoresis device," Lab on a Chip, vol. 11, pp. 1902-1910, 2011.

[114] C. Wilhelm and F. Gazeau, "Universal cell labelling with anionic magnetic nanoparticles," Biomaterials, vol. 29, pp. 3161-3174, Aug 2008.

[115] Sigma-Aldrich. (Accessed, 2016). “Product Specification: Iron oxide(II,III), magnetic nanoparticles solution”. [Online]. Available: http://www.sigmaaldrich.com/Graphics/COfAInfo/SigmaSAPQM/SPEC/74/747254/747254-BULK_____ALDRICH__.pdf

[116] A. J. Hughes, D. P. Spelke, Z. Xu, C.-C. Kang, D. V. Schaffer, and A. E. Herr, "Single-cell western blotting," Nature Methods, vol. 11, pp. 749, Jul 2014.

[117] C.-C. Kang, J.-M. G. Lin, Z. Xu, S. Kumar, and A. E. Herr, "Single-Cell Western Blotting after Whole-Cell Imaging to Assess Cancer Chemotherapeutic Response," Analytical Chemistry, vol. 86, pp. 10429-10436, Oct 21 2014.